Space Station Program Natural Environment Definition for Design

International Space Station Alpha

Revision B
Feburary 8, 1994

NASDA
National Space Development Agency of Japan

esa
european space agency

Canadian Space Agency | Agence spatiale canadienne

agenzia spaziale italiana
(Italian Space Agency)

National Aeronautics and Space Administration
Space Station Program Office
Johnson Space Center
Houston, Texas

REVISIONS

REV.	DESCRIPTION	PUB. DATE
	BASELINE ISSUE (REFERENCE SSCBD BB000108A EFF. 03–02–86)	03–20–86
	BASELINE ISSUE (REFERENCE SSCBD BB000258 EFF. 01–09–87)	01–15–87
A	REVISION (REFERENCE SSCBDs BB003031 EFF. 07–03–91 AND BB000727 EFF. 09–28–90)	06–91
	CHANGE A1 (REFERENCE SSCBD BB003032 EFF. 07–03–91)	07–91
B	REVISION B (REFERENCE SSBCD 00002, Dated 2–1–94)	5–13–94

SPACE STATION PROGRAM OFFICE

SPACE STATION PROGRAM NATURAL ENVIRONMENT DEFINITION FOR DESIGN

February 8, 1994

PREFACE

The contents of this document are intended to be consistent with the tasks and products to be prepared by Prime Contractor and Space Station Program (SSP) participants as defined. The Space Station Program Natural Environment Definition for Design shall be implemented on all new SSP contractual and internal activities and shall be included in any existing contracts through contract changes. This document is under the control of the Space Station Control Board, and any changes or revisions will be approved by the Program Manager.

	Signature	ORG	Date
Prepared by:	/s/Paul Boeder	ENV	2/9/94
Checked by:	/s/J. C. Lambert	ENV	2/9/94
Supervised by (Boeing):	/s/Harold Liemohn	ENV	2/9/94
Supervised by (NASA):	/s/Barry Boswell	VES	2/10/94
Approved by (Boeing):	/s/John G. Hoos	VAIT	2/9/94
Approved by (NASA):	/s/Barry Boswell	VAIT	2/10/94
DQA:	/sM. Johnson		5/12/94

NASA/ASI

INTERNATIONAL SPACE STATION ALPHA PROGRAM

SPACE STATION PROGRAM NATURAL ENVIRONMENT DEFINITION FOR DESIGN

FEBRUARY 8, 1994

/s/Dale Thomas — 3/11/94

For NASA — DATE

/s/Andrea Lorenzoni — 3/16/94

For ASI — DATE

NASA/CSA

INTERNATIONAL SPACE STATION ALPHA PROGRAM

SPACE STATION PROGRAM NATURAL ENVIRONMENT DEFINITION FOR DESIGN

FEBRUARY 8, 1994

/s/Dale Thomas — 3/11/94

For NASA — DATE

/s/R. Bryan Erb — 3/14/94

For CSA — DATE

Agreed to in principal subject to completion of detailed review by CSA and its contractor.

NASA/ESA

INTERNATIONAL SPACE STATION ALPHA PROGRAM

SPACE STATION PROGRAM NATURAL ENVIRONMENT DEFINITION FOR DESIGN

FEBRUARY 8, 1994

Dale Thomas — 3/11/94

For NASA — DATE

Helmut Heusmann — 3/23/94

For ESA — DATE

NASA/NASDA

INTERNATIONAL SPACE STATION ALPHA PROGRAM

SPACE STATION PROGRAM NATURAL ENVIRONMENT DEFINITION FOR DESIGN

FEBRUARY 8, 1994

/s/Dale Thomas — 3/11/94

For NASA — DATE

/s/Kuniaki Shiraki — 3/16/94

For NASDA Concurrence — DATE

NASA/RSA

INTERNATIONAL SPACE STATION ALPHA PROGRAM

SPACE STATION PROGRAM NATURAL ENVIRONMENT DEFINITION FOR DESIGN

FEBRUARY 8, 1994

/s/Dale Thomas _____ 3/11/94

For NASA DATE

_____ _____

For RSA DATE

SPACE STATION FREEDOM PROGRAM OFFICE

SPACE STATION PROGRAM NATURAL ENVIRONMENT DEFINITION FOR DESIGN

LIST OF CHANGES

Feburary 8, 1994

All changes to paragraphs, tables, and figures in this document are shown below:

SSCBD	ENTRY DATE	CHANGE	PARAGRAPH
00002	2–1–94	Revision B	All

TABLE OF CONTENTS

PARAGRAPH		PAGE
1.0	SCOPE AND PURPOSE	1 – 1
2.0	DOCUMENTS	2 – 1
2.1	APPLICABLE DOCUMENTS	2 – 1
2.2	REFERENCE DOCUMENTS	2 – 1
2.3	CITATIONS	2 – 1
3.0	GENERAL INFORMATION	3 – 1
3.1	FORMAT AND USE OF THE DOCUMENT	3 – 1
3.2	TERRESTRIAL SPACE	3 – 1
3.2.1	FIELDS	3 – 1
3.2.2	PLASMA AND PARTICLES	3 – 2
3.2.3	VARIABILITY	3 – 3
4.0	NEUTRAL ATMOSPHERE	4 – 1
4.1	THERMOSPHERE REGION	4 – 1
4.2	VARIATIONS	4 – 2
4.2.1	VARIATIONS WITH SOLAR ACTIVITY	4 – 3
4.2.2	VARIATIONS WITH GEOMAGNETIC ACTIVITY	4 – 3
4.2.3	THE DIURNAL VARIATION	4 – 3
4.2.4	SEMIANNUAL VARIATION	4 – 4
4.2.5	SEASONAL–LATITUDINAL VARIATIONS OF THE LOWER THERMOSPHERE DENSITY	4 – 4
4.2.6	SEASONAL–LATITUDINAL VARIATIONS OF HELIUM	4 – 4
4.2.7	THERMOSPHERIC WAVES	4 – 5
4.2.8	THERMOSPHERIC WINDS	4 – 5
4.3	SOLAR AND GEOMAGNETIC INDICES	4 – 5
4.3.1	CONTINGENCY SOLAR CONDITIONS	4 – 6
4.4	ORBITAL AND SUBORBITAL NEUTRAL ATMOSPHERE MODEL	4 – 7
4.5	MARSHALL ENGINEERING THERMOSPHERE (MET) MODEL	4 – 8
4.5.1	MARSHALL ENGINEERING THERMOSPHERE (MET) MODEL STATISTICAL ANALYSIS MODE, THERMOSPHERE VARIATIONS	4 – 9
5.0	PLASMA ENVIRONMENT	5 – 1
5.1	SPACECRAFT – PLASMA INTERACTIONS	5 – 2
5.2	IONOSPHERIC PLASMA	5 – 3
5.2.1	IONOSPHERIC DENSITY STRUCTURE*	5 – 3
5.2.2	IONOSPHERIC TEMPERATURES	5 – 5
5.2.3	IONOSPHERIC DYNAMICS	5 – 6
5.2.4	INTERNATIONAL REFERENCE IONOSPHERE 86 (IRI86)	5 – 6
5.3	AURORAL PLASMA	5 – 7
5.3.1	AURORAL MORPHOLOGY	5 – 7
5.4	POLAR IONOSPHERE AND POLAR WIND	5 – 8

5.4.1	TRANSIENT FLUXES: LOW EARTH POLAR (OR GEOSYNCHRONOUS) ORBIT	5 – 9
6.0	PENETRATING CHARGED PARTICLES	6 – 1
6.1	MAGNETOSPHERIC PARTICLES	6 – 1
6.1.1	TRAPPED RADIATION	6 – 1
6.1.2	NON–ISOTROPIC EFFECTS	6 – 3
6.2	COSMIC RAYS	6 – 3
6.2.1	GALACTIC COSMIC RAYS	6 – 4
6.2.2	SOLAR PARTICLE EVENTS	6 – 5
6.2.3	GEOMAGNETIC SHIELDING AND CUTOFF RIGIDITY	6 – 5
7.0	ELECTROMAGNETIC RADIATION	7 – 1
7.1	GALACTIC RADIO NOISE	7 – 1
7.2	SOLAR ELECTROMAGNETIC RADIATION	7 – 1
7.3	NATURAL ENVIRONMENTAL ELECTROMAGNETIC RADIATION	7 – 3
7.4	MAN–MADE NOISE	7 – 4
8.0	METEOROIDS AND ORBITAL DEBRIS	8 – 1
8.1	METEOROIDS	8 – 1
8.1.1	UNCERTAINTY IN THE METEOROID ENVIRONMENT	8 – 4
8.2	ORBITAL DEBRIS	8 – 4
8.2.1	BACKGROUND	8 – 4
8.2.2	ORBITAL DEBRIS FLUX TO A TUMBLING SURFACE	8 – 5
8.2.3	AVERAGE SHAPE AND MASS DENSITY	8 – 7
8.2.4	VELOCITY AND DIRECTION DISTRIBUTION	8 – 8
8.2.5	LIMITATIONS AND UNCERTAINTY IN THE DEBRIS FLUX MODEL	8 – 9
8.2.5.1	MEASUREMENTS OF THE CURRENT ENVIRONMENT (FACTORS WHICH ALTER THE INTERCEPT OF FLUX GROWTH CURVES)	8 – 9
8.2.5.2	TREND PROJECTION (FACTORS WHICH ALTER THE SLOPE OF FLUX GROWTH CURVES)	8 – 10
8.2.5.3	UNCERTAINTIES IN DIRECTION, VELOCITY DISTRIBUTION, AND DENSITY	8 – 13
8.3	EVALUATION OF DIRECTIONALITY EFFECTS	8 – 14
9.0	NATURAL MAGNETIC FIELD	9 – 1
10.0	THERMAL, PRESSURE, AND PHYSICAL CONSTANTS	10 – 8
10.1	SUN–EARTH CONSTANTS	10 – 8
10.2	PRESSURE PARAMETERS IN ORBIT	10 – 8
10.3	THERMAL ENVIRONMENT	10 – 8
10.3.1	GENERAL DISCUSSION	10 – 8
10.3.1.1	SOLAR CONSTANT	10 – 9
10.3.1.2	ALBEDO	10 – 9
10.3.1.3	OUTGOING LONGWAVE RADIATION	10 – 9
10.3.1.4	THE EARTH RADIATION BUDGET EXPERIMENT	10 – 10
10.3.2	THERMAL DESIGN ENVIRONMENT	10 – 10

10.3.2.1	TEMPORAL VARIATIONS	10 – 10
10.3.2.2	SOLAR ZENITH ANGLE CORRECTION FOR ALBEDO	10 – 11
10.3.2.3	CORRELATION ANALYSIS AND BENCHMARKING	10 – 12
11.0	GRAVITATIONAL FIELD	11 – 1

TABLES

TABLE		PAGE
4.3–1	MAXIMUM, MEAN, AND MINIMUM VALUES OF THE 13–MONTH SMOOTHED 10.7 CENTIMETER SOLAR RADIO NOISE FLUX (F10.7)* AND GEOMAGNETIC ACTIVITY INDEX (AP) OVER THE MEAN SOLAR CYCLE	4 – 12
4.3.1–1	RECOMMENDED SOLAR CONTINGENCY PROFILE 13–MONTH SMOOTHED F10.7	4 – 19
4.5.1–1	VARIATIONS OF GLOBAL MAXIMUM THERMOSPHERIC DENSITY	4 – 24
4.5.1–2	PROBABILITIES OF ACHIEVING A TIME INTERVAL WITHOUT ENCOUNTERING A THERMOSPHERIC DENSITY LEVEL ABOVE A GIVEN PERCENTILE VALUE	4 – 28
6.1.1–1	SPHERICAL HARMONIC COEFFICIENTS OF THE INTERNATIONAL GEOMAGNETIC REFERENCE FIELD (IGRF) 1965	6 – 7
6.1.1–2	SPHERICAL HARMONIC COEFFICIENTS OF THE INTERNATIONAL GEOMAGNETIC REFERENCE FIELD (IGRF) 1970	6 – 9
6.2.1–1	GALACTIC COSMIC RAYS* (GCRS)	6 – 11
6.2.2–1	SOLAR PARTICLE EVENTS*	6 – 24
6.2.3–1	GEOMAGNETIC CUTOFFS*	6 – 29
7.2–1	SOLAR ELECTROMAGNETIC RADIATION	7 – 6
7.2–2	PARAMETERS FOR ESTIMATING IRRADIANCE VARIABILITY OVER THE 11 YEAR SOLAR CYCLE.*	7 – 7
7.2–3	REFERENCE SOLAR IRRADIANCE, RAYLEIGH SCATTERING, OXYGEN, OZONE CROSS SECTIONS, AND ENERGY FLUX*	7 – 8
8.2.5.1–1	UNCERTAINTIES AND ACCURACY LIMITATIONS	8 – 17
9.0–1	SPHERICAL HARMONIC COEFFICIENTS OF THE INTERNATIONAL GEOMAGNETIC REFERENCE FIELD (IGRF) 1991*	9 – 4
9.0–2	SCHMIDT COEFFICIENTS	9 – 7
10.0–1	SUN–EARTH PHYSICAL CONSTANTS	10 – 14
10.0–2	EARTH THERMAL AND PRESSURE PARAMETERS	10 – 15
10.3.1.1–1	THERMAL PARAMETERS FOR 51.6 DEGREE LOW EARTH ORBIT	10 – 16
11.0–1	GRAVITATIONAL COEFFICIENTS (4 BY 4)	11 – 3

FIGURES

FIGURE		PAGE
3.2–1	SCHEMATIC VIEW OF TERRESTRIAL SPACE	3 – 4
3.2.3–1	THE SOLAR CYCLE AS REPRESENTED BY SMOOTHED SUNSPOT NUMBER FOR THE PERIOD 1700 TO 1989	3 – 5
4.1–1	NUMBER DENSITY OF ATMOSPHERIC CONSTITUENTS VERSUS ALTITUDE	4 – 29
4.2.1–1	TYPICAL ATMOSPHERIC MASS DENSITY PROFILES AT HIGH AND LOW SOLAR ACTIVITY*	4 – 30

4.2.8–1	SCHEMATIC DIAGRAM OF THE ZONAL MEAN MERIDIONAL CIRCULATION IN THE THERMOSPHERE AT EQUINOX FOR VARIOUS LEVELS OF MAGNETIC (AURORAL) ACTIVITY*	4 – 31
4.2.8–2	SCHEMATIC DIAGRAM OF THE ZONAL MEAN MERIDIONAL CIRCULATION IN THE THERMOSPHERE AT SOLSTICE FOR VARIOUS LEVELS OF MAGNETIC (AURORAL) ACTIVITY*	4 – 32
4.3–1	13–MONTH SMOOTHED VALUES OF F10.7 OVER THE MEAN SOLAR CYCLE*	4 – 33
4.3–2	13–MONTH SMOOTHED VALUES OF GEOMAGNETIC ACTIVITY INDEX (AP) OVER THE MEAN SOLAR CYCLE*	4 – 34
4.3.1–1	CONTINGENCY SOLAR FLUX ENVELOPE	4 – 35
4.5.1–1	PROBABILITY OF MEETING OR EXCEEDING A GIVE TIME INTERVAL WITHOUT EXCEEDING THE 95TH PERCENTILE DENSITY (TOP) OR 99TH PERCENTILE DENSITY (BOTTOM). THE BINS REPRESENT A RANGE OF $F_{10.7}$:1) 66–102, 2) 102–138,3) 138–174, 4) 174–210, 5) 210–246).	4 – 36
5.1–1	MODEL IONOSPHERE (IRI–86) FOR 75 DEGREES LATITUDE AND 0700 LOCAL TIME: DAWN	5 – 10
5.1–2	MODEL IONOSPHERE (IRI–86) FOR 75 DEGREES LATITUDE AND 1400 LOCAL TIME: EARLY AFTERNOON	5 – 11
5.1–3	MODEL IONOSPHERE (IRI–86) FOR 8 DEGREES LATITUDE AND 1400 LOCAL TIME: EARLY AFTERNOON	5 – 12
5.1–4	MODEL IONOSPHERE (IRI–86) FOR 8 DEGREES LATITUDE AND 0600 LOCAL TIME: DAWN	5 – 13
5.2.4–1	PLASMA DENSITY (M3) AT 400 KM FOR JULY 1 AND SOLAR MINIMUM CONDITIONS (F10.7=70.1, IRI–86 RESULTS)	5 – 14
5.2.4–2	ELECTRON ENERGIES (EV) AT 400 KM FOR JULY 1 AND SOLAR MINIMUM CONDITIONS (F10.7 = 70.1, IRI–86 RESULTS)	5 – 15
5.2.4–3	PLASMA DENSITY (M3) AS A FUNCTION OF ALTITUDE FOR JULY 1 AND SOLAR MINIMUM CONDITIONS	5 – 16
5.3–1	IONOSPHERIC ELECTRON DENSITY IN AN AURORA	5 – 9
5.3.1–1A	GLOBAL PLOTS OF THE AVERAGE INTEGRAL ENERGY FLUX (KEV/CM2.S.SR) OF PRECIPITATING ELECTRONS ARE PRESENTED IN POLAR SPECTROGRAM FORMAT, IN A MAGNETIC LOCAL TIME CORRECTED GEOMAGNETIC LATITUDE COORDINATE SYSTEM, FOR FOUR LEVELS OF KP. PLOTS APPLY GLOBALLY TO BOTH POLES*	5 – 18
5.3.1–1B	GLOBAL PLOTS OF THE AVERAGE ENERGY (KEV) OF PRECIPITATING ELECTRONS ARE PRESENTED IN POLAR SPECTROGRAM FORMAT, IN A MAGNETIC LOCAL TIME CORRECTED GEOMAGNETIC LATITUDE COORDINATE SYSTEM, FOR FOUR LEVELS OF KP. PLOTS APPLY GLOBALLY TO BOTH POLES*	5 – 20
5.4.1–1	AURORAL ELECTRON INTENSITY (CENTER OF THE ARC)*	5 – 22
5.4.1–2	DISTRIBUTION FUNCTIONS OF ELECTRONS (LEFT) AND IONS (RIGHT) FOR VERY INTENSE AURORAL FLUXES*	5 – 23
5.4.1–3	TIME HISTORY OF MODEL SUBSTORM–GEOSYNCHRONOUS PLASMA ENVIRONMENT*	5 – 24
6.1.1–1	PROTON FLUX DENSITIES AT AN ALTITUDE OF 296 KILOMETERS IN THE SOUTH ATLANTIC ANOMALY. THIS IS A REGION OF LOW MAGNETIC FIELD	6 – 30
6.1.1–2	OMNIDIRECTIONAL ISO–FLUX CONTOURS OF 1–MEV ELECTRONS: R–L PROJECTION	6 – 31
6.1.1–3	AP8MIN R–L PLOT OF ISO–FLUX CONTOURS OF PROTONS WITH AN ENERGY OF .50 MEV	6 – 32

6.1.1–4	AP8MIN EQUATORIAL OMNIDIRECTIONAL RADIAL PROFILES OF PROTON FLUX AT ENERGIES BETWEEN 0.1 AND 400 MEV	6 – 33
6.1.1–5	AP8MIN AND AP8MAX B–L PLOT OF CONSTANT INTENSITY FLUX CONTOURS OF PROTONS WITH AN ENERGY OF .50 MEV	6 – 34
6.2.1–1	CHARACTERISTICS OF GALACTIC COSMIC RAYS (GCRS)	6 – 35
6.2.1–2A	THE DIFFERENTIAL ENERGY SPECTRUM OF HYDROGEN (MOSTLY PROTONS)	6 – 36
6.2.1–2B	THE DIFFERENTIAL ENERGY SPECTRUM OF HELIUM (MOSTLY ALPHAS)	6 – 37
6.2.1–2C	THE DIFFERENTIAL ENERGY SPECTRUM OF IRON	6 – 38
6.2.2–1	EVENT–INTEGRATED PROTON FLUXES ABOVE 30 MEV FOR THE MAJOR SOLAR EVENTS OF THE 19TH AND 20TH SOLAR CYCLES	6 – 39
6.2.2–2	THE EVENT–INTEGRATED PROTON DIFFERENTIAL ENERGY SPECTRA	6 – 40
7.1–1	LEVELS OF GALACTIC RADIO NOISE AS A FUNCTION OF FREQUENCY	7 – 22
7.1–2	MEDIAN VALUES OF AVERAGE NOISE POWER EXPECTED FROM VARIOUS SOURCES (OMNIDIRECTIONAL ANTENNA NEAR SURFACE)	7 – 23
7.2–1	NORMALLY INCIDENT SOLAR RADIATION AT SEA LEVEL ON VERY CLEAR DAYS, SOLAR SPECTRAL IRRADIANCE OUTSIDE THE EARTH'S ATMOSPHERE AT 1 ASTRONOMICAL UNIT (AU), AND BLACKBODY SPECTRAL IRRADIANCE CURVE AT T = 5762 DEGREES K (NORMALIZED TO 1 AU)	7 – 24
7.3–1	POWER FLUX LEVELS FOR VARIOUS FREQUENCY RANGES OF NATURALLY–OCCURRING ELECTROMAGNETIC AND PLASMA WAVES	7 – 25
8.1–1	NORMALIZED METEOROID VELOCITY DISTRIBUTION FROM EQUATION 8.1,1	8 – 19
8.1–2	COMPARISON OF METEOROID AND ORBITAL DEBRIS FLUXES, FR, AS A FUNCTION OF SIZE.	8 – 20
8.2.4–1	NORMALIZED COLLISION VELOCITY DISTRIBUTION AS FUNCTION OF THE DEBRIS VELOCITY FOR A SPACECRAFT WITH AN ORBITAL INCLINATION OF 28.5 DEGREES.	8 – 21
8.2.4–2	ORBITAL DEBRIS REFERENCE FRAME	8 – 22
8.2.5.2–1	COMPARISON OF MODEL FLUX, FC, WITH CATALOG FLUX NOT CORRECTED FOR GEODSS RESULTS.	8 – 23
8.3–1	"K" FACTOR FOR SINGLE SIDED FLAT PLATES	8 – 24
8.3–2	"K" FACTOR FOR A RIGHT CIRCULAR CYLINDER, LENGTH TO DIAMETER RATIO = 3.1, Q = 905.	8 – 25
10.3.2.1–1	DISTRIBUTIONS OF RUNNING MEAN ALBEDOS FOR A 51.65 INCLINATION ORBIT	10–18
10.3.2.1–2	DISTRIBUTIONS OF RUNNING MEAN OUTGOING LONGWAVE RADIATION FOR A 51.65 INCLINATION ORBIT	10–19
10.3.2.2–1	YEARLY VARIATION OF ORBIT AVERAGE SOLAR ZENITH ANGLE, BETA ANGLE, AND SOLAR DECLINATION ANGLE FOR A 51.65INCLINATION ORBIT.	10–20
10.3.2.2–2	ALBEDO CORRECTION TERM	10–21
10.3.2.2–2	ALBEDO–OLR CORRELATED PAIRS	10–22
10.3.2.3–1	ALBEDO–OLR CORRELATED PAIRS	10–23

APPENDIX

APPENDIX		PAGE
A	ABBREVIATIONS AND ACRONYMS	A – 1

B MARSHALL ENGINEERING THERMOSPHERE MODEL PROGRAM LISTING . . . . . B– 1

1.0 SCOPE AND PURPOSE

The purpose of this document is to define the natural environment for design of the Space Station Program Elements (SSPEs). The natural environment includes neutral atmosphere, plasma, charged particle radiation, Electromagnetic Radiation (EMR), meteoroids, space debris, magnetic field, physical constants, and gravitational field. Communications and other unmanned satellites operate in Geosynchronous Earth Orbit (GEO). Therefore, some data are given for GEO, but the emphasis is on altitudes from 200 kilometers to 1000 kilometers (LEO) which is inclusive of the orbital design range of the SSPEs.

This document does not cover the induced environment or other effects resulting from the presence of the SSPEs. Man–made factors are included as part of the ambient natural environment; i.e., orbital debris and Radio Frequency (RF) noise generated on Earth. They are included because they are not caused by the presence of the SSPEs but form part of the ambient environment that the SSPEs experience. It is very important to take induced environments into account because they can be quite different from the unperturbed ambient natural environment.

This document does not provide techniques or engineering solutions to permit operation in the natural environment described herein.

2.0 DOCUMENTS

2.1 APPLICABLE DOCUMENTS

None

2.2 REFERENCE DOCUMENTS

None

2.3 CITATIONS

The following citations include journal articles and reports that were used to compile and formulate the information presented herein.

BRIEF CITATION	FULL CITATION
Adams, 1981	Adams, J. H., Jr., R. Silberberg, and C. H. Tsao, Cosmic ray effects on microelectronics, Part I: The near–earth particle environment, Naval Res. Lab. Memorandum Report 4506, August 25, 1981.
Adams, 1983	Adams, J. H., Jr., J. R. Letaw, and D. F Smart, Cosmic ray effects on microelectronics, Part II: The geomagnetic cutoff effects, Naval Res. Lab. Memorandum Report 5099, May 26, 1983.
Adams, 1986	Adams, J. H., Jr., Cosmic ray effects on microelectronics, Part IV. Naval Res. Lab. Memorandum Report 5901, 1986.
Anon. 1976	Anon, U.S. Standard Atmosphere, 1976, NOAA–S/T 76–1562, National Oceanic and Atmosphere Administration, National Aeronautics and Space Administration, United States Air Force, Washington D.C., October, 1976.
Anon., 1981a	Anon., Reference data for radio engineers. Intl. Telephone and Telegraph 34, 1–13, 1981.
Anon., 1981b	Anon., Solar–terrestrial research for the 1980's. Committee on Solar–Terrestrial Research. Natl. Res. 1981. 164 pp.
Anon., 1988	Anon., Space Shuttle Level II Program Definition and Requirements, National Space Transportation System Space Shuttle Flight and Ground System Specification, NSTS 07700, Vol. X, Rev. G, NASA Johnson Space Center, Houston, TX, July 13, 1988.

Barraclough, 1987	Barraclough, D. R., International Geomagnetic Reference Field: The Fourth Generation, Physics of the Earth and Planetary Interiors, Vol. 48, pp. 279–292, 1987.
Bilitza, 1986	Bilitza, D., IRI: Recent Developments, Radio Science, Vol. 21, p. 343, 1986
Bilitza, 1990	Bilitza, D., International Reference Ionosphere 1990, NSSDC/WDC–A–R&S 90–22, November 1990.
Baummer and Gross 1988	Baummer, P. and A. Gross, Worldwide Spacecraft EME Definition, Supplement 1, ECAC–CR–85–065, Supplement 1, Department of Defense, Electromagnetic Compatibility Analysis Center, Annapolis, MD. 21402, November 1988.
Cameron, 1980	Cameron, A. C. W., Elementary and Nuclidic abundances in the solar system, Harvard–Smithsonian Center for Astrophysics, preprint series No. 1357, 1980.
Comstock, 1969	Comstock, G. M., Propagation and source characteristics derived from the low–energy, multiply charged, cosmic ray nuclei. Astrophys. J. 155, 619–643, 1969.
Cour–Palais, et al., 1969	Cour–Palais, B. G., F. L. Whipple, C. T. D'Aiutolo, C. C. Dalton, J. S. Cohnanyi, M. Dubin, V. C. Frost, W. H. Kinard, I. J. Leoffler, R. J. Naumann, C. R. Nysmith, and R. C. Savin, Meteoroid Environment Model – 1969 [Near Earth to Lunar Surface]. NASA SP–8013, NASA, Washington, D.C., 1969.
Fan et al., 1966	Fan, C. Y., G. Gloeckler, and J. A. Simpson, Galactic deuterium and its energy above 20 MeV per nucleon (Galactic deuterium and energy spectrum above 20 MeV per nucleon measured by IMP–III satellite near minimum solar activity). Phys. Rev. Letters 17, 329–333, 1966.
Freier and Waddington, 1968	Freier, P. S., and C. J. Waddington, Very heavy nuclei in the primary cosmic radiation I. Observation on the energy spectrum. Phys. Rev. 175, 1641–1648, 1968.
Freier et al., 1979	Freier, P. S., J. Young, C. J. Waddington, R. Fickle, C. Gilman, and W. R. Scarlett, Charge distribution of heavy cosmic ray nuclei. 16th Intl. Cosmic Ray Conf. (Kyoto) 1, 316–321, 1979.
Garcia–Munoz et al., 1975	Garcia–Munoz, M., G. M. Mason, and J. A. Simpson, The anomalous ISUP 4/HE component in the cosmic ray spectrum at < 50 MeV per nucleon during 1972–1974. Astrophys. J. 202, 265–275, 1975.

Gussenhoven et al., 1985	Gussenhoven, M. S., D. A. Hardy, F. Rich, and W. J. Burke, High–level spacecraft charging in the low–altitude polar auroral environment. J. Geophys. Res. 90 (A11), 11009–11023, 1985.
Hardy et al., 1985	Hardy, D. A., M. S. Gussenhoven, and E. Holeman, A statistical model of auroral electron precipitation. J. Geophys. Res. 90 (A5), 4229–4248, 1985.
Hedin, 1986	Hedin, Alan E., MSIS–86 Thermospheric Model, J. Geophys. Res., Vol. 92, No. A5, pp. 4649–4662, 1987.
Heikkila, 1973	Heikkila, W. J., Aurora. EOS 54, 764, 1973.
Hickey, 1988a	Hickey, M.P., The NASA Marshall Engineering Thermosphere Model, NASA–CR–179359, 1988.
Hickey, 1988b	Hickey, M.P., An improvement in the integration procedure used in the NASA Marshall Engineering Thermosphere Model, NASA–CR–179389, 1988.
Hickey and Smith 1992	Hickey, M.P. and R.E. Smith, Ninety–Day Solar and Geomagnetic Activity Input Files for Thermospheric Variation Simulation: Simulation Data Files/Release 2, NASA Contractor Report PHY–92R031, Contract NAS8–38333.
Holland and Vaughan 1984	Holland, R.L. and W.W. Vaughan, Lagrangian Least–Squares Prediction of Solar Flux $_{(F10.7)}$, Journal of Geophysical Research, Vol. 89, No. A1, pp. 11–16, January 1, 1984.
Johnson and Smith, 1985	Johnson, D. L. and R. E. Smith, The MSFC/J70 orbital atmosphere model and the data bases for the MSFC solar activity prediction technique, NASATM–86522, 1985.
Juliusson, 1974	Juliusson, E., Charge composition and energy spectrum of cosmic–ray nuclei at energies above 20 GeV per nucleon. Ap. J. 191, 331–348, 1974.
Juliusson et al., 1983	Juliusson, E., J. J. Engelmann, J. Jorrand, L. Koch–Miramond, P. Masse, N. Petrou, N. Lund, I. L. Rasmussen, and M. Rotenberg, The galactic cosmic ray energy spectra as measured by the French–Danish instrument on HEAO–3. 18th Intl. Cosmic Ray Conf. 2, 21–24, 1983.
Jursa, 1985	Jursa, A.S., Sci. Ed., Handbook of Geophysics and the Space Environment, Air Force Geophysics Laboratory, Air Force Systems Command, 1985.
Justus et. al. 1991a	Justus, C.G., F.N. Alyea, D.M. Cunnold, W.R. Jeffries III, and D.L. Johnson, The NASA/MSFC Global Reference

	Atmosphere Model – 1990 Version (GRAM–90), Part I: Technical/User Manual, NASA TM–4268, Part I, April, 1991.
Justus et. al. 1991b	Justus, C.G., F.N. Alyea, D.M. Cunnold, W.R. Jeffries III, and D.L. Johnson, The NASA/MSFC Global Reference Atmosphere Model – 1990 Version (GRAM–90), Part II: Program/Data Listings, NASA TM–4268, Part II, June, 1991.
Kelley, 1985	Kelley, M. C., Electrical measurements in the atmosphere and the ionosphere over an active thunderstorm: 1, Campaign overview and initial results. J. Geophys. Res. 90 (A12), 9815–9823, 1985.
Kessler et al., 1989	Kessler, D. J., R. C. Reynolds, and P. D. Anz–Meador, Orbital debris environment for spacecraft designed to operate in low Earth orbit. NASA TM–100471, NASA Johnson Space Center, Houston, TX, April 1989.
Klaips et.al., 1985	Klaips, D. G., G. Dean, and R.L. Mullen, Worldwide Spacecraft EME Definition, ECAC–CR–85–065, Department of Defense, Electromagnetic Compatibility Analysis Center, Annapolis, MD. 21402, July, 1985.
Langel et.al. 1991	Langel, L.A., W. Mundt, D.R. Barraclough, C.E. Barton, V.P. Golovokow, P.J. Hood, F.J. Lowes, N.W. Peddie, Gui–Zhong Qi, and J.M. Quinn, International Geomagnetic Reference Field, 1991 Revision, Jorunal of Geomagnetism and Geoelectricity, Vol. 43, No. 12, 1991, pp. 1007–1012.
Leech and O'Gallagher, 1978	Leech, H. W., and J. J. O'Gallagher, The isotopic composition of cosmic–ray helium from 123 to 279 MeV per nucleon: A new measurement and analysis. Astrophys. J. 221, 1110–1123, 1978.
Lezniak and Webber, 1978	Lezniak, J. A., and W. R. Webber, Nuclei from 3000 MeV per nucleon to 50 GeV per nucleon. Ap. J. 223, 676–696, 1978.
Lincoln and Conkright, 1981	Lincoln, J. V. and R. O. Conkright, Eds., International, reference ionosphere – IRI 79, Rept UAG–82, World Data Center A for Solar–Terrestrial Physics, NOAA, Boulder, CO, 1981.
Marsh, et. al., 1988	Marsh, J. G., F. J. Lerch, B. H. Putney, D.C. Christodoulidis, D. E. Smith, T. L. Felsentreger, and B. V. Sanchez, A new gravitational model for the earth from satellite tracking data: GEM–T1, J. Geophys. Res., Vol. 93, No. B6, pp. 6169 –6215, 1988.

McDonald et al., 1979	McDonald, F. B., M. A. I. VanHollebeke, J. H. Trainor, N. Lal, and W. R. Webber, Galactic cosmic ray observation in the distant heliosphere. 16th Intl. Cosmic Ray Conf. (Japan) 12, 330–334, 1979.
McNeil et al., 1984	McNeil, W. J., D. A. Hardy, and R. R. O'Neal, Auroral event probability based on Defense Meteorological Satellite Program (DMSP) 2 and 4 Data. A. F. Geophys. Lab. TM–105, 1984.
Ormes, 1965	Ormes, J. F. and W. R. Webber, Measurements of the primary proton and helium spectra and their modulations using a balloon–borne Cerenkov–scintillation counter, Proc. 9th International Conference on cosmic rays, London, 349, 1965.
Orth et al., 1978	Orth, C. D., A. Buffington, G. F. Smoot, and T. S. Mast, Abundance and spectra for cosmic–ray nuclei from lithium to iron for 2 to 150 GeV per nucleon. Ap. J. 226, 1147–1161, 1978.
Price et al., 1981	Price, W. E., J. C. Pickel, T. Ellis, and F. G. Frazee, Cosmic Ray Induced Errors in I^2L Microprocessors and Logic Devices. IEEE Trans. on Nucl. Sci. NS–28, 3946–3954, 1981.
Pulliam et al., 1981	Pulliam, D. M., H. R. Anderson, K. Stammes, and M. H. Rees, Auroral electron acceleration and atmospheric interactions. J. Geophys. Res. 86 (A4), 2397–2404, 1981.
Purvis et al., 1984	Purvis, C. K., H. B. Garrett, A. C. Whittlesey, and N. J. Stevens, Design guidelines for assessing and controlling spacecraft charging effects. NASA TP 2361, 1984.
Pyle, 1961	Pyle, K. R., Private communication, 1961.
Pyle, 1981	Pyle, K. R., Private communication, 1981.
Reames and Fichtel, 1967	Reames, D. V. and C. E. Fichtel, Low–energy cosmic–ray composition and energy spectra measured in June 1965. (Low energy cosmic ray composition and energy spectra measured by sounding rockets carrying nuclear emulsions.) Phys. Rev. 162, 1291–1295, 1967.
Robinson, 1980	Robinson, R. M., Simultaneous ground and rocket–based measurements of electric fields and currents in an auroral arc. Ph.D. Thesis, Rice University, Houston, TX, 1980.
Roble, 1983	Roble, R. G., Global dynamic models of the Earth's thermosphere and ionosphere. ESA J. (Netherlands) 7, 405–429, 1983.

Ryan et al., 1972	Ryan, M. R., J. F. Ormes, and V. K. Balasubrahmanyan, Cosmic–ray proton and helium spectra above 50 GeV. Phys. Rev. Letters 28, 985–988, 1972.
Sawyer and Vette 1976	Sawyer, D. M. and J. I. Vette, AP–8 Trapped proton environment for solar maximum and solar minimum (National Space Science Data Center, Goddard Space Flight Center, NSSDC/WDC–A–R&S 76–06,) 1976.
Scarlett et al., 1978	Scarlett, W. R., P. S. Freier, and C. J. Waddington, The charge energy spectra of heavy cosmic–ray nuclei. Astrophys. and Space Sci. (Netherlands) 59, 301–311, 1978.
Simon et al., 1979	Simon, M., H. Spiegelhauer, W. K. H. Schmidt, F. Siohan, J. F. Ormes, V. K. Balasubrahmanyan, and J. F. Arens, Cosmic ray spectra of boron to iron nuclei to above 100 GeV per nucleon. 16th Intl. Cosmic Ray Conf. 1, 352–357, 1979.
Smith and West, 1982	Smith, R. E., and G. S. West, Compilers, Space and planetary environment criteria guidelines for use in space vehicle development, 1982 Revision (Volume 1), NASA TM 82478, 1982.
Smith et al., 1973	Smith, L. H., A. Buffington, G. F. Smoot, L. W. Alvarez, and W. A. Wahlig, A measurement of cosmic–ray rigidity spectra above 6 GV/C of elements from hydrogen to iron. Astrophys. J. 180, 987–1010, 1973.
Stassinopoulos and Mead, 1972	Stassinopoulos, E. G. and G. D. Mead, ALLMAG, GDALMG, LINTRA: Computer programs for geomagnectic field and field–line calculations (National Space Science Data Center, Goddard Space Flight Center, NSSDC 72–12) 1972.
Teague and Vette 1974	Teague, M. J. and J. I. Vette, A model of the trapped electron population for solar minimum (National Space Science Data Center, Goddard Space Flight Center, NSSDC 74–03) 1974.
Teague et al., 1976	Teague, M. J, K. W. Chan, and J. I. Vette, AE6: A Model environment of the trapped electrons for solar maximum (National Space Science Data Center, Goddard Space Flight Center, NSSDC/WDC–A–R&S 76–04) 1976.
Turner and Hill, 1982	Turner, R. E., and C. K. Hill, Compilers, Terrestrial environment (climatic) criteria guidelines for use in aerospace vehicle development, 1982 Revision, NASA TM 82473, 1982.

VonRosenvinge et al., 1969	VonRosenvinge, T. T., W. R. Webber, and J. F. Ormes, A comparison of the energy spectra of cosmic ray helium and heavy nuclei. Astrophys. Space Sci. 5, 342–359, 1969.
Webber and Lezniak, 1973	Webber, W. R. and J. A. Lezniak, Interplanetary radial gradients of galactic cosmic–ray protons and helium nuclei: Pioneer 8 and 9 measurements from 75 to 1.10 A.U. J. Geophys. Res. 78, 1979–2000, 1973.
Webber and Ormes, 1967	Webber, W. R., and J. F. Ormes, Cerenkov–scintillation counter measurements of nuclei heavier than helium in the primary cosmic radiation. I. Energy spectra and charge composition of nuclei heavier than helium in primary cosmic radiation from Cerenkov–scintillation counter measurements. J. Geophys Res. 72, 5957–5976, 1967.
Webber et al., 1973	Webber, W. R., J. A. Lezniak, and J. Kish, Differences in the spectra of cosmic ray nuclear species below approximately 5 GeV/nuc. Proc. 13th Intl. Cosmic Ray Conf. 1, 248–253, 1973.
Webber et al., 1979	Webber, W. R., E. C. Stone, and R. E. Vogt, The elemental composition of quiet time low energy cosmic ray measured on the Voyager spacecraft. 16th Intl. Cosmic Ray Conf. 5, 357–362, 1979.
World Meteorological Org., 1985	World Meteorological Org., Compiler, Atmospheric Ozone 1985, Assessment of Our Understanding of the Processes Controlling Its Present Distribution and Change, World Meteorological Organization Rept. No. 16, Vol. 1, Ch. 7, 1985.
Zendell et. al., 1975	Zendell, A., R. D. Brown, and S. Vincent, Gravity fields of the solar system, NASA SP–8117, 1975.

3.0 GENERAL INFORMATION

This section describes the format and use of the document and the general character of terrestrial space, which includes the Space Station Program Elements (SSPEs) orbital operating environment around the Earth.

3.1 FORMAT AND USE OF THE DOCUMENT

The format of this document is such that each section contains an explanation and numerical description of the natural environment phenomenon to which it is devoted. It is intended that these data will be sufficient for most SSPE design purposes. For additional information, the user is referred to the citations in paragraph 2.0 of this document. Background material appears in: Smith and West, 1982; Turner and Hill, 1982; and, Anon., 1988. Requests for natural environment data not specified herein should be made to the National Aeronautics and Space Administration (NASA) Space Station Program Office, Houston, Texas.

Where natural environment data or models other than those designated in this document are utilized, the burden of proof rests with the user to demonstrate to the chairman of the SSCB that the data or models meet or exceed the natural environment definitions for design specified herein.

3.2 TERRESTRIAL SPACE

This region of space extends from the base of the ionosphere at about 60 kilometers (km) above the surface of the Earth to the boundary of the magnetosphere beyond which interplanetary space is unaffected by the Earth. This distance is about 95,000 km above the surface of the Earth [16 Radii of the Earth (R_E)] in the sunward direction and several times this in the antisunward direction. This region is loosely referred to as the magnetosphere although more strictly speaking, this term means the (major) part of terrestrial space into which the Earth's magnetic field extends. The morphology is roughly axisymmetric within $4R_E$ of Earth's center, but at greater distances it becomes very unsymmetric with a long tail extending in the antisunward direction. The principal regions and their interacting phenomena are described below and illustrated in Figure 3.2–1.

3.2.1 FIELDS

The gravitational field results from the mass of the solid Earth and reflects the distribution of that mass. It traps the neutral atmosphere, constrains its motion, and controls the motion of meteoroids and debris. However, it has little effect on the rest of terrestrial space because electrical forces are so much stronger.

The magnetic field has two sources: (1) currents inside the Earth that produce about 99 percent of the field at the surface and (2) currents in the magnetosphere. The latter becomes relatively more important beyond a few R_E because the internal field decreases as the inverse distance cubed from the Earth's center.

For many purposes, the Earth's field may be regarded as a dipole tilted 11 degrees from the rotation axis and offset from the geometric center of the Earth by 430 km in the direction of southeast Asia. Many phenomena are related to magnetic latitude which, as a result of the tilt, is 11 degrees greater than geographic latitude in the longitude of eastern North America and 11 degrees less on the opposite side of the world. The offset puts the surface of the Earth, or a circular orbit, at a higher altitude within the geomagnetic field in the region of the South Atlantic off the coast of Brazil than it is elsewhere. This region is called the South Atlantic Anomaly.

There are also electric fields that result from motion of the magnetospheric plasma. In the ionosphere, these are perpendicular to the magnetic field and have magnitudes up to 0.1 to 0.5 volts per meter.

3.2.2 PLASMA AND PARTICLES

The neutral atmosphere extends from the surface to 2500 kilometers altitude or more where its density has dropped to approximately 1.0E–20 grams per cubic centimeter. Its density continues to decrease at greater altitudes, so an outer limit is not rigorously defined.

Sunlight and, to a lesser extent, fast–charged particles ionize some of the neutral atmosphere creating a plasma consisting of equal number densities of ions and electrons. In the altitude range of about 60 to 1000 km, this is called the ionosphere. The number density of the plasma is less than that of the neutral atmosphere below about 1000 km. However, collisions between plasma and neutrals are infrequent enough above about 150 km that the two are decoupled and electrical forces dominate the behavior of the ionosphere and other plasma. Between about 60 km and 150 km, the neutral atmosphere and ionosphere are coupled in a complicated way.

Plasma fills the rest of terrestrial space as well and is given various names in different regions. The region out to the field lines at $4.5R_E$ (L=4.5) is sometimes referred to as the outer ionosphere and sometimes as the plasmasphere. Beyond that, the plasma density declines to its interplanetary value of about 10 ions per cubic centimeter. Plasma is electrically neutral (equal ion and electron number densities) and its particles' distribution in energy may be described by one or more temperatures (Maxwellian distributions). Plasma may have a bulk streaming velocity as well.

In addition, there are fluxes of fast moving particles with very nonthermal energy distributions such as the trapped radiation (Van Allen belts), the aurora, and cosmic rays.

These are called penetrating charged particles. The shape of the magnetosphere, the motion of plasma, and the acceleration of the fast particles are caused by the interactions of the Earth's magnetic field rotating with the Earth, the ionosphere, and the solar wind plasma flowing past the magnetic field. (The solar wind is a very tenuous plasma that flows radially outward from the Sun through interplanetary space.)

3.2.3 VARIABILITY

Processes within terrestrial space are partly controlled by the level of solar activity. The solar activity varies more or less cyclically with an average period of 11 years. The electromagnetic radiation (EMR) emitted by the Sun varies (although not much in the visible) as does the output of solar wind, solar magnetic field, and the production of solar cosmic rays. The exact level of activity cannot be predicted very accurately although the phase within the 11–year period can be well established. Figure 3.2.3–1 shows solar activity from 1700 to 1989. In addition, regions on the Sun's surface sometimes tend to emit plasma, radio noise, and energetic particles more than the rest of the Sun. These active regions and some coronal features persist longer than the solar rotation period of 27 days, and they affect the Earth when they face it. Thus, enhanced solar activity can be estimated with some precision 27 or more days in advance.

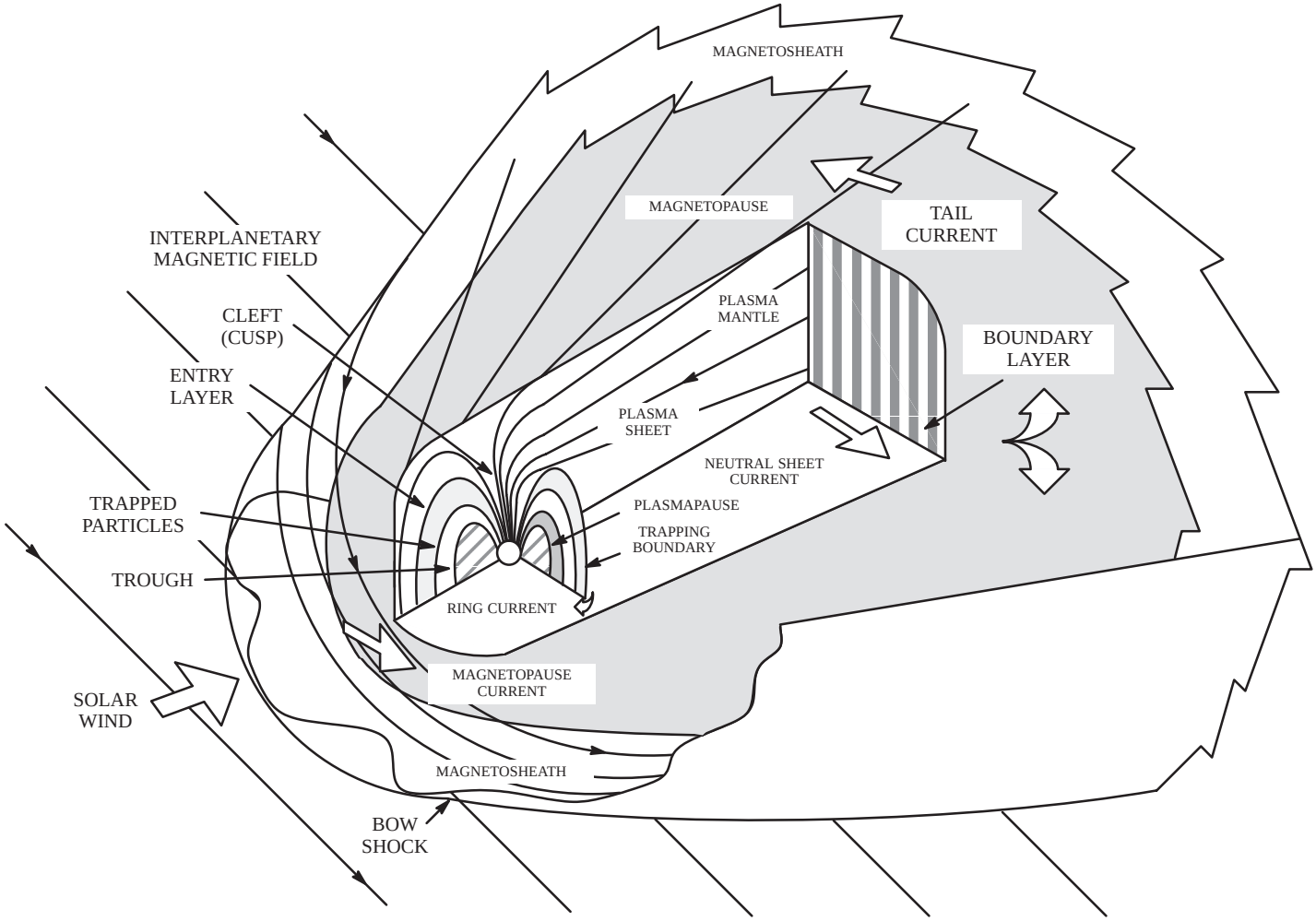

FIGURE 3.2–1 SCHEMATIC VIEW OF TERRESTRIAL SPACE

(Heikkila, 1973)

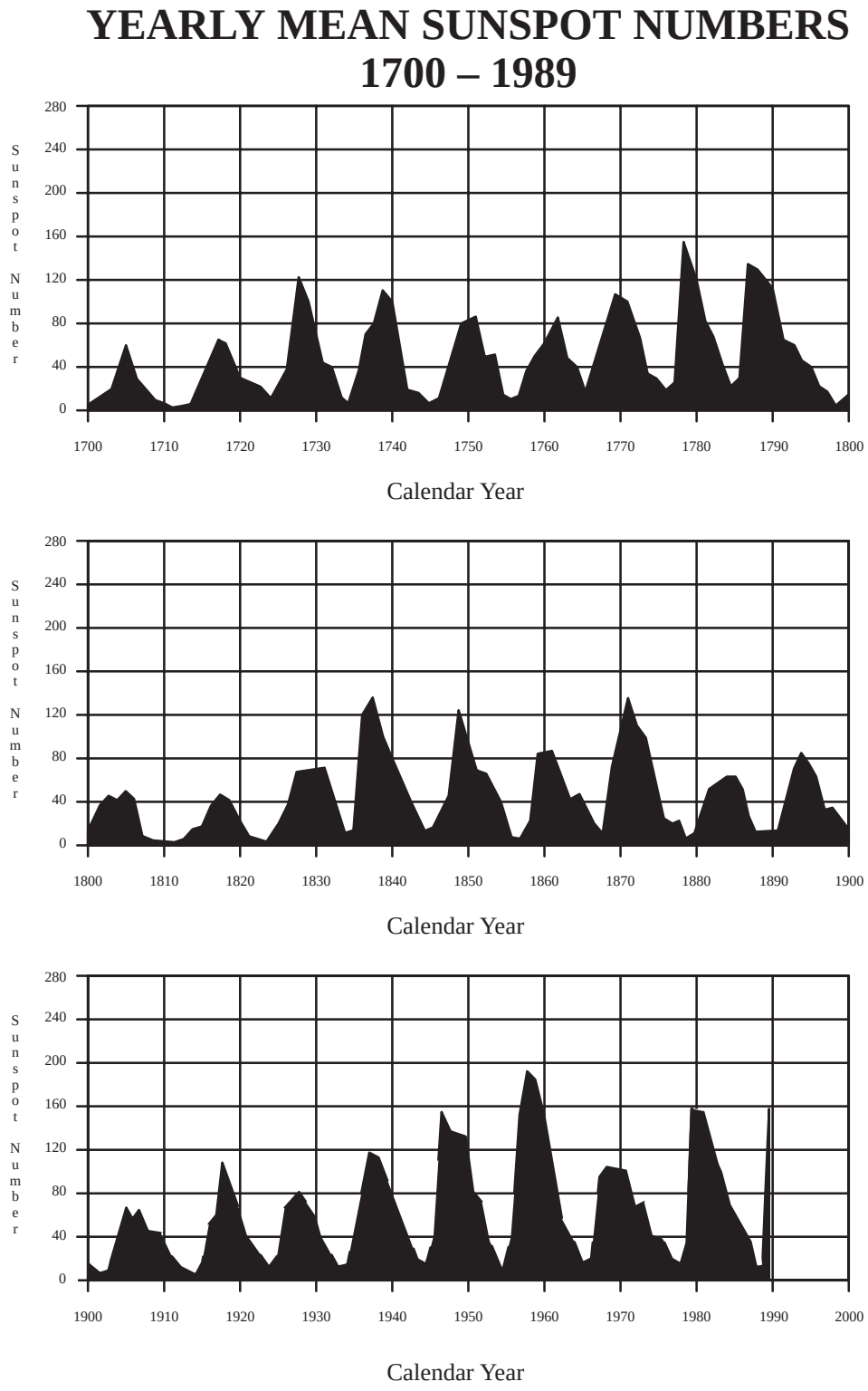

FIGURE 3.2.3–1 THE SOLAR CYCLE AS REPRESENTED BY SMOOTHED SUNSPOT NUMBER FOR THE PERIOD 1700 TO 1989

4.0 NEUTRAL ATMOSPHERE

The state of the neutral atmosphere is most conveniently described in terms of a mean, with spatial and temporal variations about that mean. For Space Station Program Element (SSPE) operations, the neutral atmosphere is significant for two reasons. First, even at its low density, it produces torques and drag on the SSFPEs. Second, the density height profile of the atmosphere above 100 kilometers (km) altitude modulates the flux of trapped radiation encountered at SSPE orbit, as explained in paragraph 6.0 of this document.

4.1 THERMOSPHERE REGION

The region of the earth's atmosphere lying between about 90 and 500 kilometers is known as the thermosphere, while that region lying above 500 kilometers is know as the exosphere. The temperature in the lower thermosphere increases rapidly with increasing altitude from a minimum at 90 kilometers. Eventually it becomes altitude–independent at upper thermospheric altitudes. This asymptotic temperature, known as the exospheric temperature, is a constant due to the extremely short thermal conduction time.

The thermospheric gases are heated by the absorption of the solar extreme ultraviolet (EUV) radiation. At the lowest thermospheric altitudes the absorption of ultraviolet (UV) radiation is also important. The EUV and UV radiation initially heat only the dayside thermosphere, and although conductive and convective processes act to redistribute some of this energy, a large temperature gradient always exists between the daytime and the nighttime thermosphere. An average daytime exospheric temperature is 1060°K and an average nighttime exospheric temperature is 840°K. The longitudinal temperature gradient causes a wind to flow from the dayside to the nightside thermosphere, with speeds typically reaching 100 m/sec.

An additional heat source for the thermosphere is the interaction of the earth's magnetic field at very great distances (at least several earth radii) in the region known as the magnetosphere with the solar wind (a stream of high speed plasma emanating from the sun). This interaction causes energetic particles to penetrate down into the lower thermosphere at high geographic latitudes and directly heat the thermospheric gas. These energetic particles are also responsible for the aurora seen at these high latitudes. In addition, electric fields mapped down from the magnetosphere onto the high latitude ionosphere cause electric currents to flow. (The ionosphere is a small fraction of the thermosphere that remains ionized due to the solar radiation. It never totally disappears at night, and during daylight hours the ionization density never exceeds more than one percent of the neutral density.) These currents lose energy through Ohmic or Joule dissipation and heat the neutral thermospheric gas. The ions also collide directly with the neutral gas, setting the whole gas into motion. At these high latitudes the wind speeds generated by this process can be very large, at times as large as 1.5 km/sec. Eventually

viscous effects dissipate these winds and their lost kinetic energy provides an additional heat source for the neutral thermospheric gas.

The high latitude heat sources are effective both during the day and night. Although an intermittent source of energy for the thermosphere, they can at times exceed the global EUV energy absorbed by the thermosphere. In addition, although the energy is deposited at high latitudes (greater than 60° or so), the disturbance effects are transmitted to lower latitudes through the actions of winds and waves. However, the disturbance effects at low latitudes are significantly smaller than they are at higher latitudes. The high latitude ionospheric currents that flow perturb the geomagnetic field, so that such disturbances, which can be detected by ground–based magnetometers, are referred to as geomagnetic storms.

Whenever the neutral thermospheric gas is heated, it expands radially outwards. Because the undisturbed thermospheric density decreases with increasing altitude, an outward expansion of the gas results in an increase of density at high altitudes. Thus, the daytime thermospheric density is greater than the nighttime density, while during times of geomagnetic storms the high latitude density is greater than it is during undisturbed periods. This anisotropic heating leads to the so–called diurnal and polar bulges, which were first inferred from the increased drag experience by orbiting satellites.

Below the turbopause, the region where the atmosphere transitions from turbulent mixing to molecular diffusion (located at about 105 kilometers altitude), the atmosphere is well mixed by turbulence, so that the composition of the atmosphere does not vary with altitude. Above the turbopause, however, diffusion becomes so rapid that the altitude variation of the various species becomes dependent on molecular mass, with the result that composition varies with altitude. Thus, the number densities of the heavier thermospheric species (N_2 and O_2) decrease with increasing altitude much faster than those of the lighter species (H and He). This means that the heavier molecular species predominate in the lower thermosphere, while the lighter atomic species predominate in the upper thermosphere. A typical altitude profile for the individual thermospheric constituents is shown in Figure 4.1–1. Lifting of the thermosphere will cause the mean molecular weight at a given altitude to increase, while a sinking motion will cause it to decrease.

4.2 VARIATIONS

Variations in the density of the neutral atmosphere at orbital altitudes are associated with variations in solar activity, geomagnetic activity, the diurnal variation, the semiannual variation, seasonal–latitudinal variations of the lower thermosphere density, seasonal–latitudinal variations of helium, atmospheric waves, and thermospheric winds. These variations are described in the paragraphs that follow.

4.2.1 VARIATIONS WITH SOLAR ACTIVITY

The short wavelength solar electromagnetic radiation (EUV and UV) changes substantially with the level of solar activity, with the result that the thermospheric density, especially at orbital altitudes, is strongly dependent on the level of solar activity. Thus, there is an average 11–year variation in the thermospheric density, corresponding to the average 11–year solar cycle variation; similarly, there is also an average 27–day variation in density that is related to the average 27–day solar rotation period, although the variation tends to be slightly longer than 27 days early in the cycle when regions occur more frequently at higher latitude and slightly shorter than 27 days later in the cycle when regions occur more frequently closer to the Sun's equator. The appearance of coronal holes and active longitudes also affects this average 27–day variation. Changes in the thermospheric density related to changes in the level of solar (and geomagnetic) activity (e.g., flares, eruptions, coronal mass ejection (CME's) and coronal holes (CH's)) can begin almost instantaneously (mins to hrs), although more often a day or more lag is seen. Figure 4.2.1–1 shows typical neutral densities for periods of high and low solar activity.

4.2.2 VARIATIONS WITH GEOMAGNETIC ACTIVITY

As previously described, the enhanced interaction of the solar wind with the Earth's magnetosphere (referred to as geomagnetic activity) leads to a high latitude heat and momentum source for the thermospheric gases. Some of this heat and momentum is convected to low latitudes. Geomagnetic activity varies over the solar cycle and usually has two or more major peaks, one during the rise of the cycle and other, larger peaks, during the decline of the cycle. Also, more intense solar cycles seem to have more intense geomagnetic activity. Finally, there is a seasonal variation with geomagnetic activity usually being greatest in March (± 1 month) and September (± 1 month) of each year. This variation is possibly related to the tilt of the Sun's rotational axis toward the Earth.

4.2.3 THE DIURNAL VARIATION

The rotation of the earth with respect to the solar EUV heat source induces a diurnal (24 hour period) variation (or, diurnal tide) in the thermospheric temperature and density. Due to a lag in the response of the thermosphere to the EUV heat source the density maximizes around 2 p.m. local solar time at orbital altitudes at a latitude approximately equal to that of the subsolar point. The lag, which is a function of altitude, decreases with decreasing altitude. Similarly, the density minimum occurs between 3 and 4 a.m. local solar time at about the same latitude in the opposite hemisphere. In the lowest regions of the thermosphere (120 kilometers and below) where the characteristic thermal conduction time is on the order of a day or more, the diurnal variation is not a predominant effect.

The various constituents of the thermosphere do not all respond to the diurnal variation of the solar EUV heat source with the same amplitude and phase. The time lag is longer, by as much as 2 hours at orbital altitudes, for the heavier constituents (N_2, O_2 and Ar) than for O. By contrast, the lighter species number densities maximize in the early morning hours (3 a.m. and 7 a.m. local solar time, for H and He, respectively). This is due to dynamical (buoyancy) effects.

Harmonics of the diurnal tide are also induced in the Earth's atmosphere. In particular, a semi–diurnal tide (period of 12 hours) and a ter–diurnal tide (period of 8 hours) are important in the lower thermosphere (below some 160 kilometers for the semi–diurnal tide, and much lower for the ter–diurnal tide). These tides are not important at orbital altitudes.

4.2.4 SEMIANNUAL VARIATION

This variation is believed to be a conduction mode of oscillation driven by a semiannual variation in Joule heating in the high latitude thermosphere (as a consequence of a semiannual variation in geomagnetic activity). The variation is latitudinally independent, and is modified by composition effects. The amplitude of the variation is height dependent and variable from year to year with a primary minimum in July, primary maximum in October, and a secondary minimum in January followed by a secondary maximum in April. It has been found that the magnitude and altitude dependence of the semiannual oscillation vary considerably from one solar cycle to the next. This variation is important at orbital altitudes.

4.2.5 SEASONAL–LATITUDINAL VARIATIONS OF THE LOWER THERMOSPHERE DENSITY

This variation is driven in the thermosphere by the dynamics of the lower atmosphere (mesosphere and below). The amplitude of the variation maximizes in the lower thermosphere somewhere between about 105 and 120 kilometers, diminishing to zero at altitudes around 200 kilometers. Although the temperature oscillation amplitude is quite large, the corresponding density oscillation amplitude is small. This variation is not important at orbital altitudes.

4.2.6 SEASONAL–LATITUDINAL VARIATIONS OF HELIUM

Satellite mass spectrometers have measured a strong increase of helium above the winter pole. Over a year the helium number density varies by a factor of 42 at 275 km, 12 at 400 km and 3 or 4 above 500 km. The formation of this winter helium bulge has been shown to be primarily due to the effects of global scale winds that blow from the summer

to the winter hemisphere. The amplitude of the bulge decreases with increasing levels of solar activity, due to the increased effectiveness of exospheric transport above 500 km which carries helium back to the summer hemisphere. There is also a very weak dependence of the helium bulge amplitude on the magnitude of the lower thermospheric eddy diffusivity.

4.2.7 THERMOSPHERIC WAVES

Atmospheric waves have been detected in temperature and density measurements throughout the atmosphere from the ground up to at least 510 km. These fluctuations are caused by gravity waves, so named because they are primarily oscillations of the neutral gas for which the restoring force is gravity. A thermospheric gravity wave produces a corresponding wave in the ionosphere known as a travelling ionospheric disturbance.

Thermospheric gravity waves oscillate with periods typically in the range of 30 minutes to several hours, and have horizontal wavelengths in the range of hundreds of kilometers up to about 4000 km. The density amplitudes of the larger scale waves are larger at higher latitudes and diminish towards the equator. Typical values are 15% at auroral latitudes and 5% at equatorial latitudes at about 200 km altitude. The smaller scale waves have amplitudes that are essentially independent of latitude. Gravity wave amplitudes generally decrease at greater altitudes in the thermosphere due to dissipation by molecular processes. The larger scale waves survive to greater altitudes than do the smaller scale waves.

4.2.8 THERMOSPHERIC WINDS

Figures 4.2.8–1 and 4.2.8–2 show the general flow pattern of thermospheric winds as they are currently known. The wind speeds range from 100 to 200 meters per second at low latitudes (less than 28.5 degrees) while at high latitudes (greater than about 65 degrees) they can be as large as 1500 meters per second or more. Rapid (minutes) changes in wind direction (of up to 180 degrees), probably driven by gravity waves, have also been observed.

4.3 SOLAR AND GEOMAGNETIC INDICES

Various surrogate indices are used to quantitatively assess the levels of solar activity. One of these is the 10.7 cm solar radio noise flux, designated $F_{10.7}$. Although it is the EUV radiation that heats the thermosphere, it cannot be measured at the ground. The $F_{10.7}$ can be measured from the ground, and it also correlates quite well with the EUV radiation. Although there are instances when the correlation is not good, it appears unlikely that the $F_{10.7}$ radio flux will be replaced by another index in the foreseeable future.

An index that is used as a measure of geomagnetic activity is the planetary geomagnetic activity index a_p (or k_p, which is essentially the logarithm of a_p). It is based on magnetic fluctuation data taken every 3 hours at 12 stations between geomagnetic latitudes 48° and 63° and selected for good longitude coverage. Although it is the high latitude ionospheric current fluctuations that drive the magnetic field fluctuations as observed at these stations, it is not the magnetic field fluctuations which are driving the thermosphere and so good correlations between observed density changes and the a_p index are not always found. The daily planetary geomagnetic index, A_p, is the average of the 8 3–hourly a_p values for that particular day.

Table 4.3–1 lists the maximum, mean and minimum 13–month smoothed values for $F_{10.7}$ and A_p throughout an 11–year solar cycle. Figures 4.3–1 and 4.3–2 show data from this table. The data are derived from sunspot records for the period 1749 to 1947 with direct measurements thereafter. Table 4.3–1 projects a mean duration cycle of 11 years. The standard deviation about the mean is 1.23 years in the historical record. “Max” and “Min” are the historical extremes for each point in the cycle and have been determined after the data have been 13–month smoothed and constrained to the mean duration cycle. The A_p values in Table 4.3–1 and Figure 4.3–2 are derived in a similar fashion based on a data record that goes back to 1932. The data in these tables are intended for applications requiring evaluation of long–term average effects (time periods in excess of 90 days). They do not properly represent the mean and limiting values for applications sensitive to shorter time scales, nor do they represent the rates of change which may be expected on a daily or monthly basis. The statistics of short period thermospheric density variations are addressed in paragraph 4.5.1 below.

4.3.1 CONTINGENCY SOLAR CONDITIONS

Observations of the solar cycle based on sunspot number have been made since early 1600’s, more reliably since the mid 1800’s. Considering the mean cycle time of 11 years, this represents 35 activity cycles, but with only 13 of good quality data – a very small sample. Modern observations have shown that the full cycle is really 22 years, so the number is actually only half this many. Given the limitations of small sample statistics, and the fact that the data do not fit a gaussian or other simple distribution, coupled with the lack of any physical rationale that defines an upper limit of solar activity or the probability that a given level will be exceeded.

Since contingency profiles are required for Space Station applications, the following recommendation is made based on the properties of the ‘‘modern” data set, cycles 10–22. The sunspot numbers have been converted to solar flux using an algorithm from Holland and Vaugham (1984). The resulting profile is illustrated in Figure 4.3.1–1, Contingency Solar Flux Envelope. It was obtained by aligning the maxima of the six even numbered cycles of the modern record with the (tentative) maximum of cycle 22, July 1989, and

extending the data for two cycles from that point. A preliminary contingency curve was developed by taking the ‘‘mean + 2 standard deviations” value of the six data points corresponding to any time. This curve has the desirable feature that it envelops the data. The peak of this curve is at $260F_{10.7}$, or 47 units above the peak of the current cycle, cycle 22. This level is appropriate because in the modern data, and most of the earlier data as well, the peak magnitude of any odd numbered cycle has exceeded the previous even numbered cycle by between 12 and 52$F_{10.7}$ units (average 38).

Since the durations and amplitudes of the cycles vary from cycle to cycle, an envelope must be defined by shifting the example curve forward and back in time. The standard deviation of the time spans from even cycle maximum to next solar minimum is 0.74 years. The near (early) side of the envelope was defined by shifting the example curve forward two standard deviations (1.48 years) from the example curve which was based on a July 1989 date for the maximum of cycle 22. The peak of cycle 22 was very flat, however, and a long cycle 22 is a possibility. Therefore, the late side of the envelope was defined by shifting the example curve two standard deviations back from a July, 1991 reference. This accounts for the fact that there is great uncertainty predicting the time of the next minimum. The result is the recommended contingency envelope in Table 4.3.1–1, illustrated in Figure 4.3.1–1. Also shown are the early and late cycle curves which define the leading and trailing edges of the envelope, respectively, which together define the example profile. Note that the solar flux would not be expected to stay at the peak level from mid 1998 to late 2003. The envelope shows the maximum level expected at any time in the future while the early and late curves show the expected extreme profiles. For applications requiring a minimum activity contingency profile, the minimum $F_{10.7}$ and A_p profiles form Table 4.3–1 are recommended.

4.4 ORBITAL AND SUBORBITAL NEUTRAL ATMOSPHERE MODEL

A single continuous representation of the neutral atmosphere from the Earth’s surface to 2500 kilometers altitude is provided by the Marshall Space Flight Center (MSFC) Global Reference Atmosphere Model (GRAM–90). GRAM–90 consists of a four dimensional (latitude, longitude, altitude and time) model of the atmosphere from the surface to 25 kilometers, that is faired to a Groves model of the atmosphere from 30 to 115 kilometers, which is then faired to the Marshall Engineering Thermosphere (MET) model that extends from 90 to 2500 kilometers. Justus et. al 1991a,b and section 3.8.1 of Turner and Hill, 1982, describe the model. The computer program for the GRAM–90 and the appropriate input parameters for the model, which depend upon the date assumed for the application, are available upon request from the Space Station Program Office, Johnson Space Center, Houston, Texas.

4.5 MARSHALL ENGINEERING THERMOSPHERE (MET) MODEL

The Marshall Engineering Thermosphere (MET) model has been developed to represent, in so far as practical for engineering applications, the variability of the ambient mass density at orbital altitudes. It is the standard neutral atmospheric density model used for control and lifetime studies involving all orbiting spacecraft projects. A listing of the FORTRAN source code appears in Appendix B, and a description of the model can be found in Johnson and Smith, 1985 and Hickey, 1988a,b. The computer program for the MET orbital atmosphere model is available upon request from the Space Station Program Office, Johnson Space Center, Houston, Texas.

The MET model is an empirical model whose coefficients were obtained from satellite drag analyses. It is a static diffusion model and is essentially the Smithsonian's Jacchia 1970 model with two additions from the Jacchia 1971 model. Inputs to the model are time (year, month, day, hour and minute), position (altitude and geographic latitude and longitude), the previous day's solar radio flux ($F_{10.7}$), the centered solar radio flux averaged over 6 solar rotations ($F_{10.7}B$) and the a_p index at 6 to 7 hours before the time in question (for some studies the daily planetary geomagnetic index, A_p, may be used instead of the 3–hourly a_p value).

With these inputs the exospheric temperature can be calculated. It should be stressed that in the original development of the model the prime objective was to model the total neutral density of the thermosphere by adjusting temperature profiles until agreement between modelled and measured total densities was achieved. Thus, agreement between modelled and measured temperature is not always achieved. Thomson–scatter temperature measurements generally show that the temperature lags the density by a couple of hours, whereas in the MET model the temperature and density are in phase.

With the exospheric temperature specified the temperature can be calculated for any altitude between the lower boundary (90 kilometers) and the upper level (2500 kilometers) of the model from an empirically determined temperature profile. The density for all points on the globe at 90 kilometers altitude is assumed constant, and mixing prevails to 105 kilometers. Between these two altitudes the mean molecular mass varies as a result of the dissociation of molecular to atomic oxygen. At 120 kilometers altitude the ratio of atomic to molecular oxygen is assumed to be 1.5. Density between 90 and 105 kilometers is calculated by integration of the barometric equation. For altitudes above 105 kilometers the diffusion equation for each of the individual species (O_2, O, N_2, He and Ar) is integrated upwards from the 105 kilometer level. For hydrogen the integration of the diffusion equation proceeds upwards from 500 kilometers altitude. The total mass density is calculated by summing the individual specie mass densities.

The total density is then further modified by the effects of the seasonal–latitudinal density variation of the lower thermosphere below 170 kilometers altitude and seasonal–latitudinal variations of helium above 500 kilometers. These two effects have

been incorporated in the MET model using equations developed by Jacchia for his 1971 thermospheric model.

The final output of the MET model is total mass density, temperature, pressure, individual specie number densities, mean molecular weight, scale–height, specific heats and the local gravitational acceleration.

The total mass density, the temperature and the individual species all have the same phase variation in the MET model (i.e., they all maximize at the same local time). For some studies involving the effects of various species on an orbiting spacecraft it may be required to use the MSIS (Mass Spectrometer Incoherent Scatter) model (Hedin, 1986) if accurate phases of the various species are required.

4.5.1 MARSHALL ENGINEERING THERMOSPHERE (MET) MODEL STATISTICAL ANALYSIS MODE, THERMOSPHERE VARIATIONS

For applications where only long–term averages of thermospheric properties need to be considered (e.g., estimation of degradation rate for a material surface), the 13–month smoothed solar and geomagnetic data from Table 4.3.–1 may be entered into the MET model in place of the daily $F_{10.7}$, 162–day averaged radio flux $F_{10.7}B$, and a_p. Because there is always substantial uncertainty in solar activity predictions, the 13–month smoothed numbers can generally be used to evaluate expected thermospheric properties for periods as short as 90 days without loss of accuracy. However, for periods shorter than 90 days these data no longer represent the statistics of the proper model inputs. For systems which are sensitive to thermospheric effects and variations over time periods of a few days or less (e.g., control and pointing systems) representative samples of daily model inputs should be used. Samples are documented in Hickey and Smith, 1992, and are available in electronic format from the Space Station Program Office, Johnson Space Center, Houston, Texas. Alternatively, for some applications the variations may be treated statistically based on the information provided below. The intent is to account for both daily changes in model input parameters and other factors (such as the use of proxy input parameters, other inaccuracies in the models, gravity and tidal wave phenomena, etc.,) whose significance increases as shorter time periods are considered. As an indicator of the magnitude of some of these effects, note that for low inclination satellites, the post–flight comparison of actual daily changes in orbit parameters with the expected changes from analysis using the MET or MSIS models indicates that the standard deviation of the relative difference between daily calculated and measured values is about 16 percent (15 to 20 percent, depending upon altitude and model).

As an initial step in describing the properties of these shorter period variations, a special MET – Statistical Analysis Mode, MET–SAM, has been developed which describes the effects of the solar $F_{10.7}$ and geomagnetic a_p variations. The statistics of these variations from 1947 to 1990 (the time span of the $F_{10.7}$ data set) were analyzed and the results are

described according to the range of the 13–month smoothed $F_{10.7}$ flux. Thus, the variations may be related to the portion of the solar cycle expected at the time of interest. MET–SAM is not yet available for general release, so an output summary table of expected density variations is provided in Table 4.5.1–1. This table presents the statistics of the global (spatial) maximum densities for averaging periods as short as three hours, the temporal resolution of the a_p data set.

Table 4.5.1–1 shows the median value of the global maximum densities for the altitude and $F_{10.7}$ bin indicated, computed over the period of record. It also gives the differences between the global maximum density and the median value of the maximum density for several percentile ranges. ‘‘Percentile” refers to the fraction of time the density was equal to or less than the indicated value. These data may be used directly to indicate the magnitudes of the variations in the global maximum density which occur over time periods of a few days. If appropriate for the application, an additional increment may be added to account for model inaccuracies and variations related to other sources. To obtain a conservative (upper limit) estimate, we recommend assuming these added variations are gaussian with a standard deviation equal to 0.2 times the total density.

To aid in understanding the frequency of occurrence of these variations, Table 4.5.1–2 provides the probabilities of encountering intervals of 10 and 30 days without exceeding the indicated percentile level. (As with Table 4.5.1–1, only solar and geomagnetic variations are considered.) Probabilities for other time intervals can be estimated from Figure 4.5.1–1. If one of these higher percentile levels is exceeded it typically drops back down within a short time (hours, a few days at most). The reader should also note that the distributions are highly skewed. Once a level has been exceeded, it is usually exceeded again with a few days. On the other hand, if the sun is quiet it may remain so for several months. Thus, consideration of conditional probabilities, i.e., ‘‘given that a level has not been exceeded for 10 or 20 days, what is the probability of going an additional 10 or 30 days with exceeding the level, ‘‘improves the figures of Table 4.5.1–2 from one to fifteen percent, depending on the case considered.

As an example of the application of these tables, suppose one is interested in estimating the variations which should be expected at a 400 km altitude near the peak of a mean solar cycle. The 13–month smoothed $F_{10.7}$ would be expected to fall in the 138–174 bin (148.7 from Table 4.3–1), so that the median global maximum density in this case is, from Table 4.5.1–1, 6.990 E–12 kg m^{-3}. To estimate the peak density that would be encountered in a 30 day interval, we note from Table 4.5.1–2 (b) that the probability that the density will remain under the 95th percentile is only 44 percent, 77 percent for the 99th percentile. Selecting the 99th percentile level, from Table 4.5.1–1 we see that the corresponding density excursion is 5.850 E–12 kg m^{-3} above the median. Thus, in one out of four cases (23 percent), the density will nearly double the expected median value for at least a short time with a 30–day period. The data presented here are for the global maximum of the density, but the global minimum and orbital average densities can be

expected to behave in similar fashion. These statistics only address the variations in model input. For some applications, the limitations in model accuracy, as discussed above, may also need to be addressed.

TABLE 4.3–1 MAXIMUM, MEAN, AND MINIMUM VALUES OF THE 13–MONTH SMOOTHED 10.7 CENTIMETER SOLAR RADIO NOISE FLUX ($F_{10.7}$)* AND GEOMAGNETIC ACTIVITY INDEX (A_p) OVER THE MEAN SOLAR CYCLE (PAGE 1 OF 7)

DATE			CYCLE	$F_{10.7}$	$F_{10.7}$	$F_{10.7}$	A_p	A_p	A_p
YR		MO	PT	MAX	MEAN	MIN	MAX	MEAN	MIN
1993	.0013	JAN	77	178.6	121.5	87.8	22.6	15.9	11.5
	.0846	FEB	78	176.3	120.5	86.5	22.5	15.8	11.3
	.1680	MAR	79	174.9	119.5	85.9	21.6	15.7	11.3
	.2513	APR	80	171.1	117.9	85.0	21.0	15.4	11.3
	.3346	MAY	81	164.5	116.3	83.6	21.1	15.2	11.2
	.4180	JUN	82	158.1	114.6	82.3	21.6	15.2	11.2
	.5013	JUL	83	154.4	112.9	81.6	22.2	15.4	11.4
	.5846	AUG	84	152.7	111.1	81.5	22.0	15.3	11.3
	.6680	SEP	85	150.8	109.5	81.9	22.0	15.2	11.4
	.7513	OCT	86	148.1	108.0	81.6	22.2	15.0	11.3
	.8346	NOV	87	145.0	106.4	81.4	22.5	14.9	11.3
	.9180	DEC	88	141.1	104.9	80.2	22.8	14.7	11.2
1994	.0013	JAN	89	137.0	103.4	80.3	23.5	14.7	11.1
	.0846	FEB	90	132.4	101.9	80.0	24.2	14.7	11.0
	.1680	MAR	91	125.4	100.3	78.9	24.7	14.8	11.3
	.2513	APR	92	119.5	98.9	77.6	25.0	14.8	11.3
	.3346	MAY	93	118.4	97.7	76.6	24.9	14.8	11.2
	.4180	JUN	94	118.7	96.6	74.8	24.5	14.8	11.4
	.5013	JUL	95	119.4	95.6	74.0	23.6	14.7	11.6
	.5846	AUG	96	119.8	94.8	73.4	22.8	14.7	11.3
	.6680	SEP	97	119.0	93.9	73.2	22.1	14.7	11.1
	.7513	OCT	98	117.7	92.8	73.1	21.8	14.8	11.1
	.8346	NOV	99	116.4	91.7	72.7	21.4	14.8	11.2
	.9180	DEC	100	114.6	90.6	71.7	21.1	14.8	11.2
1995	.0013	JAN	101	110.8	89.6	71.1	20.5	14.7	10.5
	.0846	FEB	102	105.4	88.4	70.6	19.7	14.4	9.9
	.1680	MAR	103	103.2	87.3	70.1	19.7	14.3	9.5
	.2513	APR	104	102.0	86.5	69.9	19.8	14.1	9.2

*$F_{10.7}$ is expressed in units of 10^4 Jansky, one Jansky equals 10^{-26} watts m^{-2} Hz^{-1} Bandwidth.

TABLE 4.3–1 MAXIMUM, MEAN, AND MINIMUM VALUES OF THE 13–MONTH SMOOTHED 10.7 CENTIMETER SOLAR RADIO NOISE FLUX ($F_{10.7}$)* AND GEOMAGNETIC ACTIVITY INDEX (A_p) OVER THE MEAN SOLAR CYCLE (PAGE 2 OF 7)

DATE			CYCLE	$F_{10.7}$	$F_{10.7}$	$F_{10.7}$	A_p	A_p	A_p
YR		MO	PT	MAX	MEAN	MIN	MAX	MEAN	MIN
1995	.3346	MAY	105	100.4	85.7	70.0	19.5	14.0	9.0
	.4180	JUN	106	98.2	84.8	69.9	19.1	13.8	8.9
	.5013	JUL	107	96.6	83.6	69.7	18.6	13.8	8.8
	.5846	AUG	108	94.6	82.5	69.5	17.9	13.8	8.7
	.6680	SEP	109	93.8	81.8	69.4	17.0	13.7	8.7
	.7513	OCT	110	92.7	81.1	69.3	16.5	13.6	8.8
	.8346	NOV	111	92.0	80.3	69.0	16.7	13.5	8.9
	.9180	DEC	112	91.8	79.6	68.8	16.9	13.4	9.0
1996	.0013	JAN	113	91.4	78.9	68.5	17.1	13.3	9.0
	.0846	FEB	114	90.8	78.2	68.2	17.4	13.3	9.0
	.1680	MAR	115	90.1	77.5	68.2	17.7	13.1	9.0
	.2513	APR	116	89.1	76.9	68.2	17.6	12.9	9.2
	.3346	MAY	117	88.2	76.4	68.2	17.4	12.7	9.3
	.4180	JUN	118	87.0	75.9	68.3	16.9	12.5	9.2
	.5013	JUL	119	85.4	75.3	68.3	16.1	12.2	9.1
	.5846	AUG	120	83.2	74.8	68.3	14.7	11.8	9.1
	.6680	SEP	121	80.5	74.2	68.3	13.6	11.5	9.1
	.7513	OCT	122	78.5	73.5	67.9	13.7	11.2	8.9
	.8346	NOV	123	77.6	72.9	67.6	13.4	10.9	8.5
	.9180	DEC	124	77.1	72.3	67.4	13.0	10.6	8.1
1997	.0013	JAN	125	76.9	72.0	67.4	12.7	10.5	8.0
	.0846	FEB	126	76.7	71.6	67.2	12.4	10.3	8.0
	.1680	MAR	127	76.5	71.3	67.1	11.7	10.1	8.0
	.2513	APR	128	76.2	70.9	67.0	11.2	9.9	8.0
	.3346	MAY	129	75.2	70.6	67.0	11.0	9.8	7.9
	.4180	JUN	130	74.2	70.3	67.0	10.9	9.1	7.2
	.5013	JUL	131	74.0	70.1	67.0	11.1	9.2	7.4
	.5846	AUG	132	73.5	69.9	67.0	11.4	9.4	7.6

*$F_{10.7}$ is expressed in units of 10^4 Jansky, one Jansky equals 10^{-26} watts m^{-2} Hz^{-1} Bandwidth.

TABLE 4.3–1 MAXIMUM, MEAN, AND MINIMUM VALUES OF THE 13–MONTH SMOOTHED 10.7 CENTIMETER SOLAR RADIO NOISE FLUX ($F_{10.7}$)* AND GEOMAGNETIC ACTIVITY INDEX (A_p) OVER THE MEAN SOLAR CYCLE (PAGE 3 OF 7)

DATE			CYCLE	$F_{10.7}$	$F_{10.7}$	$F_{10.7}$	A_p	A_p	A_p
YR		MO	PT	MAX	MEAN	MIN	MAX	MEAN	MIN
1997	.6680	SEP	1	73.3	69.6	67.0	11.5	9.5	7.6
	.7513	OCT	2	73.4	69.7	67.0	11.7	9.6	7.7
	.8346	NOV	3	74.0	70.0	67.0	11.8	9.7	7.7
	.9180	DEC	4	74.5	70.4	67.0	11.9	9.7	7.6
1998	.0013	JAN	5	74.9	70.7	67.0	11.9	9.7	7.4
	.0846	FEB	6	76.2	71.1	67.1	12.2	9.9	7.3
	.1680	MAR	7	78.4	71.6	67.2	12.5	10.0	7.2
	.2513	APR	8	79.8	72.2	67.3	12.9	10.3	7.3
	.3346	MAY	9	81.5	72.8	67.4	13.3	10.6	7.8
	.4180	JUN	10	84.1	73.6	67.5	14.1	10.9	8.1
	.5013	JUL	11	87.7	74.5	67.7	15.1	11.2	8.2
	.5846	AUG	12	93.4	75.7	67.9	15.7	11.5	8.3
	.6680	SEP	13	97.9	77.0	68.0	15.9	11.8	8.3
	.7513	OCT	14	101.7	78.4	68.0	16.4	12.0	8.3
	.8346	NOV	15	107.7	80.1	68.0	17.4	12.3	8.5
	.9180	DEC	16	114.5	82.0	68.0	18.4	12.7	8.4
1999	.0013	JAN	17	121.1	84.0	68.1	18.7	12.9	8.5
	.0846	FEB	18	129.1	86.2	68.4	18.8	13.1	8.7
	.1680	MAR	19	137.6	88.5	68.5	18.6	13.2	9.0
	.2513	APR	20	143.4	91.0	68.6	18.3	13.2	9.3
	.3346	MAY	21	147.6	93.7	68.8	18.1	13.2	9.7
	.4180	JUN	22	151.7	96.3	68.7	18.4	13.4	9.5
	.5013	JUL	23	155.7	98.9	68.8	18.4	13.5	9.3
	.5846	AUG	24	160.1	101.6	69.2	17.6	13.5	9.0
	.6680	SEP	25	164.8	104.4	69.7	17.1	13.6	9.0
	.7513	OCT	26	169.1	107.2	70.1	17.4	13.6	9.1
	.8346	NOV	27	173.0	110.2	70.6	17.4	13.6	9.4
	.9180	DEC	28	177.1	113.2	70.7	18.5	13.8	9.8

*$F_{10.7}$ is expressed in units of 10^4 Jansky, one Jansky equals 10^{-26} watts m^{-2} Hz^{-1} Bandwidth.

TABLE 4.3–1 MAXIMUM, MEAN, AND MINIMUM VALUES OF THE 13–MONTH SMOOTHED 10.7 CENTIMETER SOLAR RADIO NOISE FLUX ($F_{10.7}$)* AND GEOMAGNETIC ACTIVITY INDEX (A_p) OVER THE MEAN SOLAR CYCLE (PAGE 4 OF 7)

DATE			CYCLE	$F_{10.7}$	$F_{10.7}$	$F_{10.7}$	A_p	A_p	A_p
YR		MO	PT	MAX	MEAN	MIN	MAX	MEAN	MIN
2000	.0013	JAN	29	186.1	116.2	71.3	19.9	14.0	10.0
	.0846	FEB	30	191.5	119.3	72.2	19.9	14.1	10.0
	.1680	MAR	31	194.3	122.0	72.6	19.9	14.1	10.1
	.2513	APR	32	196.9	124.3	73.3	20.1	14.1	10.4
	.3346	MAY	33	199.6	126.5	73.9	20.4	14.2	10.2
	.4180	JUN	34	204.2	128.6	74.1	20.8	14.2	10.3
	.5013	JUL	35	210.6	131.0	74.4	20.9	14.1	10.6
	.5846	AUG	36	214.8	133.3	74.5	21.0	14.0	10.6
	.6680	SEP	37	217.2	135.6	74.6	21.2	14.0	10.5
	.7513	OCT	38	221.6	137.6	74.5	21.6	14.1	10.4
	.8346	NOV	39	226.9	139.6	74.1	22.1	14.1	10.6
	.9180	DEC	40	229.9	141.4	73.6	22.2	14.0	10.8
2001	.0013	JAN	41	231.7	143.2	73.5	21.0	13.7	10.7
	.0846	FEB	42	233.7	144.6	73.6	20.1	13.4	10.4
	.1680	MAR	43	235.6	145.6	74.0	19.8	13.3	10.5
	.2513	APR	44	238.8	146.7	75.1	19.3	13.3	10.7
	.3346	MAY	45	242.8	147.2	75.8	19.2	13.3	10.8
	.4180	JUN	46	245.2	147.7	76.5	19.0	13.4	11.0
	.5013	JUL	47	244.5	148.1	78.1	18.8	13.3	10.7
	.5846	AUG	48	243.3	148.4	80.1	18.6	13.4	10.8
	.6680	SEP	49	244.7	148.7	82.5	18.6	13.4	10.6
	.7513	OCT	50	245.7	148.2	84.0	18.3	13.4	10.2
	.8346	NOV	51	243.3	146.8	85.5	18.2	13.5	10.6
	.9180	DEC	52	239.4	145.7	87.9	18.7	13.8	11.3
2002	.0013	JAN	53	235.0	145.1	89.5	19.2	14.1	11.4
	.0846	FEB	54	232.9	144.9	92.2	19.6	14.2	11.3
	.1680	MAR	55	233.3	144.9	93.8	20.3	14.4	11.3
	.2513	APR	56	233.1	144.7	94.9	21.0	14.6	11.5

*$F_{10.7}$ is expressed in units of 10^4 Jansky, one Jansky equals 10^{-26} watts m^{-2} Hz^{-1} Bandwidth.

TABLE 4.3–1 MAXIMUM, MEAN, AND MINIMUM VALUES OF THE 13–MONTH SMOOTHED 10.7 CENTIMETER SOLAR RADIO NOISE FLUX ($F_{10.7}$)* AND GEOMAGNETIC ACTIVITY INDEX (A_p) OVER THE MEAN SOLAR CYCLE (PAGE 5 OF 7)

DATE			CYCLE	$F_{10.7}$	$F_{10.7}$	$F_{10.7}$	A_p	A_p	A_p
YR		MO	PT	MAX	MEAN	MIN	MAX	MEAN	MIN
2002	.3346	MAY	57	231.2	144.2	95.0	21.4	14.8	11.6
	.4180	JUN	58	229.1	143.5	94.7	21.2	14.8	11.6
	.5013	JUL	59	228.1	142.7	94.9	20.4	14.7	11.8
	.5846	AUG	60	227.6	142.3	96.5	20.7	14.8	12.1
	.6680	SEP	61	226.7	142.1	97.3	21.9	15.1	12.2
	.7513	OCT	62	225.6	141.3	96.8	22.7	15.2	12.0
	.8346	NOV	63	223.0	140.1	96.0	22.7	15.1	11.6
	.9180	DEC	64	218.6	138.4	96.0	22.3	15.1	11.2
2003	.0013	JAN	65	215.2	136.8	96.6	21.7	15.1	11.2
	.0846	FEB	66	212.0	135.5	96.7	21.5	15.1	11.2
	.1680	MAR	67	206.9	134.3	95.1	22.1	15.1	11.2
	.2513	APR	68	204.0	133.0	95.0	23.1	15.5	11.3
	.3346	MAY	69	203.6	131.6	96.3	23.5	15.6	11.3
	.4180	JUN	70	200.4	129.8	96.5	23.4	15.6	11.2
	.5013	JUL	71	196.8	128.3	94.7	23.3	15.7	11.1
	.5846	AUG	72	195.7	127.3	93.6	23.1	15.5	10.8
	.6680	SEP	73	194.8	126.5	93.5	22.2	15.7	10.9
	.7513	OCT	74	191.5	125.1	91.9	22.1	15.6	11.1
	.8346	NOV	75	187.4	123.5	88.7	22.2	15.6	11.7
	.9180	DEC	76	182.9	122.3	86.6	22.5	15.8	11.6
2004	.0013	JAN	77	178.6	121.5	87.8	22.6	15.9	11.5
	.0846	FEB	78	176.3	120.5	86.5	22.5	15.8	11.3
	.1680	MAR	79	174.9	119.5	85.9	21.6	15.7	11.3
	.2513	APR	80	171.1	117.9	85.0	21.0	15.4	11.3
	.3346	MAY	81	164.5	116.3	83.6	21.1	15.2	11.2
	.4180	JUN	82	158.1	114.6	82.3	21.6	15.2	11.2
	.5013	JUL	83	154.4	112.9	81.6	22.2	15.4	11.4
	.5846	AUG	84	152.7	111.1	81.5	22.0	15.3	11.3
	.6680	SEP	85	150.8	109.5	81.9	22.0	15.2	11.4
	.7513	OCT	86	148.1	108.0	81.6	22.2	15.0	11.3
	.8346	NOV	87	145.0	106.4	81.4	22.5	14.9	11.3
	.9180	DEC	88	141.1	104.9	80.2	22.8	14.7	11.2

*$F_{10.7}$ is expressed in units of 10^4 Jansky, one Jansky equals 10^{-26} watts m^{-2} Hz^{-1} Bandwidth.

TABLE 4.3–1 MAXIMUM, MEAN, AND MINIMUM VALUES OF THE 13–MONTH SMOOTHED 10.7 CENTIMETER SOLAR RADIO NOISE FLUX ($F_{10.7}$)* AND GEOMAGNETIC ACTIVITY INDEX (A_p) OVER THE MEAN SOLAR CYCLE (PAGE 6 OF 7)

DATE			CYCLE	$F_{10.7}$	$F_{10.7}$	$F_{10.7}$	A_p	A_p	A_p
YR		MO	PT	MAX	MEAN	MIN	MAX	MEAN	MIN
2005	.0013	JAN	89	137.0	103.4	80.3	23.5	14.7	11.1
	.0846	FEB	90	132.4	101.9	80.0	24.2	14.7	11.0
	.1680	MAR	91	125.4	100.3	78.9	24.7	14.8	11.3
	.2513	APR	92	119.5	98.9	77.6	25.0	14.8	11.3
	.3346	MAY	93	118.4	97.7	76.6	24.9	14.8	11.2
	.4180	JUN	94	118.7	96.6	74.8	24.5	14.8	11.4
	.5013	JUL	95	119.4	95.6	74.0	23.6	14.7	11.6
	.5846	AUG	96	119.8	94.8	73.4	22.8	14.7	11.3
	.6680	SEP	97	119.0	93.9	73.2	22.1	14.7	11.1
	.7513	OCT	98	117.7	92.8	73.1	21.8	14.8	11.1
	.8346	NOV	99	116.4	91.7	72.7	21.4	14.8	11.2
	.9180	DEC	100	114.6	90.6	71.7	21.1	14.8	11.2
2006	.0013	JAN	101	110.8	89.6	71.1	20.5	14.7	10.5
	.0846	FEB	102	105.4	88.4	70.6	19.7	14.4	9.9
	.1680	MAR	103	103.2	87.3	70.1	19.7	14.3	9.5
	.2513	APR	104	102.0	86.5	69.9	19.8	14.1	9.2
	.3346	MAY	105	100.4	85.7	70.0	19.5	14.0	9.0
	.4180	JUN	106	98.2	84.8	69.9	19.1	13.8	8.9
	.5013	JUL	107	96.6	83.6	69.7	18.6	13.8	8.8
	.5846	AUG	108	94.6	82.5	69.5	17.9	13.8	8.7
	.6680	SEP	109	93.8	81.8	69.4	17.0	13.7	8.7
	.7513	OCT	110	92.7	81.1	69.3	16.5	13.6	8.8
	.8346	NOV	111	92.0	80.3	69.0	16.7	13.5	8.9
	.9180	DEC	112	91.8	79.6	68.8	16.9	13.4	9.0
2007	.0013	JAN	113	91.4	78.9	68.5	17.1	13.3	9.0
	.0846	FEB	114	90.8	78.2	68.2	17.4	13.3	9.0
	.1680	MAR	115	90.1	77.5	68.2	17.7	13.1	9.0
	.2513	APR	116	89.1	76.9	68.2	17.6	12.9	9.2
	.3346	MAY	117	88.2	76.4	68.2	17.4	12.7	9.3

*$F_{10.7}$ is expressed in units of 10^4 Jansky, one Jansky equals 10^{-26} watts m^{-2} Hz^{-1} Bandwidth.

TABLE 4.3–1 MAXIMUM, MEAN, AND MINIMUM VALUES OF THE 13–MONTH SMOOTHED 10.7 CENTIMETER SOLAR RADIO NOISE FLUX ($F_{10.7}$)* AND GEOMAGNETIC ACTIVITY INDEX (A_p) OVER THE MEAN SOLAR CYCLE (PAGE 7 OF 7)

DATE			CYCLE	$F_{10.7}$	$F_{10.7}$	$F_{10.7}$	A_p	A_p	A_p
YR		MO	PT	MAX	MEAN	MIN	MAX	MEAN	MIN
2007	.4180	JUN	118	87.0	75.9	68.3	16.9	12.5	9.2
	.5013	JUL	119	85.4	75.3	68.3	16.1	12.2	9.1
	.5846	AUG	120	83.2	74.8	68.3	14.7	11.8	9.1
	.6680	SEP	121	80.5	74.2	68.3	13.6	11.5	9.1
	.7513	OCT	122	78.5	73.5	67.9	13.7	11.2	8.9
	.8346	NOV	123	77.6	72.9	67.6	13.4	10.9	8.5
	.9180	DEC	124	77.1	72.3	67.4	13.0	10.6	8.1
2008	.0013	JAN	125	76.9	72.0	67.4	12.7	10.5	8.0
	.0846	FEB	126	76.7	71.6	67.2	12.4	10.3	8.0
	.1680	MAR	127	76.5	71.3	67.1	11.7	10.1	8.0
	.2513	APR	128	76.2	70.9	67.0	11.2	9.9	8.0
	.3346	MAY	129	75.2	70.6	67.0	11.0	9.8	7.9
	.4180	JUN	130	74.2	70.3	67.0	10.9	9.1	7.2
	.5013	JUL	131	74.0	70.1	67.0	11.1	9.2	7.4
	.5846	AUG	132	73.5	69.9	67.0	11.4	9.4	7.6

This table may be extended by repetition of the eleven year cycle.

*$F_{10.7}$ is expressed in units of 10^4 Jansky, one Jansky equals 10^{-26} watts m^{-2} Hz^{-1} Bandwidth.

TABLE 4.3.1–1 RECOMMENDED SOLAR CONTINGENCY PROFILE 13–MONTH SMOOTHED $F_{10.7}$ (Page 1 of 5)

Year	Months Since Maximum	$F_{10.7}$ Envelope	Early	Late
1995.0010	66	180.0	86.8	180.0
1995.0850	67	177.0	90.0	177.0
1995.1680	68	172.1	93.1	172.1
1995.2510	69	168.2	96.6	168.2
1995.3350	70	166.0	100.7	166.0
1995.4180	71	164.7	104.6	164.7
1995.5010	72	162.8	107.9	162.8
1995.5850	73	160.4	111.0	160.4
1995.6680	74	156.9	113.9	156.9
1995.7510	75	152.3	117.5	152.3
1995.8350	76	147.2	121.5	147.2
1995.9180	77	142.9	125.0	142.9
1996.0010	78	140.2	128.8	140.2
1996.0850	79	138.4	134.3	138.4
1996.1680	80	139.9	139.9	136.9
1996.2510	81	144.8	144.8	135.9
1996.3350	82	149.4	149.4	135.1
1996.4180	83	154.2	154.2	134.1
1996.5010	84	159.6	159.6	132.7
1996.5850	85	166.2	166.2	130.3
1996.6680	86	174.1	174.1	128.4
1996.7510	87	181.3	181.3	128.2
1996.8350	88	187.1	187.1	127.8
1996.9180	89	192.2	192.2	126.5
1997.0010	90	196.5	196.5	124.8
1997.0850	91	199.6	199.6	122.4
1997.1680	92	200.6	200.6	119.8
1997.2510	93	201.6	201.6	117.0
1997.3350	94	204.6	204.6	113.1
1997.4180	95	207.8	207.8	108.8
1997.5010	96	211.9	211.9	105.9
1997.5850	97	216.4	216.4	104.3
1997.6680	98	218.8	218.8	102.4

TABLE 4.3.1–1 RECOMMENDED SOLAR CONTINGENCY PROFILE 13–MONTH SMOOTHED $F_{10.7}$ (Page 2 of 5)

Year	Months Since Maximum	$F_{10.7}$ Envelope	Early	Late
1997.7510	99	222.3	222.3	99.8
1997.8350	100	228.6	228.6	97.5
1997.9180	101	233.6	233.6	96.1
1998.0010	102	238.2	238.2	95.7
1998.0850	103	244.1	244.1	95.2
1998.1680	104	249.3	249.3	94.1
1998.2510	105	252.8	252.8	93.4
1998.3350	106	255.9	255.9	93.2
1998.4180	107	258.3	258.3	92.7
1998.5010	108	259.1	259.1	91.8
1998.5850	109	259.2	259.2	90.5
1998.6680	110	259.4	259.4	89.0
1998.7510	111	260.0	257.6	87.5
1998.8350	112	260.0	254.0	85.4
1998.9180	113	260.0	250.8	83.2
1999.0010	114	260.0	248.4	81.6
1999.0850	115	260.0	246.9	80.5
1999.1680	116	260.0	245.5	79.7
1999.2510	117	260.0	243.8	78.2
1999.3350	118	260.0	241.7	76.7
1999.4180	119	260.0	240.1	75.8
1999.5010	120	260.0	239.2	75.8
1999.5850	121	260.0	237.1	76.6
1999.6680	122	260.0	234.9	77.7
1999.7510	123	260.0	233.1	79.3
1999.8350	124	260.0	230.1	81.7
1999.9180	125	260.0	226.4	85.0
2000.0010	126	260.0	222.0	88.1
2000.0850	127	260.0	218.3	91.0
2000.1680	128	260.0	216.5	94.5
2000.2510	129	260.0	214.7	98.2
2000.3350	130	260.0	212.6	102.2
2000.4180	131	260.0	210.4	106.1

TABLE 4.3.1–1 RECOMMENDED SOLAR CONTINGENCY PROFILE 13–MONTH SMOOTHED $F_{10.7}$ (Page 3 of 5)

Year	Months Since Maximum	$F_{10.7}$ Envelope	Early	Late
2000.5010	132	260.0	207.8	109.2
2000.5850	133	260.0	205.6	112.0
2000.6680	134	260.0	204.2	115.4
2000.7510	135	260.0	203.1	119.2
2000.8350	136	260.0	200.8	122.8
2000.9180	137	260.0	197.6	126.5
2001.0010	138	260.0	195.2	130.9
2001.0850	139	260.0	191.1	136.4
2001.1680	140	260.0	185.6	142.2
2001.2510	141	260.0	180.6	146.6
2001.3350	142	260.0	175.1	151.0
2001.4180	143	260.0	170.2	156.5
2001.5010	144	260.0	166.9	162.0
2001.5850	145	260.0	162.7	169.1
2001.6680	146	260.0	155.5	177.5
2001.7510	147	260.0	148.3	183.7
2001.8350	148	260.0	143.7	189.0
2001.9180	149	260.0	141.9	194.2
2002.0010	150	260.0	140.6	198.1
2002.0850	151	260.0	138.4	200.1
2002.1680	152	260.0	135.7	200.7
2002.2510	153	260.0	132.2	202.8
2002.3350	154	260.0	128.0	205.7
2002.4180	155	260.0	123.8	209.4
2002.5010	156	260.0	118.8	214.1
2002.5850	157	260.0	115.2	217.3
2002.6680	158	260.0	115.2	219.9
2002.7510	159	260.0	116.0	224.9
2002.8350	160	260.0	115.7	230.6
2002.9180	161	260.0	114.3	235.4
2003.0010	162	260.0	111.9	240.5
2003.0850	163	260.0	108.5	246.2
2003.1680	164	260.0	105.4	251.0

TABLE 4.3.1–1 RECOMMENDED SOLAR CONTINGENCY PROFILE 13–MONTH SMOOTHED $F_{10.7}$ (Page 4 of 5)

Year	Months Since Maximum	$F_{10.7}$ Envelope	Early	Late
2003.2510	165	260.0	102.8	254.0
2003.3350	166	260.0	100.3	257.0
2003.4180	167	260.0	99.0	258.8
2003.5010	168	260.0	98.3	259.1
2003.5850	169	259.6	96.3	259.6
2003.6680	170	258.9	93.2	258.9
2003.7510	171	256.1	90.1	256.1
2003.8350	172	252.8	87.1	252.8
2003.9180	173	249.6	85.2	249.6
2004.0010	174	247.7	84.0	247.7
2004.0850	175	246.4	83.3	246.4
2004.1680	176	244.8	82.7	244.8
2004.2510	177	243.0	82.2	243.0
2004.3350	178	240.9	81.3	240.9
2004.4180	179	239.8	80.2	239.8
2004.5010	180	238.4	79.6	238.4
2004.5850	181	236.2	79.9	236.2
2004.6680	182	234.3	80.6	234.3
2004.7510	183	232.0	81.2	232.0
2004.8350	184	228.9	82.1	228.9
2004.9180	185	224.4	83.9	224.4
2005.0010	186	220.2	85.6	220.2
2005.0850	187	217.7	86.4	217.7
2005.1680	188	215.8	87.9	215.8
2005.2510	189	213.8	91.0	213.8
2005.3350	190	211.9	94.9	211.9
2005.4180	191	209.2	98.1	209.2
2005.5010	192	206.8	101.1	206.8
2005.5850	193	205.0	104.4	205.0
2005.6680	194	203.8	108.6	203.8
2005.7510	195	202.5	113.6	202.5
2005.8350	196	199.5	118.3	199.5
2005.9180	197	196.7	121.9	196.7

TABLE 4.3.1–1 RECOMMENDED SOLAR CONTINGENCY PROFILE 13–MONTH SMOOTHED $F_{10.7}$ (Page 5 of 5)

Year	Months Since Maximum	$F_{10.7}$ Envelope	Early	Late
2006.0010	198	193.9	126.3	193.9
2006.0850	199	189.0	132.7	189.0
2006.1680	200	183.5	138.1	183.5
2006.2510	201	178.4	142.1	178.4
2006.3350	202	173.1	146.4	173.1
2006.4180	203	168.7	152.0	168.7
2006.5010	204	165.7	159.0	165.7
2006.5850	205	166.4	166.4	160.2
2006.6680	206	171.7	171.7	152.0
2006.7510	207	176.8	176.8	146.0
2006.8350	208	183.1	183.1	142.9
2006.9180	209	187.9	187.9	141.5
2007.0010	210	190.6	190.6	139.7
2007.0850	211	192.1	192.1	137.6
2007.1680	212	193.2	193.2	134.2
2007.2510	213	193.4	193.4	130.5
2007.3350	214	193.5	193.5	126.7
2007.4180	215	196.0	196.0	121.5
2007.5010	216	199.4	199.4	116.9
2007.5850	217	203.0	203.0	115.0
2007.6680	218	206.5	206.5	115.7
2007.7510	219	208.3	208.3	116.0
2007.8350	220	209.1	209.1	115.3

TABLE 4.5.1–1 VARIATIONS OF GLOBAL MAXIMUM THERMOSPHERIC DENSITY (Page 1 of 4)

NOTE: The top row of each block gives the median value of Global Maximum Density, the density at 14:00 local time at the subsolar latitude, for the altitude and $F_{10.7}$B Bin indicated. Subsequent rows give the deviation from the median required to compute the density for the indicated percentile level, e.g. n^{th} percentile density = deviation + median. Units are kg/m^3.

F10.7B	Bin 1	Bin 2	Bin 3	Bin 4	Bin 5	All
Range	66–102	102–138	138–174	174–210	210–246	66–246

Altitude 250 km

Median	5.941E–11	8.411E–11	1.050E–10	1.239E–10	1.363E–10	8.629E–11
1%	–1.554E–11	–2.191E–11	–2.827E–11	–3.497E–11	–2.560E–11	–4.066E–11
5%	–1.209E–11	–1.707E–11	–2.063E–11	–2.481E–11	–2.000E–11	–3.559E–11
33%	–3.760E–12	–4.970E–12	–5.570E–12	–6.400E–12	–5.100E–12	–1.718E–11
67%	4.460E–12	5.750E–12	6.000E–12	6.100E–12	6.100E–12	1.921E–11
95%	1.816E–11	2.359E–11	2.140E–11	2.090E–11	2.130E–11	5.291E–11
99%	2.724E–11	3.529E–11	3.060E–11	2.940E–11	2.680E–11	6.621E–11
100%	6.099E–11	6.859E–11	4.670E–11	4.590E–11	3.740E–11	8.741E–11

Altitude 275 km

Median	3.123E–11	4.721E–11	6.184E–11	7.595E–11	8.574E–11	4.869E–11
1%	–9.330E–12	–1.425E–11	–1.956E–11	–2.546E–11	–1.975E–11	–2.576E–11
5%	–7.310E–12	–1.119E–11	–1.446E–11	–1.837E–11	–1.554E–11	–2.277E–11
33%	–2.320E–12	–3.330E–12	–4.020E–12	–4.880E–12	–4.040E–12	–1.135E–11
67%	2.780E–12	3.920E–12	4.400E–12	4.780E–12	5.030E–12	1.350E–11
95%	1.161E–11	1.660E–11	1.607E–11	1.683E–11	1.796E–11	3.946E–11
99%	1.770E–11	2.534E–11	2.333E–11	2.405E–11	2.286E–11	5.060E–11
100%	4.209E–11	5.223E–11	3.680E–11	3.875E–11	3.266E–11	6.971E–11

Altitude 300 km

Median	1.721E–11	2.767E–11	3.793E–11	4.843E–11	5.609E–11	2.868E–11
1%	–5.720E–12	–9.360E–12	–1.356E–11	–1.851E–11	–1.513E–11	–1.658E–11
5%	–4.510E–12	–7.410E–12	–1.014E–11	–1.355E–11	–1.201E–11	–1.476E–11
33%	–1.450E–12	–2.240E–12	–2.880E–12	–3.700E–12	–3.200E–12	–7.570E–12
67%	1.760E–12	2.690E–12	3.210E–12	3.700E–12	4.060E–12	9.510E–12
95%	7.530E–12	1.169E–11	1.201E–11	1.336E–11	1.491E–11	2.934E–11
99%	1.164E–11	1.818E–11	1.771E–11	1.940E–11	1.915E–11	3.854E–11
100%	2.922E–11	3.968E–11	2.874E–11	3.232E–11	2.801E–11	5.542E–11

TABLE 4.5.1–1 VARIATIONS OF GLOBAL MAXIMUM THERMOSPHERIC DENSITY
(Page 2 of 4)

F10.7B	Bin 1	Bin 2	Bin 3	Bin 4	Bin 5	All
Range	66–102	102–138	138–174	174–210	210–246	66–246

Altitude 325 km

Median	9.838E–12	1.679E–11	2.402E–11	3.183E–11	3.777E–11	1.748E–11
1%	–3.582E–12	–6.250E–12	–9.480E–12	–1.349E–11	–1.154E–11	–1.085E–11
5%	–2.839E–12	–4.970E–12	–7.150E–12	–1.000E–11	–9.230E–12	–9.725E–12
33%	–9.230E–13	–1.530E–12	–2.070E–12	–2.800E–12	–2.510E–12	–5.100E–12
67%	1.142E–12	1.850E–12	2.340E–12	2.840E–12	3.240E–12	6.730E–12
95%	4.952E–12	8.270E–12	8.960E–12	1.051E–11	1.221E–11	2.183E–11
99%	7.762E–12	1.308E–11	1.339E–11	1.549E–11	1.585E–11	2.932E–11
100%	2.046E–11	3.012E–11	2.232E–11	2.662E–11	2.368E–11	4.397E–11

Altitude 350 km

Median	5.786E–12	1.047E–11	1.561E–11	2.142E–11	2.602E–11	1.095E–11
1%	–2.283E–12	–4.223E–12	–6.687E–12	–9.880E–12	–8.790E–12	–7.212E–12
5%	–1.818E–12	–3.382E–12	–5.090E–12	–7.400E–12	–7.080E–12	–6.504E–12
33%	–5.980E–13	–1.057E–12	–1.500E–12	–2.110E–12	–1.960E–12	–3.488E–12
67%	7.460E–13	1.290E–12	1.710E–12	2.180E–12	2.570E–12	4.790E–12
95%	3.307E–12	5.900E–12	6.690E–12	8.240E–12	9.910E–12	1.628E–11
99%	5.244E–12	9.470E–12	1.013E–11	1.230E–11	1.299E–11	2.234E–11
100%	1.448E–11	2.291E–11	1.731E–11	2.176E–11	1.980E–11	3.487E–11

Altitude 375 km

Median	3.479E–12	6.670E–12	1.035E–11	1.470E–11	1.826E–11	7.008E–12
1%	–1.474E–12	–2.886E–12	–4.753E–12	–7.271E–12	–6.710E–12	–4.856E–12
5%	–1.180E–12	–2.323E–12	–3.641E–12	–5.497E–12	–5.430E–12	–4.404E–12
33%	–3.930E–13	–7.340E–13	–1.084E–12	–1.600E–12	–1.530E–12	–2.408E–12
67%	4.950E–13	9.120E–13	1.270E–12	1.680E–12	2.030E–12	3.442E–12
95%	2.236E–12	4.240E–12	5.020E–12	6.450E–12	8.010E–12	1.221E–11
99%	3.586E–12	6.900E–12	7.690E–12	9.740E–12	1.059E–11	1.709E–11
100%	1.034E–11	1.750E–11	1.344E–11	1.771E–11	1.645E–11	2.770E–11

TABLE 4.5.1–1 VARIATIONS OF GLOBAL MAXIMUM THERMOSPHERIC DENSITY
(Page 3 of 4)

F10.7B	Bin 1	Bin 2	Bin 3	Bin 4	Bin 5	All
Range	66–102	102–138	138–174	174–210	210–246	66–246

Altitude 400 km

Median	2.128E–12	4.327E–12	6.990E–12	1.026E–11	1.302E–11	4.567E–12
1%	–9.610E–13	–1.994E–12	–3.415E–12	–5.393E–12	–5.145E–12	–3.306E–12
5%	–7.730E–13	–1.613E–12	–2.635E–12	–4.114E–12	–4.186E–12	–3.015E–12
33%	–2.600E–13	–5.160E–13	–7.980E–13	–1.219E–12	–1.200E–12	–1.681E–12
67%	3.330E–13	6.490E–13	9.390E–13	1.290E–12	1.600E–12	2.496E–12
95%	1.528E–12	3.076E–12	3.780E–12	5.050E–12	6.460E–12	9.203E–12
99%	2.479E–12	5.072E–12	5.850E–12	7.710E–12	8.600E–12	1.312E–11
100%	7.460E–12	1.342E–11	1.045E–11	1.438E–11	1.360E–11	2.205E–11

Altitude 425 km

Median	1.321E–12	2.848E–12	4.788E–12	7.257E–12	9.405E–12	3.019E–12
1%	–6.319E–13	–1.389E–12	–2.472E–12	–4.022E–12	–3.957E–12	–2.270E–12
5%	–5.112E–13	–1.129E–12	–1.920E–12	–3.092E–12	–3.234E–12	–2.081E–12
33%	–1.740E–13	–3.660E–13	–5.890E–13	–9.290E–13	–9.360E–13	–1.182E–12
67%	2.250E–13	4.650E–13	7.000E–13	9.980E–13	1.275E–12	1.823E–12
95%	1.052E–12	2.247E–12	2.867E–12	3.963E–12	5.205E–12	6.979E–12
99%	1.727E–12	3.752E–12	4.480E–12	6.123E–12	6.985E–12	1.013E–11
100%	5.424E–12	1.034E–11	8.152E–12	1.167E–11	1.123E–11	1.761E–11

Altitude 450 km

Median	8.298E–13	1.898E–12	3.320E–12	5.196E–12	6.873E–12	2.021E–12
1%	–4.173E–13	–9.744E–13	–1.801E–12	–3.020E–12	–3.058E–12	–1.570E–12
5%	–3.393E–13	–7.960E–13	–1.408E–12	–2.339E–12	–2.510E–12	–1.446E–12
33%	–1.171E–13	–2.620E–13	–4.380E–13	–7.130E–13	–7.360E–13	–8.380E–13
67%	1.530E–13	3.350E–13	5.250E–13	7.750E–13	1.009E–12	1.339E–12
95%	7.292E–13	1.652E–12	2.183E–12	3.123E–12	4.197E–12	5.321E–12
99%	1.211E–12	2.793E–12	3.445E–12	4.864E–12	5.677E–12	7.854E–12
100%	3.972E–12	8.016E–12	6.387E–12	9.494E–12	9.257E–12	1.411E–11

TABLE 4.5.1–1 VARIATIONS OF GLOBAL MAXIMUM THERMOSPHERIC DENSITY
(Page 4 of 4)

F10.7B	Bin 1	Bin 2	Bin 3	Bin 4	Bin 5	All
Range	66–102	102–138	138–174	174–210	210–246	66–246

Altitude 475 km

Median	5.271E–13	1.277E–12	2.326E–12	3.758E–12	5.073E–12	1.366E–12
1%	–2.767E–13	–6.860E–13	–1.320E–12	–2.279E–12	–2.374E–12	–1.091E–12
5%	–2.262E–13	–5.634E–13	–1.038E–12	–1.778E–12	–1.956E–12	–1.010E–12
33%	–7.900E–14	–1.870E–13	–3.270E–13	–5.500E–13	–5.800E–13	–5.955E–13
67%	1.045E–13	2.440E–13	3.960E–13	6.040E–13	8.040E–13	9.900E–13
95%	5.079E–13	1.221E–12	1.671E–12	2.469E–12	3.398E–12	4.080E–12
99%	8.539E–13	2.091E–12	2.661E–12	3.883E–12	4.622E–12	6.122E–12
100%	2.927E–12	6.243E–12	5.025E–12	7.732E–12	7.647E–12	1.135E–11

Altitude 500 km

Median	3.384E–13	8.677E–13	1.644E–12	2.743E–12	3.777E–12	9.322E–13
1%	–1.841E–13	–4.856E–13	–9.711E–13	–1.728E–12	–1.850E–12	–7.616E–13
5%	–1.512E–13	–4.009E–13	–7.689E–13	–1.358E–12	–1.531E–12	–7.087E–13
33%	–5.350E–14	–1.349E–13	–2.450E–13	–4.260E–13	–4.590E–13	–4.257E–13
67%	7.160E–14	1.773E–13	3.000E–13	4.720E–13	6.420E–13	7.348E–13
95%	3.551E–13	9.063E–13	1.285E–12	1.958E–12	2.756E–12	3.142E–12
99%	6.048E–13	1.572E–12	2.065E–12	3.107E–12	3.771E–12	4.793E–12
100%	2.168E–12	4.883E–12	3.970E–12	6.314E–12	6.323E–12	9.168E–12

TABLE 4.5.1–2. PROBABILITIES OF ACHIEVING A TIME INTERVAL WITHOUT ENCOUNTERING A THERMOSPHERIC DENSITY LEVEL ABOVE A GIVEN PERCENTILE VALUE. (TO BE USED WITH TABLE 4.5.1–1).

A) PROBABILITY OF GOING AT LEAST 10 DAYS WITHOUT EXCEEDING THE INDICATED PERCENTILE DENSITY LEVEL (Random Start):

13–MONTH SMOOTHED $F_{10.7}$ RANGE	PERCENTILE LEVEL 66%	90%	95%	99%
66 to 102	0.13	0.46	0.63	0.86
102 to 138	0.21	0.55	0.71	0.90
138 to 174	0.28	0.55	0.68	0.89
174 to 210	0.35	0.60	0.75	0.93
210 to 246	0.38	0.65	0.76	0.87

B) PROBABILITY OF GOING AT LEAST 30 DAYS WITHOUT EXCEEDING THE INDICATED PERCENTILE DENSITY LEVEL (Random Start):

13–MONTH SMOOTHED $F_{10.7}$ RANGE	PERCENTILE LEVEL 66%	90%	95%	99%
66 to 102	0.03	0.23	0.40	0.72
102 to 138	0.05	0.28	0.48	0.76
138 to 174	0.08	0.33	0.44	0.77
174 to 210	0.12	0.37	0.52	0.82
210 to 246	0.12	0.38	0.57	0.75

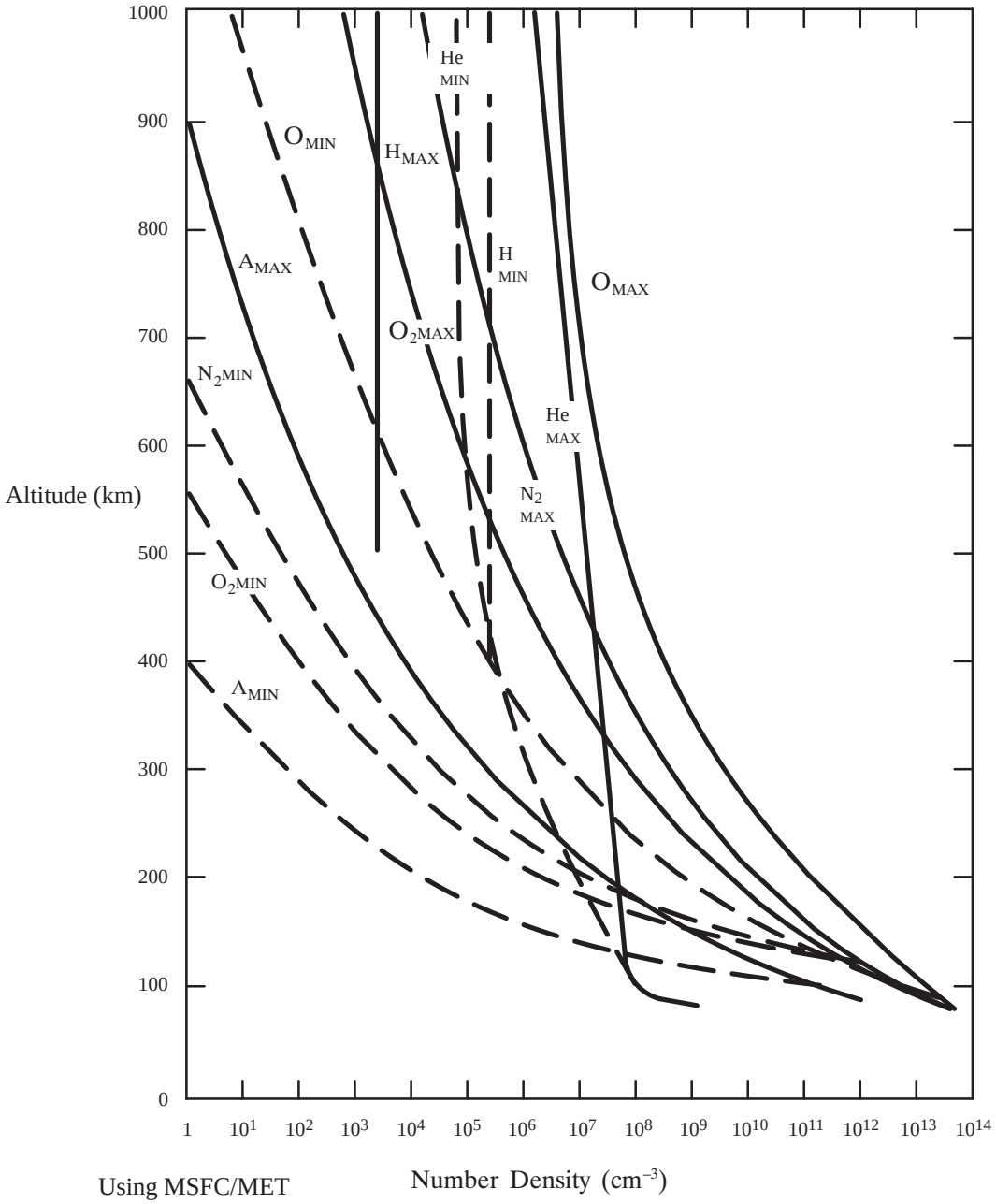

Dashed Lines Represent Solar Minimum Conditions; 0400hrs, Using $F_{10.7}$ = 70 and A_p = 0

Solid Lines Represent Solar Maximum Conditions; 1400hrs, Using $F_{10.7}$ = 230 and A_p = 140

FIGURE 4.1–1 NUMBER DENSITY OF ATMOSPHERIC CONSTITUENTS VERSUS ALTITUDE

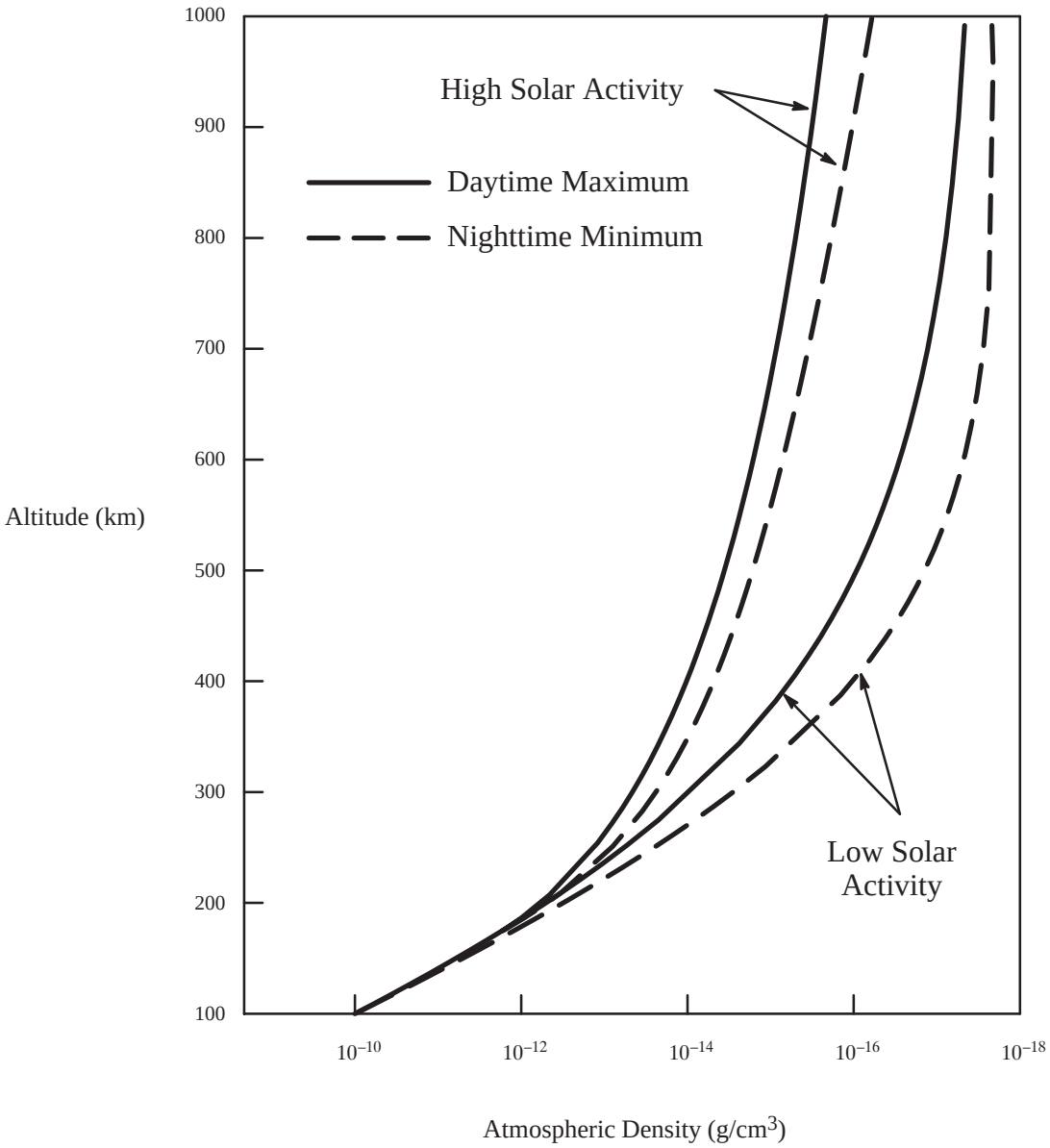

FIGURE 4.2.1–1 TYPICAL ATMOSPHERIC MASS DENSITY PROFILES AT HIGH AND LOW SOLAR ACTIVITY*

* For information only — not for design use

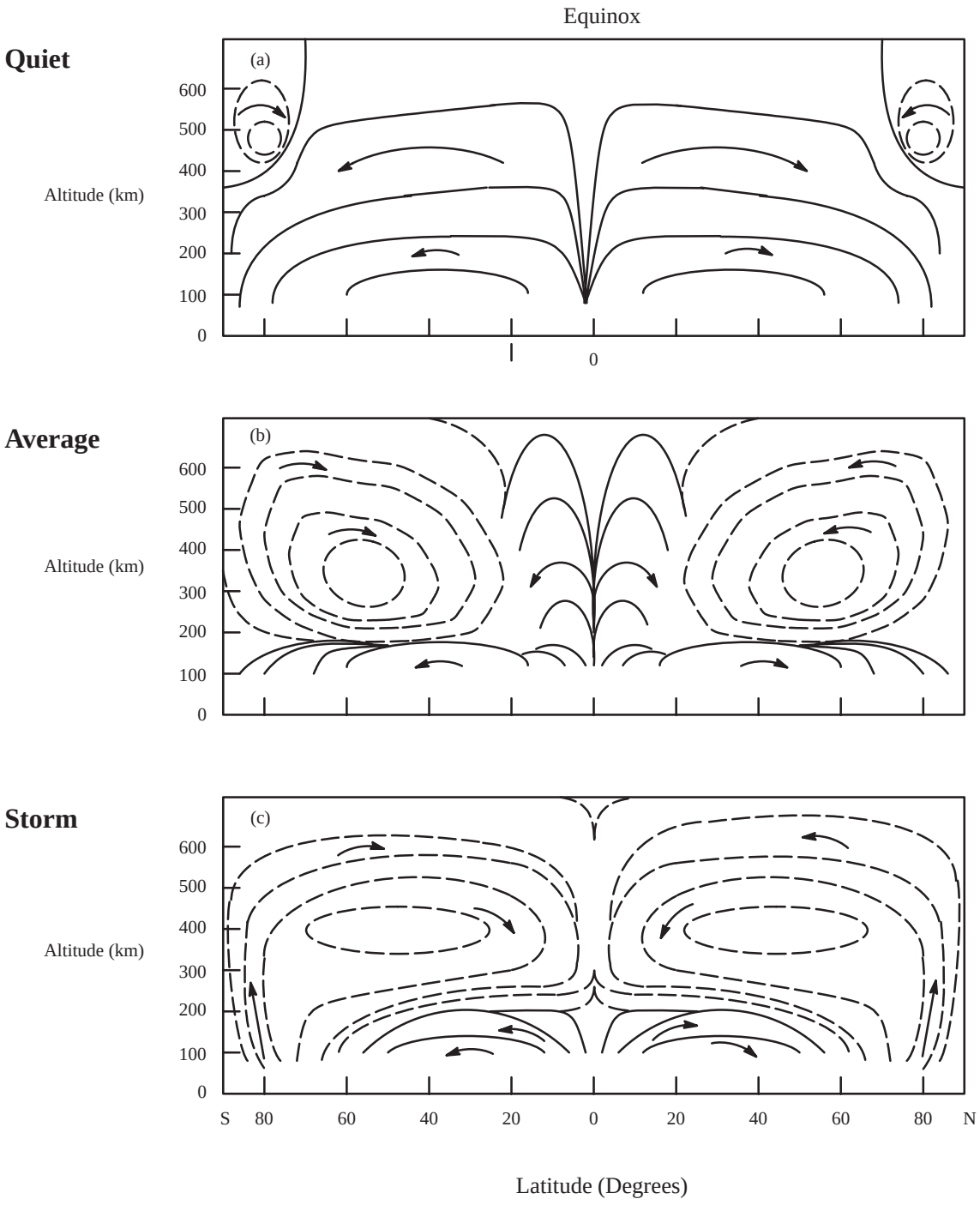

FIGURE 4.2.8–1 SCHEMATIC DIAGRAM OF THE ZONAL MEAN MERIDIONAL CIRCULATION IN THE THERMOSPHERE AT EQUINOX FOR VARIOUS LEVELS OF MAGNETIC (AURORAL) ACTIVITY*

* Maximum velocities are typically 100's of meters per second
*(Roble, 1983)

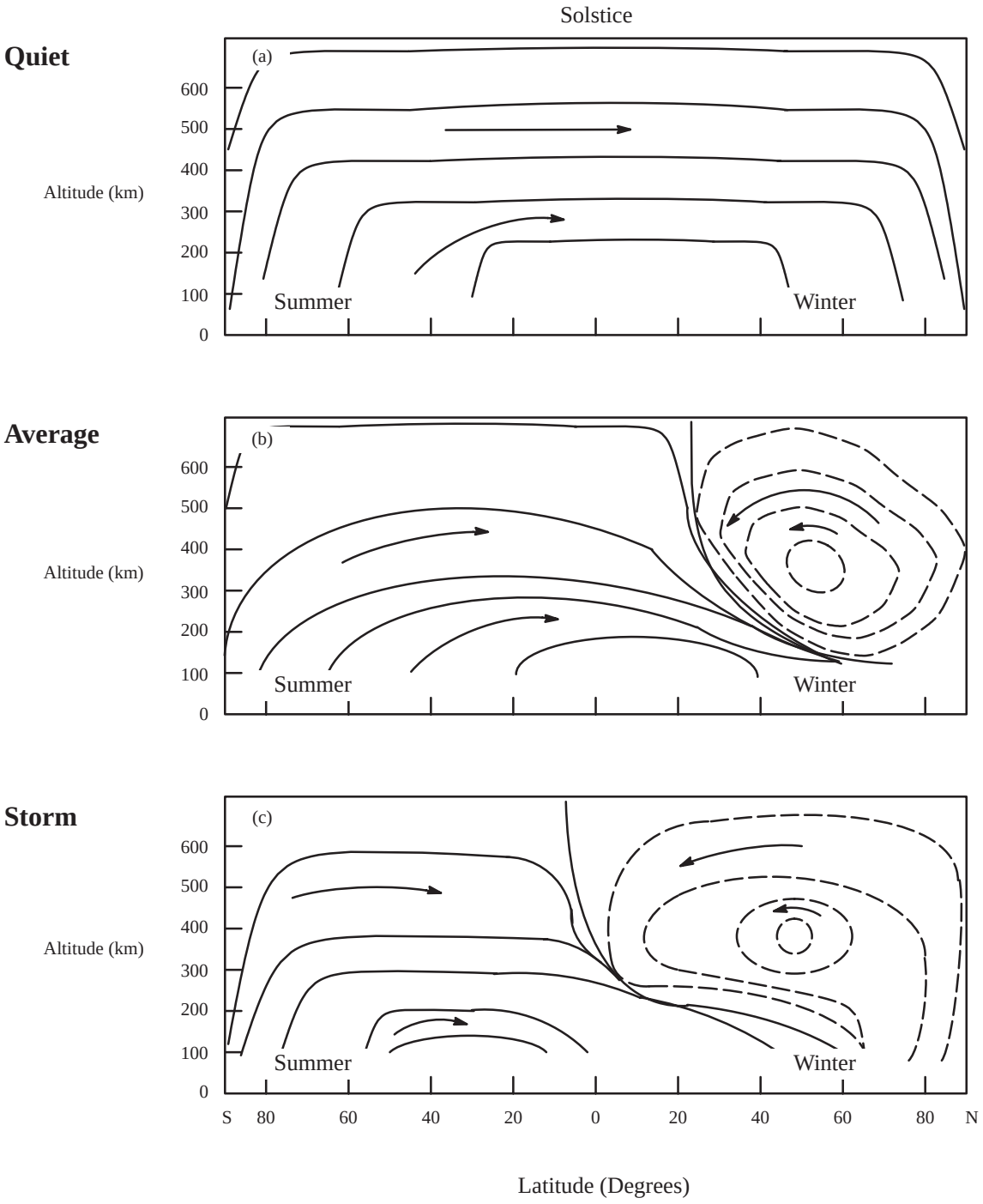

FIGURE 4.2.8–2 SCHEMATIC DIAGRAM OF THE ZONAL MEAN MERIDIONAL CIRCULATION IN THE THERMOSPHERE AT SOLSTICE FOR VARIOUS LEVELS OF MAGNETIC (AURORAL) ACTIVITY*

*Maximum velocities are typically 100's of meters per second

*(Roble, 1983)

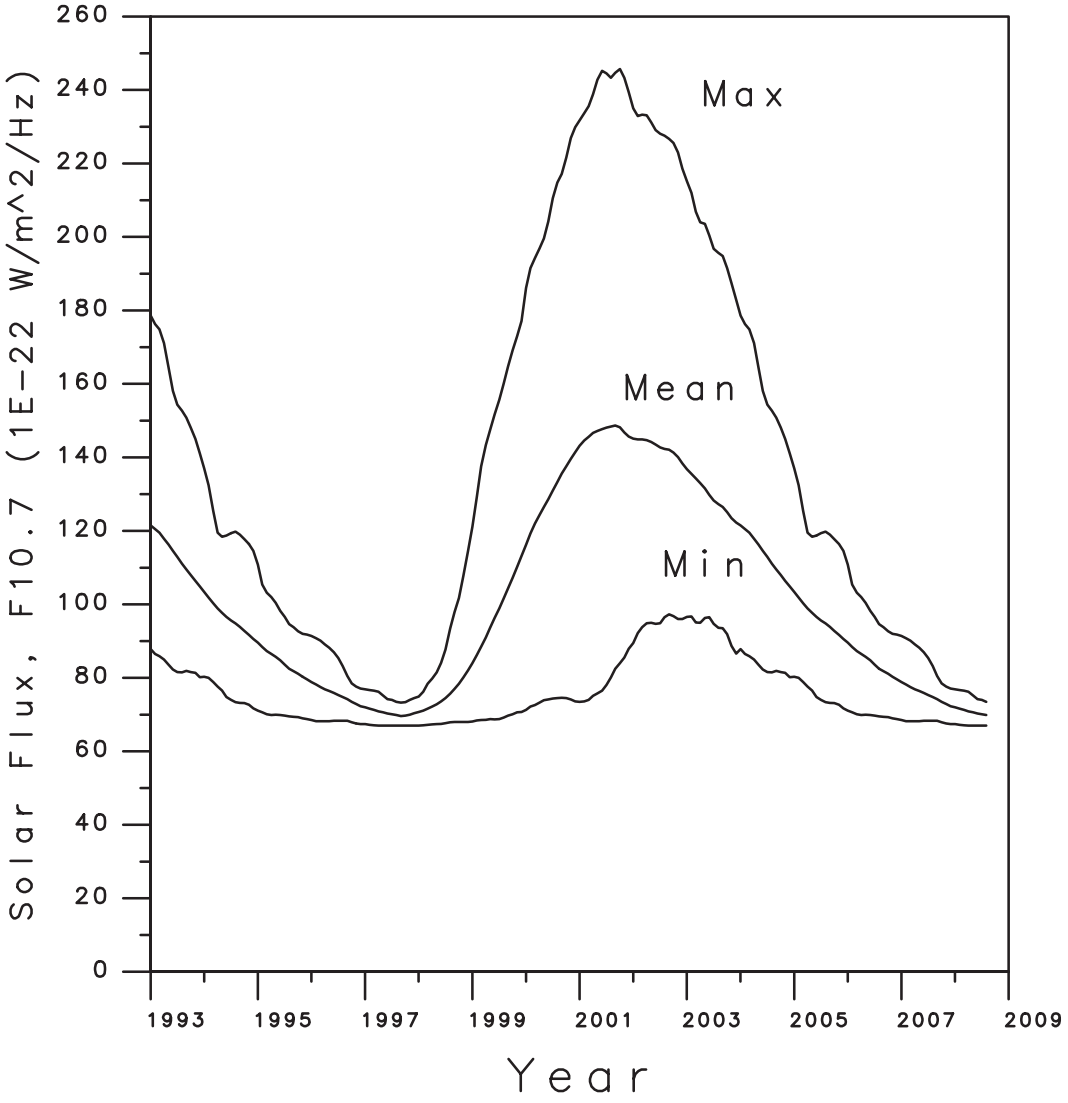

NOTE: The standard deviation in the duration of the cycle is 1.23 years.

FIGURE 4.3–1 13–MONTH SMOOTHED VALUES OF $F_{10.7}$ OVER THE MEAN SOLAR CYCLE*

* Use Table 4.3–1 for numerical values

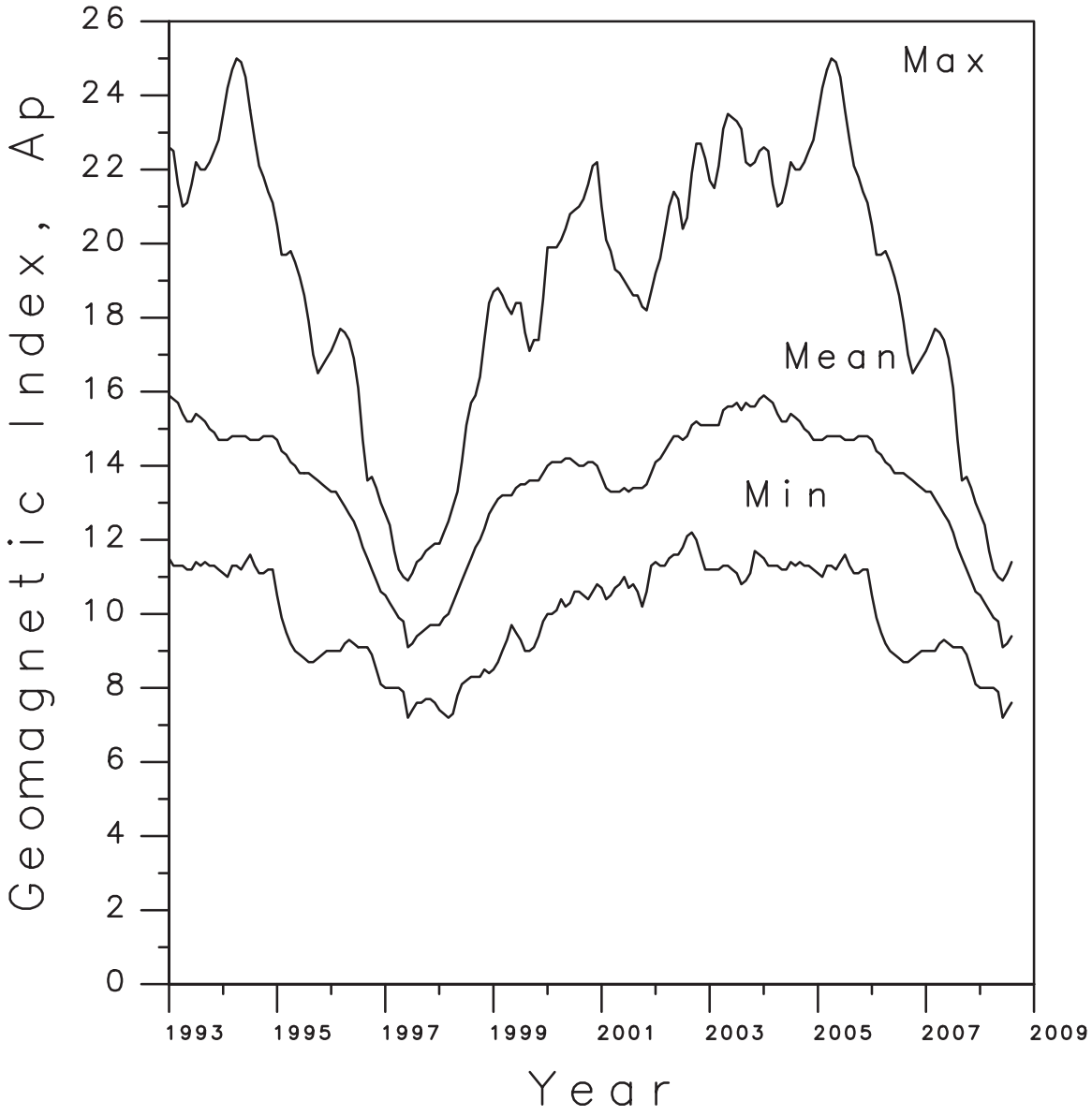

FIGURE 4.3–2 13–MONTH SMOOTHED VALUES OF GEOMAGNETIC ACTIVITY INDEX (A_p) OVER THE MEAN SOLAR CYCLE*

* Use Table 4.3–1 for numerical values

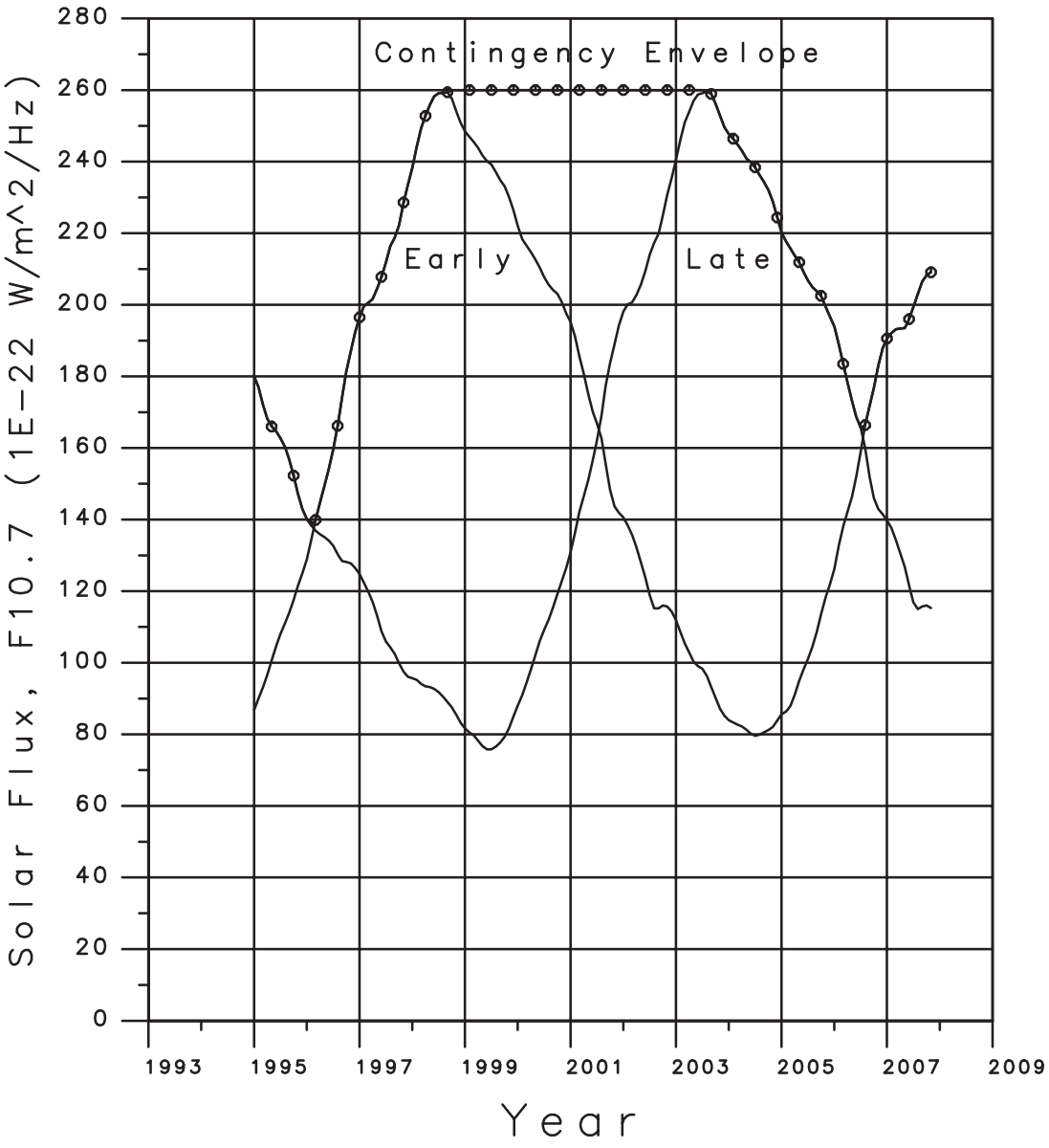

FIGURE 4.3.1–1 CONTINGENCY SOLAR FLUX ENVELOPE

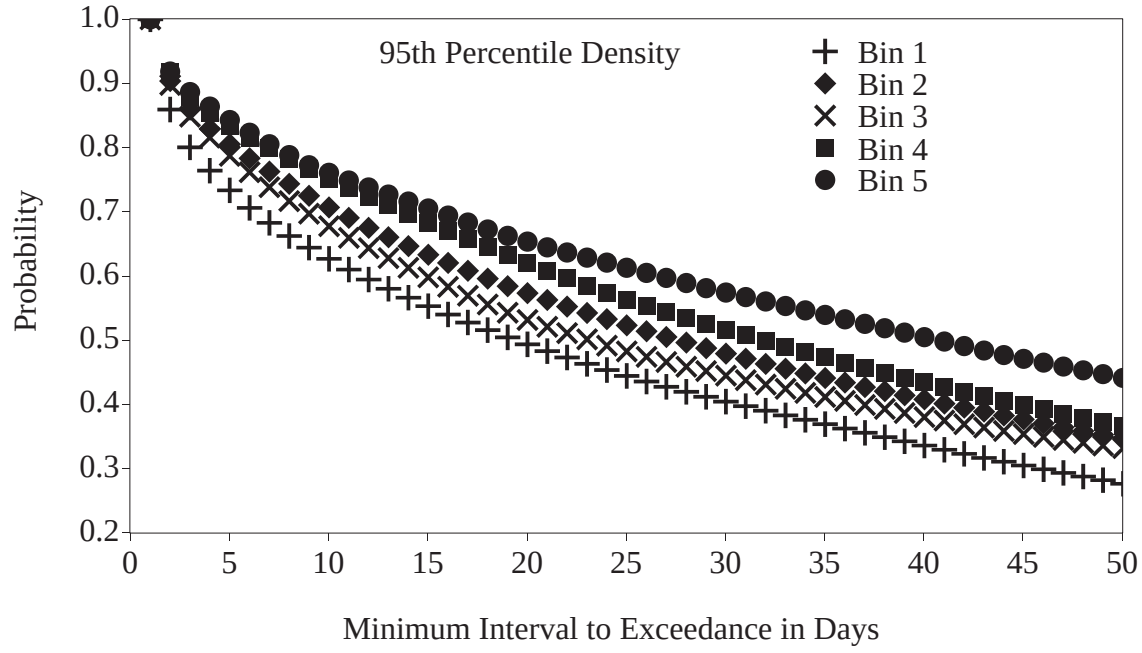

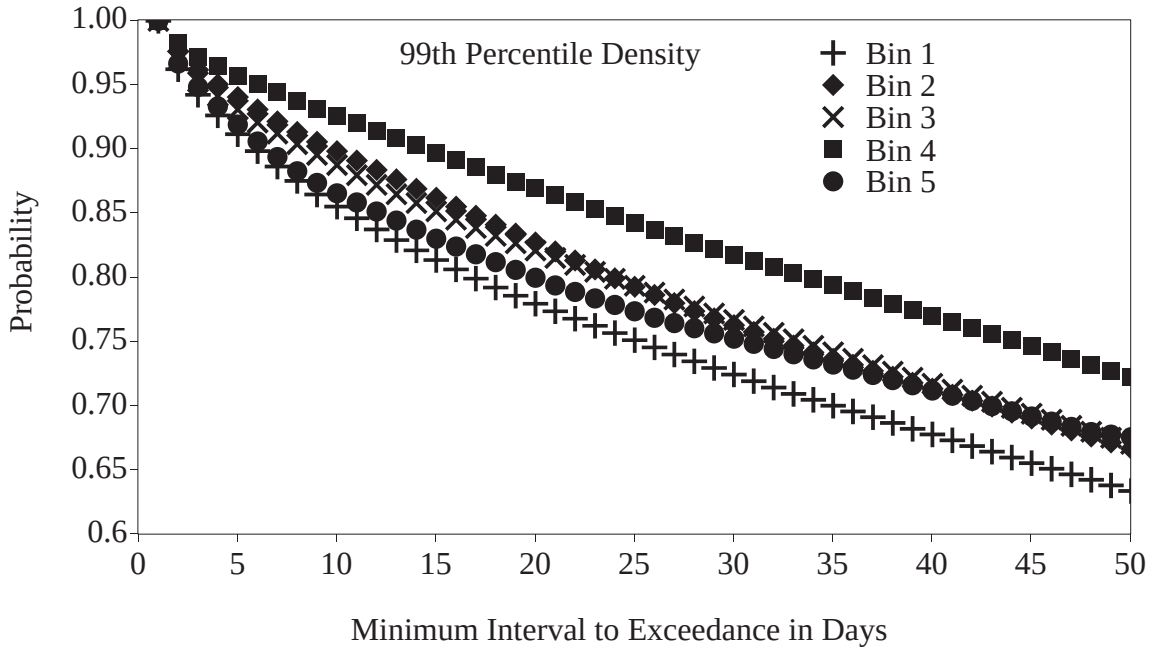

FIGURE 4.5.1–1. PROBABILITY OF MEETING OR EXCEEDING A GIVEN TIME INTERVAL WITHOUT EXCEEDING THE 95TH PERCENTILE DENSITY (TOP) OR 99TH PERCENTILE DENSITY (BOTTOM). THE BINS REPRESENT A RANGE OF $F_{10.7}$: 1) 66–102, 2) 102–138, 3) 138–174, 4) 174–210, 5) 210–246.

5.0 PLASMA ENVIRONMENT

Slightly below the temperature transition discussed in section 4 that marks the lower boundary of the thermosphere – and associated changes in composition of the neutral species – there is an important transition related to the electromagnetic properties of the gas. At roughly 80 km altitude there is a division between the lower turbulent neutral gas mixture region where all the meteorological processes occur and the upper region where solar irradiation produces a partially ionized plasma composed of O, N_2, O_2, He, H, O^+, H^+, He^+, NO^+, O_2^+, N_2^+, and electrons. This upper region is electrically neutral with the most abundant neutral being N_2 and the most abundant ion being O^+ up to about 1000 km altitude where H^+ and He^+ become dominant. A plasma is a quasi–neutral gas of charged and neutral particles that exhibits collective behavior. The particles' movements are controlled to a great extent by the Earth's magnetic field and the solar wind, but their collective behavior and movement generate electric and magnetic fields that, in turn, affect the particle's motion and the motion of other charged particles far away.

Plasmas are usually described by their density (expressed as electron number density n_e m^{-3}), the chemical composition of the ions (often expressed as percentage of total ions), and the electron and ion temperatures, (expressed in Kevin, T or as energy, in electron volts eV). The high energy particles which also may be present (megaelectron volts (MeV) range) cannot be so described, and they interact differently with a vehicle than the plasma does. They are discussed in paragraph 6.0 of this document.

The plasma environment may be conceptually divided into three regions: the ionosphere, which is contained within the magnetosphere; the magnetosphere; and the solar wind. The ionosphere is characterized by its low temperature and high density relative to the other regions, as well as its predominantly O^+ composition. Frequently this region is considered to extend to about 1000 km, the altitude where the ion density begins to exceed the neutral density. Alternately, an arbitrary density criterion of 10^9 m^{-3} places the ‘‘ionopause” at a few thousand kilometers altitude in the polar regions and at a few tens of thousands of kilometers in the equatorial regions. The equatorial extension of the ionosphere is predominantly composed of lighter ions, H^+ and He^+, and is usually referred to as the plasmasphere. Above the ionopuase/plasmapause, but within the region of closed particles but the density decreases and the temperature increases owing to energy inputs from the solar wind.

Even as low as about 60 km altitude there are sufficient long–lived free charged particles to affect the propagation of electromagnetic waves, to support various modes of electrostatic waves, and to support detectable (or sometimes significant) currents in the presence of electric fields. As altitude increases the charged densities increase through a series of layers to something on the order of 10^{12} m^{-3} (on the day side) at the peak density altitude (250–300 km). With additional increases in altitude they decrease to the order of 10^7 m^{-3} in the solar wind and magnetospheric plasma sheet or to even lower densities which are found in magnetospheric tail lobes, ~0.1 x 10^6 m^{-3}. See Figure

3.2–1. At low altitudes the temperatures of these plasmas are typically 300 K to 3500 K (0.05 to 0.3 eV) except in the polar auroral regions. In the auroral regions an intense, energetic electron flux often precipitates from the plasma sheet. The high altitude plasma is much more energetic; typically 10^5 K (10 eV) for ions and 1–5 x10^5 K (10–50 eV) for electrons in the solar wind, ~3 x 10^7K (3 kiloelectron volts (keV)) for electrons and ~1 x 10^8 K (10 keV) for ions in the magnetospheric plasma sheet. However, the dynamics of the intervening region are such that temperatures can sometimes be 1 to 2 orders of magnitude higher. Contact of this energetic plasma with the atmosphere produces the aurora.

The boundaries between the other regions are termed the ‘‘geopause”, where the terrestrial plasma is replaced by the solar wind plasma leaking into the magnetosphere, and the ‘‘magnetopause” where the geomagnetic field is replaced by the interplanetary or solar wind magnetic field. At the subsolar point the altitude of the geopause is just less than the altitude of the magnetopause: however, in the extended tail the altitude of the geopuase is much less than that of the magnetopuase owing to the penetration of the solar wind as it moves along the flanks of the magnetosphere. The magnetopause ranges from 6 to 10 earth radii in the sunward direction to hundreds of earth radii in the anti–sunward direction.

5.1 SPACECRAFT – PLASMA INTERACTIONS

Plasma interactions can be quite complicated and there are significant differences between a space vehicle’s interactions with the relatively cold, dense plasma of the ionosphere, the hot tenuous plasma at very high orbits, and interactions in the auroral regions where the higher energy plasma characteristic of higher altitudes penetrates to low Earth orbit. In all regimes, a spacecraft accumulates electric charge from the plasma in order to establish electrical equilibrium with the plasma, a process called spacecraft charging. Equilibrium requires that no net current be collected by the vehicle. Both the plasma properties and the spacecraft design and operating characteristics influence the process.

The plasma electrons have much less mass than the positive ions. Since, at a given energy, the thermal velocity is inversely related to the particle mass, the thermal electron flux to passive spacecraft surfaces and structure is greater than the corresponding thermal ion flux. As a result, surfaces tend to accumulate negative charge. At low latitudes in LEO, the plasma is relatively dense and of low energy, so equilibrium is established within a few volts negative of the reference plasma potential. Thus charging of passive surfaces is usually not a problem in this regime. However, for active surfaces, e.g., solar arrays and structure tied electrically to them, arcing and related significant effects can occur, depending upon the grounding scheme and the magnitude of the spacecraft imposed voltages.

Spacecraft passing through the auroral zone can be charged to large negative potentials by energetic electrons precipitating from the magnetosphere. This is because large surface potentials are required to retard this flux and allow equilibrium (no net current) to be achieved. Also in this region, conditions occur in the wake of large structures, or they may occur naturally so that the entire vehicle is involved, where the low energy plasma density is depleted. This makes it ineffective in balancing the current from the high energy electron flux and the charging process is enhanced. This is similar to the situation in GEO where the plasma is very energetic but tenuous. In GEO thermal current densities can be three orders of magnitude less than in LEO, so that photoelectron emission from surfaces can play a significant role in balancing currents to a spacecraft. Sun/shade effects become important to the point that potentials as large as several kV can develop between sunlit and shaded surfaces (depending on geometry and material properties).

5.2 IONOSPHERIC PLASMA

The ionospheric plasma is generated principally by photoionization of the ambient neutral atmosphere and by magnetospheric particles interacting with the thermosphere in the 100 to 200 km altitude region. The transport of the plasma is controlled by the geomagnetic field. Hence, as discussed in Smith and West (1982), the plasma characteristics vary with geomagnetic latitude, altitude, local time, season, and level of solar and geomagnetic activity but only weakly with goemagnetic longitude. The plasma density drops at night due to the loss of solar ultraviolet to maintain the production of free ions and electrons. The plasma density tends to be higher in the equatorial regions than the polar regions, with a dip near the geomagnetic equator. The temperature tends to be about 1000K during the day but two to three times that in the morning and eveining. The plasmas in the polar regions (above 60° geomagnetic latitude) have a signficatnt contribution from the solar wind and can be more similar to the magnetospheric plasma than the ionospheric plasma.

5.2.1 IONOSPHERIC DENSITY STRUCTURE*

Ionospheric structure is generally discussed in terms of three fundamental altitude regimes which differ, in addition to differences in neutral gas properties, in the energy and source regions of the interacting particles precipitating from the magnetosphere. They are referred to as the D (50–90km), E (90–160 km) and F (160 –500+ km) regions. Above the D layer the neutral gases are in diffusive equilibrium, however, layering of the electron density profile is exhibited within these regions due to competing particle production, loss and transport processes. The highest electron densities are at the F2 layer peak, 250 to 350 km at mid–latitudes and 350 to 500 km at equatorial latitudes. The density in the E layer, typically located at 100 to 120 km altitude, is an order of

magnitude less than the F2 layer peak. Under certain conditions a valley or an F1 ledge can be observed between these two layers. The density in the D layer, below the E layer peak, decreases rapidly with decreasing altitude. In the D layer ionization is primarily caused by solar x–rays and depends strongly upon the solar zenith angle. The highest values, 10^8 to 10^9 m^{-3} occur during the summer noon. Below about 70 km altitude ionization by cosmic rays is the major electron source; therefore, the electron density is negatively correlated with the solar cycle below 70 km and positively correlated above.

The E layer is composed primarily of atomic oxygen ions and electrons, the result of ionization by solar EUV radiation. The daily maximum is near noon,the seasonal maximum is in the summer and density varies directly with solar activity. The nighttime density is more than an order of magnitude less than the daytime due to recombination. Although thin and patch, a sporadic E layer, Es, with a density that can exceed the E and F2 peaks occurs irregularly.

The F region consist of the overlapping F1 and F2 layers. The F1 layer, at about 150 to 200 km altitude, is of lesser importance. It is under strong solar control. The density distribution in the F layer in general is determined by transport process, ambipolar diffusion, electrodynamic drift and neutral wind drag, because neutral densities decrease rapidly with increasing altitude. Therefore, the F2 layer peak and the topside ionosphere are highly variable, 10 to 30% day to day. The F2 layer peak density maximizes in the afternoon in winter. There are two crests at $\pm$ 15° magnetic latitude with a minimum at the magnetic equator in a latitudinal profile of the F layer. At night and higher altitudes the two crests merge into a single crest at the magnetic equator. The so called ‘fountain’ causes this ‘equatorial anomaly’. The charged particles are pushed upwards by the equatorial electric field where they then drift downward along magnetic field lines.

At high latitudes the ionosphere is strongly coupled to the magnetosphere and to the solar wind. The transition from closed to open field lines and the influx of energetic particles profoundly affect the ionospheric plasma. The boundary region, the auroral oval, is marked by the beautiful display of auroras. Surrounding the magnetic poles, the oval extends to near 75° geomagnetic latitude at noon and 65° at local midnight. On the nightside the oval is well marked by a depletion in electron density, the sol–called trough. On the dayside one finds a region of enhanced densities just inside the oval, the so–called magnetospheric cleft, the electron density at the tip of the cleft is almost an order of magnitude greater than it is at the bottom of the trough. During magnetic storms the trough moves equatorward 2° per unit increase in K_p. The region inside the oval is called the polar cap.

A wide variety of ionospheric irregularities have been observed, predominantly at high latitudes and during the equatorial nighttime. The plasma fluctuations range in scale from hundreds of kilometers down to centimeters. Plasma instabilities play an important role in the generation of medium–scale (kilometers) and small–scale (meters) irregularities. Examples of irregularities are patches of enhanced ionization in the E

region(sporadic E) and of depleted ionization in the F region (spread F). Spread F is most frequently observed in the equatorial nightime ionosphere. The irregularities cause signal fluctuations in traversing radio waves, known as scintillations.

Influx of solar plasma into the tail of the magnetosphere, sometimes preceded by solar flares, can cause complex ionospheric disturbances (storms): the most consistent pattern is an enhancement in D region ionization. These effects are most dramatic at auroral latitudes, but significant modifications in the ionosphere occur at all latitudes. A particularly severe event, called a polar cap absorption (PCA) event, is due to protons arriving from the sun and causing a radio communications blackout over a considerable time period.

5.2.2 IONOSPHERIC TEMPERATURES

The main source of energy for the terrestrial ionosphere is extremely ultraviolet radiation from the sun. The electrons are heated most efficiently and their temperature exceeds the temperatures of the ions and neutrals. Electron temperatures increase from about 300K at 100 km altitude to about 3500 K at 800 km altitude. Ion temperatures are close to the neutral temperature below about 400 km altitude and increase toward the electron temperature about that altitude. Below 150 km altitude the high neutral densities and the high collision frequencies result in the same temperature for electrons, ions, and neutrals. During nighttime the temperatures of all species are close together.

In general, plasma temperatures are lowest at the geomagnetic equator and increase towards higher latitudes, due to the increased influence of heating by precipitating particles at auroral latitudes. At low altitudes, however, the electron temperature peaks at the magnetic equator, reaches minimal values at about $\pm$ 20°, and then increases towards high latitudes. This behavior is the mirror image of the equatorial anomaly of the electron density and illustrates the strong anti–correlation between electron density and temperature.

Roughly speaking, the temperatures increase from an almost constant nightime value to an almost constant daytime value. The most significant departure from this behavior is the early morning peak in electron temperature. It is most pronounced at the the magnetic equator at about 300 km altitude (the peak temperature exceeds the daytime value by a factor of 2 to 3): its magnitude decreases rapidly towards higher and lower altitudes and towards higher latitudes. The temperature peak is a result of the sharp increase in solar heating coupled with the still low electron densities from the preceding night.

The electron temperature is almost unaffected by the solar cycle, in contrast to the increase of almost all other neutral and ionized parameters. This again is a result of the close coupling with the electron density which determines both energy gain and loss of

the electron gas: the simultaneous increase of both terms leaves the electron temperature nearly unchanged.

5.2.3 IONOSPHERIC DYNAMICS

The sun–induced thermospheric winds provide the energy source needed to drive the so–called ionospheric dynamo which maintains the system of ionospheric currents and fields. On the sunlit side of the Earth two large vortices of electric current exist in the quiet equinox ionosphere; the current flows counterclockwise in the northern hemisphere and clockwise in the southern hemisphere (Sq currents). The concentrated current at the magnetic equator represents the equatorial electrojet. Magnetic storms severely affect thermospheric winds and ionospheric currents. The thermospheric winds and ionospheric drifts are of the order of 100 m/s and can reach 1000 m/s and more during magnetic storms. Ionospheric current densities are of the order of 10μ A m^{-2} and electric fields are of the order of 10 mV m^{-1}. The Earth's magnetic field strength is typically 3 x 10^{-5} Tessla at ionospheric altitudes.

The solar wind blowing past the Earth's magnetic field creates a magnetospheric dynamo which drives a plasma across the polar cap. The empirically found dependence of the auroral plasma convection on solar wind parameters illustrates the strong coupling between the solar wind and the high latitude ionosphere.

5.2.4 INTERNATIONAL REFERENCE IONOSPHERE 86 (IRI86)

A computer code, IRI86, that describes the ionosphere in the 85 to 1000 km altitude range for geomagnetic latitudes up to about 60° (the auroral zones) is available. (Bilitza, 1986) It calculates monthly mean electron and ion species [H_2^+, H_e^+, O^+, NO^+, and O_2^+] densities and temperatures as a function of latitude, longitude (geomagnetic or geocentric), time of day, day of year, altitude and solar $F_{10,7}$ radio flux. [However, the model has not been extended to cover the ionosphere during the intense solar maximum of the current solar cycle.] The error bars on the model during quiet times are a factor of two to four of the indicated value at altitudes below the F2 peak, and these are primarily the result of small scale variations in the ionosphere. Above the F2 peak problems with the scale height could lead to error bars of up to a factor of ten.

The IRI86, was used to generate Figures 5.2.4–1 and 5.2.4–2 which show global density and temperature contours at 400 km altitude on July 1, a few days past the summer solstice. Figures 5.2.4–3 and 5.2.4–7 show the variation of density and temperature with altitude. A recent revision of the IRI86 code, the IRI90 is also available, Bilitza 1990. The ion composition option is the primary improvement applicable to Space Station environment. Otherwise the codes are very similar. Therefore the baseline for Station remains the IRI86 model since it is currently believed to be the best representation of the

ionospheric plasma for Space Station applications. The IRI86 is available from the Space Station Project Office, Johnson Space Center, Houston, Texas. These models are improved periodically and later editions may produce finer detail but are not expected to alter the general character and range of the parameters.

5.3 AURORAL PLASMA

As mentioned previously, the aurora is primarily produced by high energy charged particles precipitating into the atmosphere along magnetic field lines. One result of these fluxes is the increase of local plasma density by factors of up to 100 over regions of tens of kilometers in latitudinal dimension and hundreds or thousands of kilometers in longitudinal dimension and hundreds or thousands of kilometers in longitudinal dimension in the auroral regions (60° to 70° magnetic latitude). These enhancements occur between about 100 and 250 km altitude (see Figure 5.3–1). Above 250 kilometers the thermal plasma may be depleted above intense aurora in the midnight sector, falling far below $1.0E^{10}$ m^{-3}. In this region there is no clear distinction between magnetospheric and ionospheric phenomena. There is a very wide range of scales, both spatially and temporally, in the dynamics present. Small–scale (meters to dekameters) irregularities exist and move with the prevailing ambient plasma drifts. Ion–ion and ion–neutral collisions in the lower thermosphere tend to make the temperature distribution isotropic while anisotropies still remain at higher altitudes (near 600km). Plasma property anisotropies are introduced by the geomagnetic field.

5.3.1 AURORAL MORPHOLOGY

Aurora occur in all three altitude regimes, D, E, and F, with the E layer dominant in terms of total auroral precipitation energy. Electron density profiles in the auroral region are dependent upon the energy distribution of the incident precipitating particles while the auroral emissions are dependent upon the photochemistry of the auroral ionosphere as well as the energy distribution of the precipitating particles. The spectrum of the precipitating particles determines the altitude at which the particle energy is deposited and therefore the applicable photochemistry, since neutral composition and density depend strongly on altitude. Enhanced electron densities are produced by impact ionization due to precipitating electron fluxes. The auroral E region extends about 2° farther equatorward than the F region and this extension is formed by proton precipitation, in contrast to the mainly electron precipitation that forms the F region. There is a strong seasonal and universal time (UT) control of the auroral ionosphere.

The aurora occurs at all local times in the auroral ovals that are rings at about 65° magnetic latitude around each magnetic pole. The most intense and energetic fluxes occur near local midnight. The location of the aurora and its intensity vary with solar

(and resulting magnetospheric) activity. Figures 5.3.1–1A and 5.3.1–1B illustrates the spatial distribution. Global plots s of the average integral energy flux and the average energy of precipitating electrons are presented in polar spectrogram format in a magnetic local time–corrected geomagnetic latitude coordinate system, for each of four levels of K_p. Plots apply to both poles. A statistical analysis of the probability of encountering various levels of aurora particle flux may be found in McNeil et al. (1984), and a detailed discussion of auroral morphology may be found in Jursa, 1985.

In the dayside auroral zone magnetic field lines extend to the dayside magnetopause and provide fairly direct access for the solar plasma to the topside ionosphere. The solar plasma strongly heats and drives winds in the day side auroral ionosphere generally in the direction away form the sun and across the polar cap towards the nightside. The strong ionospheric heating associated with this process generates the largest outflows of ionospheric plasma anywhere at the Earth, and forms a global scale ‘‘ion fountain” across the polar cap. Global electric current systems flow along magnetic field lines into and out of the auroral ionosphere. Where these are most intense and in the upward direction, they exceed the capacity of the plasma to carry them with thermal motions, and discharges occur in which electrons are accelerated downward and ions are accelerated upward. These discharges greatly enhance the brightness of the aurora where the electrons are incident and produce outward flowing ion beams which are far out of local thermodynamic equilibrium and unstable, generating natural plasma wave noise at a variety of frequencies.

5.4 POLAR IONOSPHERE AND POLAR WIND

The magnetosphere configuration depends on whether Bz, the component of the Interplanetary Magnetic Field (IMF) normal to the ecliptic plane with positive values northward, is directed northward or southward. The differences between the configurations are even stronger in the polar cap. Current understanding of the polar cap convection under southward IMF conditions is well developed even though the convection is complex and multiple flow entry regions exist. However, observed traveling convection vortices in the polar cleft region are inconsistent with present–day current–closure models. Density structures in both the E and F regions show that in darkness the ratio of enhanced density to the background density remains constant for many tens of hours and that the vortices only disappeared when they were convected into regions of sunlight or auroral precipitation. There are systematic differences between the winter electron density signatures in the topside ionosphere in the southern and northern polar regions with the southern hemisphere having the lower densities. The region above the polar ionosphere contains mainly ionospheric plasma flowing generally away from the sun across the polar cap and upward into the magnetosphere. Only weak fluxes of energetic components of the solar wind plasma enter the polar cap region, sometimes referred to as ‘‘polar rain”. The light ion component of the ionospheric plasma, which

flows upward into the magnetosphere even without solar wind energy inputs, is referred to as the polar wind. The heavy ion component responds to energy inputs from the solar wind, to heat–driven thermospheric dynamics, the solar cycle in UV inputs to the thermosphere, and magnetic activity. This combined light and heavy ion source of plasma to the magnetosphere provides much of the material from which the energetic particle populations are generated. Theoretical research on this area has shown that results are highly model dependent and that two–dimensional models produce different results that three–dimensional models. Caution in use of models is strongly advised.

The polar cap region becomes active with Sun–aligned auroral arcs when the IMF is northward. Field–aligned electrodynamic systems which close in the ionosphere are associated with these arcs both sunward and anti–sunward drifts occur.

Models of the ionosphere have not progressed to the point where they can be used for reliable forecasts of future conditions especially those related to magnetic storm and substorm dynamics. Major questions of convection patterns are still unanswered. Even static conditions predicted by the IRI90 model frequently do not match observational data. Great care must be exercised in the use of all ionospheric models.

5.4.1 TRANSIENT FLUXES: LOW EARTH POLAR (OR GEOSYNCHRONOUS) ORBIT

In polar low–Earth orbit, the important transient and energetic fluxes occur in the auroral zone. Figure 5.4.1–1 shows typical aurora fluxes from rocket measurements at about 320 km and Figure 5.4.1–2 shows extreme values for space vehicle design derived form satellite measurements made at 840 km. Distribution functions of electrons (left) and ions (right) for very intense auroral fluxes are shown in Figure 5.4.1–2. These particles are not very penetrating but may be significant for charging at altitudes above 250 km.

The fluxes in GEO can be quite energetic and are highly variable with magnetic activity especially during geomagnetic substorms. See the discussion in Purvis et. al., 1984. Figure 5.4.1–3 illustrates a time history of a geomagnetic substrom.

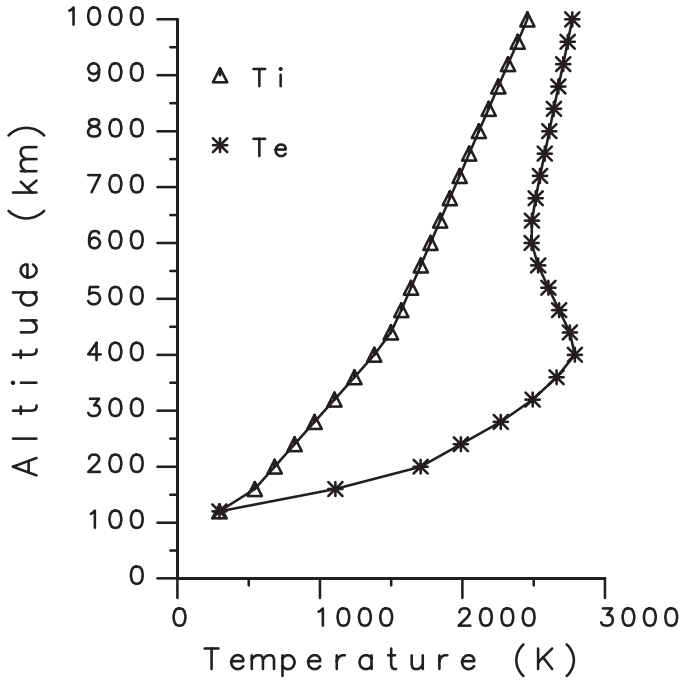

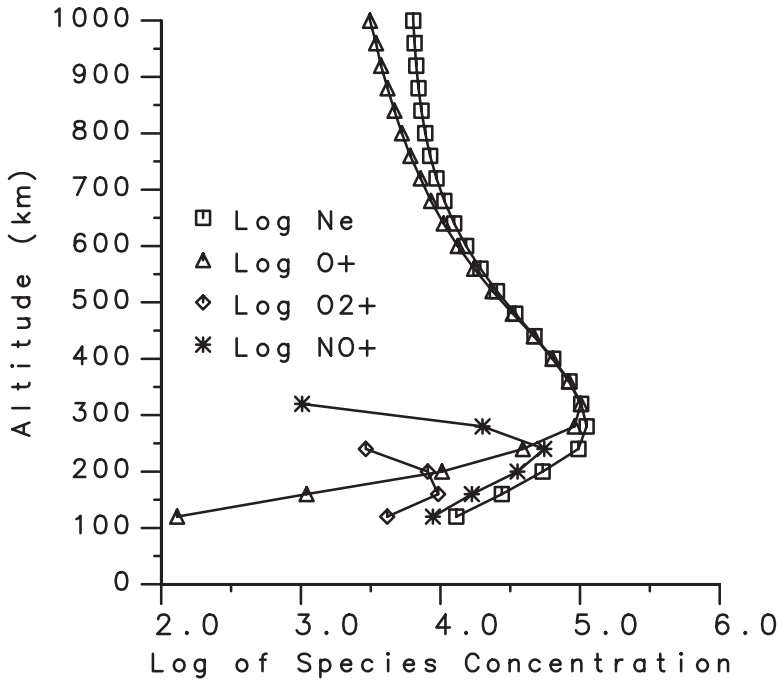

LAT = 75
LONG = 20

R = 10
MODIP = 70

MONTH = 3
LOCAL TIME = 7

FIGURE 5.1–1 MODEL IONOSPHERE (IRI–86) FOR 75 DEGREES LATITUDE AND 0700 LOCAL TIME: DAWN

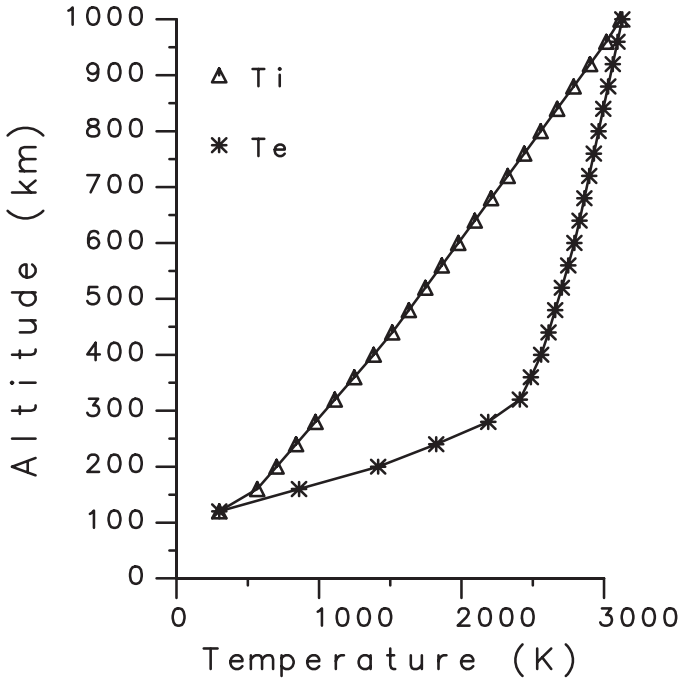

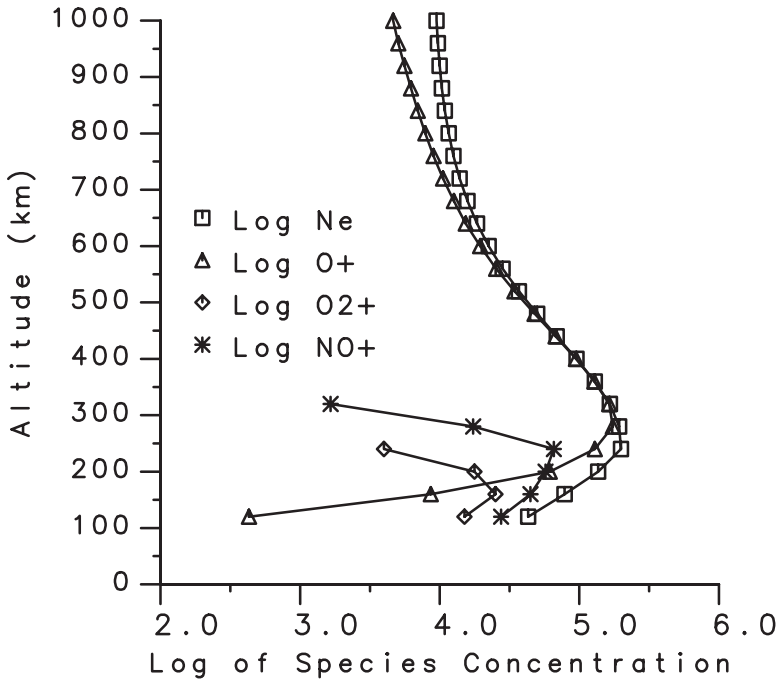

LAT = 75 R = 10 MONTH = 3
LONG = 20 MODIP = 70 LOCAL TIME = 14

FIGURE 5.1–2 MODEL IONOSPHERE (IRI–86) FOR 75 DEGREES LATITUDE AND 1400 LOCAL TIME: EARLY AFTERNOON

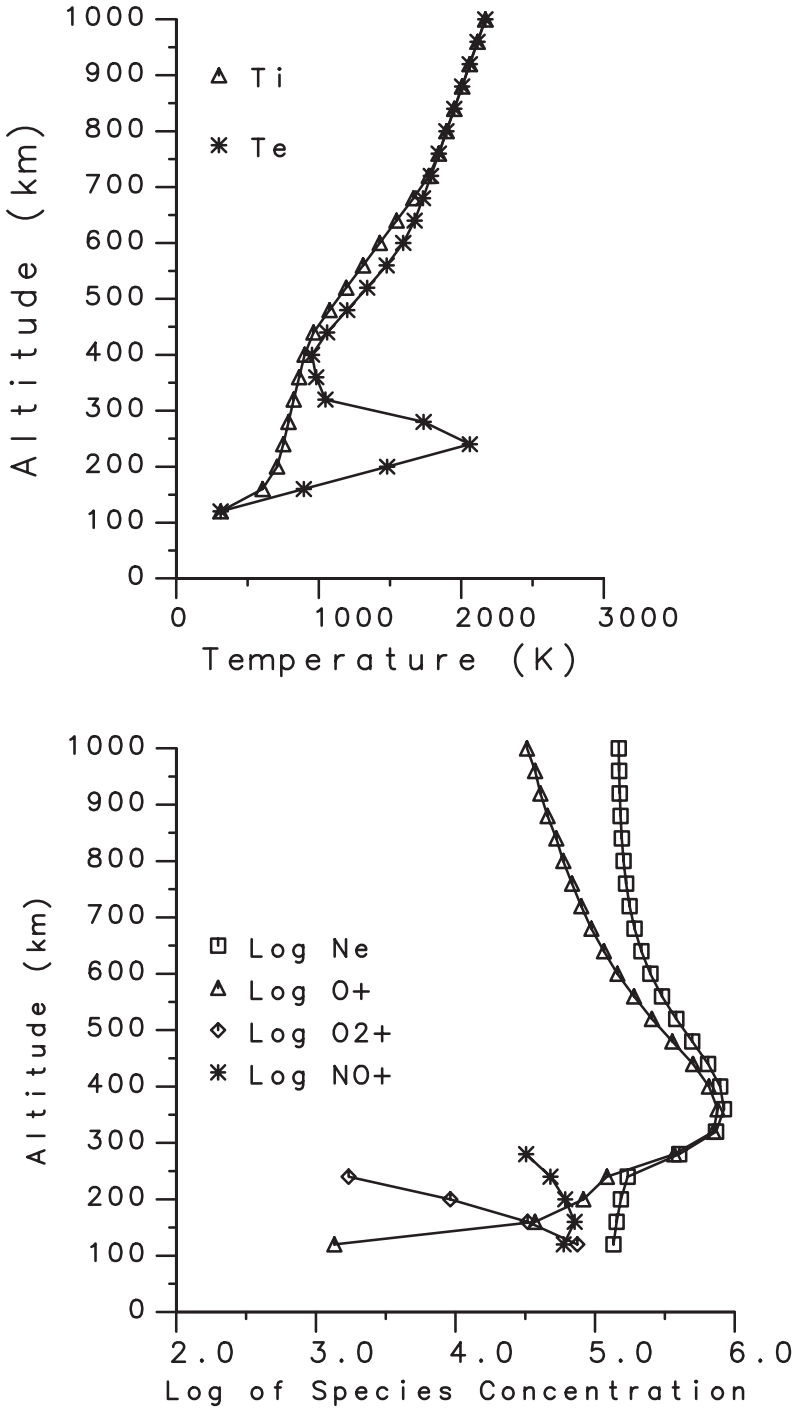

LAT = 8 R = 10 MONTH = 3
LONG = 20 MODIP = –10 LOCAL TIME = 14

FIGURE 5.1–3 MODEL IONOSPHERE (IRI–86) FOR 8 DEGREES LATITUDE AND 1400 LOCAL TIME: EARLY AFTERNOON

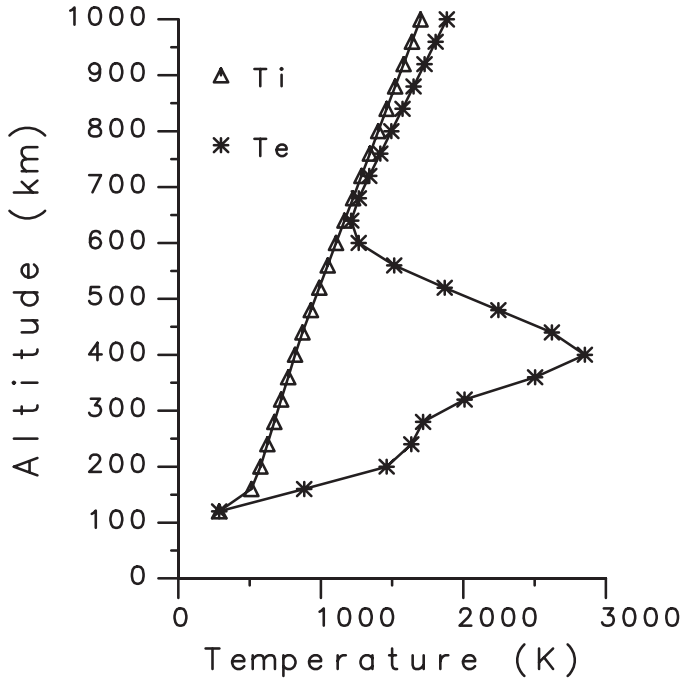

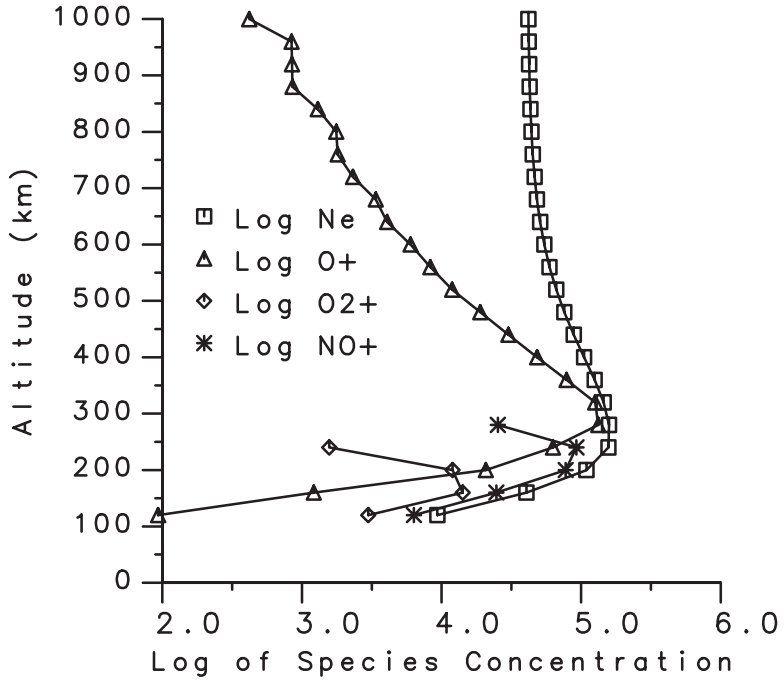

LAT = 8 R = 10 MONTH = 3
LONG = 20 MODIP = –10 LOCAL TIME = 6

FIGURE 5.1–4 MODEL IONOSPHERE (IRI–86) FOR 8 DEGREES LATITUDE AND 0600 LOCAL TIME: DAWN

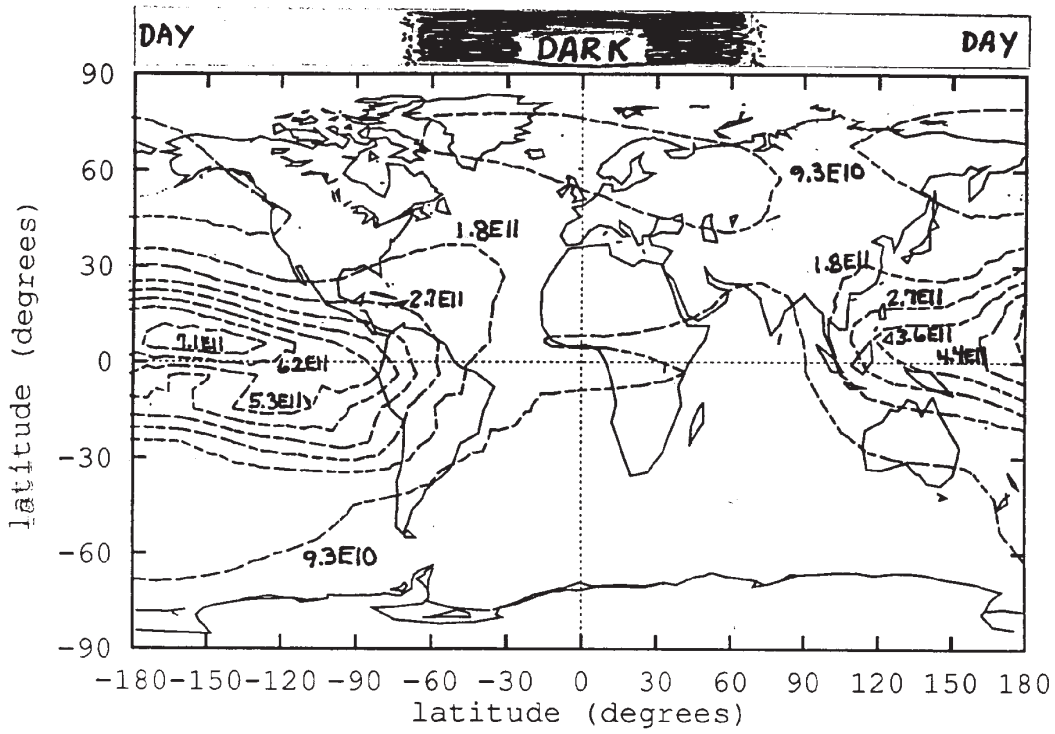

FIGURE 5.2.4–1 PLASMA DENSITY (m^3) AT 400 KM FOR JULY 1 AND SOLAR MINIMUM CONDITIONS ($F_{10.7}$=70.1, IRI–86 RESULTS)

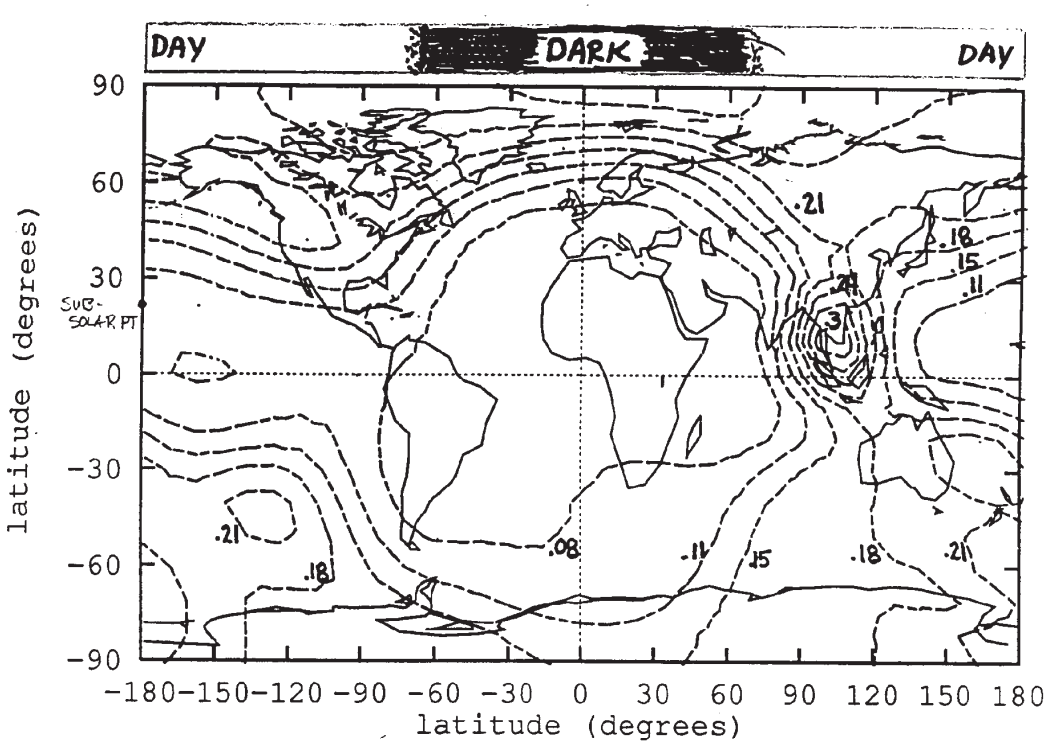

FIGURE 5.2.4–2 ELECTRON ENERGIES (eV) AT 400 KM FOR JULY 1 AND SOLAR MINIMUM CONDITIONS ($F_{10.7}$ = 70.1, IRI–86 RESULTS)

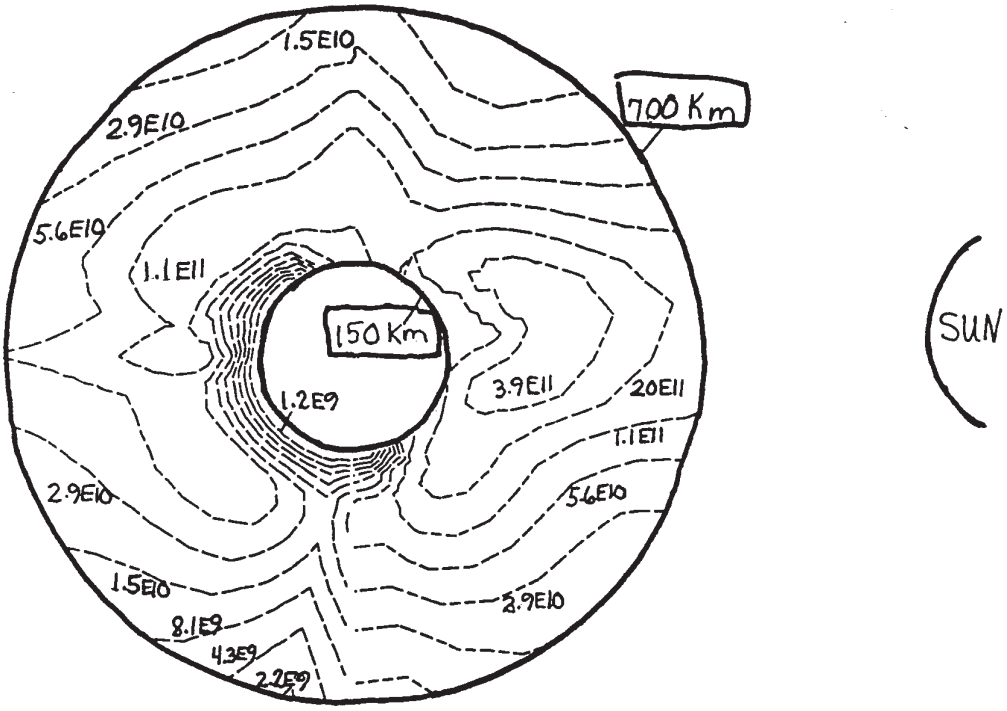

FIGURE 5.2.4–3 PLASMA DENSITY (m3) AS A FUNCTION OF ALTITUDE FOR JULY 1 AND SOLAR MINIMUM CONDITIONS

Contours are in the 0 – 180° longitude cross–section with the subsolar point on the 180° longitude. IRI–86 model results, $F_{10.7}$ – 70.1.

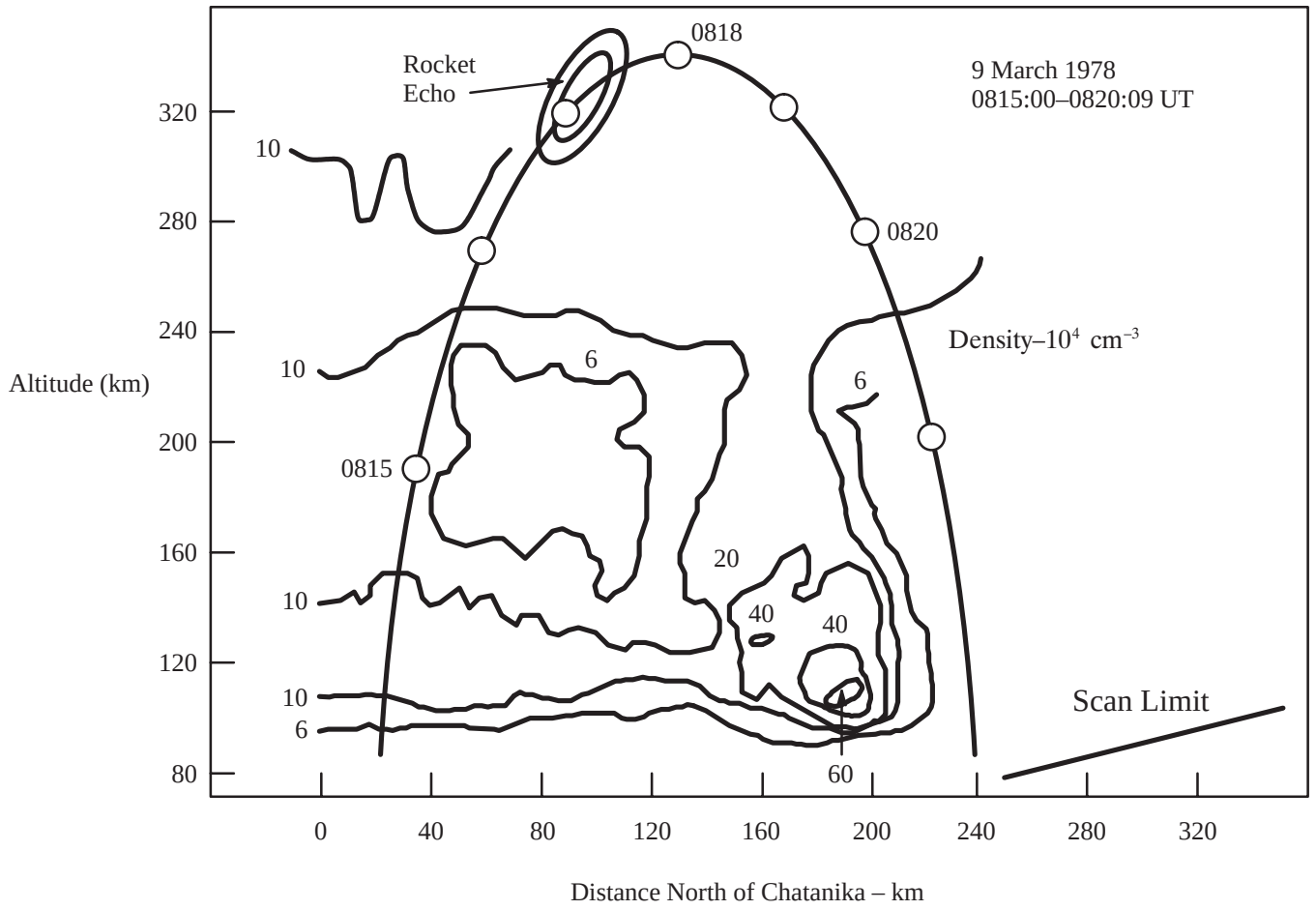

FIGURE 3–1 IONOSPHERIC ELECTRON DENSITY IN AN AURORA

*(Robinson, 1980)

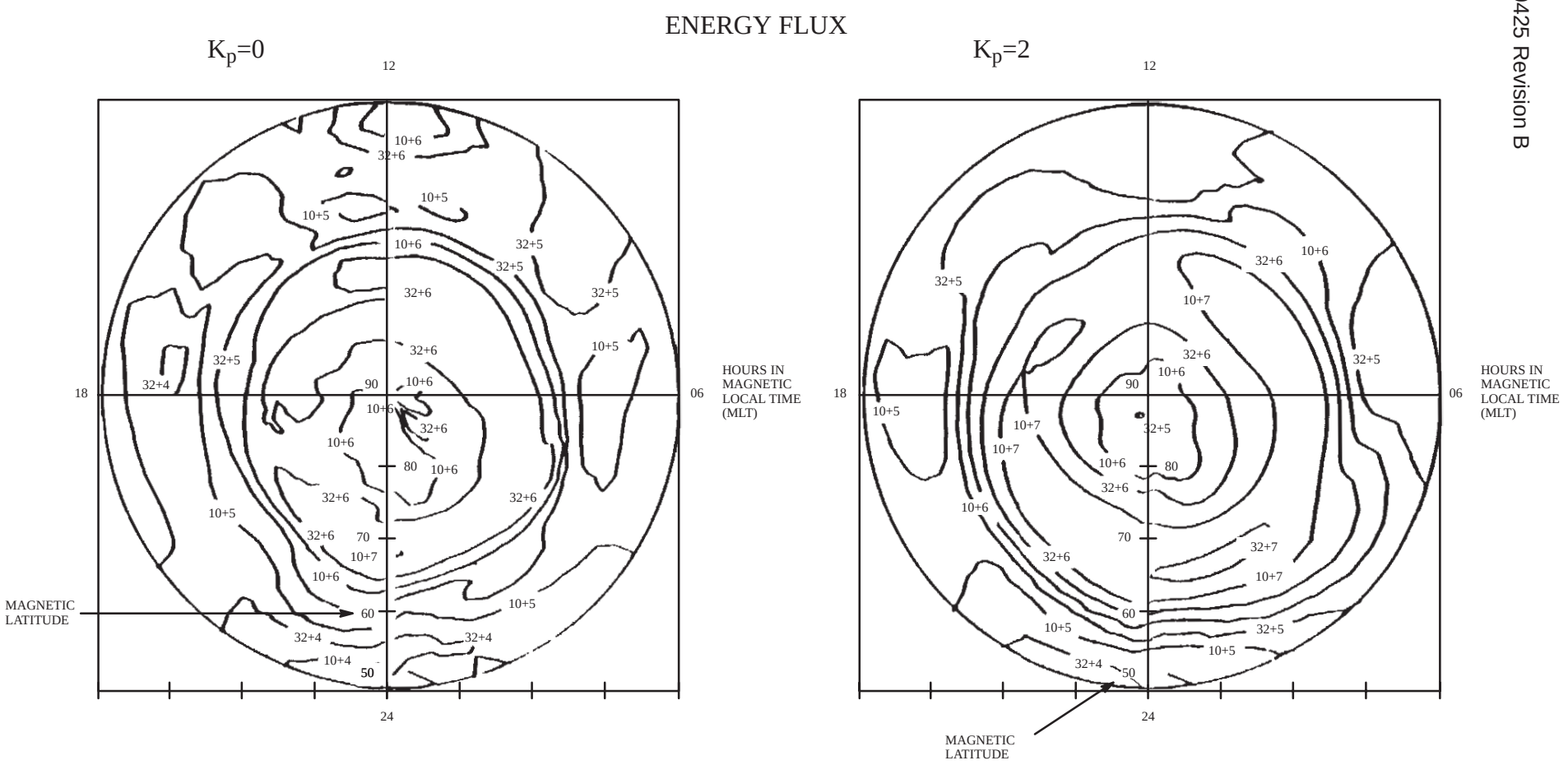

FIGURE 5.3.1–1A GLOBAL PLOTS OF THE AVERAGE INTEGRAL ENERGY FLUX (keV/cm^2·s·sr) OF PRECIPITATING ELECTRONS ARE PRESENTED IN POLAR SPECTROGRAM FORMAT, IN A MAGNETIC LOCAL TIME CORRECTED GEOMAGNETIC LATITUDE COORDINATE SYSTEM, FOR FOUR LEVELS OF K_p. PLOTS APPLY GLOBALLY TO BOTH POLES* (PAGE 1 OF 2)

*(Hardy et al., 1985)

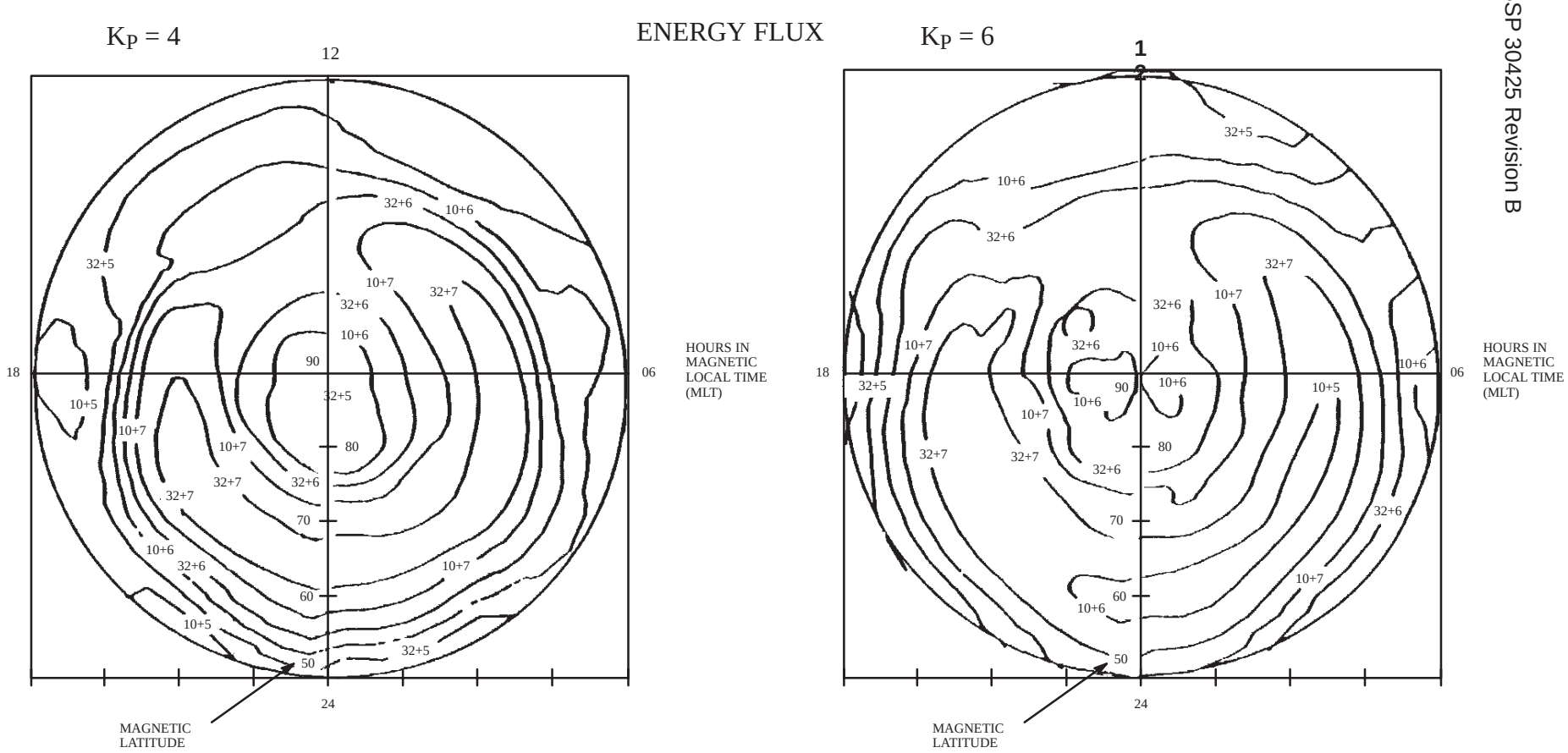

FIGURE 5.3.1–1A GLOBAL PLOTS OF THE AVERAGE INTEGRAL ENERGY FLUX (keV/cm^2·s·sr) OF PRECIPITATING ELECTRONS ARE PRESENTED IN POLAR SPECTROGRAM FORMAT, IN A MAGNETIC LOCAL TIME CORRECTED GEOMAGNETIC LATITUDE COORDINATE SYSTEM, FOR FOUR LEVELS OF K_P. PLOTS APPLY GLOBALLY TO BOTH POLES* (PAGE 2 OF 2)

*(Hardy et al., 1985)

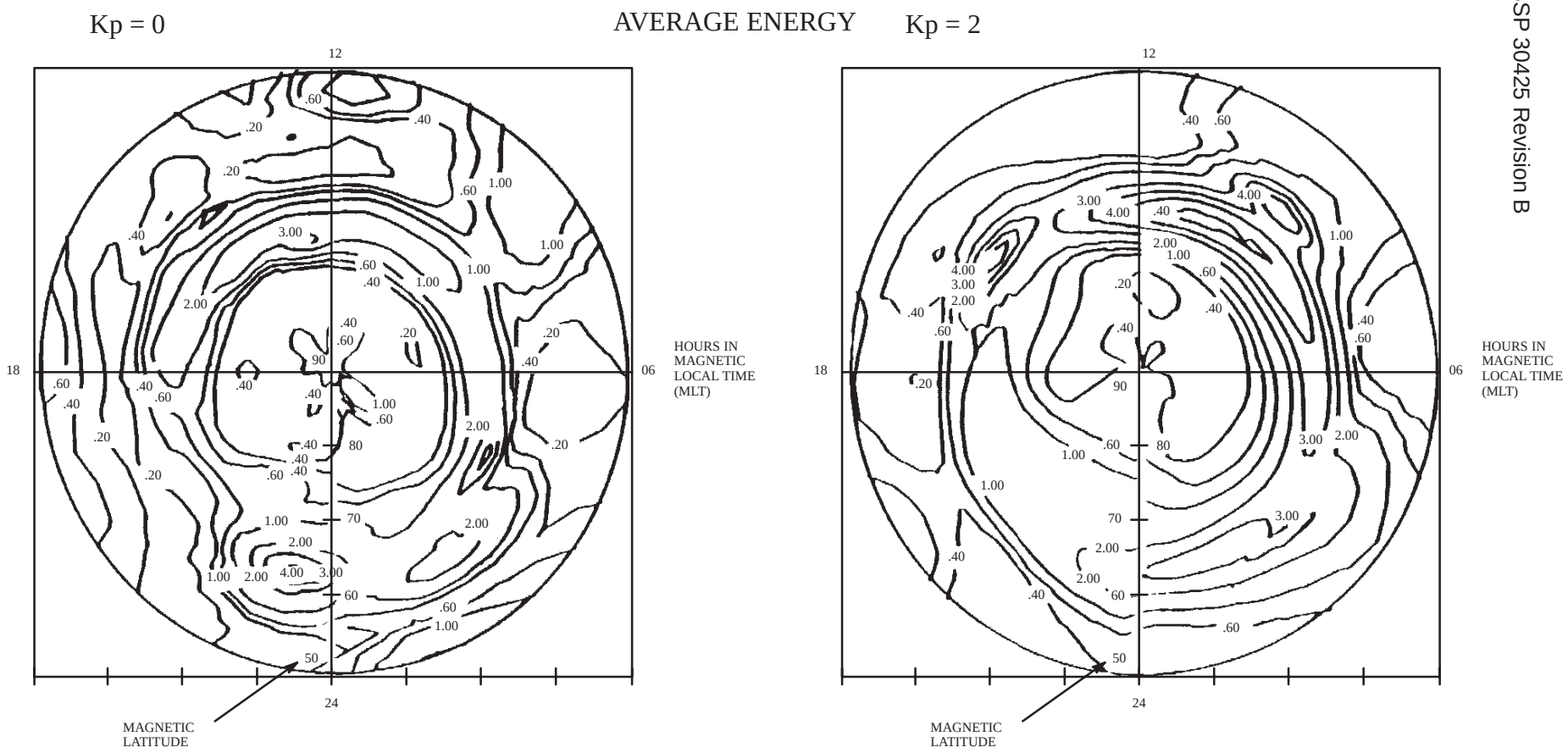

FIGURE 5.3.1–1B GLOBAL PLOTS OF THE AVERAGE ENERGY (keV) OF PRECIPITATING ELECTRONS ARE PRESENTED IN POLAR SPECTROGRAM FORMAT, IN A MAGNETIC LOCAL TIME CORRECTED GEOMAGNETIC LATITUDE COORDINATE SYSTEM, FOR FOUR LEVELS OF K_p. PLOTS APPLY GLOBALLY TO BOTH POLES* (PAGE 1 OF 2)

*(Hardy et al., 1985)

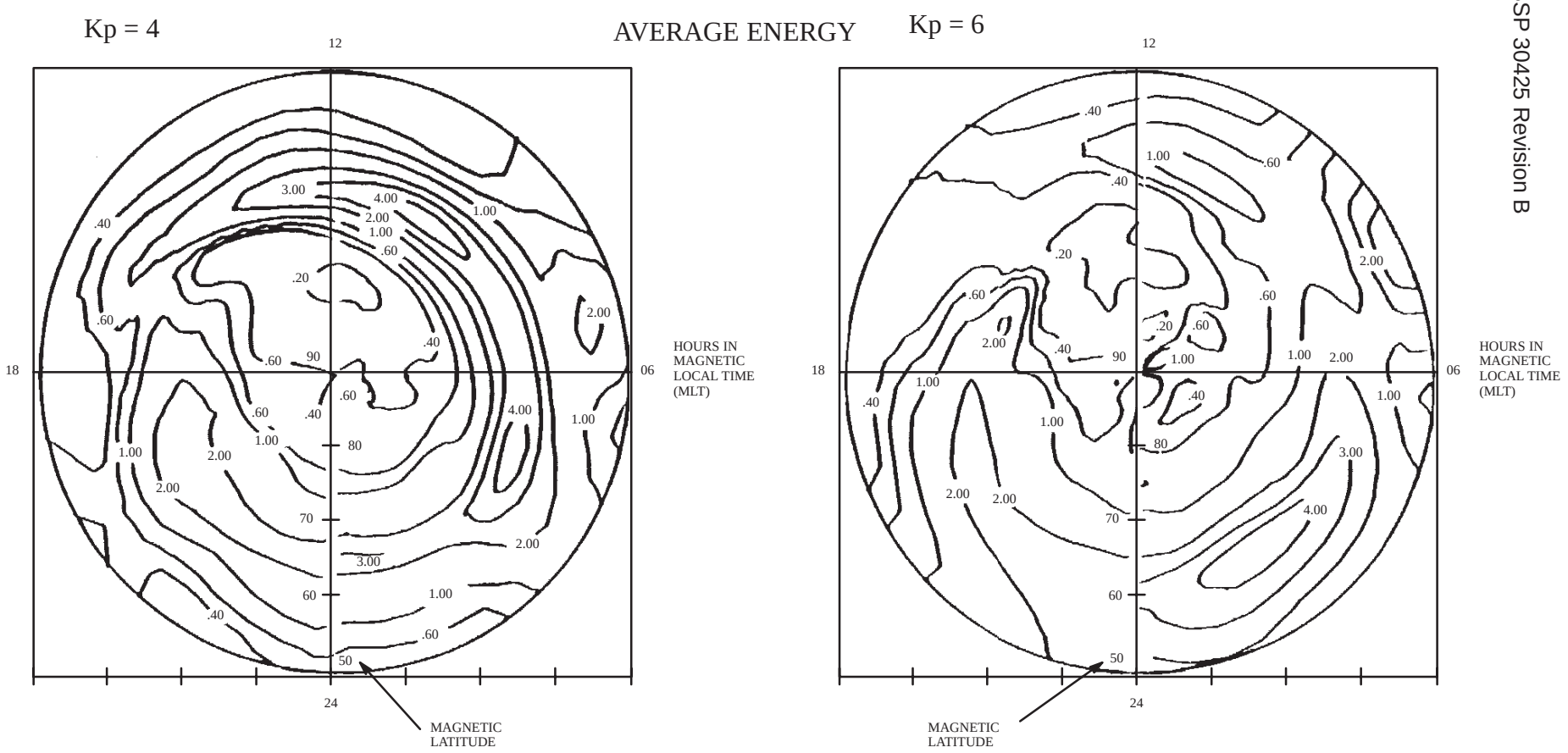

FIGURE 5.3.1–1B GLOBAL PLOTS OF THE AVERAGE ENERGY (keV) OF PRECIPITATING ELECTRONS ARE PRESENTED IN POLAR SPECTROGRAM FORMAT, IN A MAGNETIC LOCAL TIME CORRECTED GEOMAGNETIC LATITUDE COORDINATE SYSTEM, FOR FOUR LEVELS OF K_p. PLOTS APPLY GLOBALLY TO BOTH POLES* (PAGE 2 OF 2)

*(Hardy et al., 1985)

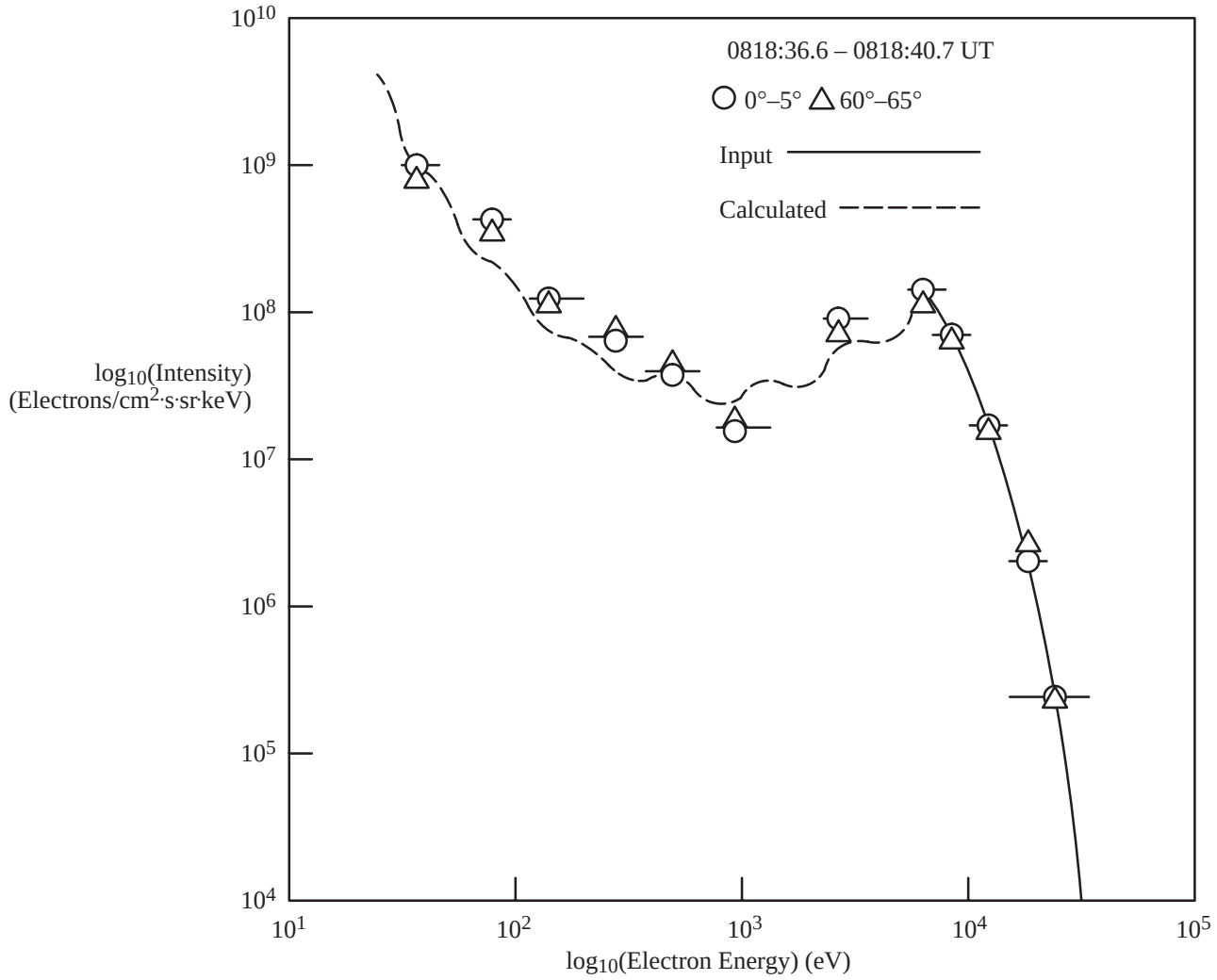

FIGURE 5.4.1–1 AURORAL ELECTRON INTENSITY (CENTER OF THE ARC)*

*(Pulliam, et. al., 1981)

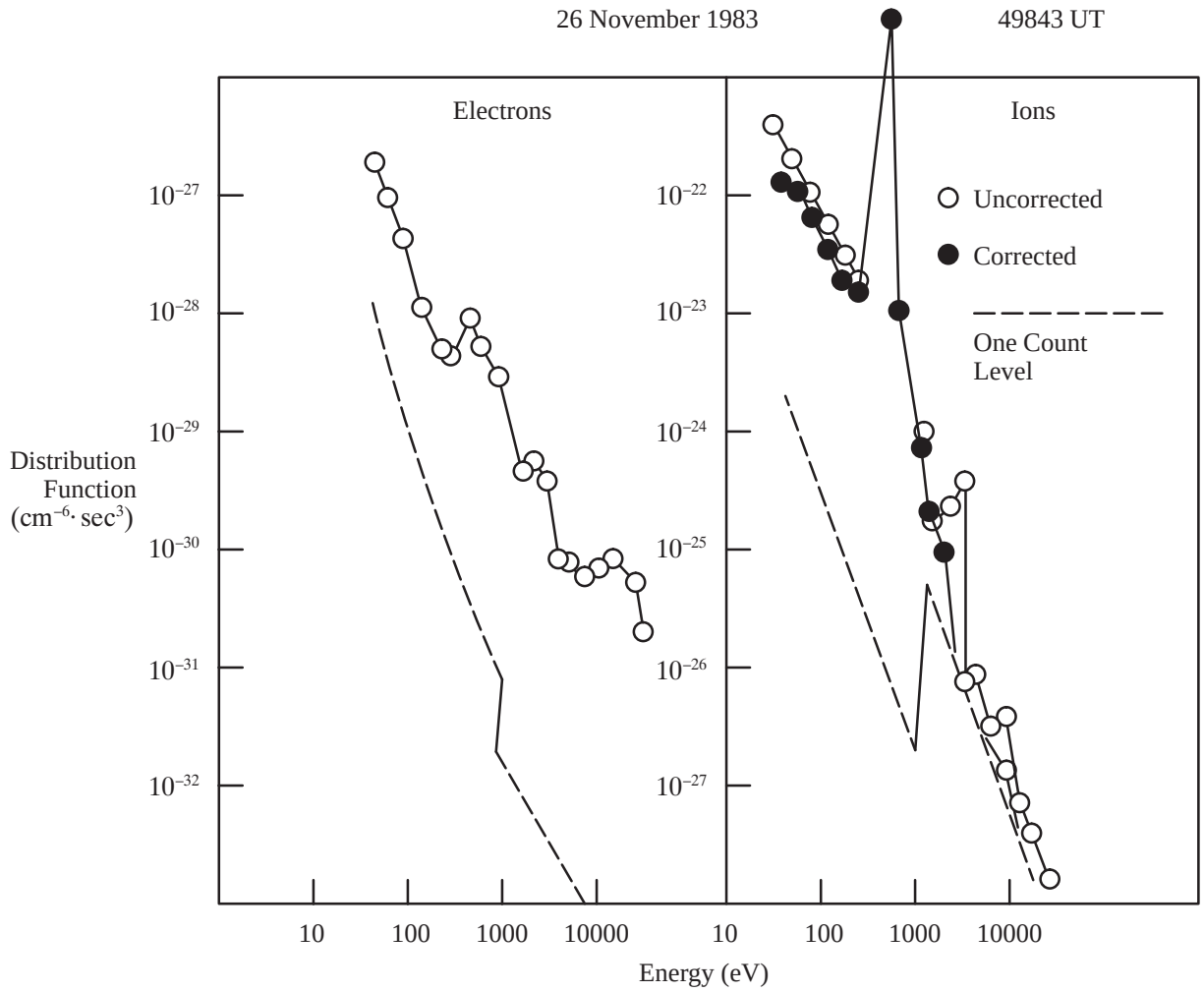

FIGURE 5.4.1–2 DISTRIBUTION FUNCTIONS OF ELECTRONS (LEFT) AND IONS (RIGHT) FOR VERY INTENSE AURORAL FLUXES*

*(Gussenhoven et al., 1985)

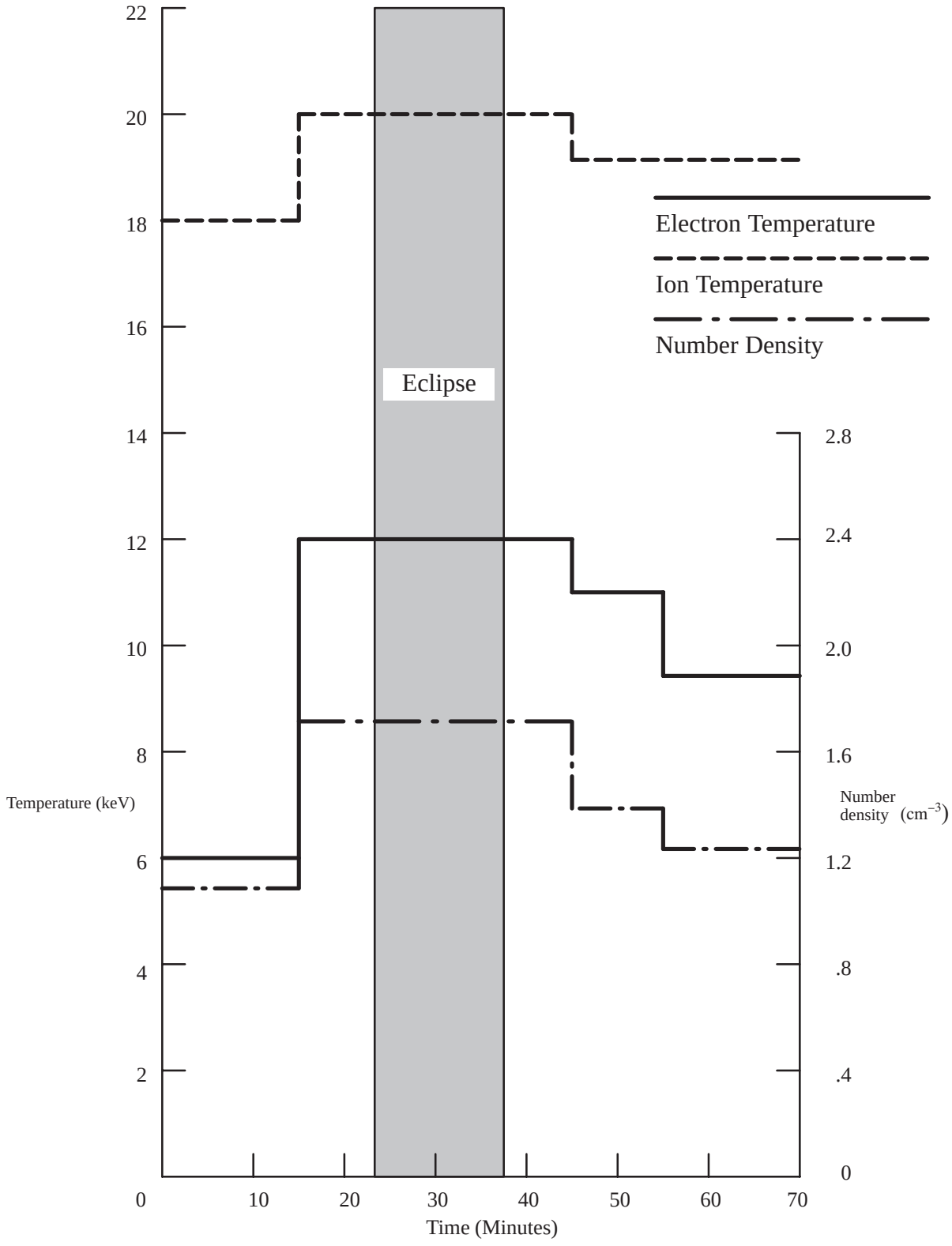

FIGURE 5.4.1–3 TIME HISTORY OF MODEL SUBSTORM–GEOSYNCHRONOUS PLASMA ENVIRONMENT*

*(Purvis et al., 1984)

6.0 PENETRATING CHARGED PARTICLES

Penetrating charged particles, often referred to as charged–particle radiation or corpuscular radiation, present a significant challenge to design and operation of a spacecraft. This is because many of the particles have sufficient energy to penetrate several centimeters of metal and to produce significant levels of ionization (radiation dose rate) inside the spacecraft. A high level of radiation will significantly affect materials, chemical processes, and living organisms, especially the crew. It will also affect electronics by causing soft upsets [referred to as Single Event Upsets (SEUs)], degrading performance and producing permanent damage. In addition, ionizing radiation will affect the propagation of light through optical materials by altering their optical properties. The quantitative relationship between the amount of ionization and the effects depends upon the nature of the radiation in a complicated way.

It is convenient to divide the charged particles into two groups, magnetospheric particles and cosmic rays. Magnetospheric particles are accelerated from (thermal, low energy) plasma by processes inside the magnetosphere and occur only within terrestrial space. Cosmic rays exist in interplanetary space and therefore enter terrestrial space from outside. Within terrestrial space, the motion of both kinds of charged particles is controlled by the geomagnetic field.

6.1 MAGNETOSPHERIC PARTICLES

6.1.1 TRAPPED RADIATION

These particles are trapped in the geomagnetic field and perform many oscillations between hemispheres and around the Earth during their lifetime. (Other terms for these particles are durably trapped, geomagnetically trapped, or Van Allen radiation.) The range of energies is rather large and is centered in the tens of kiloelectron volts (keV) for electrons and Megaelectron volts (MeV) for protons. The fluxes are generally stable in time except during great magnetic storms, and the iso–flux contours have axisymmetry around the Earth. (More precisely, the flux in three–dimensional space may be mapped into a function of two variables: field strength B and L or B and λ. The L–shell value is defined in paragraph 9.0 of this document. This means that the flux contours in a meridian plane can represent the entire three–dimensional morphology). Both protons and electrons occur. See Smith and West, 1982, for a general discussion.

These particles may originate on the sun, in the atmosphere, or may be produced by cosmic ray albedo neutron decay. They are guided and transported by geomagnetic and electric fields. In the absence of fluctuations, the particles retain their energy and move on a constant L–shell. Decaying neutrons projected upward from the atmosphere are the major source for trapped protons.

Particles leave the radiation belts when they collide with the neutral atmosphere. This is more likely to occur the deeper an orbit goes into the neutral atmosphere.

The general shape of the Van Allen belts follows the shape of the geomagnetic field. This means that the Space Station Program Elements (SSPEs) penetrate most deeply into the belts in the region of the South Atlantic Anomaly. Because the flux is increasing with altitude in the region of 300 to 1000 kilometers, the most intense radiation is encountered in the anomaly, as shown in Figure 6.1.1–1. The distributions of electron and proton fluxes in a meridional plane are shown in Figures 6.1.1–2 and 6.1.1–3, and the profile of proton flux with altitude at solar minimum is shown in Figure 6.1.1–4. The very steep inner gradient is controlled by the exact altitude dependence of the neutral atmospheric density which varies with solar activity. The atmosphere is more extended (higher density at a given altitude) when the sun is active. Thus, at 500 km the trapped proton flux is greater when the Sun is quiet. The profile at the inner edge is primarily controlled by the atmosphere modulated by solar activity. These changes do not show clearly on the figures listed above. However, they can be shown by a contour plot against B and L as shown in Figure 6.1.1–5.

The trapped flux environment at solar maximum and minimum is defined by the computer codes AP8MAX and AP8MIN for protons (Sawyer and Vette, 1976) and AE8MAX and AE8MIN for electrons (Teague and Vette, 1974; Teague et al., 1976). (These computer codes are available upon request from the Space Station Freedom Program Office, Reston, Virginia). It is essential that the magnetic field used with these models be the model of 1965 (Epoch 1964), i.e. IGRF 1965 80–term projection to 1964 model and the coefficients in Table 6.1.1–1, for solar minimum and 1970 (Epoch 1970), i.e., The Hurwitz US C&GS 1970 field and the coefficients in Table 6.1.1–2, for solar maximum (Stassinopoulos and Mead, 1972). Use of current (1985 model) field values, or those projected for the 1990s, will give flux values far higher than real at projected operating altitudes of the SSFPEs. This is because the Earth's field is decaying, which lowers the mirror point altitudes, resulting in loss of particles to the atmosphere at these low altitudes. Since the magnetic moment value of 0.31165300 was only appropriate near 1960, the ALLMAG routines (Stassinopoulos and Mead, 1972) for computing B and L and the ORP program for looking up fluxes in the AP and AE models must be modified by replacing the constant magnetic moment value with the following:

$$M = (G^2_{12} + G^2_{22} + G^2_{21})^{1/2}/100000$$

where G_{nm} are the field expansion coefficients. The revised computer code is available upon request from the Space Station Program Office, Houston, Texas.

In calculating total dose in Low Earth Orbit (LEO) it will be found that trapped protons contribute nearly the entire amount with three exceptions: at the lowest altitudes (below about 300 km), the contribution from trapped particles becomes so small that galactic cosmic rays (GCRs) make the largest contribution. For very thin shields (<0.3 g/cm^2), trapped electrons are more important than trapped protons. At high inclination orbits, solar

flare event particles make significant contributions. To repeat, because of the rapid variation with altitude, it is essential that the correct numerical models be used with the correct input parameters. It should be borne in mind that these models are correct only to within a factor of three for trapped proton fluxes and within a factor of five for trapped electrons. Variations can occur during very large magnetic storms that last a few days.

6.1.2 NON–ISOTROPIC EFFECTS

Since the Space Station is planned to be stabilized with respect to the velocity vector and local vertical, it will pass through the South Atlantic Anomaly where most of the geomagnetically trapped proton flux is encountered in much the same attitude on each pass. The proton flux is non–isotropic in this region, a factor which will affect the results of calculations involving complex shielding geometry. The flux is non–isotropic because the protons follow a helical path about a magnetic field line. As the field intensity increases, both the diameter and the pitch of the helix decrease until the pitch becomes zero. The point with zero pitch angle is called the mirror point and the center of the helical path is called the guiding center. From here the helix reverses direction and protons travel up the field line toward decreasing field intensity and away from the Earth. In the South Atlantic Anomaly almost all the protons observed are near their mirror points. Thus the flux is anisotropic with most of the flux arriving from a narrow band perpendicular to the local geomagnetic field direction. Any protons there which are not nearly mirroring will travel deep into the atmosphere and be scattered or stopped by atmospheric interactions.

Atmospheric interactions also affect the proton angular distribution in another fashion. Protons that are observed traveling eastward are following guiding centers above the observation point and protons traveling westward are following guiding centers below the observation point. The gyroradius for energetic protons in the Anomaly is on the same order as the atmospheric density scale height. Thus westward traveling protons encounter a significantly denser atmosphere and are more likely to suffer atmospheric interactions and be lost. The resulting energy–dependent anisotropy is called the east–west effect. For typical values of the magnetic field parameters and atmospheric scale height in the Anomaly, the ratio of eastward traveling to westward traveling flux is 3 for 50 MeV protons, 22 for 400 MeV protons.

Evaluation of the anisotropic effects is complex, but a computer code for use in conjunction with the AP8MAX and AP8MIN models is available from the Space Station Program Office, Houston, Texas.

6.2 COSMIC RAYS

For the purpose of this document, the term “cosmic rays” applies to electrons, protons, and the nuclei of all elements. Outside the Earth’s magnetosphere, all galactic cosmic rays may be treated as isotropic (to within about 10 percent).

Within the Earth's magnetic field, the less energetic nuclei are deflected by the field, and at lower altitudes, the flux becomes anisotropic while the energy spectrum, the total flux, and the directional characteristics are modified by geomagnetic shielding. For every SSPE mission phase, this effect must be evaluated and integrated over many orbits.

The source of cosmic rays is either galactic or solar. Galactic cosmic rays (GCRs) originate outside the solar system and are thought to permeate our galaxy. Since the condition of the interplanetary medium through which cosmic rays propagate depends on solar activity, the number reaching the Earth's orbit is modulated by the 11–year solar cycle. During the maximum activity phase, the intensity near the Earth decreases, and during the minimum activity phase, it increases.

Solar particle events, in contrast, originate in the Sun and are produced only occasionally in solar flares. They are lower in energy than GCRs (1 Megaelectron volt (MeV) to 1 Gigaelectron volt (GeV)/nucleon) and are mostly protons and alpha particles. They are a significant hazard during years of maximum solar activity. Although the occurrence of large flares is not yet predictable, especially with long leads times, it is now known that large flares tend to occur in large, highly sheared, magnetically–complex active regions; so, prediction of events with <24 hr notice may someday be possible.

6.2.1 GALACTIC COSMIC RAYS

GCRs consist of the nuclei of the elements and of about 2 percent electrons. Their energies cover the range from 10 MeV per particle to above 1.0E16 MeV per particle. The flux is highest during periods of minimum solar activity. At these energies, the nuclei are completely ionized. A small flux of X–rays and γ–rays from celestial sources is sometimes included in GCRs, but for SSPE design purposes, only cosmic ray nuclei are significant, and this section will be confined to them. GCRs consist of the nuclei of the elements from hydrogen through iron in roughly the same proportions as are found in the solar system but with the heavier nuclei more abundant in the cosmic rays. Nuclei heavier than nickel are extremely rare.

Figure 6.2.1–1 gives the relative abundances and energy spectra of GCRs of interest. The figure covers the energy range of importance in essentially all SSPE radiation effects studies. In spite of their small number, the heavy elements are very important due to their densely ionizing tracks. They are responsible for many effects in detectors and microelectronics. From Figure 6.2.1–1 it can be seen that the flux of each nuclear species decreases rapidly with increasing energy. At the lowest energies observed outside the magnetosphere, the flux is limited by magnetic fields carried by the solar wind. The energies observed and the flux at these energies vary inversely with the solar cycle.

Although the contribution from GCRs to the total dose in rads inside a spacecraft is typically less than 15 percent for most geocentric orbits, these nuclei are responsible for

such effects as “single event upsets” (SEU’s) and “latch–up” in microcircuits [Large Scale Integration (LSI) and Very Large Scale Integrated Devices (VLSID)]. Along with the trapped radiation–belt protons, the nuclei are also responsible for the induced radioactivity in most materials in orbit. Noise induced directly by ionization in sensitive devices such as charge–coupled devices (CCDs) and via Cerenkov and fluorescence radiation in photomultiplier tubes are other effects of GCRs that must frequently be considered. The designer should also consider the possible effects of GCRs on materials as well as the probability of production of secondary particles and their effects.

The available data have been fit to an empirical model which is summarized in Table 6.2.1–1. Figures 6.2.1–2A, 6.2.1–2B, and 6.2.1–2C show the differential spectra of protons, alpha–particles, and iron nuclei at various levels of solar activity and the fit of the model. This model should be used to define the GCR environment.

6.2.2 SOLAR PARTICLE EVENTS

Solar particle events are sporadic interplanetary phenomena with durations of a few days at irregular intervals from a few weeks to a few years depending on the intensity threshold considered. Their most significant components consist of solar flare protons at energies from a few MeV to a few hundred MeV. The proton spectra may exhibit intensities that vary over several orders of magnitude, both from event to event and within the time profile of an individual event. The solar particles will, however, envelop the Earth within minutes after a solar flare event and reach peak intensity in a few hours and decay in 1 or 2 days. They are less likely to occur during solar cycle minima. Within the Earth’s magnetosphere, the solar flare protons reach LEO most freely in the polar regions at magnetic latitudes above about 63 degrees because the magnetic energetic cutoff goes to near zero at higher latitudes (see below).

An empirical representation of the probability of solar particle events has been provided, and Table 6.2.2–1 summarizes this model. Figure 6.2.2–1 shows a history of solar proton events over two solar cycles, and Figure 6.2.2–2 gives differential spectra integrated over various events.

6.2.3 GEOMAGNETIC SHIELDING AND CUTOFF RIGIDITY

The Earth’s magnetic field deflects incoming cosmic rays (solar and galactic) to a degree which depends on the energy of the particles, preventing those with lower energies from penetrating deep into the magnetosphere (cut–off rigidity). In LEO the minimum rigidity, P_{min}/Z, that a particle can have and reach a latitude λ from the vertical is

$$P_{min}/Z = 15\ GV \frac{\cos^4 \lambda}{(r/R_E)^2}$$

where rigidity is defined as momentum P divided by the charge Z on the particle (the usual unit is volts or billions of volts, GV), r/R_E is the radial distance from the center of the Earth in units of Earth radii, and λ is the latitude. The minimum cutoff drops to near zero somewhat faster than the formula predicts at magnetic latitudes above about 65 degrees. The cutoff is also lower at high altitude for a given latitude, as can be seen from the r/R_E dependence. Thus, spacecraft orbiting the Earth may either be continuously exposed to the unattenuated interplanetary cosmic ray intensities (e.g., high altitude polar orbits, geostationary orbits, etc.), may be intermittently exposed (e.g., low altitude polar orbits), or may be completely shielded up to an energy of approximately 10 MeV for low–inclination, low–altitude orbits, and to about 10 GeV for equatorial orbits. To approximate the average exposure of the SSPE to cosmic rays, calculations must be performed over many orbital revolutions. An approach to this is summarized in Table 6.2.3–1.

TABLE 6.1.1–1 SPHERICAL HARMONIC COEFFICIENTS OF THE INTERNATIONAL GEOMAGNETIC REFERENCE FIELD (IGRF) 1965 (PAGE 1 OF 2)

n	m	g_n^m	h_n^m	gt_n^m	ht_n^m
0	0	1		10	
1	0	–30339		153	
1	1	–2123	5758	87	–23
2	0	–1654		–244	
2	1	2994	–2006	3	–118
2	2	1567	130	–16	–167
3	0	1297		2	
3	1	–2036	–403	–108	42
3	2	1289	242	7	7
3	3	843	–176	–38	–77
4	0	958		–7	
4	1	805	149	2	–1
4	2	492	–280	–30	16
4	3	–392	8	–1	29
4	4	256	–265	–21	–42
5	0	–223		19	
5	1	357	16	11	23
5	2	246	125	29	17
5	3	–26	–123	6	–24
5	4	–161	–107	0	8
5	5	–51	77	13	–3
6	0	47		–1	
6	1	60	–14	–3	–9
6	2	4	106	11	–4
6	3	–229	68	19	20
6	4	3	–32	–4	–11
6	5	–4	–10	–4	1
6	6	–112	–13	–2	9
7	0	71		–5	
7	1	–54	–57	–3	–11
7	2	0	–27	–7	3
7	3	12	–8	–5	4
7	4	–25	9	3	2
7	5	–9	23	0	4
7	6	13	–19	–2	2
7	7	–2	–17	–6	3
8	0	10		1	
8	1	9	3	4	1

TABLE 6.1.1–1 SPHERICAL HARMONIC COEFFICIENTS OF THE INTERNATIONAL GEOMAGNETIC REFERENCE FIELD (IGRF) 1965 (PAGE 2 0F 2)

n	m	g_n^m	h_n^m	gt_n^m	ht_n^m
8	2	–3	–13	6	–2
8	3	–12	5	0	–3
8	4	–4	–17	0	–2
8	5	7	4	–1	–3
8	6	–5	22	3	–4
8	7	12	–3	–3	–3
8	8	6	–16	–5	–3

TABLE 6.1.1–2 SPHERICAL HARMONIC COEFFICIENTS OF THE INTERNATIONAL GEOMAGNETIC REFERENCE FIELD (IGRF) 1970 (PAGE 1 OF 2)

n	m	g_n^m	h_n^m
0	0	10	
1	0	–302059	
1	1	–20664	57446
2	0	–17917	
2	1	29971	–20582
2	2	16086	430
3	0	12899	
3	1	–20708	–3699
3	2	12760	2456
3	3	8334	–1880
4	0	9475	
4	1	8009	1617
4	2	4579	–2758
4	3	–3690	185
4	4	2436	–2788
5	0	–2145	
5	1	3595	157
5	2	2490	1420
5	3	–290	–1310
5	4	–1669	–911
5	5	–582	808
6	0	460	
6	1	651	–171
6	2	95	1146
6	3	–2188	625
6	4	20	–323
6	5	–22	–78
6	6	–1125	38
7	0	734	
7	1	–546	–666
7	2	46	–265
7	3	175	–34
7	4	–210	81
7	5	–32	209
7	6	143	–240
7	7	41	–186
8	0	121	

TABLE 6.1.1–2 SPHERICAL HARMONIC COEFFICIENTS OF THE INTERNATIONAL GEOMAGNETIC REFERENCE FIELD (IGRF) 1970 (PAGE 2 OF 2)

n	m	g_n^m	h_n^m
8	1	77	121
8	2	–32	–160
8	3	–124	22
8	4	–44	–176
8	5	45	46
8	6	34	189
8	7	125	–46
8	8	94	–187
9	0	107	
9	1	57	–174
9	2	23	163
9	3	–110	14
9	4	131	–27
9	5	33	–32
9	6	2	80
9	7	15	137
9	8	9	–4
9	9	–4	–14
10	0	–39	
10	1	–26	27
10	2	7	19
10	3	–19	0
10	4	–15	35
10	5	74	–45
10	6	46	22
10	7	6	–31
10	8	–8	56
10	9	22	–1
10	10	14	–63

TABLE 6.2.1–1 GALACTIC COSMIC RAYS* (GCRs) (PAGE 1 OF 13)

The following paragraphs and seven sub–tables present an algorithm for computing the differential energy spectra of the most important charged particle populations in the Earth's vicinity. These equations were devised to fit the data and are intended to have no physical interpretation. This analytic formula may be easily programmed for a digital computer of almost any size and is intended to become a subroutine in a program which will be used to estimate the soft error rates in satellite–borne electronics.

GCRs consist of electrons and the nuclei of all the elements in the periodic table; the first 28 elements are the most important for cosmic ray effects on microelectronics. These particles are from outside the solar system, and their flux at low energies is anticorrelated with solar activity (i.e., more cosmic rays at solar minimum). The differential energy spectra in particles per square meter steradian second million electron volts per atomic mass unit (i.e., $\text{particles}/\text{m}^2 \cdot \text{sr} \cdot \text{s} \cdot \text{MeV}/\mu$) are given in the following paragraphs.

The spectra for protons (hydrogen nuclei), alpha–particles (helium nuclei), and iron nuclei are given below for energies above 10 MeV/μ:

$$F(E,t) = A(E) \sin[W (t-t_0)] + B(E) \qquad \text{(T6.2.1–1,1)}$$

where $W = 0.576$ radian/year,

$t_0 = 1950.6$ A.D. date,

t = current date in years,

E = particle energy in MeV/nucleon

$$B(E) = 0.5 [f_{min}(E) + f_{max}(E)], \qquad \text{(T6.2.1–1,2)}$$

$$A(E) = 0.5 [f_{min}(E) - f_{max}(E)] \qquad \text{(T6.2.1–1,3)}$$

f_{max} and f_{min} differ only by the choice of constants in the equation,

$$f(E) = 10^m (E/E_0)^a \qquad \text{(T6.2.1–1,4)}$$

where, $$a = a_0 \{1 - \exp[-X_1 (\log_{10} E)^b]\} \qquad \text{(T6.2.1–1,5)}$$

and $$m = C_1 \exp[-X_2 (\log_{10} E)^2] - C_2 \qquad \text{(T6.2.1–1,6)}$$

*(Table 6.2.1–1 is from Adams et al., 1981, 1986.)

TABLE 6.2.1–1 GALACTIC COSMIC RAYS (GCRs)* (PAGE 2 OF 13)

The values of the constants a_0, E_0 b, X_1, X_2, C_1, and C_2 are given in Table 6.2.1–1.1 for each of the elements hydrogen (H), helium (He), and iron (Fe) for the conditions of solar maximum and solar minimum.

TABLE 6.2.1–1.1 CONSTANTS USED IN EQUATIONS (T6.2.1–1,4) THROUGH (T6.2.1–1,6) TO COMPUTE THE DIFFERENTIAL ENERGY SPECTRA OF H, He, AND Fe AT SOLAR MAXIMUM AND SOLAR MINIMUM

Element	a_0	E_0	b	X_1	X_2	C_1	C_2
H–min	–2.20	1.1775E+5	2.685	0.117	0.80	6.52	4.00
H–max	–2.20	1.1775E+5	2.685	0.079	0.80	6.52	4.00
He–min	–2.35	8.2700E+4	2.070	0.241	0.83	4.75	5.10
He–max	–2.35	8.2700E+4	2.070	0.180	0.83	4.75	5.10
Fe–min	–2.14	1.1750E+5	2.640	0.140	0.65	6.63	7.69
Fe–max	–2.14	1.1750E+5	2.640	0.102	0.65	6.63	7.69

TABLE 6.2.1–1 GALACTIC COSMIC RAYS (GCRs)* (PAGE 3 OF 13)

The differential energy spectra for carbon (C), oxygen (O), fluorine (F), neon (Ne), sodium (Na), aluminum (Al), and phosphorus (P) are obtained by multiplying the helium spectrum (obtained from equation (T6.2.1–1,1)) by the appropriate scaling factor in Table 6.2.1–1.2.

TABLE 6.2.1–1.2 THE RATIO OF THE ABUNDANCE OF VARIOUS NUCLEI TO HELIUM

Element	Ratio	Element	Ratio
C	3.04E–2		
O	2.84E–2	Al	1.07E–3
F	6.06E–4		
Ne	4.63E–3	P	2.34E–4
Na	1.02E–3		

TABLE 6.2.1–1 GALACTIC COSMIC RAYS (GCRs)* (PAGE 4 OF 13)

The differential energy spectra for calcium (Ca), cobalt (Co), and nickel (Ni) are obtained by multiplying the iron spectrum (obtained from equation (T6.2.1–1,1)) by the scaling factors listed in Table 6.2.1–1.3.

TABLE 6.2.1–1.3 THE RATIOS OF THE ABUNDANCE OF VARIOUS ELEMENTS TO IRON

Element	Ratio
Ca	2.1E–1
Co	3.4E–3
Ni	5.0E–2

TABLE 6.2.1–1 GALACTIC COSMIC RAYS (GCRs)* (PAGE 5 OF 13)

The spectra of the elements lithium (Li), beryllium (Be), and boron (B) are obtained from the helium spectrum, F_{He}, modified by the equation:

$$F^* = \begin{cases} 0.021\ F_{He} & E < 3000\ MeV/\mu \\ 0.729\ E^{-0.443}\ F_{He,} & E \geq 3000\ MeV/\mu \end{cases} \qquad \text{(T6.2.1–1,7)}$$

to obtain the combined spectrum of (Li + Be + B). Equation (T6.2.1–1,7) is then multiplied by the ratio in Table 6.2.1–1.4 to obtain the individual elemental spectra.

TABLE 6.2.1–1.4 THE RELATIVE FRACTIONS OF Li, Be, AND B IN THE COMBINED TOTAL ABUNDANCE Li + Be + B

Element	Ratio
Li	0.330
Be	0.176
B	0.480

The spectrum of the element nitrogen (N) is obtained by modifying the helium spectrum, F_{He} as shown below:

$$F_N = \{8.7E{-}3\ \exp[-0.4\ (\log_{10}E - 3.15)^2] + 7.6E{-}3\ \exp[-0.9\ (\log_{10}E - 0.8)^2]\}\ F_{He} \qquad \text{(T6.2.1–1,8)}$$

where E is in MeV/μ

The spectra of the elements magnesium (Mg), silicon (Si), and sulfur (S) are obtained by modifying the helium spectrum, F_{He}, as shown:

$$F^* = \begin{cases} F_{He} & E < 2200 \\ (1 + 1.56E{-}5\ (E{-}2200))F_{He.} & E \geq 2200 \end{cases} \qquad \text{(T6.2.1–1,9)}$$

TABLE 6.2.1–1 GALACTIC COSMIC RAYS (GCRs)* (PAGE 6 OF 13)

The individual spectra for these elements are obtained by multiplying F* by the ratio of Table 6.2.1–1.5.

TABLE 6.2.1–1.5 THE RATIOS OF Mg, Si, AND S TO AN ADJUSTED HELIUM SPECTRUM

Element	Ratio
Mg	6.02E–3
Si	4.63E–3
S	9.30E–4

The spectra for the elements chlorine (Cl), argon (Ar), potassium (K), scandium (Sc), titanium (Ti), vanadium (V), chromium (Cr), and manganese (Mn) are all obtained by modifying the iron spectrum, F_{Fe}, as shown below:

$$F^* = Q(E)\, F_{Fe} \qquad \text{(T6.2.1–1,10)}$$

where

$$Q(E) = 16\,[1 - \exp(-0.075\, E^{0.4})]\, E^{-0.33} \qquad \text{(T6.2.1–1,11)}$$

where E is in MeV/μ.

TABLE 6.2.1–1 GALACTIC COSMIC RAYS (GCRs)* (PAGE 7 OF 13)

The F*, from the sub–iron spectrum (equation (T6.2.1–1,10)) is multiplied by the appropriate ratio in Table 6.2.1–1.6 to obtain the individual elemental spectra.

TABLE 6.2.1–1.6 THE FRACTIONAL ABUNDANCE OF EACH ELEMENT IN THE SUB–IRON GROUP

Element	Ratio	Element	Ratio
Cl	0.070	Ti	0.147
Ar	0.130	V	0.070
K	0.090	Cr	0.140
Sc	0.042	Mn	0.100

TABLE 6.2.1–1 GALACTIC COSMIC RAYS (GCRs)* (PAGE 8 OF 13)

The differential energy spectra for elements from copper to uranium are obtained by multiplying the iron spectrum (from equation (T6.2.1–1, 1)) by the scaling factors listed in Table 6.2.1–1.7.

TABLE 6.2.1–1.7 THE RATIO OF THE ABUNDANCES OF VARIOUS NUCLEI TO IRON (PAGE 1 OF 2)

Element	Ratio	Element	Ratio
Cu	6.8E–4	Pm	1.9E–7
Zn	8.8E–4	Sm	8.7E–7
Ga	6.5E–5	Eu	1.5E–7
Ge	1.4E–4	Gd	7.0E–7
As	9.9E–6	Tb	1.7E–7
Se	5.8E–5	Dy	7.0E–7
Br	8.3E–6	Ho	2.6E–7
Kr	2.3E–5	Er	4.3E–7
Rb	1.1E–5	Tm	8.9E–8
Sr	3.6E–5	Yb	4.4E–7
Y	6.8E–6	Lu	6.4E–8
Zr	1.7E–5	Hf	4.0E–7
Nb	2.6E–6	Ta	3.6E–8
Mo	7.1E–6	W	3.8E–7
Tc	1.6E–6	Re	1.3E–7
Ru	5.3E–6	Os	5.6E–7
Rh	1.5E–6	Ir	3.7E–7
Pd	4.5E–6	Pt	7.2E–7

TABLE 6.2.1–1 GALACTIC COSMIC RAYS (GCRs)* (PAGE 9 OF 13)

TABLE 6.2.1–1.7 THE RATIO OF THE ABUNDANCES OF VARIOUS NUCLEI TO IRON (PAGE 2 OF 2)

Element	Ratio	Element	Ratio
Ag	1.3E–6	Au	1.3E–7
Cd	3.6E–6	Hg	2.3E–7
In	1.4E–6	Tl	1.8E–7
Sn	7.5E–6	Pb	1.7E–6
Sb	9.9E–7	Bi	9.0E–8
Te	5.7E–6	Po	0
I	1.5E–6	At	0
Xe	3.5E–6	Rn	0
Cs	5.8E–7	Fr	0
Ba	6.0E–6	Ra	0
La	5.3E–7	Ac	0
Ce	1.6E–6	Th	9.0E–8
Pr	3.0E–7	Pa	0
Nd	1.1E–6	U	5.4E–8

The formula given above is correct for quiet periods in the interplanetary medium when only the GCRs are present. These conditions are often disturbed, especially at low energies, by small solar flares, co–rotating events, etc. To allow for typical disturbed conditions, a worst–case spectrum should be employed. With 90 percent confidence, the instantaneous particle flux should never be more intense than described by this case at any energy.

TABLE 6.2.1–1 GALACTIC COSMIC RAYS (GCRs)* (PAGE 10 OF 13)

To construct the worst–case spectrum for protons, compute the "H–min" spectrum (using equation (T6.2.1–1,4)) and then compute $F_{H–worst}$ as shown below:

$$F_{H–worst} = [1897e^{-E/9.66} + 1.64]\, F_{H–min} \qquad \text{(T6.2.1–1,12)}$$

This applies for $E \leq 100$ MeV/μ. For higher energies, use the GCR spectrum for the appropriate mission time t (in Equation (T6.2.1–1,1)).

In like manner, the solar minimum case for helium and iron spectra (obtained from Equation (T6.2.1–1,4)) is multiplied by:

$$28.4\ e^{-E/13.84} + 1.64 \qquad \text{(T6.2.1–1,13)}$$

for $E \leq 100$ MeV/μ.

The worst–case spectra of H, He, and Fe for any element for E > 100 MeV/μ are approximated by a multiple of the solar minimum spectra:

$$F_{worst} = 1.64\ F_{min} \qquad \text{(T6.2.1–1,14)}$$

The resulting spectra are employed as described above to obtain the other elemental spectra, i.e., in the same way as F_{He} and F_{Fe} were used.

In addition to galactic cosmic rays, some particles are believed to be accelerated in the interplanetary medium. The most important of these is called the anomalous component. The contribution of the anomalous component to the helium spectrum is important for cosmic ray effects on microelectronics. For periods of decaying or minimum solar activity the cosmic ray helium spectrum should be modified as follows:

1. Determine the maximum values of the cosmic–ray spectra from Equation (T6.2.1–1,4) using the He–max and He–min constants from Table 6.2.1–1.1.

2. Modify equation (T6.2.1–1,4) so that these maximum values apply for all energies below the energy at which the maxima occurs, i.e., for solar minimum:

$$f^*_{He–min} = \begin{cases} 0.33, & E < 200\ \text{MeV}/\mu \\ f_{He–min}\ [\text{from Eqn. (T6.2.1–1,4)}] & E \geq 200\ \text{MeV}/\mu \end{cases} \qquad \text{(T6.2.1–1,15)}$$

3. Make the same type of modification, $f^*_{He–max}$ for solar maximum:

$$f^*_{He–max} = \begin{cases} 0.079, & E < 300\ \text{MeV}/\mu \\ f_{He–max}\ [\text{from Eqn. (T6.2.1–1,4)}] & E \geq 300\ \text{MeV}/\mu \end{cases} \qquad \text{(T6.2.1–1,16)}$$

TABLE 6.2.1–1 GALACTIC COSMIC RAYS (GCRs)* (PAGE 11 OF 13)

4. Combine the resulting spectra as before using equations (T6.2.1–1,1) through (T6.2.1–1,3).

NOTE: This applies only to He. Use the regular He spectra of equations (T6.2.1–1,1) through (T6.2.1–1,6) for obtaining the spectra of other elements.

Besides helium, the anomalous component contributes to the oxygen and nitrogen spectra at low energies. For years with decaying or minimum solar activity these contributions should be added to the GCR oxygen and nitrogen spectra.

For oxygen, use:

$$f(E) = 6E{-}2 \exp[-(\ln (E) - 1.79)^2/0.70]$$

$$(\text{particles}/\text{m}^2 \cdot \text{sr} \cdot \text{s} \cdot \text{MeV}/\mu) \qquad \text{(T6.2.1–1,17)}$$

This spectrum crosses over the galactic spectrum at approximately 30 MeV/μ. The two spectra should be matched at that point with equation (T6.2.1–1,17) replacing the galactic spectrum at lower energies.

Similarly for nitrogen:

$$f(E) = 1.54E{-}2 \exp[-(\ln (E) - 1.79)^2/0.70]$$

$$(\text{particles}/\text{m}^2 \cdot \text{sr} \cdot \text{s} \cdot \text{MeV}/\mu) \qquad \text{(T6.2.1–1,18)}$$

Again, this crosses with the GCR spectrum at approximately 30 MeV/μ and should replace it below this energy.

The spectra of the remaining elements are unaffected or affected at too low an energy to matter.

There is a possibility that the anomalous component is singly ionized. If this is so, it will have an extraordinary ability to penetrate the Earth's magnetosphere. In this case, the differential energy spectra shown below are assumed for the helium, carbon, nitrogen, oxygen, neon, magnesium, silicon, argon, and iron spectra of the anomalous component. There probably are anomalous components in the spectra of the nuclei heavier than iron, but there are no data on them at this time.

TABLE 6.2.1–1 GALACTIC COSMIC RAYS (GCRs)* (PAGE 12 OF 13)

For singly–ionized helium,

$$F = \begin{cases} 0.4, & E < 195 \\ 1.54X10^{4}\ E^{-2}. & E \geq 195 \end{cases} \qquad \text{(T6.2.1–1,19)}$$

For singly–ionized carbon,

$$F = \begin{cases} 4.00X10^{3}\ \exp[-(1n(E) - 1.79)^{2}\ /0.7], & E < 10 \\ 0.27\ E^{-2}. & E \geq 10 \end{cases} \qquad \text{(T6.2.1–1,20)}$$

For singly–ionized nitrogen,

$$F = \begin{cases} 1.54X10^{-2}\ \exp[-(1n(E) - 1.79)^{2}\ /0.7], & E < 20 \\ 0.773\ E^{-2}. & E \geq 20 \end{cases} \qquad \text{(T6.2.1–1,21)}$$

For singly–ionized oxygen,

$$F = \begin{cases} 6.00X10^{-2}\ \exp[-(1n(E) - 1.79)^{2}\ /0.7], & E < 30 \\ 1.32\ E^{-2}. & E \geq 30 \end{cases} \qquad \text{(T6.2.1–1,22)}$$

For singly–ionized neon,

$$F = \begin{cases} 8.00X10^{-3}\ \exp[-(1n(E) - 1.79)^{2}\ /0.7], & E < 20 \\ 0.40\ E^{-2}. & E \geq 20 \end{cases} \qquad \text{(T6.2.1–1,23)}$$

For singly–ionized magnesium,

$$F = \begin{cases} 8.00X10^{-4}\ \exp[-(1n(E) - 2.30)^{2}\ /0.7], & E < 20 \\ 0.16\ E^{-2}. & E \geq 20 \end{cases} \qquad \text{(T6.2.1–1,24)}$$

For singly–ionized silicon,

$$F = \begin{cases} 1.00X10^{-3}\ \exp[-(1n(E) - 2.20)^{2}\ /0.4], & E < 10 \\ 0.10\ E^{-2}. & E \geq 10 \end{cases} \qquad \text{(T6.2.1–1,25)}$$

For singly–ionized argon,

$$F = \begin{cases} 5.40X10^{-4}\ \exp[-(1n(E) - 1.79)^{2}\ /0.7], & E < 20 \\ 0.28\ E^{-2}. & E \geq 20 \end{cases} \qquad \text{(T6.2.1–1,26)}$$

TABLE 6.2.1–1 GALACTIC COSMIC RAYS (GCRs)* (PAGE 13 OF 13)

For singly–ionized iron,

$$F = \begin{cases} 6.00X10^{-4} \ \exp[-(1n(E) - 2.48)^2 \ /2.0], & E < 30 \\ 0.35 \ E^{-2}. & E \geq 30 \end{cases} \qquad \text{(T6.2.1–1,27)}$$

Since these anomalous component particles are assumed to be singly–ionized, they will have a higher magnetic rigidity than galactic cosmic rays of the same energy. The magnetic rigidity of galactic cosmic rays is

$$R = (A/Z) \ (E^2 + 1862.324 \ E)^{1/2} \ /1000, \qquad \text{(T6.2.1–1,28)}$$

in GeV/ec. The rigidity of singly ionized nuclei is

$$R = A \ (E^2 + 1862.324 \ E)^{1/2} \ /1000. \qquad \text{(T6.2.1–1,29)}$$

To add the singly–ionized anomalous component, it is necessary to modulate both the galactic cosmic ray spectra and the anomalous component spectra given above using the geomagnetic cutoff transmission function. After calculating this function (discussed in Adams et. al., 1983, 1986), the resulting modulated spectra are then added together.

TABLE 6.2.2–1 SOLAR PARTICLE EVENTS* (PAGE 1 OF 5)

Solar flare particle events are sporadic occurrences lasting one to five days. When these events occur, they can be the dominant cause of soft errors. For statistical treatment, they are broken into two classes: Ordinary (OR) and Anomalously Large (AL). The probability of having more than a number of events, n, in a time, t, is given by:

$$P(n,t,N,T) = 1 - \sum_{i=0}^{n} (i + N)!(t/T)^i/[i!\ N!\ (1 + t/T)^{1+i+N}] \qquad \text{(T6.2.2–1,1)}$$

where T and t are in years, and N is the number of flares that have occurred in T years.

For ordinary events, equation (T6.2.2–1,1) becomes:

P_{OR} = P(n,t,24,7) for the decreasing portion of the solar cycle

and (T6.2.2–1,2)

P_{OR} = P(n,t,6,8) for the increasing portion of the solar cycle,

where there is a probability, P_{OR} of having more than n ordinary events in t years. Similarly for anomalously large events:

$$P_{AL} = P(n,t,1,7) \qquad \text{(T6.2.2–1,3)}$$

The peak proton flux differential energy spectrum for ordinary events is, typically:

$$f_{OR} = 2.45E4(e^{-E/27.5} + 173\ e^{-E/4}) \quad \text{protons}/(m^2 \cdot sr \cdot s \cdot MeV) \qquad \text{(T6.2.2–1,4)}$$

where E is in MeV, and no worse than:

$$f_{WOR} = 2.06E5(e^{-E/24.5} + 63.6\ e^{-E/4}) \ \text{protons}/(m^2 \cdot sr \cdot s \cdot MeV) \qquad \text{(T6.2.2–1,5)}$$

with a confidence of approximately 90 percent.

*(Table 6.2.2–1 is from Adams et al., 1981 and 1986.)

TABLE 6.2.2–1 SOLAR PARTICLE EVENTS* (PAGE 2 OF 5)

Using the August 1972 flare as a model AL event, the peak proton flux differential energy spectrum is:

$$f_{AL} = \begin{cases} 9.3E9\ (dP/dE)\ \exp(-P/0.10) & E < 150\ MeV \\ 1.76E5\ (dP/dE)\ p^{-9} & E \geq 150\ MeV \end{cases} \qquad \text{(T6.2.2–1,6)}$$

in protons/($m^2 \cdot sr \cdot s \cdot MeV$), where

$$P = [(E/1000)^2 + 1.86E{-}3E]^{1/2} \qquad \text{(T6.2.2–1,7)}$$

and E is in MeV.

To model the worst flare that is ever likely to occur, use the composite of the August 1972 flare and the February 1956 flare. The composite worst–case flare proton spectrum is taken to be the peak of the 1972 spectrum, as given by Eq. (T6.2.2–1,6), and the 1956 peak spectrum, given below.

$$f_{1956} = 1.116E + 8\ (E^{-1.248})(0.248 + 2.5E + 5\ x1.7xEPOW)\ EXPOW + 4.7E + 19\ (E^{-5.3})(4.3x(1–EXPOW) – 6.32E–15\ x4.7xEPOWxEXPOW), \qquad \text{(T6.2.2–1,8)}$$

where

$$EPOW = E^{1.7}$$

and

$$EXPOW = \exp(-2.5E{-}5\ EPOW).$$

The composition of flare particles is also highly variable from flare to flare. Table 6.2.2–1.1 gives the composition relative to hydrogen for the elements through nickel. Both mean and (90 percent confidence level) worst cases are given. To obtain the spectrum of any element in a flare, just multiply the abundance ratio from the Table 6.2.2–1.1 by the appropriate flare proton spectrum.

TABLE 6.2.2–1 SOLAR PARTICLE EVENTS* (PAGE 3 OF 5)

TABLE 6.2.2–1.1 MEAN AND WORST CASE FLARE COMPOSITIONS

	MEAN CASE	WORST CASE
H	1	1
He	1.0E–2	3.3E–2
Li	0	0
Be	0	0
B	0	0
C	1.6E–4	4.0E–4
N	3.8E–5	1.1E–4
O	3.2E–4	1.0E–3
F	0	0
Ne	5.1E–5	1.9E–4
Na	3.2E–6	1.3E–5
Mg	6.4E–5	2.5E–4
Al	3.5E–6	1.4E–5
Si	5.8E–5	1.9E–4
P	2.3E–7	1.1E–6
S	8.0E–6	5.0E–5
Cl	1.7E–7	8.0E–7
Ar	3.3E–6	1.8E–5
K	1.3E–7	6.0E–7
Ca	3.2E–6	2.0E–5
Sc	0	0
Ti	1.0E–7	5.0E–7
V	0	0
Cr	5.7E–7	4.0E–6
Mn	4.2E–7	2.3E–6
Fe	4.1E–5	4.0E–4
Co	1.0E–7	5.5E–7
Ni	2.2E–6	2.0E–5

TABLE 6.2.2–1 SOLAR PARTICLE EVENTS* (PAGE 4 OF 5)

The mean case compositions for the elements from copper to uranium are taken from Cameron, 1980. The ratios of these abundances to hydrogen are given in Table 6.2.2–1.2.

TABLE 6.2.2–1.2 MEAN FLARE COMPOSITIONS

Cu	2.0E–8	Pm	0
Zn	6.0E–8	Sm	1.0E–11
Ga	2.0E–9	Eu	4.0E–12
Ge	5.0E–9	Gd	2.0E–11
As	3.0E–10	Tb	3.0E–12
Se	3.0E–9	Dy	2.0E–11
Br	4.0E–10	Ho	4.0E–12
Kr	2.0E–9	Er	1.0E–11
Rb	3.0E–10	Tm	2.0E–12
Sr	1.0E–9	Yb	9.0E–12
Y	2.0E–10	Lu	2.0E–12
Zr	5.0E–10	Hf	8.0E–12
Nb	4.0E–11	Ta	9.0E–13
Mo	2.0E–10	W	1.0E–11
Tc	0	Re	2.0E–12
Ru	9.0E–11	Cs	3.0E–11
Rh	2.0E–11	Ir	3.0E–11
Pd	6.0E–11	Pt	6.0E–11
Ag	2.0E–11	Au	1.0E–11
Cd	7.0E–11	Hg	1.0E–11
In	9.0E–12	Tl	9.0E–12
Sn	2.0E–10	Pb	1.0E–10
Sb	1.4E–11	Bi	6.0E–12
Te	3.0E–10	Po	0
I	6.0E–11	At	0
Xe	2.7E–10	Rn	0
Cs	2.0E–11	Fr	0
Ba	2.0E–10	Ra	0
La	2.0E–11	Ac	0
Ce	5.0E–11	Th	2.0E–12
Pr	8.0E–12	Pa	0
Nd	4.0E–11	U	1.2E–12

TABLE 6.2.2–1 SOLAR PARTICLE EVENTS* (PAGE 5 OF 5)

The worst–case compositions of the elements from copper to uranium are obtained by multiplying the abundance ratios of Table 6.2.2–1.2 by:

$$(C_W\ (O)/C_t\ (O))0.48\ \exp(Z^{0.78}\ /6.89), \qquad \text{(T6.2.2–1,9)}$$

where C_W (O) and C_t (O) are the worst–case and mean abundance coefficients for oxygen in Table 6.2.2–1.1.

TABLE 6.2.3–1 GEOMAGNETIC CUTOFFS*

The modulation of cosmic ray spectra by the Earth's magnetic field requires a more thorough treatment than can be offered here, but some guidance will be provided. The geomagnetic cutoff is a value of magnetic rigidity below which cosmic rays will not reach a specified point in the magnetosphere from a specified direction. The magnetic rigidity, P, in GeV/ec may be computed from the particles' energy using:

$$P = \frac{A[(E/1000)^2 + 1.86\ E{-}3\ E]^{1/2}}{Z} \qquad \text{(T6.2.3–1,1)}$$

where A and Z are the atomic mass and charge of the nucleus in question.

The cutoff at any point for particles arriving from the zenith is most simply computed with:

$$P_c = 15.96/L^{2.005}\ \ \text{GeV/ec} \qquad \text{(T6.2.3–1,2)}$$

where L is McIlwain's L parameter (i.e., the radial distance, in Earth radii, from the center of the Earth to the point in the geometric equatorial plane where it is crossed by the magnetic field line that also passes through the point of observation).

Design consideration must be given to solar flare spectra, because (1) the flare particle intensity changes on a time scale comparable to or shorter than an orbital period, (2) there is no certain proof that solar flare particles are fully ionized, and (3) the geomagnetic cutoff is suppressed to some extent during a flare. The geomagnetic cutoff during a flare, P_F, should be computed from the "quiet time" cutoff, P_0, using:

$$\delta\ P/P_0 = 0.54\ \exp(-P_0/2.9) \qquad \text{(T6.2.3–1,3)}$$

and

$$P_F = P_0 - \delta\ P \qquad \text{(T6.2.3–1,4)}$$

where P_F, P_0, and δP are in GeV/ec.

*(Adams, 1986)

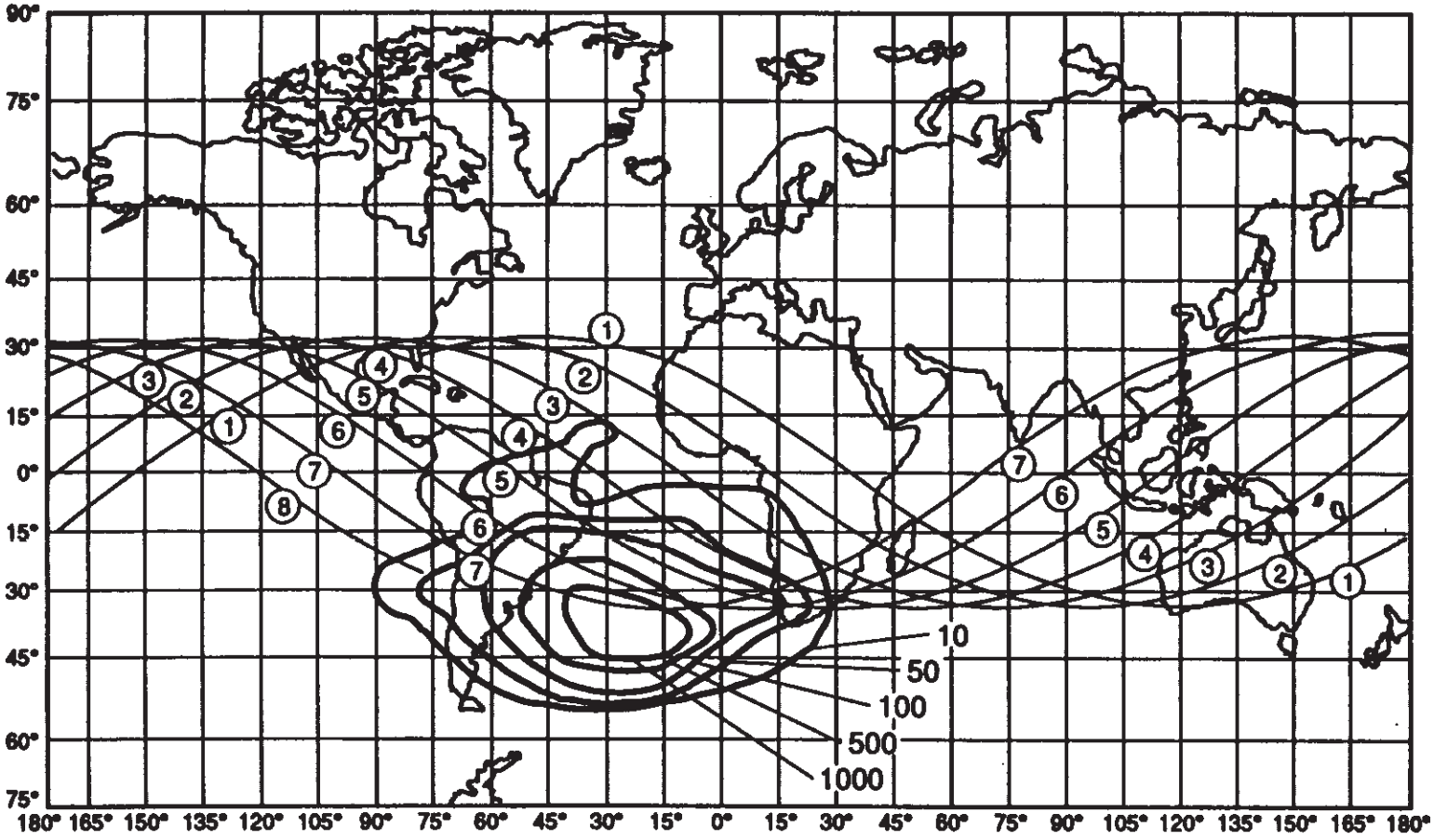

OMNIDIRECTIONAL FLUX (PROTONS/CM^2 SEC) ENERGY > 30 MeV

FIGURE 6.1.1–1 PROTON FLUX DENSITIES AT AN ALTITUDE OF 296 KILOMETERS IN THE SOUTH ATLANTIC ANOMALY. THIS IS A REGION OF LOW MAGNETIC FIELD

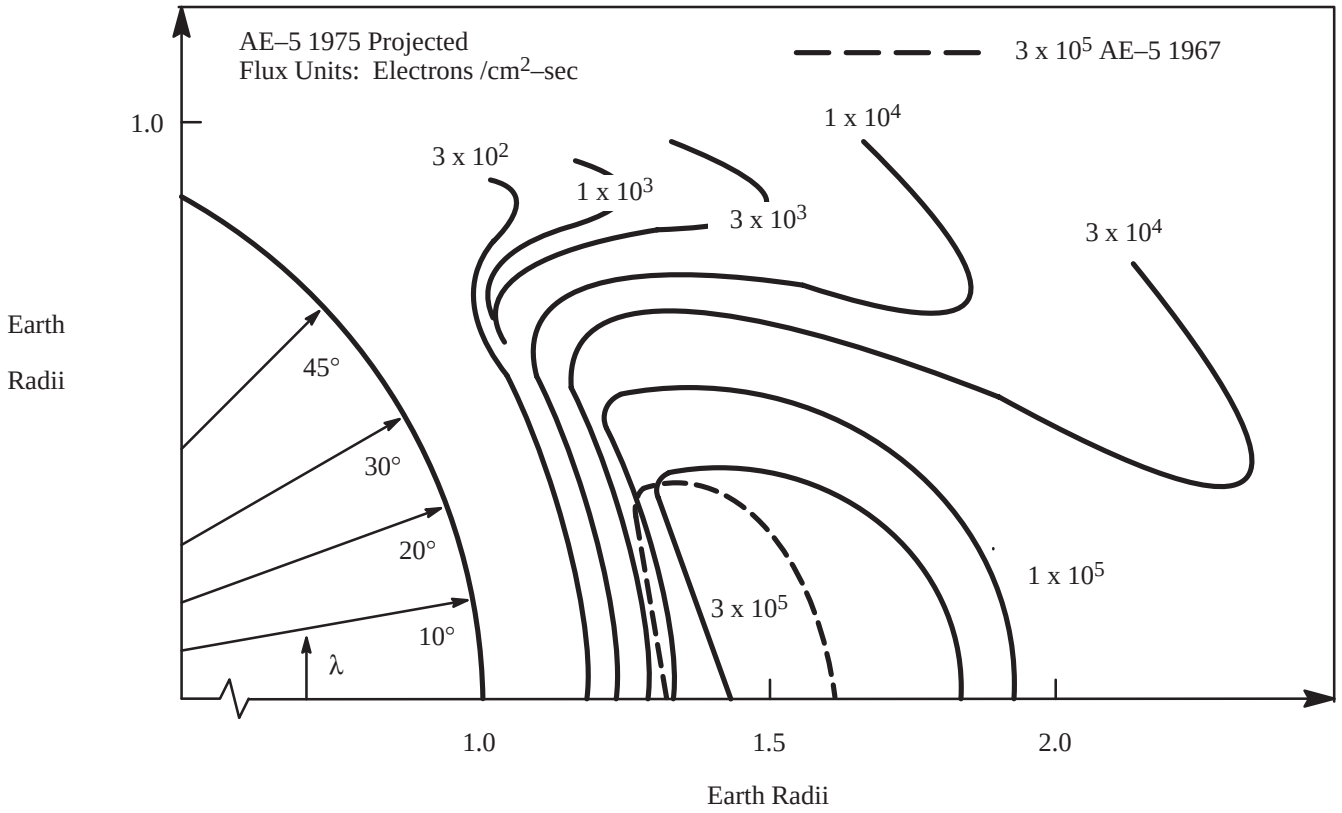

FIGURE 6.1.1–2 OMNIDIRECTIONAL ISO–FLUX CONTOURS OF 1–MeV ELECTRONS: R–λ PROJECTION

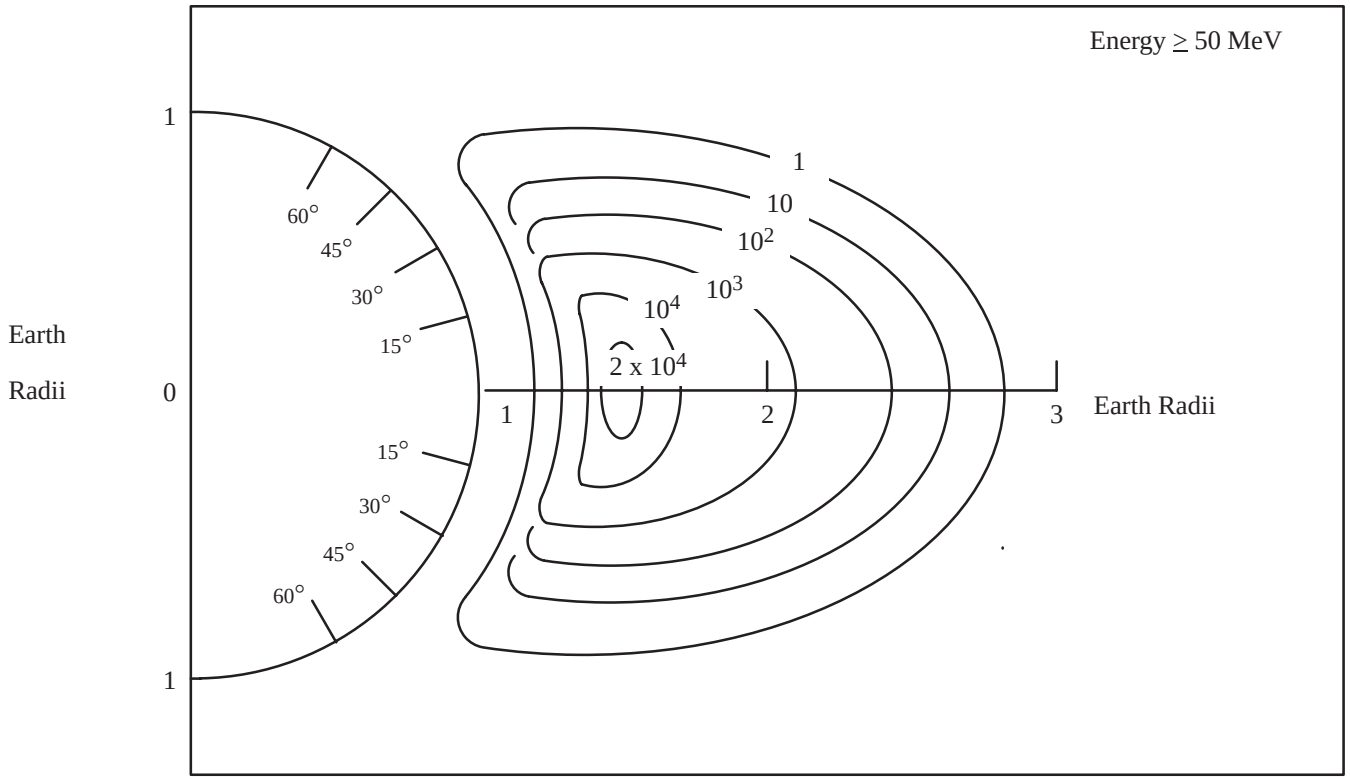

FIGURE 6.1.1–3 AP8MIN R–λ PLOT OF ISO–FLUX CONTOURS OF PROTONS WITH AN ENERGY OF ≥50 MeV

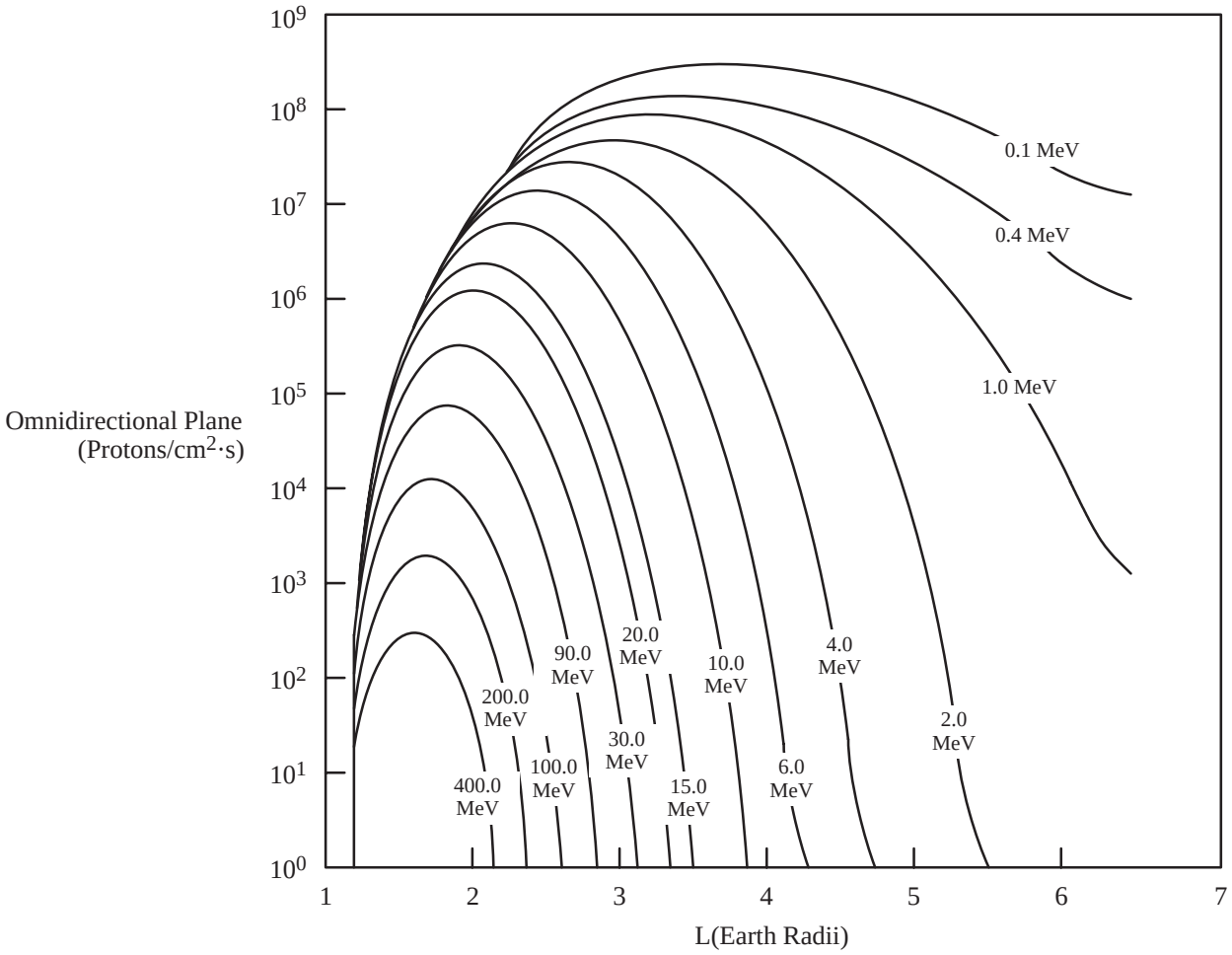

FIGURE 6.1.1–4 AP8MIN EQUATORIAL OMNIDIRECTIONAL RADIAL PROFILES OF PROTON FLUX AT ENERGIES BETWEEN 0.1 AND 400 MeV

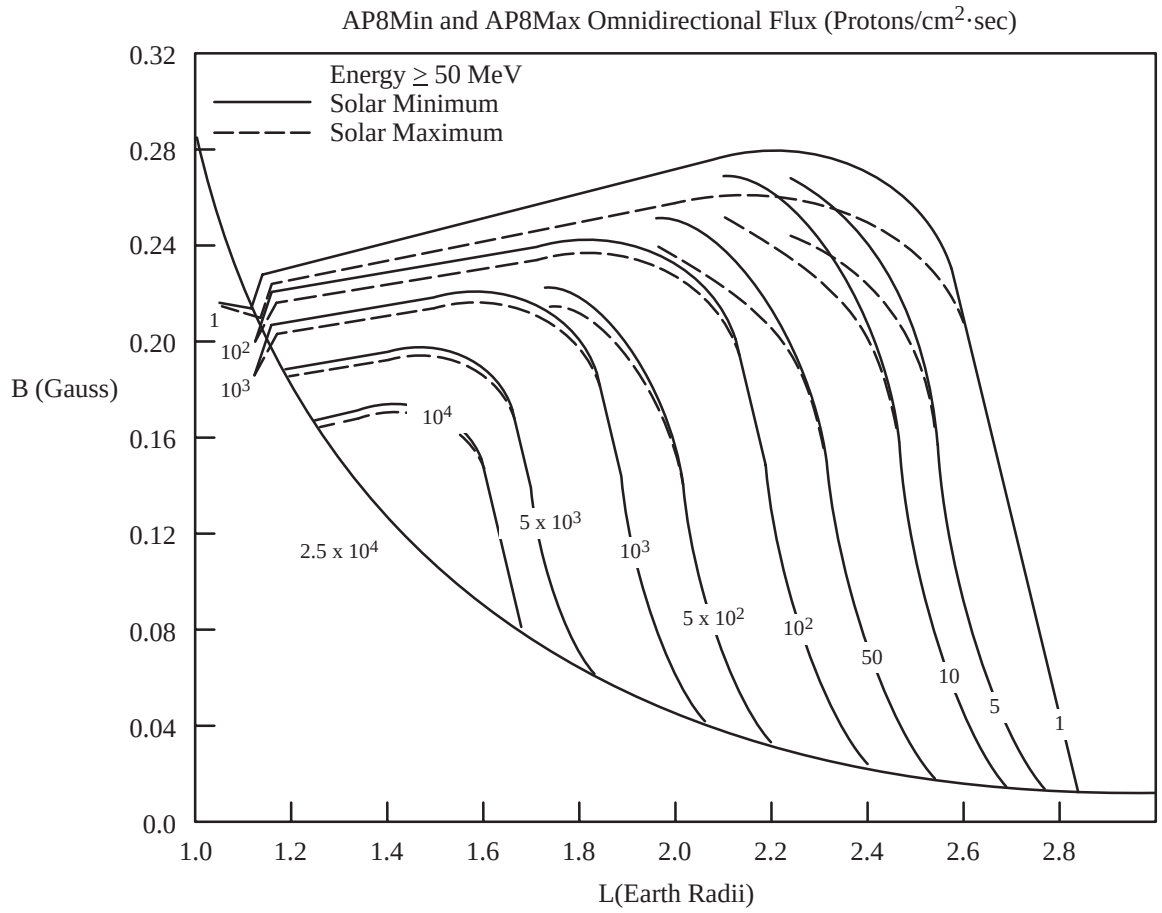

FIGURE 6.1.1–5 AP8MIN AND AP8MAX B–L PLOT OF CONSTANT INTENSITY FLUX CONTOURS OF PROTONS WITH AN ENERGY OF ≥50 MeV

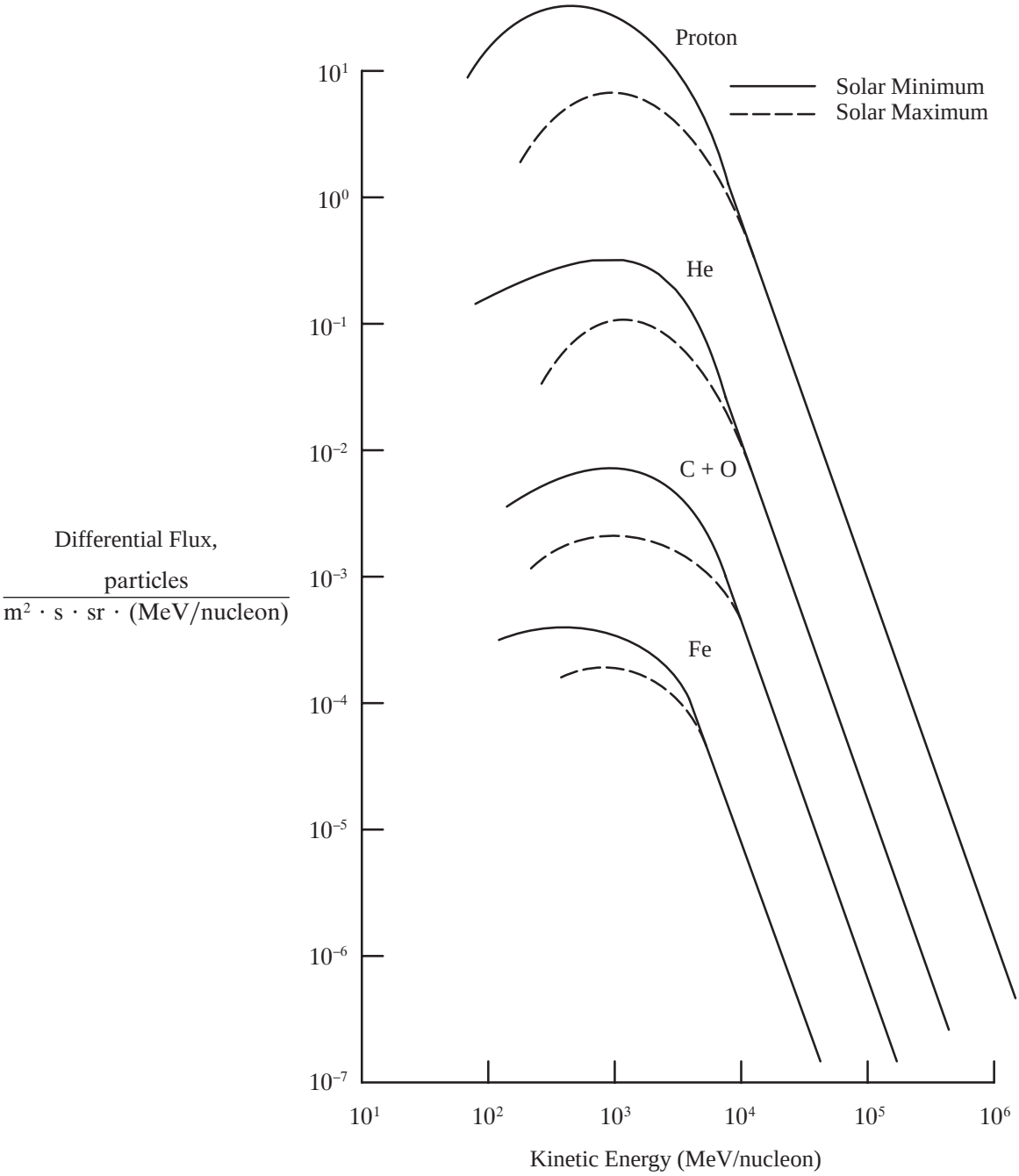

FIGURE 6.2.1–1 CHARACTERISTICS OF GALACTIC COSMIC RAYS (GCRs)

Differential energy spectra for GCRs outside the magnetosphere at maximum and minimum solar activity (as defined by sunspot number)

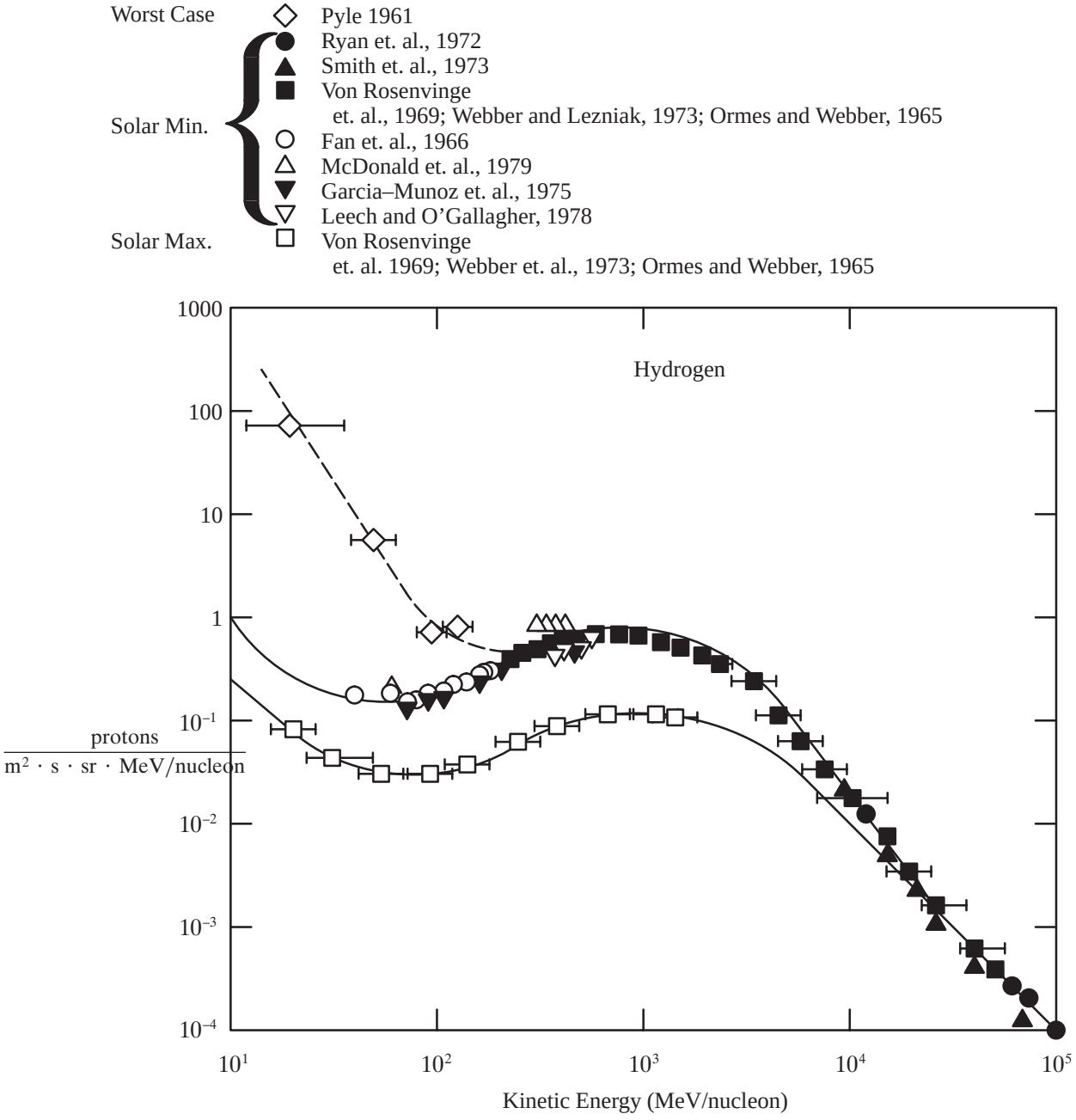

FIGURE 6.2.1–2A THE DIFFERENTIAL ENERGY SPECTRUM OF HYDROGEN (MOSTLY PROTONS)

The data are selected to show the solar maximum and solar minimum fluxes. The dashed curve is a worst case spectrum.

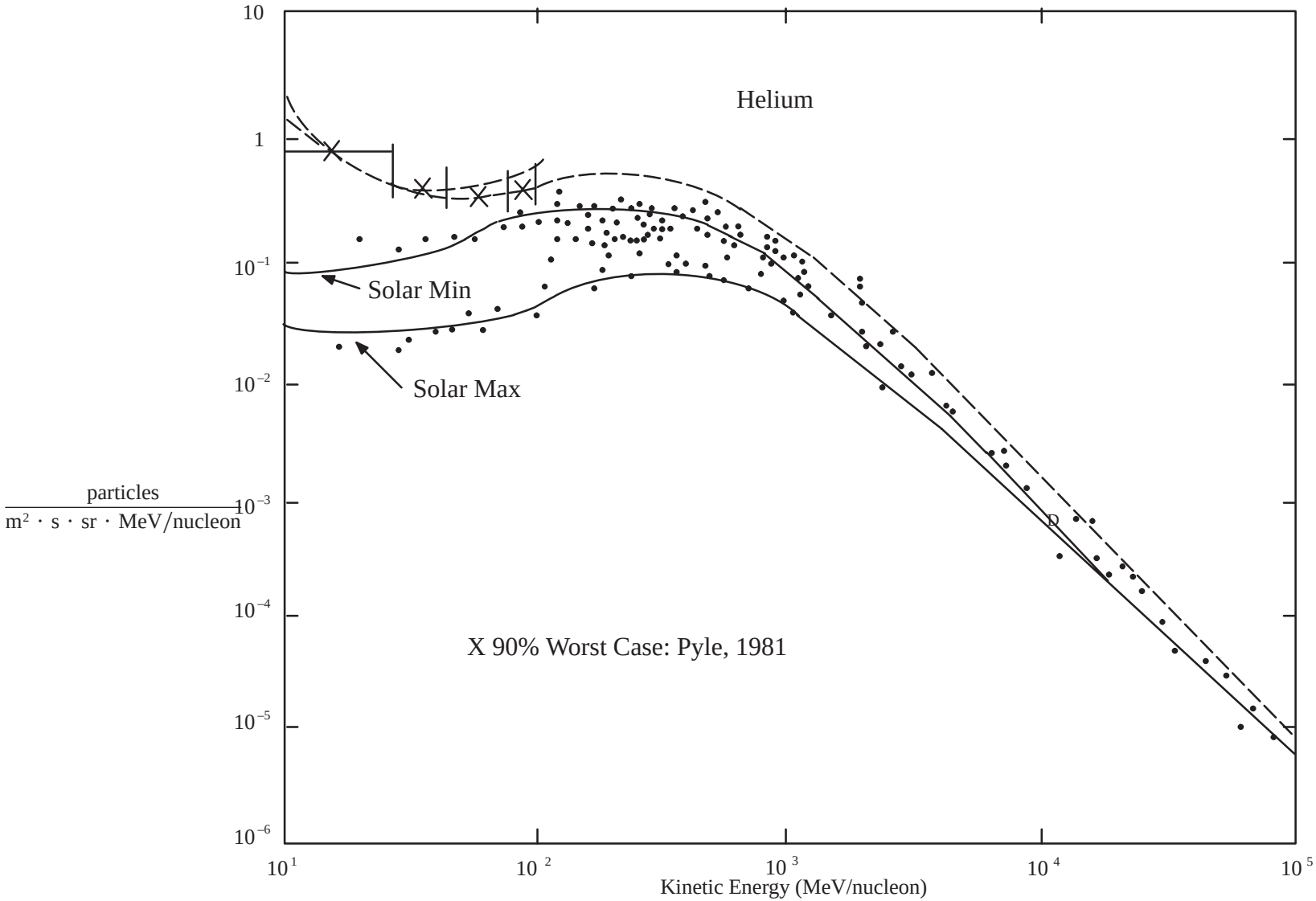

FIGURE 6.2.1–2B THE DIFFERENTIAL ENERGY SPECTRUM OF HELIUM (MOSTLY ALPHAS)

The data are selected to show the solar maximum and solar minimum fluxes. The dashed curve is a worst case spectrum.

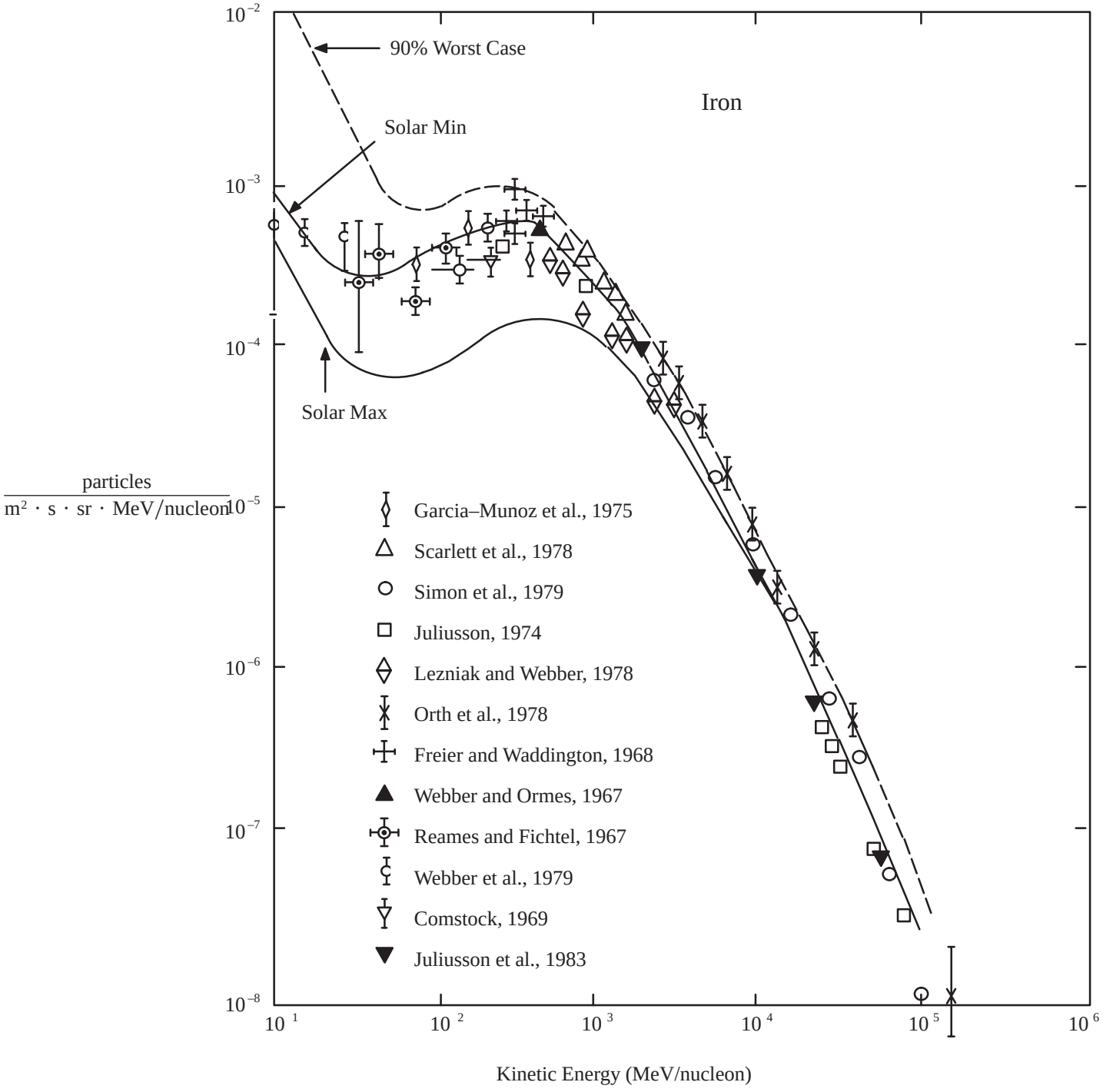

FIGURE 6.2.1–2C THE DIFFERENTIAL ENERGY SPECTRUM OF IRON

The data are selected to show the solar maximum and solar minimum fluxes. The dashed curve is a worst case spectrum.

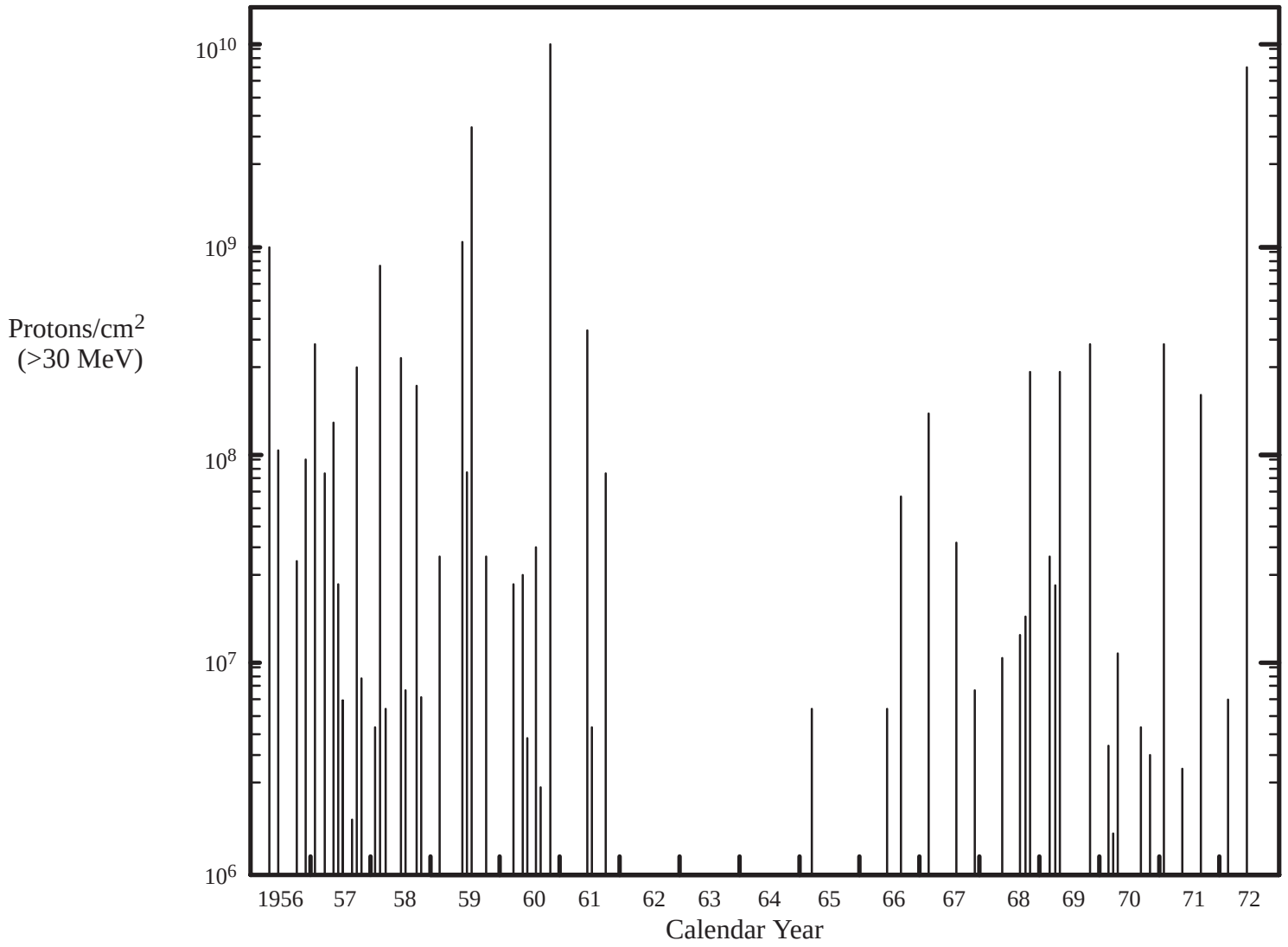

FIGURE 6.2.2–1 EVENT–INTEGRATED PROTON FLUXES ABOVE 30 MeV FOR THE MAJOR SOLAR EVENTS OF THE 19TH AND 20TH SOLAR CYCLES

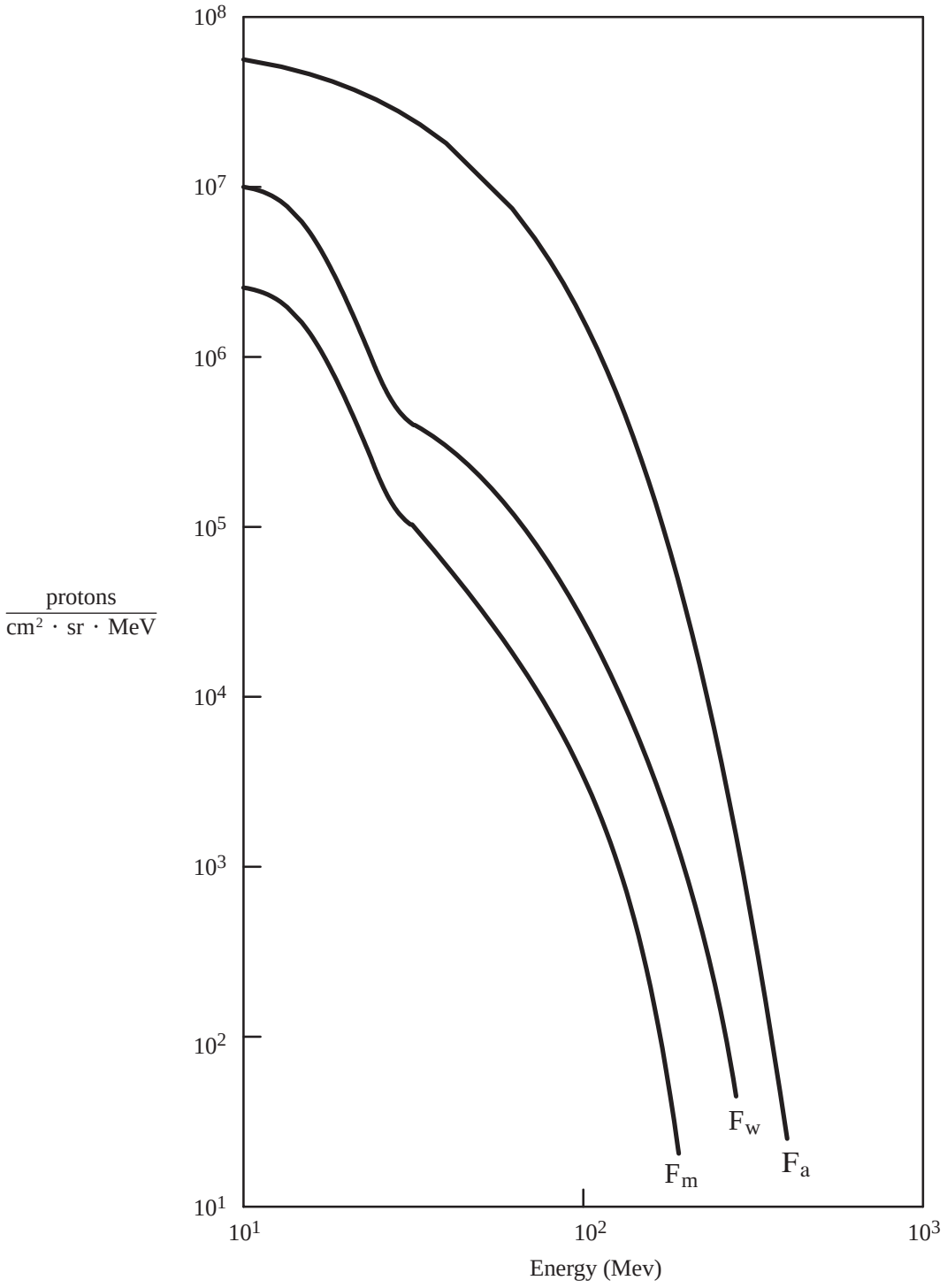

FIGURE 6.2.2–2 THE EVENT–INTEGRATED PROTON DIFFERENTIAL ENERGY SPECTRA

For F_m, a typical ordinary event; F_w, a worst–case ordinary event (90 percent confidence level); and F_a, an anomalously large solar event.

7.0 ELECTROMAGNETIC RADIATION

Important sources of electromagnetic noise exist over the entire frequency spectrum from direct current (dc) to X–ray at the altitudes planned for the Space Station Program Elements (SSPEs). These noise sources broadly separate into four categories: galactic, solar, near–Earth natural plasma, and man–made radio noise. The highest power density occurs at the visible and infrared (IR) frequencies and amounts to the solar constant of 1371 ± 5 W/m^2. This section discusses the nature of these noise sources and the manner in which the natural ionospheric environment may affect the propagation of these signals to the SSPEs. Only natural and remote man–made electromagnetic radiation (EMR) are considered.

The orbits of the SSPEs will be above the peak ionospheric electron density of n_e = 1.0E4 to 1.0E6 per cubic centimeter at 200 to 300 kilometers altitude. (See section 5.0 of this document.) These densities correspond to a peak in the natural electron plasma frequency (Langmuir oscillations) of about 0.8 to 8 MHz. EMR below this frequency cannot propagate through the peak electron density region without strong attenuation. Thus, sub–ionospheric and ground–based sources below this frequency will generally not reach the SSPEs except for ducted propagation for some plasma waves. Note, however, that the density and position of this peak electron density vary significantly with solar activity and the time of day.

High levels of power in the radio frequency (RF) spectral region are primarily a result of Earth–based and onboard radiation sources that are man–made. The major ground–based transmitters resulting in high power levels in the ionosphere are in the 100 MHz to 5 GHz range used by radars. They generally have very narrow spatial distributions.

7.1 GALACTIC RADIO NOISE

Galactic noise reaching the altitude of the SSPEs extends from frequencies of 15 Megahertz (MHz) to 100 Gigahertz (GHz). The source is broadly directional toward and perpendicular to the galactic plane and varies by about 10 dBW/Hz. Figure 7.1–1 is a spectrum of the galactic noise as a function of frequency. SSPE radio engineers will find that this galactic noise is a dominant factor for a typical radio receiver operating between 40 and 250 MHz. See Figure 7.1–2. For comparison between cosmic noise levels and natural near–Earth noise, see paragraph 7.3 below.

7.2 SOLAR ELECTROMAGNETIC RADIATION

Solar electromagnetic energy flux near the Earth but outside the Earth's atmosphere (at one Astronomical Unit) is about 1371 ± 5 W/m^2. The irradiance spectrum approximates a black body curve, T = 5762°K, which peaks in the visible frequency range; see Figure 7.2–1. The integrated irradiance of the near ultraviolet portion of the

electromagnetic flux (0.18 μm < λ < 0.4 μm) is approximately 118 W/m^2, i.e. about 8.6% of the solar constant. The far ultraviolet portion (λ < 0.18 μm) contributes about 0.023 W/m^2. Irradiance levels for the extreme high energy spectrum are summarized in Table 7.2–1.

The ultraviolet portion (λ < 0.3 μm) of the electromagnetic spectrum is of particular importance in determining the effects of solar radiation on material properties. For "terrestrial space" the ultraviolet radiation is independent of orbit geometry; however, the spacecraft surface geometry, orientation, and orbit geometry will affect the exposure level over a given orbital lifetime. Recent measurements have greatly improved the data base for this portion of the spectrum. These results, derived from the review in World Meteorological Org., 1985, have been incorporated into this specification, see Table 7.2–2. They provide data that give a good indication of the irradiance variability over the 27 day solar rotation period and somewhat longer time scales; however, the time span covered by good quality data is still too short to provide high confidence in estimates of irradiance variations over the 11 year solar cycle.

The Lyman alpha (Ly–α) emission line at 0.1216 mm is the primary emission line below 0.1300 μm and its integrated irradiance varies by roughly a factor of 2 over the 11 year solar cycle with an uncertainty of ±15%. For estimates of the Ly–α flux at any level of solar activity, the following relationship is the best available:

$$q\ (Ly–\alpha) = 2.25E11 + 0.014E11\ (F_{10.7} - 65) \qquad (7.2,1)$$

where q is expressed in photons $\cdot\ cm^{-2} \cdot s^{-1}$.

The variation in the integrated 0.130–0.175 μm wavelength flux over the solar cycle is a factor of two with error bars on the recent measurements of ±20%. The percent change of the short term variation is less than that at Lyman–alpha and most values lie between 7.6E11 and 8.7E11 photons $\cdot\ cm^{-2} \cdot s^{-1}$ for solar activity levels prevailing in 1982–1984.

It is now generally accepted that the spectral region 0.175 – 0.210 μm varies with the 27 day solar rotation and the 11 year solar cycle. In this spectral region the root mean square deviations from the Reference Solar Irradiance Spectrum in Table 7.2–3 are less than 10% in most cases although the quoted uncertainty in any single measurement is typically ±15–20%.

Typical uncertainty limits for the measurements in the 0.210– 0.3275 μm spectral region are ±15–20%; however, once again root mean square deviations from the Reference Solar Irradiance Spectrum are less than 10%.

Between 0.175 and 0.210 μm, the maximum irradiance tends to be 1.05 to 1.07 times the minimum value with a peak ratio approaching 1.10. Between 0.210 and 0.250 μm, the maximum to minimum irradiance ratio is typically 1.03 and, beyond 0.260 μm, drops to 1.01 or less. Table 7.2–2 presents estimates of the solar cycle variability in selected wavelength bins spanning the region 0.175 to 0.300 μm. The quantity, R_{sc} is a measure

of the ratio of solar maximum irradiance to solar minimum irradiance. R_{27} is an estimate of the 27 day irradiance variation. The ratio of the maximum to minimum irradiance during a solar cycle is the product of R_{27} and R_{sc}. The maximum and minimum irradiances over a solar cycle are related to the mean reference cycle of Table 7.2–3 by:

$$F_{max}(i) = F_{ref}(i) \frac{2\ R_{27}(i)\ R_{sc}(i)}{1 + R_{27}(i)\ R_{sc}(i)} \qquad (7.2,2)$$

and

$$F_{min}(i) = F_{ref}(i) \frac{2}{1 + R_{27}(i)\ R_{sc}(i)} \qquad (7.2,3)$$

where

R_{27} and R_{sc} are obtained from Table 7.2–2.

7.3 NATURAL ENVIRONMENTAL ELECTROMAGNETIC RADIATION

The magnetosphere–ionosphere system is filled with natural plasma emission sources which vary greatly from poles to the equator. The frequencies of these emissions generally extend down from the peak electron plasma frequencies (1 to 10 MHz) to direct current. The electron plasma frequency is found simply from the electron density as:

$$fp = \left| \frac{n_e\ e^2}{m_e \pi} \right|^{\frac{1}{2}} (cgs) = 0.90\ MHz \left| \frac{n_e}{10^4/cm^3} \right|^{\frac{1}{2}} \qquad (7.3,1)$$

where

n_e is the electron density per cm^3,

e^2 is square of the electronic charge 94.8E–10, and

m_e is the electron mass in grams (0.911E–27).

Note that this is independent of temperature. A wide variety of natural electromagnetic emissions are related to electron cyclotron waves from wave particle phenomena in the Earth's dipole magnetic field. These emissions are generally in the frequency range of 0.5 kHz to 30 kHz and include very low frequency whistler–mode noise such as hiss and chorus. They are highly position dependent since, although they are electromagnetic waves, they have a plasma component which affects the wave propagation vector. At typical LEO velocities in the 5 to 10 kilometer per second range, one can expect natural plasma structures of small scale size (i.e., 0.01 to 10 kilometers) to introduce an effective noise source at SSPE receivers. This noise source is due to natural phenomena such as auroral arcs and ionospheric irregularities. Figure 7.3–1 presents an overview of the natural plasma noise levels from near–Earth, solar, and cosmic sources. The figure shows power flux levels for various frequency ranges of naturally–occurring

electromagnetic and plasma waves in the Earth's environment and in astrophysical sources as observed at the Earth.

As mentioned above, noise sources below about 1 MHz are likely to be negligible at the Space Station if they have sources below 200 kilometers. However, it is possible for certain impulsive radiation bursts such as lightning generated sferics to penetrate the ionosphere. In particular, recent indications are that direct lightning generated waveforms with frequencies above about 1 Hz can result in transient electric fields up to about 50 mV/m in the ionosphere. In general, all EMR field strengths are smaller at higher frequencies. The largest field strengths are for quasi–static field structures which occasionally reach 0.1 to 0.5 V/m but usually range between 10 to 50 mV/m. Such large quasi–static fields are generally found poleward of 50 degrees latitude in association with the aurora.

These direct current fields should be compared to the apparent direct current electric field due to the Lorentz transformation of the motion of the vehicle across magnetic field lines. This field, on the order of a few hundred mV/m, can create significant potential drops across large objects.

7.4 MAN–MADE NOISE

Although man–made noise sources below the peak plasma frequency of about 1 TO 10 MHz are not likely be a problem at orbital altitudes above the ionospheric peak because they cannot propagate through the lower ionosphere without significant attenuation, it is likely that many narrow–band sources from 1 MHz to 300 GHz will be detectable and perhaps important noise sources for an orbiting space vehicle.

The electric field E (mV/m) at a distance z (kilometers) from any RF transmitter can be estimated with the formula:

$$E = (30\ ERP)^{1/2}\ /z, \qquad (7.4,1)$$

where ERP (watts) is the effective radiated power which equals the product of the transmitter power and the antenna gain.

Thus, a radar with a power of 10 kW and an antenna gain of 40 dB (10,000) will result in fields of over 100 mV/m at 500 km altitude. Presumably a source such as a radar will have a very narrow beam width (perhaps less than a degree) but will be swept over wide loci of look directions. Occasionally ionosphere research transmitters are also operated which produce measurable heating of the ionospheric plasma and have power levels in the same range as the defense radars but wider beam patterns. In June 1983, the U.S. Air Force Space Division requested the Department of Defense Electromagnetic Compatibility Analysis Center (ECAC) to identify the worldwide radio frequency electromagnetic environment (EME) for hypothetical spacecraft in various low Earth orbits. The results of this task are documented in the ‘‘Worldwide Spacecraft EME Definition”, report number ECAC–CR–85–065, USAF Space Division. (Baummer and Gross, 1988, Klaips et. al. 1985).

TABLE 7.2–1 SOLAR ELECTROMAGNETIC RADIATION

Type	Wavelength (nm)	Level (W/m^2)
UV	100–150	7.5E–3
EUV	10–100	2E–3
X–RAYS	1–10	5E–5
FLARE X–RAYS	0.1–1	1E–4
COSMIC RAYS*		1E–3
SOLAR WIND*		1E–4

*Not electromagnetic but included for comparison.

(Anon., 1981b)

TABLE 7.2–2 PARAMETERS FOR ESTIMATING IRRADIANCE VARIABILITY OVER THE 11 YEAR SOLAR CYCLE.*

Wavelength Range (nm)	R_{sc} (max/min)	R_{27}
175 – 190	1.020 (±0.020)	1.07
190 – 210	1.030 (±0.020)	1.06
210 – 240	1.026 (±0.020)	1.03
240 – 300	1.005 (±0.020)	1.01

R_{SC} is the ratio of a 27 day mean irradiance near solar maximum to a 27 day mean at solar minimum.

R_{27} is the ratio of the maximum irradiance observed during a typical 27 day solar rotation to the minimum irradiance during this rotation.

*(World Meteorological Org., 1985)

TABLE 7.2–3 REFERENCE SOLAR IRRADIANCE, RAYLEIGH SCATTERING, OXYGEN, OZONE CROSS SECTIONS, AND ENERGY FLUX* (PAGE 1 OF 14)

WAVELENGTH RANGE** (nm)	SOLAR IRRADIANCE (phot/cm^2 –s)	RAYLEIGH SCATTER σ_{RS} (cm^2)	OXYGEN HERZBERG σ_{HZ} (O_2) (cm^2)	OZONE*** $\sigma(O_3)$ (cm^2)	ENERGY FLUX (W/m^2)
1 175.439–176.991	1.74E+11	6.79E–25	4.61E–24	8.11E–19	1.96E–3
2 176.991–178.571	2.10E+11	6.49E–25	5.03E–24	7.99E–19	2.34E–3
3 178.571–180.180	2.38E+11	6.20E–25	5.46E–24	7.86E–19	2.64E–3
4 180.180–181.818	3.04E+11	5.93E–25	5.88E–24	7.63E–19	3.35E–3
5 181.818–183.486	3.19E+11	5.66E–25	6.29E–24	7.29E–19	3.47E–3
6 183.486–185.185	2.93E+11	5.41E–25	6.68E–24	6.88E–19	3.16E–3
7 185.185–186.916	3.62E+11	5.16E–25	7.04E–24	6.40E–19	3.87E–3
8 186.916–188.679	4.73E+11	4.93E–25	7.36E–24	5.88E–19	5.00E–3
9 188.679–190.476	5.61E+11	4.70E–25	7.64E–24	5.31E–19	5.88E–3
10 190.476–192.308	6.63E+11	4.49E–25	7.87E–24	4.80E–19	6.88E–3
11 192.308–194.175	6.90E+11	4.28E–25	8.04E–24	4.38E–19	7.09E–3

*(World Meteorological Org., 1985)

**Wavelength range for spectral intervals 1–49 correspond to 500 wavenumbers. Wavelength range for remainder of spectral intervals is 5 nm.

***T=203 K and T=273 K

TABLE 7.2–3 REFERENCE SOLAR IRRADIANCE, RAYLEIGH SCATTERING, OXYGEN, OZONE CROSS SECTIONS, AND ENERGY FLUX* (PAGE 2 OF 14)

WAVELENGTH RANGE** (nm)	SOLAR IRRADIANCE (phot/cm^2 –s)	RAYLEIGH SCATTER σ_{RS} (cm^2)	OXYGEN HERZBERG σ_{HZ} (O_2) (cm^2)	OZONE*** $\sigma(O_3)$ (cm^2)	ENERGY FLUX (W/m^2)
12 194.175–196.078	9.56E+11	4.08E–25	8.14E–24	4.11E–19	9.74E–3
13 196.078–198.020	1.15E+12	3.89E–25	8.17E–24	3.69E–19	1.16E–2
14 198.020–200.000	1.27E+12	3.71E–25	8.13E–24	3.30E–19	1.27E–2
15 200.000–202.020	1.52E+12	3.53E–25	8.01E–24	3.26E–19	1.50E–2
16 202.020–204.082	1.78E+12	3.36E–25	7.84E–24	3.26E–19	1.74E–2
17 204.082–206.186	2.20E+12	3.20E–25	7.63E–24	3.51E–19	2.13E–2
18 206.186–208.333	2.69E+12	3.05E–25	7.33E–24	4.11E–19	2.58E–2
19 208.333–210.526	4.54E+12	2.90E–25	6.99E–24	4.84E–19	4.31E–2
20 210.526–212.766	7.14E+12	2.76E–25	6.45E–24	6.26E–19	6.70E–2
21 212.766–215.054	8.35E+12	2.62E–25	5.81E–24	8.57E–19	7.75E–2
22 215.054–217.391	8.39E+12	2.49E–25	5.23E–24	1.17E–18	7.71E–2

*(World Meteorological Org., 1985)

**Wavelength range for spectral intervals 1–49 correspond to 500 wavenumbers. Wavelength range for remainder of spectral intervals is 5 nm.

***T=203 K and T=273 K

TABLE 7.2–3 REFERENCE SOLAR IRRADIANCE, RAYLEIGH SCATTERING, OXYGEN, OZONE CROSS SECTIONS, AND ENERGY FLUX* (PAGE 3 OF 14)

WAVELENGTH RANGE** (nm)	SOLAR IRRADIANCE (phot/cm^2 –s)	RAYLEIGH SCATTER σ_{RS} (cm^2)	OXYGEN HERZBERG σ_{HZ} (O_2) (cm^2)	OZONE*** $\sigma(O_3)$ (cm^2)	ENERGY FLUX (W/m^2)
23 217.391–219.780	1.08E+13	2.36E–25	4.71E–24	1.52E–18	9.82E–2
24 219.780–222.222	1.18E+13	2.24E–25	4.26E–24	1.97E–18	1.06E–1
25 222.222–224.719	1.60E+13	2.13E–25	3.80E–24	2.55E–18	1.42E–1
26 224.719–227.273	1.34E+13	2.02E–25	3.35E–24	3.24E–18	1.18E–1
27 227.273–229.885	1.41E+13	1.92E–25	2.90E–24	4.00E–18	1.23E–1
28 229.885–232.558	1.57E+13	1.82E–25	2.45E–24	4.83E–18	1.35E–1
29 232.558–235.294	1.38E+13	1.72E–25	2.05E–24	5.79E–18	1.17E–1
30 235.294–238.095	1.60E+13	1.63E–25	1.69E–24	6.86E–18	1.34E–1
31 238.095–240.964	1.45E+13	1.54E–25	1.30E–24	7.97E–18	1.20E–1
32 240.964–243.902	2.20E+13	1.46E–25	0.93E–24	9.00E–18	1.80E–1

*(World Meteorological Org., 1985)

**Wavelength range for spectral intervals 1–49 correspond to 500 wavenumbers. Wavelength range for remainder of spectral intervals is 5 nm.

***T=203 K and T=273 K

TABLE 7.2–3 REFERENCE SOLAR IRRADIANCE, RAYLEIGH SCATTERING, OXYGEN, OZONE CROSS SECTIONS, AND ENERGY FLUX* (PAGE 4 OF 14)

WAVELENGTH RANGE** (nm)	SOLAR IRRADIANCE (phot/cm^2–s)	RAYLEIGH SCATTER σ_{RS} (cm^2)	OXYGEN HERZBERG $\sigma_{HZ}(O_2)$ (cm^2)	OZONE*** $\sigma(O_3)$ (cm^2)	ENERGY FLUX (W/m^2)
33					
243.902–246.914	1.99E+13	1.38E–25	0.00E–00	1.00E–17	1.61E–1
34					
246.914–250.000	1.97E+13	1.31E–25	–	1.08E–17	1.58E–1
35					
250.000–253.165	1.94E+13	1.23E–25	–	1.13E–17	1.53E–1
36					
253.165–256.410	2.91E+13	1.17E–25	–	1.15E–17	2.27E–1
37					
256.410–259.740	4.95E+13	1.10E–25	–	1.12E–17	3.81E–1
38					
259.740–263.158	4.53E+13	1.04E–25	–	1.06E–17	3.44E–1

*(World Meteorological Org., 1985)

**Wavelength range for spectral intervals 1–49 correspond to 500 wavenumbers. Wavelength range for remainder of spectral intervals is 5 nm.

***T=203 K and T=273 K

TABLE 7.2–3 REFERENCE SOLAR IRRADIANCE, RAYLEIGH SCATTERING, OXYGEN, OZONE CROSS SECTIONS, AND ENERGY FLUX* (PAGE 5 OF 14)

WAVELENGTH RANGE** (nm)	SOLAR IRRADIANCE (phot/cm^2–s)	RAYLEIGH SCATTER σ_{RS} (cm^2)	OXYGEN $\sigma(O_3)$ T=203K (cm^2)	OZONE $\sigma(O_3)$ T=273K (cm^2)	ENERGY FLUX (W/m^2)
39					
263.158–266.667	1.07E+14	9.78E–26	9.59E–18	9.65E–18	8.02E–1
40					
266.667–270.270	1.20E+14	9.22E–26	8.31E–18	8.34E–18	8.88E–1
41					
270.270–273.973	1.10E+14	8.68E–26	6.89E–18	6.92E–18	8.03E–1
42					
273.973–277.778	1.04E+14	8.17E–26	5.35E–18	5.42E–18	7.49E–1
43					
277.778–281.690	8.24E+13	7.68E–26	3.91E–18	4.02E–18	5.85E–1
44					
281.690–285.714	1.52E+14	7.22E–26	2.67E–18	2.77E–18	1.06
45					
285.714–289.855	2.15E+14	6.78E–26	1.73E–18	1.79E–18	1.48
46					
289.855–294.118	3.48E+14	6.36E–26	1.04E–18	1.09E–18	2.37
47					
294.118–298.507	3.40E+14	5.97E–26	5.85E–19	6.24E–19	2.28
48					
298.507–303.030	3.22E+14	5.59E–26	3.16E–19	3.43E–19	2.13
49					
303.030–307.692	4.23E+14	5.24E–26	1.66E–19	1.85E–19	2.75
50					
307.692–312.5	4.95E+14	4.90E–26	8.67E–20	9.80E–20	3.17
51					
312.5–317.5	5.44E+14	4.58E–26	4.33E–20	5.01E–20	3.43

*(World Meteorological Org., 1985)

**Wavelength range for spectral intervals 1–49 correspond to 500 wavenumbers. Wavelength range for remainder of spectral intervals is 5 nm.

TABLE 7.2–3 REFERENCE SOLAR IRRADIANCE, RAYLEIGH SCATTERING, OXYGEN, OZONE CROSS SECTIONS, AND ENERGY FLUX* (PAGE 6 OF 14)

WAVELENGTH RANGE** (nm)	SOLAR IRRADIANCE (phot/cm^2–s)	RAYLEIGH SCATTER σ_{RS} (cm^2)	OXYGEN $\sigma(O_3)$ (cm^2) T=203K	OZONE $\sigma(O_3)$ (cm^2) T=273K	ENERGY FLUX (W/m^2)
52					
317.5–322.5	5.93E+14	4.28E–26	2.09E–20	2.49E–20	3.68
53					
322.5–327.5	6.95E+14	4.01E–26	9.37E–21	1.20E–20	4.25
54					
327.5–332.5	8.15E+14	3.75E–26	4.71E–21	6.17E–21	4.91
55					
332.5–337.5	7.81E+14	3.52E–26	1.98E–21	2.74E–21	4.63
56					
337.5–342.5	8.35E+14	3.31E–26	7.77E–22	1.17E–21	4.88
57					
342.5–347.5	8.14E+14	3.11E–26	1.77E–22	5.88E–22	4.69
58					
347.5–352.5	8.53E+14	2.92E–26	–	2.66E–22	4.84
59					
352.5–357.5	9.17E+14	2.75E–26	–	1.09E–22	5.13
60					
357.5–362.5	8.38E+14	2.60E–26	–	5.49E–23	4.62
61					
362.5–367.5	1.04E+15	2.45E–26	–	–	5.66
62					
367.5–372.5	1.10E+15	2.31E–26	–	–	5.91
63					
372.5–377.5	9.79E+14	2.19E–26	–	–	5.19
64					
377.5–382.5	1.13E+15	2.07E–26	–	–	5.91

*(World Meteorological Org., 1985)

**Wavelength range for spectral intervals 1–49 correspond to 500 wavenumbers. Wavelength range for remainder of spectral intervals is 5 nm.

TABLE 7.2–3 REFERENCE SOLAR IRRADIANCE, RAYLEIGH SCATTERING, OXYGEN, OZONE CROSS SECTIONS, AND ENERGY FLUX* (PAGE 7 OF 14)

WAVELENGTH RANGE** (nm)	SOLAR IRRADIANCE (phot/cm^2–s)	RAYLEIGH SCATTER σ_{RS} (cm^2)	OZONE*** $\sigma(O_3)$ (cm^2)	ENERGY FLUX (W/m^2)
65				
382.5–387.5	8.89E+14	1.96E–26	–	4.59
66				
387.5–392.5	1.14E+15	1.86E–26	–	5.81
67				
392.5–397.5	9.17E+14	1.76E–26	–	4.61
68				
397.5–402.5	1.69E+15	1.67E–26	–	8.39
69				
402.5–407.5	1.70E+15	1.59E–26	–	8.34
70				
407.5–412.5	1.84E+15	1.51E–26	2.91E–23	8.91
71				
412.5–417.5	1.87E+15	1.44E–26	3.14E–23	8.95
72				
417.5–422.5	1.95E+15	1.37E–26	3.99E–23	9.22
73				
422.5–427.5	1.81E+15	1.30E–26	6.54E–23	8.46
74				
427.5–432.5	1.67E+15	1.24E–26	6.83E–23	7.72
75				
432.5–437.5	1.98E+15	1.18E–26	8.66E–23	9.04
76				
437.5–442.5	2.02E+15	1.13E–26	1.25E–22	9.12

*(World Meteorological Org., 1985)

**Wavelength range for spectral intervals 1–49 correspond to 500 wavenumbers. Wavelength range for remainder of spectral intervals is 5 nm.

***T=203K and T=273K

TABLE 7.2–3 REFERENCE SOLAR IRRADIANCE, RAYLEIGH SCATTERING, OXYGEN, OZONE CROSS SECTIONS, AND ENERGY FLUX* (PAGE 8 OF 14)

WAVELENGTH RANGE** (nm)	SOLAR IRRADIANCE (phot/cm^2–s)	RAYLEIGH SCATTER σ_{RS} (cm^2)	OZONE*** $\sigma(O_3)$ (cm^2)	ENERGY FLUX (W/m^2)
77				
442.5–447.5	2.18E+15	1.08E–26	1.49E–22	9.73
78				
447.5–452.5	2.36E+15	1.03E–26	1.71E–22	1.04E+1
79				
452.5–457.5	2.31E+15	9.85E–27	2.12E–22	1.01E+1
80				
457.5–462.5	2.39E+15	9.42E–27	3.57E–22	1.03E+1
81				
462.5–467.5	2.38E+15	9.01E–27	3.68E–22	1.02E+1
82				
467.5–472.5	2.39E+15	8.63E–27	4.06E–22	1.01E+1
83				
472.5–477.5	2.44E+15	8.26E–27	4.89E–22	1.02E+1
84				
477.5–482.5	2.51E+15	7.92E–27	7.11E–22	1.04E+1
85				
482.5–487.5	2.30E+15	7.59E–27	8.43E–22	9.42
86				
487.5–492.5	2.39E+15	7.28E–27	8.28E–22	9.69
87				
492.5–497.5	2.48E+15	6.99E–27	9.09E–22	9.95
88				
497.5–502.5	2.40E+15	6.71E–27	1.22E–21	9.54

*(World Meteorological Org., 1985)

**Wavelength range for spectral intervals 1–49 correspond to 500 wavenumbers. Wavelength range for remainder of spectral intervals is 5 nm.

***T=203K and T=273K

TABLE 7.2–3 REFERENCE SOLAR IRRADIANCE, RAYLEIGH SCATTERING, OXYGEN, OZONE CROSS SECTIONS, AND ENERGY FLUX* (PAGE 9 OF 14)

WAVELENGTH RANGE** (nm)	SOLAR IRRADIANCE (phot/cm^2–s)	RAYLEIGH SCATTER σ_{RS} (cm^2)	OZONE*** $\sigma(O_3)$ (cm^2)	ENERGY FLUX (W/m^2)
89				
502.5–507.5	2.46E+15	6.44E–27	1.62E–21	9.68
90				
507.5–512.5	2.49E+15	6.19E–27	1.58E–21	9.70
91				
512.5–517.5	2.32E+15	5.95E–27	1.60E–21	8.95
92				
517.5–522.5	2.39E+15	5.72E–27	1.78E–21	9.13
93				
522.5–527.5	2.42E+15	5.50E–27	2.07E–21	9.16
94				
527.5–532.5	2.55E+15	5.30E–27	2.55E–21	9.56
95				
532.5–537.5	2.51E+15	5.10E–27	2.74E–21	9.32
96				
537.5–542.5	2.49E+15	4.91E–27	2.88E–21	9.16
97				
542.5–547.5	2.55E+15	4.73E–27	3.07E–21	9.30
98				
547.5–552.5	2.53E+15	4.56E–27	3.17E–21	9.14
99				
552.5–557.5	2.54E+15	4.34E–27	3.36E–21	9.09
100				
557.5–562.5	2.50E+15	4.18E–27	3.88E–21	8.87

*(World Meteorological Org., 1985)

**Wavelength range for spectral intervals 1–49 correspond to 500 wavenumbers. Wavelength range for remainder of spectral intervals is 5 nm.

***T=203K and T=273K

TABLE 7.2–3 REFERENCE SOLAR IRRADIANCE, RAYLEIGH SCATTERING, OXYGEN, OZONE CROSS SECTIONS, AND ENERGY FLUX* (PAGE 10 OF 14)

WAVELENGTH RANGE** (nm)	SOLAR IRRADIANCE (phot/cm^2–s)	RAYLEIGH SCATTER σ_{RS} (cm^2)	OZONE*** $\sigma(O_3)$ (cm^2)	ENERGY FLUX (W/m^2)
101				
562.5–567.5	2.57E+15	4.04E–27	4.31E–21	9.04
102				
567.5–572.5	2.58E+15	3.90E–27	4.67E–21	8.99
103				
572.5–577.5	2.67E+15	3.76E–27	4.75E–21	9.22
104				
577.5–582.5	2.67E+15	3.63E–27	4.55E–21	9.14
105				
582.5–587.5	2.70E+15	3.51E–27	4.35E–21	9.17
106				
587.5–592.5	2.62E+15	3.39E–27	4.42E–21	8.82
107				
592.5–597.5	2.69E+15	3.28E–27	4.61E–21	8.98
108				
597.5–602.5	2.63E+15	3.17E–27	4.89E–21	8.71
109				
602.5–607.5	2.68E+15	3.06E–27	4.84E–21	8.80
110				
607.5–612.5	2.66E+15	2.96E–27	4.54E–21	8.66
111				
612.5–617.5	2.59E+15	2.87E–27	4.24E–21	8.37
112				
617.5–622.5	2.69E+15	2.77E–27	3.90E–21	8.62

*(World Meteorological Org., 1985)

**Wavelength range for spectral intervals 1–49 correspond to 500 wavenumbers. Wavelength range for remainder of spectral intervals is 5 nm.

***T=203K and T=273K

TABLE 7.2–3 REFERENCE SOLAR IRRADIANCE, RAYLEIGH SCATTERING, OXYGEN, OZONE CROSS SECTIONS, AND ENERGY FLUX* (PAGE 11 OF 14)

WAVELENGTH RANGE** (nm)	SOLAR IRRADIANCE (phot/cm^2–s)	RAYLEIGH SCATTER σ_{RS} (cm^2)	OZONE*** $\sigma(O_3)$ (cm^2)	ENERGY FLUX (W/m^2)
113				
622.5–627.5	2.61E+15	2.68E–27	3.60E–21	8.30
114				
627.5–632.5	2.62E+15	2.60E–27	3.43E–21	8.26
115				
632.5–637.5	2.62E+15	2.52E–27	3.17E–21	8.20
116				
637.5–642.5	2.63E+15	2.44E–27	2.74E–21	8.17
117				
642.5–647.5	2.60E+15	2.36E–27	2.61E–21	8.01
118				
647.5–652.5	2.55E+15	2.29E–27	2.42E–21	7.79
119				
652.5–657.5	2.48E+15	2.22E–27	2.20E–21	7.52
120				
657.5–662.5	2.57E+15	2.15E–27	2.20E–21	7.73
121				
662.5–667.5	2.61E+15	2.09E–27	1.85E–21	7.80
122				
667.5–672.5	2.61E+15	2.03E–27	1.67E–21	7.74
123				
672.5–677.5	2.62E+15	1.97E–27	1.54E–21	7.71
124				
677.5–682.5	2.62E+15	1.91E–27	1.42E–21	7.66

*(World Meteorological Org., 1985)

**Wavelength range for spectral intervals 1–49 correspond to 500 wavenumbers. Wavelength range for remainder of spectral intervals is 5 nm.

***T=203K and T=273K

TABLE 7.2–3 REFERENCE SOLAR IRRADIANCE, RAYLEIGH SCATTERING, OXYGEN, OZONE CROSS SECTIONS, AND ENERGY FLUX* (PAGE 12 OF 14)

WAVELENGTH RANGE** (nm)	SOLAR IRRADIANCE (phot/cm^2–s)	RAYLEIGH SCATTER σ_{RS} (cm^2)	OZONE*** $\sigma(O_3)$ (cm^2)	ENERGY FLUX (W/m^2)
125				
682.5–687.5	2.57E+15	1.85E–27	1.25E–21	7.45
126				
687.5–692.5	2.52E+15	1.80E–27	1.12E–21	7.25
127				
692.5–697.5	2.60E+15	1.75E–27	1.02E–21	7.43
128				
697.5–702.5	2.58E+15	1.70E–27	9.20E–22	7.32
129				
702.5–707.5	2.52E+15	1.65E–27	8.40E–22	7.10
130				
707.5–712.5	2.51E+15	1.60E–27	7.70E–22	7.02
131				
712.5–717.5	2.48E+15	1.56E–27	6.90E–22	6.89
132				
717.5–722.5	2.45E+15	1.52E–27	6.30E–22	6.76
133				
722.5–727.5	2.48E+15	1.47E–27	5.70E–22	6.79
134				
727.5–732.5	2.45E+15	1.43E–27	5.25E–22	6.67
135				
732.5–737.5	2.44E+15	1.39E–27	4.75E–22	6.60
136				
737.5–742.5	2.39E+15	1.36E–27	4.47E–22	6.41

*(World Meteorological Org., 1985

**Wavelength range for spectral intervals 1–49 correspond to 500 wavenumbers. Wavelength range for remainder of spectral intervals is 5 nm.

***T=203K and T=273K

TABLE 7.2–3 REFERENCE SOLAR IRRADIANCE, RAYLEIGH SCATTERING, OXYGEN, OZONE CROSS SECTIONS, AND ENERGY FLUX* (PAGE 13 OF 14)

WAVELENGTH RANGE** (nm)	SOLAR IRRADIANCE (phot/cm^2–s)	RAYLEIGH SCATTER σ_{RS} (cm^2)	OZONE*** $\sigma(O_3)$ (cm^2)	ENERGY FLUX (W/m^2)
137				
742.5–747.5	2.40E+15	1.32E–27	4.20E–22	6.40
138				
747.5–752.5	2.41E+15	1.29E–27	3.75E–22	6.38
139				
752.5–757.5	2.40E+15	1.25E–27	3.25E–22	6.32
140				
757.5–762.5	2.38E+15	1.22E–27	2.92E–22	6.22
141				
762.5–767.5	2.34E+15	1.19E–27	2.76E–22	6.08
142				
767.5–772.5	2.32E+15	1.16E–27	2.70E–22	5.99
143				
772.5–777.5	2.30E+15	1.13E–27	2.80E–22	5.89
144				
777.5–782.5	2.33E+15	1.10E–27	2.85E–22	5.93
145				
782.5–787.5	2.34E+15	1.07E–27	2.52E–22	5.92
146				
787.5–792.5	2.29E+15	1.04E–27	2.20E–22	5.76
147				
792.5–797.5	2.29E+15	1.02E–27	1.82E–22	5.72
148				
797.5–802.5	2.27E+15	9.90E–28	1.63E–22	5.64

*(World Meteorological Org., 1985)

**Wavelength range for spectral intervals 1–49 correspond to 500 wavenumbers. Wavelength range for remainder of spectral intervals is 5 nm.

***T=203K and T=273K

TABLE 7.2–3 REFERENCE SOLAR IRRADIANCE, RAYLEIGH SCATTERING, OXYGEN, OZONE CROSS SECTIONS, AND ENERGY FLUX* (PAGE 14 OF 14)

WAVELENGTH RANGE** (nm)	SOLAR IRRADIANCE (phot/cm^2–s)	RAYLEIGH SCATTER σ_{RS} (cm^2)	OZONE*** $\sigma(O_3)$ (cm^2)	ENERGY FLUX (W/m^2)
149				
802.5–807.5	2.27E+15	9.66E–28	1.75E–22	5.60
150				
807.5–812.5	2.20E+15	9.42E–28	1.90E–22	5.40
151				
812.5–817.5	2.22E+15	9.19E–28	1.85E–22	5.41
152				
817.5–822.5	2.l8E+15	8.96E–28	1.70E–22	5.28
153				
822.5–827.5	2.20E+15	8.75E–28	1.52E–22	5.30
154				
827.5–832.5	2.14E+15	8.53E–28	1.42E–22	5.12
155				
832.5–837.5	2.14E+15	8.33E–28	1.40E–22	5.09
156				
837.5–842.5	2.13E+15	8.13E–28	1.40E–22	5.04
157				
842.5–847.5	2.09E+15	7.94E–28	1.42E–22	4.91
158				
847.5–852.5	2.05E+15	7.75E–28	1.45E–22	4.79

*(World Meteorological Org., 1985)

**Wavelength range for spectral intervals 1–49 correspond to 500 wavenumbers. Wavelength range for remainder of spectral intervals is 5 nm.

***T=203K and T=273K

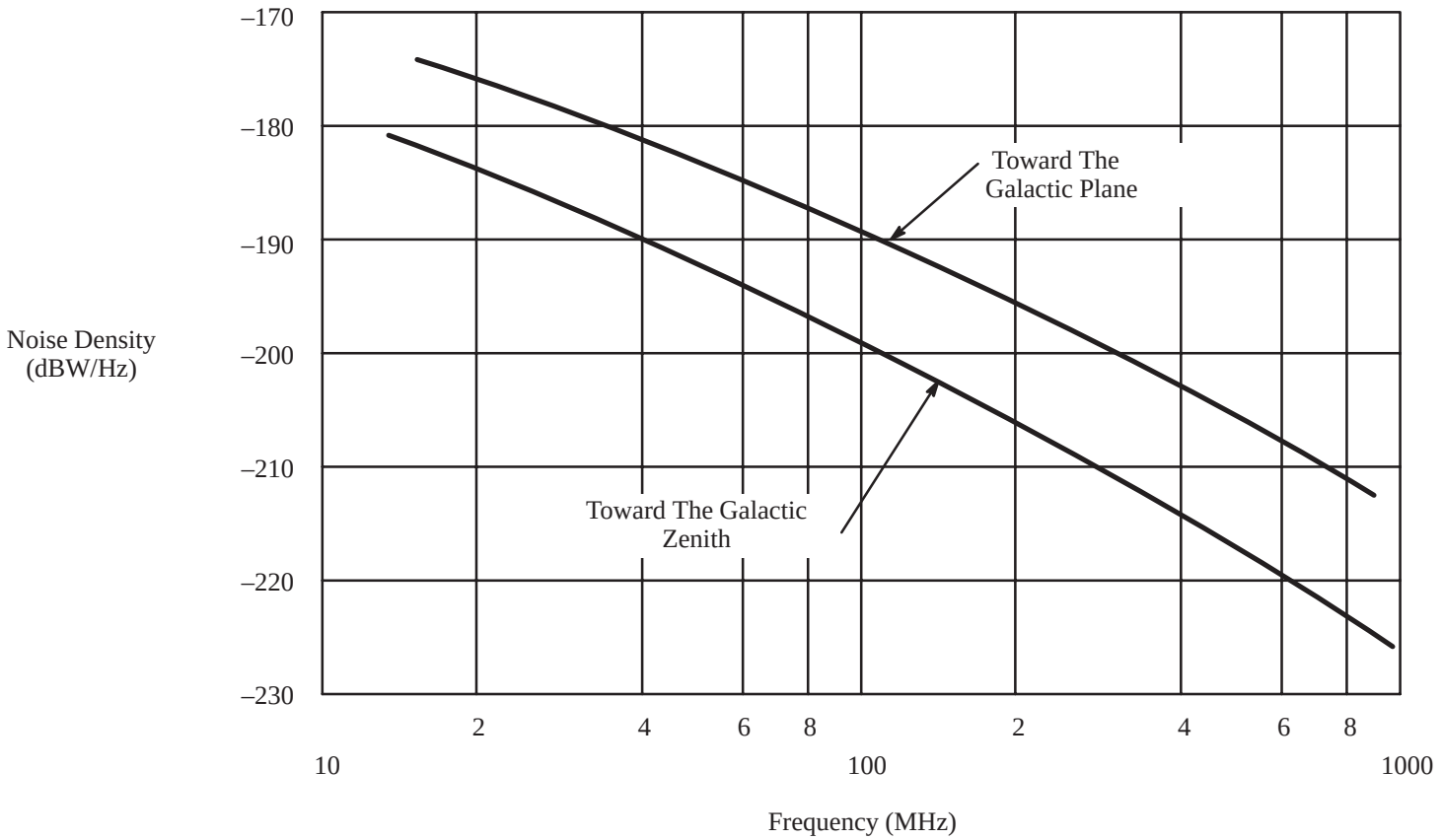

FIGURE 7.1–1 LEVELS OF GALACTIC RADIO NOISE AS A FUNCTION OF FREQUENCY

(Anon., 1981a)

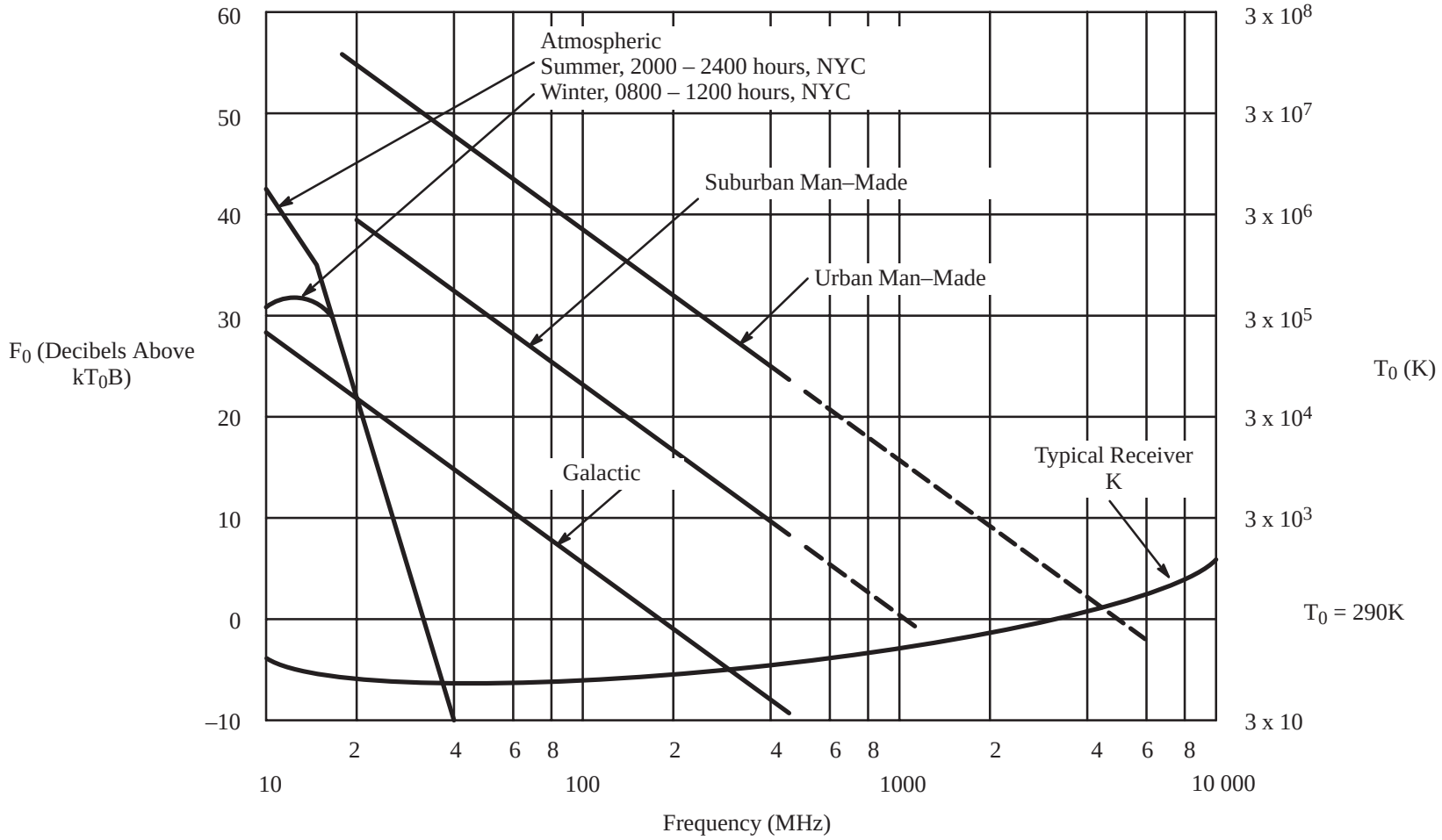

FIGURE 7.1–2 MEDIAN VALUES OF AVERAGE NOISE POWER EXPECTED FROM VARIOUS SOURCES (OMNIDIRECTIONAL ANTENNA NEAR SURFACE)

(Anon., 1981a)

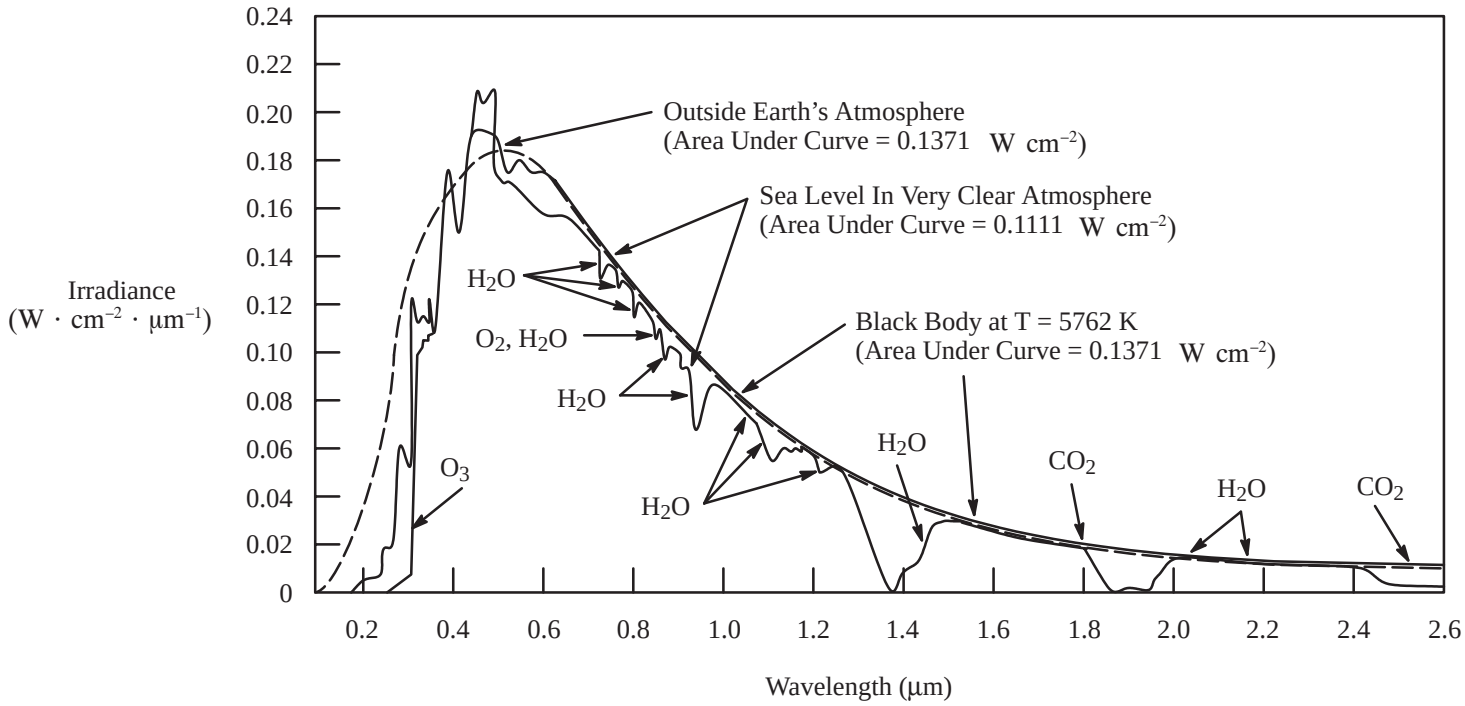

FIGURE 7.2–1 NORMALLY INCIDENT SOLAR RADIATION AT SEA LEVEL ON VERY CLEAR DAYS, SOLAR SPECTRAL IRRADIANCE OUTSIDE THE EARTH'S ATMOSPHERE AT 1 ASTRONOMICAL UNIT (AU), AND BLACKBODY SPECTRAL IRRADIANCE CURVE AT T = 5762 DEGREES K (NORMALIZED TO 1 AU)

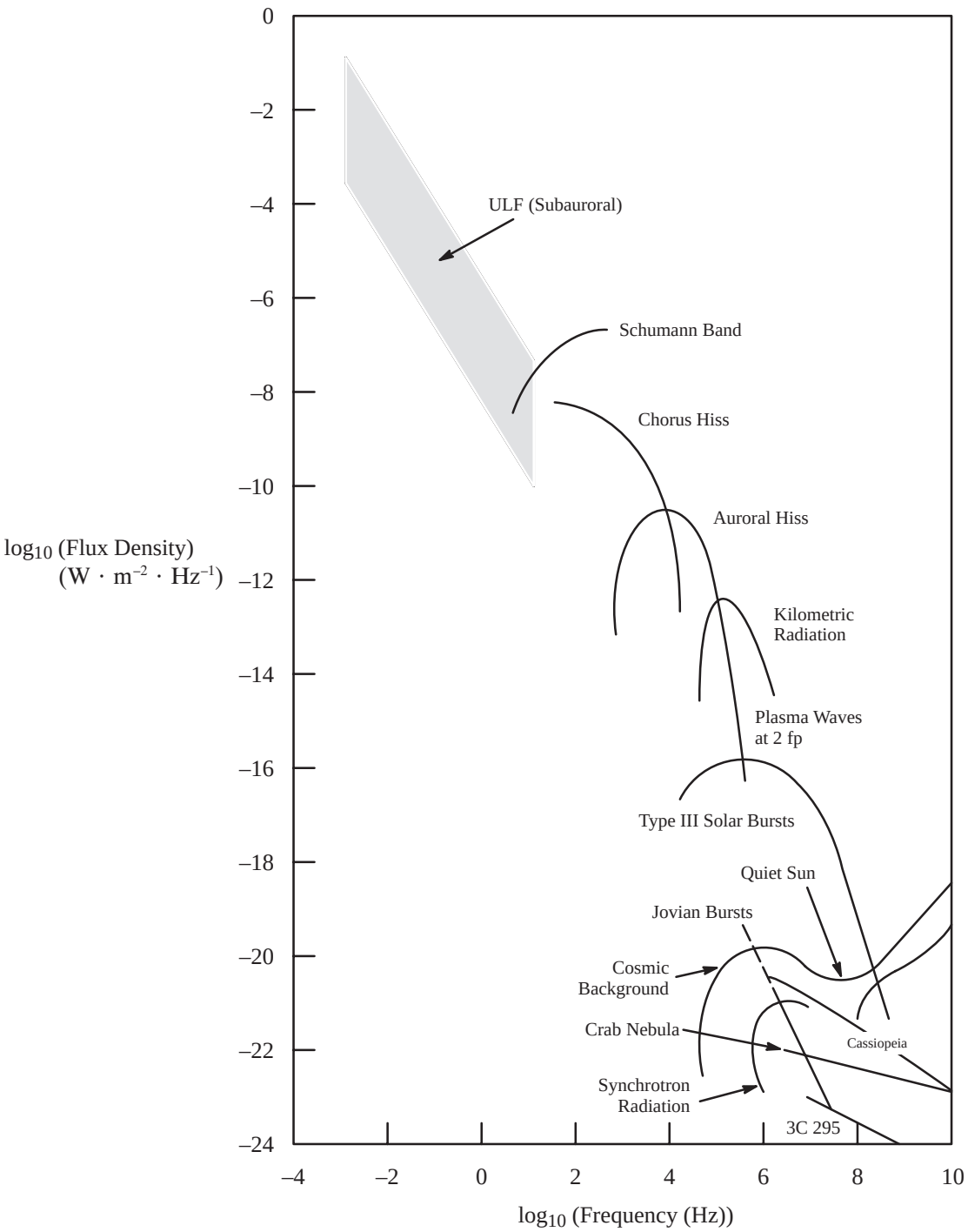

FIGURE 7.3–1 POWER FLUX LEVELS FOR VARIOUS FREQUENCY RANGES OF NATURALLY–OCCURRING ELECTROMAGNETIC AND PLASMA WAVES

(Kelley, 1985)

8.0 METEOROIDS AND ORBITAL DEBRIS

Once in orbit, the Space Station Program Elements (SSPEs) will encounter meteoroids and orbital debris. Either type of object can pose a serious threat of damage or decompression to the SSPE upon impact. Meteoroids are natural in origin, and debris is the result of man–made material remaining in Earth orbit. General information and discussion appears in Grun et al., 1985, and Kessler et al., 1989.

For historical reasons related to measurement method, the meteoroid and debris environments are usually specified as a time–averaged flux, F_r, against a single sided, randomly tumbling surface. Flux is defined as number of intercepted objects per unit time and area. For F_r, the relevant area is the actual surface area of the satellite. One may also define a "cross sectional area flux", F_c, for a randomly tumbling satellite, where the relevant area is the time averaged cross sectional area. A useful theorem which is obvious for a tumbling sphere, but which holds for objects of arbitrary non–self–shielding shape (no concave surfaces), is that $F_c = 4F_r$.

For spacecraft which fly with a fixed orientation, the meteoroid and orbital debris fluxes are treated as vector quantities, **F**, and the effects of directionality must be carefully evaluated. Some effects of impact will be direction dependent. To simply evaluate the expected number, N, or probability of impacts from either meteoroids or debris (or both), one may use a "k factor" method and the appropriate F_r, such that:

$$N = \int_{t}^{t+T} \sum_{i} k_i \; F_r \; A_i \; dt \qquad (8.0,1)$$

where the summation is over the i surfaces of the spacecraft, each of area A_i, and $k_i F_r$ is the actual flux on surface A_i. The calculation of k_i is discussed in paragraph 8.3.

Once an N has been determined, the probability of exactly n impacts occurring in the corresponding time interval is found from Poisson statistics, thus;

$$P_n = \frac{N^n}{n!} \; . \; e^{-N} \qquad (8.0,2)$$

8.1 METEOROIDS

The meteoroid environment encompasses only particles of natural origin. Nearly all meteoroids originate from comets or asteroids. Meteoroids that retain the orbit of their parent body and create periods of high flux are called streams. Random fluxes with no apparent pattern are called sporadic.

The average total meteoroid environment presented here is comprised of the average sporadic meteoroids and a yearly average of the stream meteoroids. The mass density for meteoroids spans a wide range, from approximately 0.2 g/cm^3 or less for a portion of the population to values as large as 8 g/cm^3. The values for average mass density quoted in the literature vary widely, so that a value can only be estimated. Recommended mean values are 2 g/cm^3 for meteoroids smaller than 10^{-6} g; 1 g/cm^3 for meteoroids between 10^{-6} and 0.01 g; and 0.5 g/cm^3 for masses above 0.01 g. The uncertainty in density is not too serious because the model presented below was derived from crater and impact data, so it will provide a good representation of expected damage even though the absolute mass calibration could conceivably be in error by as much as a factor of ten for the smallest sizes.

Because of the precession of a satellite's orbit and the tilt of the Earth's equatorial plane with respect to the ecliptic plane, the meteoroid environment can be assumed to be omnidirectional relative to the Earth for design applications. However, it becomes directional relative to a spacecraft moving through the environment, with most meteoroids coming from the direction of motion. The directionality derives from the vector summation of the spacecraft velocity vector with the meteoroid velocity distribution. An additional directionality factor is introduced by the shielding provided by the Earth.

The normalized meteoroid velocity distribution with respect to the Earth is illustrated by Figure 8.1–1. It is given by the expressions (number per km/s):

$$\begin{aligned} n(v) &= 0.112, && 11.1 \le v < 16.3 \text{ km/s}, \\ n(v) &= 3.328 \times 10^5 \, v^{-5.34}, && 16.3 \le v < 55 \text{ km/s}, \\ n(v) &= 1.695 \times 10^{-4}, && 55 \le v \le 72.2 \text{ km/s}. \end{aligned} \qquad (8.1,1)$$

This distribution has an average velocity of about 17 km/s; relative to an orbiting spacecraft the average velocity is about 19 km/s. To determine the velocity and direction distributions relative to any surface on an orbiting spacecraft, the vector relationship between the meteoroid velocity and the spacecraft velocity should be used as discussed in paragraph 8.3.

Meteoroid flux is given in terms of the integral flux F_r, the number of particles/m^2/year of mass m or greater against a randomly tumbling surface. $F^{ip}{}_r$, the interplanetary flux at 1 A.U. is described mathematically as follows (for $10^{-15} \leq m \leq 10$ g):

$$F^{ip}{}_r(m) = c_0\{(c_1 m^{0.306} + c_2)^{-4.38} + c_3(m + c_4 m^2 + c_5 m^4)^{-0.36} + c_6(m + c_7 m^2)^{-0.85}\}. \quad (8.1,2)$$

where: $c_0 = 3.156 \times 10^7$,
$c_1 = 2.2 \times 10^3$,
$c_2 = 15$,
$c_3 = 1.3 \times 10^{-9}$,
$c_4 = 10^{11}$,
$c_5 = 10^{27}$,
$c_6 = 1.3 \times 10^{-16}$,
$c_7 = 10^6$.

To convert the meteoroid flux $F^{ip}{}_r$ stated above to that in Earth orbit, F_r, both Earth shielding and focusing factors must be applied, $F_r = s_f G_E F^{ip}{}_r$. The formula for shielding is:

$$\text{shielding factor} = s_f = (1 + \cos \eta)/2, \quad (8.1,3)$$

where

$\sin \eta = R_E/(R_E + H)$,
R_E= Earth radius + 100 km atmosphere (6478 km),
H = height above Earth's atmosphere (Earth's atmosphere height to be taken as 100 km for this purpose).

Consequently, the Earth shielding factor varies from 0.5 just above the atmosphere to 1.0 in deep space.

The factor G_E represents the focusing effect of the Earth's gravitational field which attracts the meteoroids and increases their flux. The factor ranges from a value of 2.0 just above the atmosphere to a value of 1.0 in deep space. The focusing factor is represented by the following equation:

$$\text{focusing factor} = G_E = 1 + (R_E/r) \quad (8.1,4)$$

where

R_E = Earth Radius + 100 km atmosphere (6478 km),
r = Orbit Radius.

The meteoroid environment at 500 km is illustrated in Figure 8.1–2.

8.1.1 UNCERTAINTY IN THE METEOROID ENVIRONMENT

Except for small cosmic dust grains collected directly from the stratosphere, the physical properties of meteoroids must be determined by relatively indirect means, examination of impact craters, optical scattering, etc.. Also, they are known to originate from both comets, which are apparently composed of low density ”ices” and dust, and asteroids which are rock–like. Therefore, there is considerable uncertainty in their properties. In particular, the uncertainty in mass tends to dominate the uncertainties in the flux measurement. For meteoroids less than 10^{-6} grams, the mass is uncertain to within a factor from about 0.2 to 5 times the estimated value, which implies the flux is uncertain to within a factor of 0.33 to 3 at a given mass. For meteoroids above this size, the flux is well defined but the associated mass is even more uncertain. This implies an effective uncertainty in the flux (at a set mass) of a factor from 0.1 to 10 (because of the slope of the functional relationship).

8.2 ORBITAL DEBRIS

8.2.1 BACKGROUND

The natural meteoroid flux discussed above represents, at any instant, a total of about 200 kg of mass within 2000 km of the Earth’s surface, most of it concentrated in the 0.1 mm meteoroids. Within this same 2000 kilometers there is an estimated 1.5 to 3 million kilograms of man–made orbiting objects as of mid 1988. Most of these are in high inclination orbits where they sweep past each other at an average speed of 10 km/s. About 1500 spent rocket stages, inactive payloads and a few active payloads account for most of this mass. These objects are currently tracked by the U.S. Space Command, as are about 4500 others totaling 20,000 kg, mostly fragments of satellites or other orbiting hardware. Recent observations indicate a total mass of about 1000 kg for orbital debris with diameters of 1 cm or smaller and about 300 kg for orbital debris sizes smaller than 1 mm. This distribution of mass makes the orbital debris environment more hazardous than the meteoroid environment in most spacecraft applications below 2000 km altitude.

The debris model presented below represents an extension of the model presented by Kessler et. al., 1989. First, a curve fit to the “current” debris environment was developed based on the best experimental data available. This was then coupled with additional terms which represent a projection of the expected environment change into the future. 1988 was selected as the base year for the “current” environment. The applicable data sets include those referenced by Kessler et. al. in 1989, i.e., the analysis of panels returned from the Solar Max satellite, data from the MIT ETS telescopes, and U.S. Space Command catalogued and uncatalogued data sets. In addition, updates were added from recent optical measurements made with the GEODSS telescope systems and from biphase radar measurements made with the Arecibo and Goldstone radars. Quick look

data from the Long Duration Exposure Facility appears to be consistent with these data sets, but analysis was not sufficiently complete to allow incorporation of this information.

Model development, especially prediction of future trends in the debris environment, is difficult and subject to substantial uncertainty. The problems may be grouped into two categories which must be treated somewhat differently. The categories are:

1) Uncertainties in the current environment. These uncertainties shift the flux by a factor which is independent of time (a change in intercept on a flux vs. time plot). They include uncertainties of measurement, statistical limitations of the data sets, and voids in the data sets, i.e., size and altitude ranges where no measurements have been made, limitations of debris shape and density information, etc..

2) Uncertainties related to trend projection. These factors alter the slope of a flux vs. time plot. They derive primarily from the assumptions which must be made to predict future trends in human activities (launch rate for example, which historically has deviated significantly from the traffic model projections), and to overcome the technical uncertainties listed above. The state of the art is such that understanding is still lacking in several important areas necessary for complete engineering analysis and numerical modeling of the environment. Key examples include incomplete knowledge of satellite and rocket body fragmentation mechanics (e.g., fragment size and velocity distributions) and uncertainty in the cause and intensity of many fragmentation events. There are also important limitations in modeling capability due to the necessity of keeping computation time and model complexity within reasonable limits. These all have important influence on the final results.

Before discussing these issues in detail, we present the numerical formalism of the model in the following three sections.

Then, in section 8.2.5, the uncertainties and assumptions are listed in detail along with a quantitative estimate of their importance.

8.2.2 ORBITAL DEBRIS FLUX TO A TUMBLING SURFACE

A vectorial description of the orbital debris environment is presented in section 8.3. However, the description is based on the flux to a randomly tumbling surface and the velocity distribution, so these concepts are presented first.

The cumulative flux of orbital debris of diameter d and larger on a randomly tumbling spacecraft orbiting at altitude h, inclination i, in the year t, when the solar activity was S one year prior to t, is given by the following equation:

$$F_r(d,h,i,t,S) = H(d)\phi(h,S)\psi(i)[F_1(d)g_1(t) + F_2(d)g_2(t)] \qquad (8.2.2,1)$$

where

F_r = flux, impacts per square meter of surface per year,

d = orbital debris diameter in cm,

t = date (year),

h = altitude in km ($h \leq 2000$ km),

S = 13 month smoothed solar radio flux $F_{10.7}$ for t – 1 year, expressed in 10^4 Jy from Table 4.3–1,

i = inclination in degrees,

and

$$H(d) = \left[10^{\exp(-(\log_{10} d - 0.78)^2/0.637^2)}\right]^{1/2}$$

$\phi(h,S) = \phi_1(h,S)/(\phi_1(h,S) + 1)$,

$\phi_1(h,S) = 10^{(h/200 - S/140 - 1.5)}$,

$F_1(d) = 1.22 \times 10^{-5}\, d^{-2.5,}$

$F_2(d) = 8.1 \times 10^{10}\, (d + 700)^{-6}$,

p = the assumed annual growth rate of intact objects in orbit = 0.05,

q and q′ = the estimated growth rate of fragments; q = 0.02; q′ = 0.04. The q′ term is only used for 2011 and later dates.

$g_1(t) = (1 + q)^{(t - 1988)}$ for $t < 2011$,

$g_1(t) = (1 + q)^{23}\, (1 + q')^{(t - 2011)}$ for $t \geq 2011$,

$g_2(t) = 1 + [p(t - 1988)]$.

The inclination–dependent function ψ(i) defines the relationship between the flux on a spacecraft in an orbit of inclination i and the flux incident on a spacecraft in the current population's average inclination of about 50°. Values for ψ(i) are as follows:

Inclination i (degrees)	ψ(i)
28.5	0.91
30	0.92
40	0.96
50	1.02
60	1.09
70	1.26
80	1.71
90	1.37
100	1.78
120	1.18

An example orbital debris flux is compared with the meteoroid flux from equation 8.1,2 in Figure 8.1–2 for h = 500 km, t = 1995, i = 28.5º, and S(t–1yr) = 97.0.

8.2.3 AVERAGE SHAPE AND MASS DENSITY

The state of knowledge of debris shape and density is very scant. Actual shapes are irregular, including flat plates, rods, hollow structures, and crumpled metal. As size decreases, the objects tend to be somewhat less irregular. For the purposes of this model, the objects are assumed to be spherical, with a size dependent mass density function to approximate these irregularities and the probability that they may impact with any orientation.

The average mass density for debris 0.62 cm and larger is:

$$\rho = 2.8d^{-0.74}. \qquad (g/cm^3, \text{ d in cm}). \qquad (8.2.3,1)$$

For debris smaller than 0.62 cm,

$$\rho = 4\ g/cm^3, \qquad (d < 0.62\ cm).$$

That is, for small objects the mean density should be assumed to be a constant, 4 g/cm^3, independent of size. Actual shape and density distributions are very broad. This issue, in particular material density as opposed to object density, is addressed further in section 8.2.5.3.

8.2.4 VELOCITY AND DIRECTION DISTRIBUTION

Averaged over all altitudes, the non–normalized collision velocity distribution, i.e. the number of impacts with velocities between v and v + dv, relative to a spacecraft with orbital inclination i, is given by the following equations:

$$f(v) = \{2\, v\, v_o - v^2\}\ \{G \exp(-((v - A\, v_o)/(B\, v_o))^2) + F \exp(-((v - D\, v_0)/(E\, v_o))^2)\} + H\, C\, (4\, v\, v_o - v^2) \qquad (8.2.4,1)$$

where v is the collision velocity in km/s, A is constant, and B, C, D, E, F, G, H, and v_o are functions of the orbital inclination of the spacecraft. The values for these constants and parameters are as follows:

A =	2.5	
	0.5	i<60
B =	0.5–0.0.1(i–60)	60<i<80
	0.3	i>80
	0.0125	i<100
C =	0.0125 + 0.00125(i – 100)	i>100
D =	1.3 – 0.01(i – 30)	
E =	0.55 + 0.005(i – 30)	
	$0.3 + 0.0008(i–50)^2$	i<50
F =	0.3 – 0.01(i–50)	50<i<80
	0.0	i>80
	18.7	i<60
G =	$18.7 + 0.0289(i – 60)^3$	60<i<80
	250.0	i>80
H =	$1.0 – 0.0000757(i–60)^2$	
	7.25 + 0.015(i – 30)	i<60
v_o =	7.7	i>60

When f(v) is less than zero the function is to be reset equal to zero. The user may find it convenient to numerically normalize f(v) so that;

$$f'(v) = \frac{f(v)}{\int_0^\infty f(v)\ dv} \qquad (8.2.4,2)$$

When normalized in this manner, f′(v) over any 1 km/s velocity interval becomes the fraction of debris impacts within a 1 km/s incremental velocity band. The function is illustrated in Figure 8.2.4–1. Any average velocity moment may be defined as

$$\bar{v}^{\,n} = \int_0^\infty v^n\ f'(v)\ dv \qquad (8.2.4,3)$$

The frequency of impact from a given direction can be estimated by using this velocity distribution. The direction of impact is assumed to be specified by the intersection of the spacecraft velocity vector and another circular orbit. That is, the relative velocity vectors may be obtained by vector addition in a plane tangent to the earth's surface. Since a spacecraft velocity of 7.7 km/s was used to calculate relative velocity, the direction of the relative velocity vector is given by the relationship:

$$\cos(\pm\ \alpha\ ) = \frac{v}{v_{MAX}} = \frac{v}{15.4}, \qquad (8.2.4,4)$$

where α is the angle between the impact velocity vector and the spacecraft velocity vector in a coordinate system fixed with respect to the Station, v is the impact velocity, and v_{MAX} is the maximum possible velocity difference between the debris and the spacecraft. The coordinate system is illustrated in Figure 8.2.4–2.

8.2.5 LIMITATIONS AND UNCERTAINTY IN THE DEBRIS FLUX MODEL

8.2.5.1 MEASUREMENTS OF THE CURRENT ENVIRONMENT (FACTORS WHICH ALTER THE INTERCEPT OF FLUX GROWTH CURVES)

For orbital debris sizes larger than 10 cm diameter the environment is generally measured by ground radars. The most extensive measurements are made by the USAF Space Command, which also maintains a catalog of the debris population. While this data

provides an adequate description of the distributions of large debris with respect to altitude and inclination, and of historical trends, analysis of GEODSS optical telescope data has shown that the radars are detecting, and the Space Command cataloging, less than half of the population in this size range. This information has been incorporated in the model presented here, so that the model represents the current environment in this size range accurately to within the range 1.5 to 0.5 times the flux, i.e., the “90 percent confidence” upper limit flux equals 1.5 times the flux from equation 8.2.2,1, etc.. Table 8.2.5.1–1 summarizes the uncertainties and accuracy limitations in the orbital debris flux model.

Measurement of the debris flux at the other size extreme, sizes smaller than 0.05 cm, is made by analysis of impact craters on pieces of space hardware returned from orbit. Meteoroid impacts are distinguished from debris impacts by analysis of the chemical elements retained in the crater. For these sizes the flux has only been measured on hardware flown at about 500 km; at this altitude the environment is known within the range 2 to 0.5 times the flux.

Until recently, the only measurements between the two debris size extremes was a limited set of optical telescope data from the MIT ETS telescopes. This provided an indication of the cumulative flux for objects believed to be 2 cm and larger. For intermediate sizes, the environment was estimated by a simple straight line interpolation on a log–log, flux versus size plot, as in Figure 8.1–2. This practice was retained for the current model, but in this case the interpolation is confirmed by recent measurements by Arecibo and Goldstone radars in the important mid– range between 0.2 and 2 cm. These show a detection rate which is consistent with the current model, but both systematic and random errors in these measurements leave the environment uncertain within 3 to 0.33 times the flux for these sizes. Measurements were only made between 500 and 600 km altitude. Between 2 and 10 cm no measurements exist, but interpolation of the data from either side and modeling this region also yield an estimated uncertainty between 3 and 0.33 times the best estimate.

8.2.5.2 TREND PROJECTION (FACTORS WHICH ALTER THE SLOPE OF FLUX GROWTH CURVES)

As is the case with any analysis or model, the results hold only so long as the underlying assumptions remain valid. The following are the key assumptions upon which the model rests:

1) It is assumed that the rate of accumulation of objects in low Earth orbit is constant, with the annual increase equal to 5 percent of the amount accumulated by 1988. This matches the historical trend over the last few decades.

2) The relative use of different orbits is assumed to remain constant. For example, the history of launches by the USSR has been such that 80 percent of their payloads re–enter

within two years of launch. These do not contribute significantly to the debris environment. If this practice changed with increased the use of higher, longer life orbits, the population of objects in orbit would grow at a proportionally increased rate.

3) It is assumed that the efforts to minimize fragmentation of satellites in orbit will continue such that fragmentation events will continue at the rate of only one per year in low Earth orbit (29 percent of past practice). In the last decade, intentional (or apparently intentional) fragmentation of satellites accounted for about 71 percent of the known fragmentation events. Apparently, recent publicity and increased awareness of the hazards associated with orbital debris has generated policy shifts among the space faring nations. No intentional fragmentation events above 300 km have been observed in the last two years and steps have been taken to lessen the likelihood of unintentional events.

4) It is assumed that the debris size distribution is independent of altitude. One would expect small debris in circular orbits to decay faster than large debris, implying an altitude dependent distribution. However, consideration of the population of small fragments in elliptical orbits, assuming a trend similar to the one for large fragments, leads to a dependent distribution with the opposite trend. Therefore, pending further measurements and research, an intermediate assumption has been made.

5) It is assumed that future solar cycles will follow the mean of past cycles.

The uncertainties associated with these factors differ from those discussed above in that they alter the growth terms in equation 8.2.2,1, rather than entering as multipliers of the total flux. Thus the variations are expressed as variations of the p, q, and S terms.

The first two of these assumptions relate to the predicted future accumulation of objects in low Earth orbit. This is a key determinant of the expected debris growth rate – the value of p. The combination of a decreasing launch rate for the United States with an increasing rate for the rest of the world has led to the relatively constant historical trend. It is not clear, however, that this trend will continue. Expected launch rates are subject to political and economic influences which may change unpredictably, and many new countries are becoming involved in space activities. Current traffic models extended to the year 2010 predict that future growth will be at a compounded rate between 5 and 10 percent per year. The lower limit of these models corresponds to a value of $p = 0.05$ compounded annually. These models represent the projects that are planned, and since some projects are either canceled or postponed, the actual rate has always fallen below the traffic models. Therefore the baselined rate is a constant (not compounded) $p = 0.05$. A substantially lower rate would only be expected in the case of a world–wide economic depression or similar event. A higher rate is possible, especially if an increased launch rate is coupled with an increased use of higher, long life orbits. A compounded 10% per year increase, or $p = 0.1$, represents the “90 percent confidence level” upper limit.

The value of q, which represents the expected growth rate of small debris, primarily depends on the frequency of expected satellite breakup, assumption 3). Breakups may be

intentional, or they may result from accidents and random collisions. Thus the breakup rate is partially controllable, partially not. The value selected for this model, q = 0.02, assumes no intentional breakups, and an accidental breakup rate of 1/yr. The range of possible q values is from 0.0 (random collisions are not important and improved precautions lower the accidental rate below historical values) to 0.06 (both accidental and intentional fragmentation rates match the 1980 – 87 rates). Technically, negative values of q are possible if all fragmentation events are prevented, but this is not considered a credible possibility. At the other extreme, if fragmentation rates rise above the 1/yr and the rate of accumulation of mass in orbit increases, on orbit collisions become important and q will approach 2p.

Unintentional fragmentation events can result from either explosions or collisions between objects. The first of these represents a simple linear source, the population growth is directly related to the fragmentation rate. The second is exponential in nature, since the number of fragmentation events is a function of the square of the population. Thus the coupling between p and q uncertainty limits noted above. Modeling these processes indicates that the first process will be dominant until about the year 2010. About that time, under the assumptions of the current model, the second process becomes significant and the small particle population will grow at an increasing rate. If the assumptions of the current model hold and current practices continue, q is expected to increase to 0.04 beginning about the year 2010.

Uncertainties in the mechanics of fragmentation events; i.e., fragment size, number, and velocity distribution impact the capability to model and analyze the debris environment. Fragmentation events have multiple possible causes and may vary widely in intensity. Direct data from simulations of these processes is quite limited. In the analysis supporting the current model, these limitations were overcome by tuning the fragmentation models so that the historical fragmentation record reproduced the current environment. This approach provides the “best estimate” fragmentation models for the analysis, but it is very limiting in the sense that there is no independent check of the analysis. Since there are only recent measurements of the small fragment environment, there is no second point to check the analysis against. The associated uncertainty has been included within the 2p factor described above.

Assumption 4 is necessary because there are no measurements of debris smaller than 2 cm at other than in the 500 to 600 km altitude range, and because poor knowledge of the fragment velocity distributions (and computer run–time limitations) make it impractical to model small fragments in highly elliptical orbits. Analysis of these limitations indicates that the actual flux of small material could trend either above or below the large object distribution with altitude, depending upon the assumptions used. The model presented here assumes that the distribution with altitude for the small material matches the catalog distribution. The actual amount that these fluxes differ could be as high as a factor from 5 to 0.2 for every 200 km away from the 500 km altitude. The distribution

with respect to altitude is also assumed to be smooth. Actually, the U.S. Space Command data (sizes larger than 10 cm) gives fluxes at 800 km and 1000 km which approach the level predicted by the recommended flux model, as shown in Figure 8.2.5.2–1, not allowing for the correction factor from the GEODSS telescope study.

With respect to assumption 5, the possible variance of solar activity can be well defined based on the historical record. A high solar cycle will increase the depletion rate for debris in low altitude orbits, compared to a mean or low cycle, but prediction of the solar activity level beyond about one year is highly uncertain. Table 4.3–1 provides profiles of maximum and minimum solar activity, and these values may be used in equation 8.2.2,1 to estimate the range of variation.

An important short term factor which is not included in the model and thus contributes an additional uncertainty, is the flux arising from the intentional or inadvertent fragmentation of a satellite in an orbit at or near Space Station operating altitudes. In the region of the breakup, an enhanced flux may be apparent for a considerable period of time, depending upon the altitude of the breakup, and the size and velocity distribution of the debris. Analysis and modeling of various scenarios indicate that such an event would probably cause increases in the flux environment by factors of a few tens of percent for a year or more, although a factor of 4 may be possible as an extreme worst case.

8.2.5.3 UNCERTAINTIES IN DIRECTION, VELOCITY DISTRIBUTION, AND DENSITY

The fact that orbital debris objects are not in exactly circular orbits will introduce a small error in direction. As a result of the currently small eccentricities of debris orbits, the actual directions of impacts are within 1° for most velocities derived from section 8.2.4. For velocities less than 2 km/s, the uncertainty is much larger with a significant fraction being more than 20º from the direction derived from section 8.2.4. These errors in direction can be in the local horizontal plane, or they can appear as direction errors above or below this plane.

Uncertainty in the distribution of debris orbit inclinations leads to an uncertainty in the velocity distribution which can affect penetration analysis. Since inclinations are only known for large (catalogued) debris, the small fragments may have a different distribution, or the distribution may change with time as a result of orbit selection and fragmentation events. These considerations imply that the slow fraction of the population, i.e., the fraction of debris objects with a relative speed less than 5 km/s with respect to the Station, could shift or be in error by a factor from 0.5 to 3.

The expression for debris density given in section 8.2.3 for objects larger than 0.5 cm has been verified by direct measurements of actual objects, studies of orbit decay, and fragmentation experiments. Thus, it is believed to be a good representation of the mean density of the debris population (within a factor of 0.5 to 2), especially for sizes above 30

cm. However, it represents the mean of a broad distribution; the density of individual objects can vary widely.

For small fragments the density issue is more difficult because information is extremely scant. To illustrate the problem, consider the following materials density profile based on a summary review of Space Shuttle materials usage (neglecting tiles):

ESTIMATED VOLUME FRACTION	SPECIFIC GRAVITY	REPRESENTATIVE MATERIALS
0.65	2.8	Aluminum, Glass
0.15	1.8	Epoxy–glass, Rubber
0.05	4.5	Titanium
0.15	7.8 to 8.9	Copper, Steel

One might expect this would be typical of many spacecraft, but it may underestimate the fraction of dense materials for several reasons. First, many objects involved in fragmentation events are believed to have had a higher fraction of dense materials used in their construction. The Delta second stages, for example, contain about 70 percent steel, 20 percent aluminum, and 10 percent titanium. Second, low density objects are more affected by drag and thus decay from orbit more rapidly. However, fragment shape is also an important determinant of effective density. The thickness of the Delta walls is between 0.2 and 0.5 cm, so fragments larger than this would be irregular in shape with an effective density less than that of steel. Since definitive studies have not been done, uncertainty bounds can not be defined at this time. For study purposes the recommended "heavy" distribution is: 10% (by volume) at 1.8, 50% at 2.8, 10% at 4.5, 30% at 8.9 g/cm^3. This gives a mean density of 4.7 g/cm^3 for solid spheres.

8.3 EVALUATION OF DIRECTIONALITY EFFECTS

The parameter k which appears in equation 8.0,1 is defined as the ratio of the flux against an oriented surface to the flux against a randomly tumbling surface. Introduction of the k factor allows application of the flux equation 8.2.2,1 to evaluate the expected number and probability of impacts on surfaces flying with fixed orientation, such as Space Station. Evaluation of penetration probability should be by numerical techniques which account for the directional dependence of both the penetration equations and the meteoroid and debris fluxes, although the k factor may be useful for quick approximations.

The value of k can theoretically range from 0 to 4; a value of 4 can only be achieved when a surface normal vector is oriented in the direction of a monodirectional flux. It depends on the orientation of the surface with respect to the Earth vertical and the spacecraft velocity vector. If the surface is randomly oriented, then k = 1.

Care must be taken in evaluating k factors and other directional effects because of the complex directional nature of the meteoroid and debris fluxes. Unlike most fluxes with which the engineer and physicist deals, the meteoroid and debris fluxes do not have a unique direction associated with them at any given point in space. Meteoroids are equally likely to appear from any direction (except where the Earth provides shielding) in a reference frame fixed with respect to the Earth; they tend to appear from the ram direction on an orbiting satellite. The relative velocity with respect to a randomly tumbling spacecraft is about 19 km/s. The approach for evaluating k for meteoroids will be similar to the approach for debris which is presented below. As an illustration of the expected effect, the ram to lee ratio of the number of impacts was found to be about 7 to 1 in preliminary analysis of Long Duration Experiment Facility data for constant particle size, or about 18 to 1 for constant crater size (Zook, 1990). It is expected that meteoroids were dominant in this case.

For orbital debris the directionality in a reference frame fixed with respect to the Station is defined by combining equations 8.2.4,2 and 8.2.4,4. That is, the directionality can be written as a function of velocity alone, so differential pseudo–vector fluxes can be defined in terms of the velocity distributions such that:

$$-\,d\mathbf{F}_{+}(v) = F\,\{\,(f'(v)/2)\,d\mathbf{v}_{+}\,\} \quad \text{and}$$
$$-\,d\mathbf{F}_{-}(v) = F\,\{\,(f'(v)/2)\,d\mathbf{v}_{-}\,\}, \qquad (8.3,1)$$

where $f'(v)$ is defined by equation 8.2.4,2 and the + and – subscripts are associated with the $+\alpha$ and $-\alpha$ angles of equation 8.2.4,4, i.e., the left and right lobes of the “butterfly” shaped debris distribution (symmetric about the direction of flight). Our sign convention is such that $d\mathbf{F}$ is positive in the minus $d\mathbf{v}$ direction. (See Figure 8.2.4–2.) By solving the problem of the flux against a sphere it can be shown that $F = 4\,F_r = F_c$, where F_r is defined by equation 8.2.2,1

To find the expected rate of impacts on a surface, A, flying with fixed orientation one must solve the following:

$$R(A) = \int_{v}\int_{A} dF_{+}(v)\cdot N_a\ da \;+\; \int_{v}\int_{A} dF_{-}(v)\cdot N_a\ da \qquad (8.3,2)$$

where $\mathbf{N_a}$ is the outward unit vector normal to the surface element da.

IMPORTANT: The limits on the surface integrals must be such that all of the surface where the dot product is positive is included, and portions where it is negative are excluded. [A negative dot product corresponds to flux leaving the surface.] The k factor for the surface A is simply:

$$k = \frac{R(A)}{A \; F_r}$$

Figures 8.3–1 and 8.3–2 illustrate k factors for a flat plate and a right circular cylinder at various orientations.

REFERENCES:

Grun, E., H. A. Zook, H. Fectig, and R. H. Giese; "Collisional Balance of the Meteoritic Complex", Icarus **62**, 244–272, 1985.

Kessler, Donald J., Robert C. Reynolds and Phillip D. Anz–Meador, "Orbital Debris Environment for Spacecraft Designed to Operate in Low Earth Orbit", NASA TM 100471, April, 1989.

Zook, H. A., "Flux vs Direction of Impacts on LDEF by Meteoroids and Orbital Debris", Proceedings of the 21st Lunar and Planetary Science Conference, pp 1385–1386, 1990.

Zook, H. A., "The State of Meteoritic Material on the Moon", Proceedings of the 6th Lunar Science Conference, pp 1653–1672, 1975.

TABLE 8.2.5.1–1 UNCERTAINTIES AND ACCURACY LIMITATIONS (PAGE 1 OF 2)

UNCERTAINTY IN CURRENT ENVIRONMENT (INTERCEPT SHIFT)

	TREATMENT	"90 % CONFIDENCE"	NOTES
FLUX MEASUREMENTS (d>10 cm)	BEST EST	1.5 to 0.5 x (1988 FLUX)	
FLUX MEASUREMENTS (0.05 cm < d < 10 cm)	BEST EST	3 to 0.33 x (1988 FLUX) IN THIS SIZE RANGE	DUE TO STATISTICAL & MEASUREMENT LIMITATIONS IN PORTIONS OF RANGE. DATA MISSING (INTERPOLATION USED) IN REST OF RANGE
FLUX MEASUREMENTS (d < 0.05 cm)	BEST EST	2 to 0.5 x (1988 FLUX) IN THIS SIZE RANGE	
ALTITUDE DISTRIBUTION (d < 10 cm)	BEST EST	5 to 0.2 x (1988 FLUX) PER 200 km AWAY FROM 500 km	DUE TO DIFFICULTY IN DETERMINING FLUX IN HIGHLY ELLIPTICAL ORBITS.
ALTITUDE DISTRIBUTION (d ≥ 10 cm)	SMOOTHED BEST EST	2 to 0.5 x (1988 FLUX) SEE FIGURE 8.2.5.2–1	UNCERTAINTY IS SOMEWHAT WORSE IN 800 AND 1000 km REGIONS
DEBRIS DENSITY (d < 1 cm)	SIMPLIFIED BEST EST	0.10 @ 1.8 / 0.5 @ 2.8 0.10 @ 4.5 / 0.3 @ 8.9	ESTIMATED TYPICAL "HEAVY" DISTRIBUTION. INSUFFICIENT DATA TO DEVELOP A TRUE UNCERTAINTY LIMIT ESTIMATE.
DEBRIS DENSITY (d > 1 cm)	SIMPLIFIED BEST EST	2 to 0.5 MEAN DENSITY	MEAN VALUES ARE FAIRLY WELL DEFINED BUT NUMBER VS. DENSITY DISTRIBUTION IS BROAD.
DEBRIS SHAPE	SIMPLIFIED NON–CONSERV.		SPHERICAL SHAPE IS ASSUMED, ACTUAL DEBRIS WILL BE IRREGULAR.
VELOCITY DISTRIBUTION, FRACTION < 5 km/s	BEST EST	0.5 to 3x (SLOW FRACTION)	DISTRIBUTION OF ORBIT INCLINATIONS COULD BE IN ERROR OR CHANGE WITH TIME.

TABLE 8.2.5.1–1 UNCERTAINTIES AND ACCURACY LIMITATIONS (PAGE 1 OF 2)

UNCERTAINTY IN TREND PROJECTION (SLOPE SHIFT)

	TREATMENT	"90 % CONFIDENCE"	NOTES
LAUNCH RATE	BEST EST	p = 0.04 to "comp p" = 0.1 q = 0 to 2p	"comp p" IMPLIES $g_2 = (1 \pm p)^{(t-1988)}$. WORST CASE ASSUMES COMBINED EFFECT OF INCREASED TRAFFIC AND INCREASED USE OF LEO ABOVE 400 km
ORBIT USE PROFILE	BEST EST		
FRAGMENTATION RATE	BEST EST	q = 0 to 0.10	ASSUMING NO CHANGES IN PROJECTED LAUNCH RATE AND ORBIT USE PROFILE
FRAGMENTATION MECHANICS	BEST EST		
STATISTICAL VARIATION OF FRAGMENTATIONS	BEST EST	0.5 to 1.5 x (CURRENT FLUX)	
SOLAR ACTIVITY	BEST EST	SUBSTITUTE "MAX"&"MIN" s VALUES FROM TABLE 4.3–1	MODEL TENDS TO OVERESTIMATE VARIATION WITH SOLAR CYCLE, SO THESE WOULD BE EXTREME LIMITS
"LOCAL" FRAGMENTATION EVENTS	NON–CONSERV.	+ 4 x (1988 FLUX) FOR 1 YEAR	DIFFICULT TO ASSESS, DEPENDS STRONGLY ON TYPE OF EVENT AND PROXIMITY TO STATION ORBIT. IGNORED IN CURRENT MODEL.

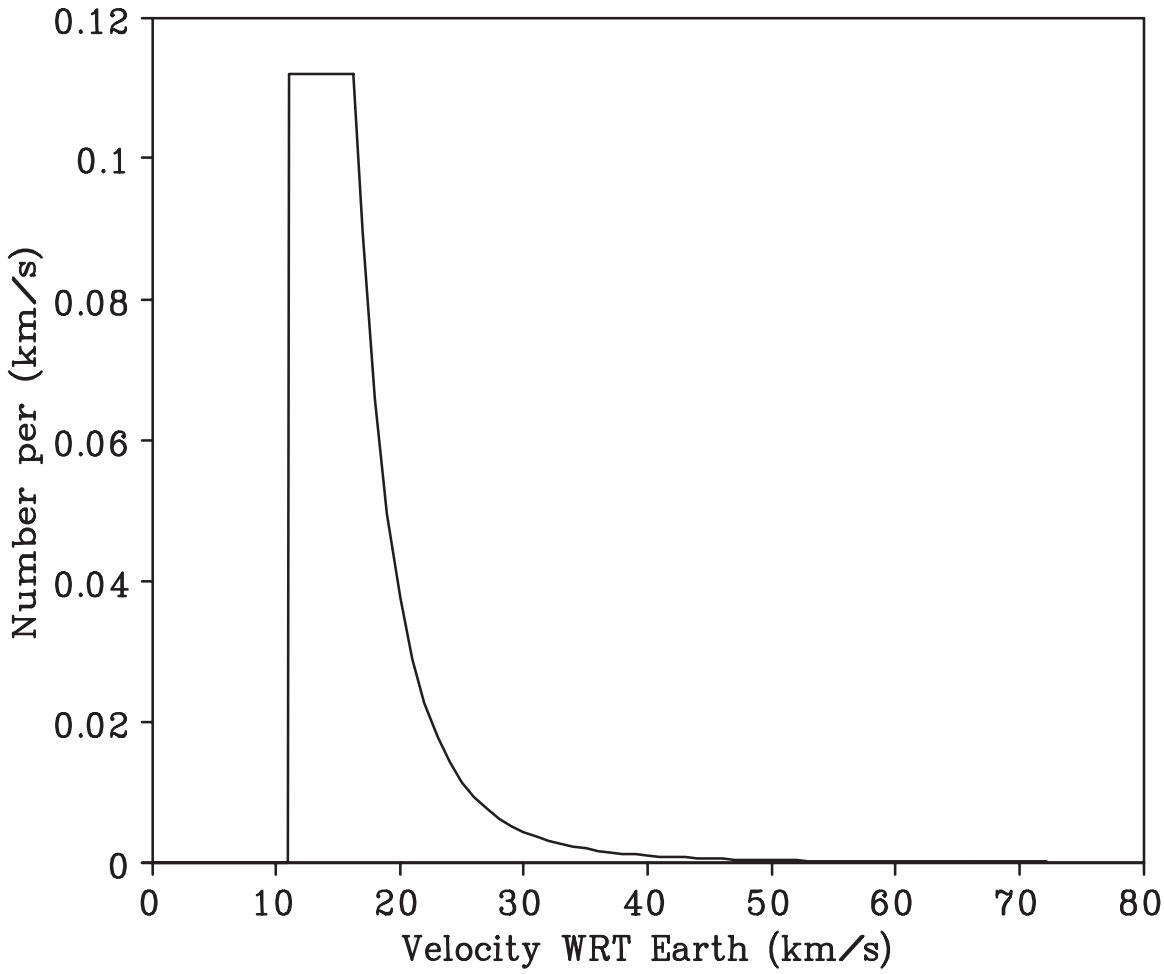

FIGURE 8.1–1 NORMALIZED METEOROID VELOCITY DISTRIBUTION FROM EQUATION 8.1,1

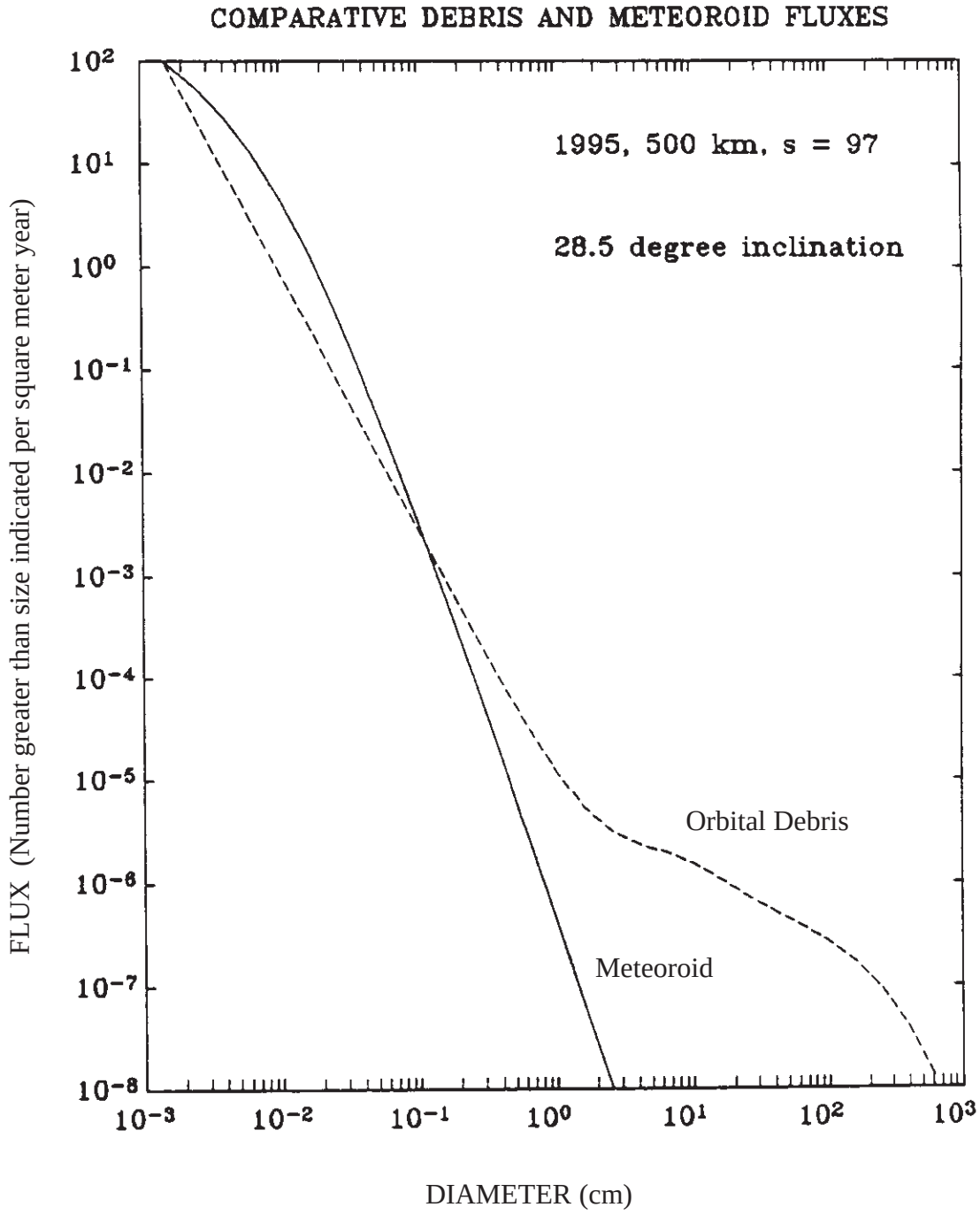

FIGURE 8.1–2 COMPARISON OF METEOROID AND ORBITAL DEBRIS FLUXES, Fr, AS A FUNCTION OF SIZE.

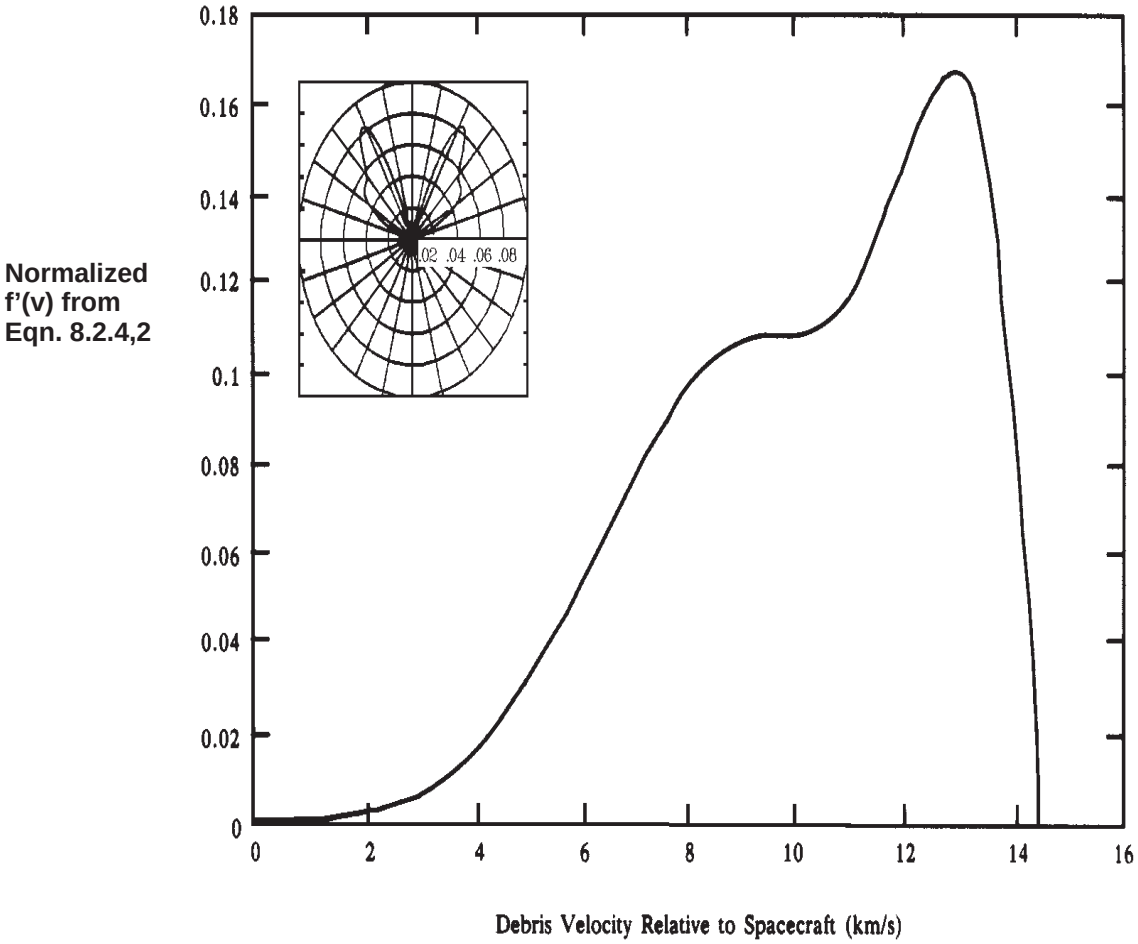

FIGURE 8.2.4–1 NORMALIZED COLLISION VELOCITY DISTRIBUTION AS FUNCTION OF THE DEBRIS VELOCITY FOR A SPACECRAFT WITH AN ORBITAL INCLINATION OF 28.5 DEGREES.

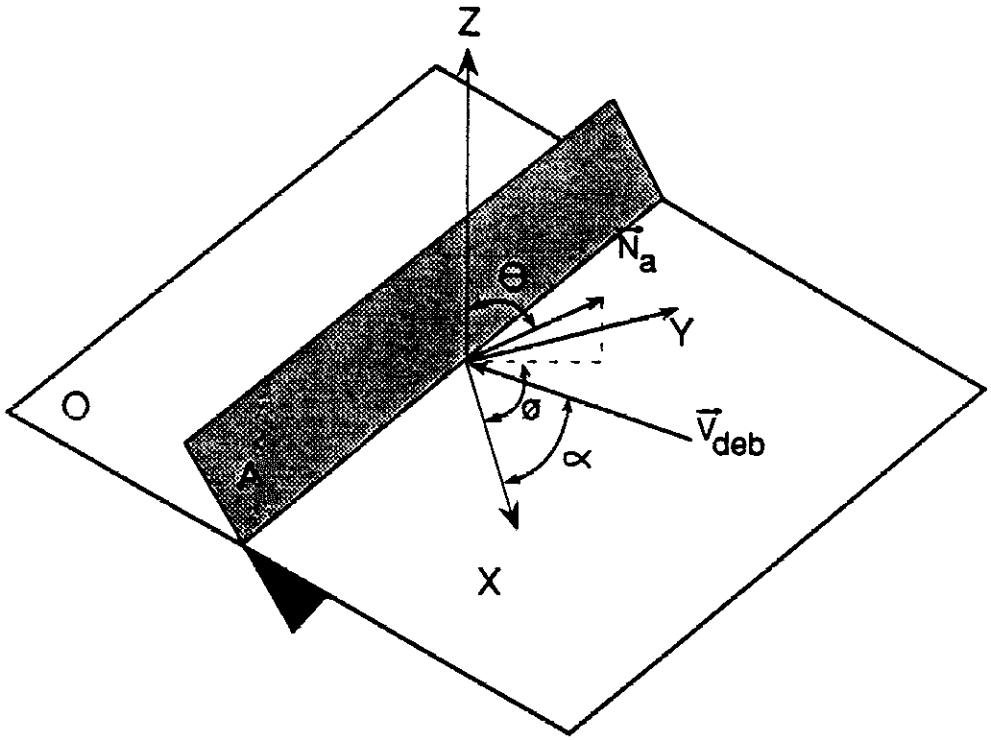

DEFINITIONS:

Plane A represents a surface of the spacecraft.

$\mathbf{N}_a$ is the unit vector normal to the plane A.

x is the direction of travel of the spacecraft.

$\mathbf{V}_{deb}$ is the debris velocity relative to the spacecraft.

O is the tangent plane (horizontal) to the spacecraft's orbit.

A right–handed coordinate system (positive x, y, z, is defined in plane O as:

x: direction of spacecraft travel

y: 90 degrees from **x** and in plane O (Port direction)

z: Earth vertical (up)

ANGLES:

α is the angle between **x** and $\mathbf{V}_{deb}$

θ is the zenith of $\mathbf{N}_a$ with respect to the Z axis in this reference frame.

ϕ is the azimuth of $\mathbf{N}_a$ with respect to the spacecraft direction of travel.

FIGURE 8.2.4–2 ORBITAL DEBRIS REFERENCE FRAME

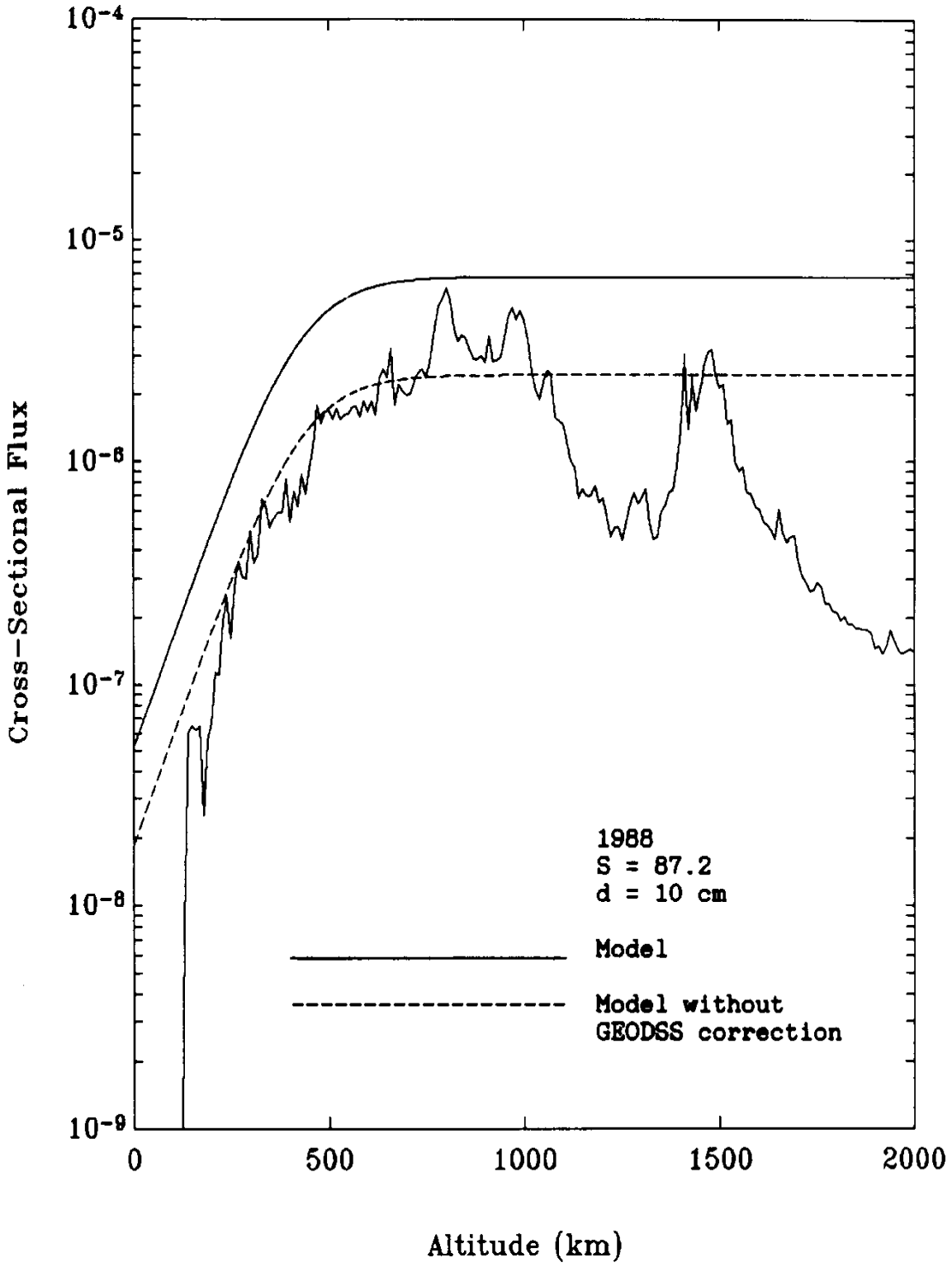

FIGURE 8.2.5.2–1 COMPARISON OF MODEL FLUX, Fc, WITH CATALOG FLUX NOT CORRECTED FOR GEODSS RESULTS.

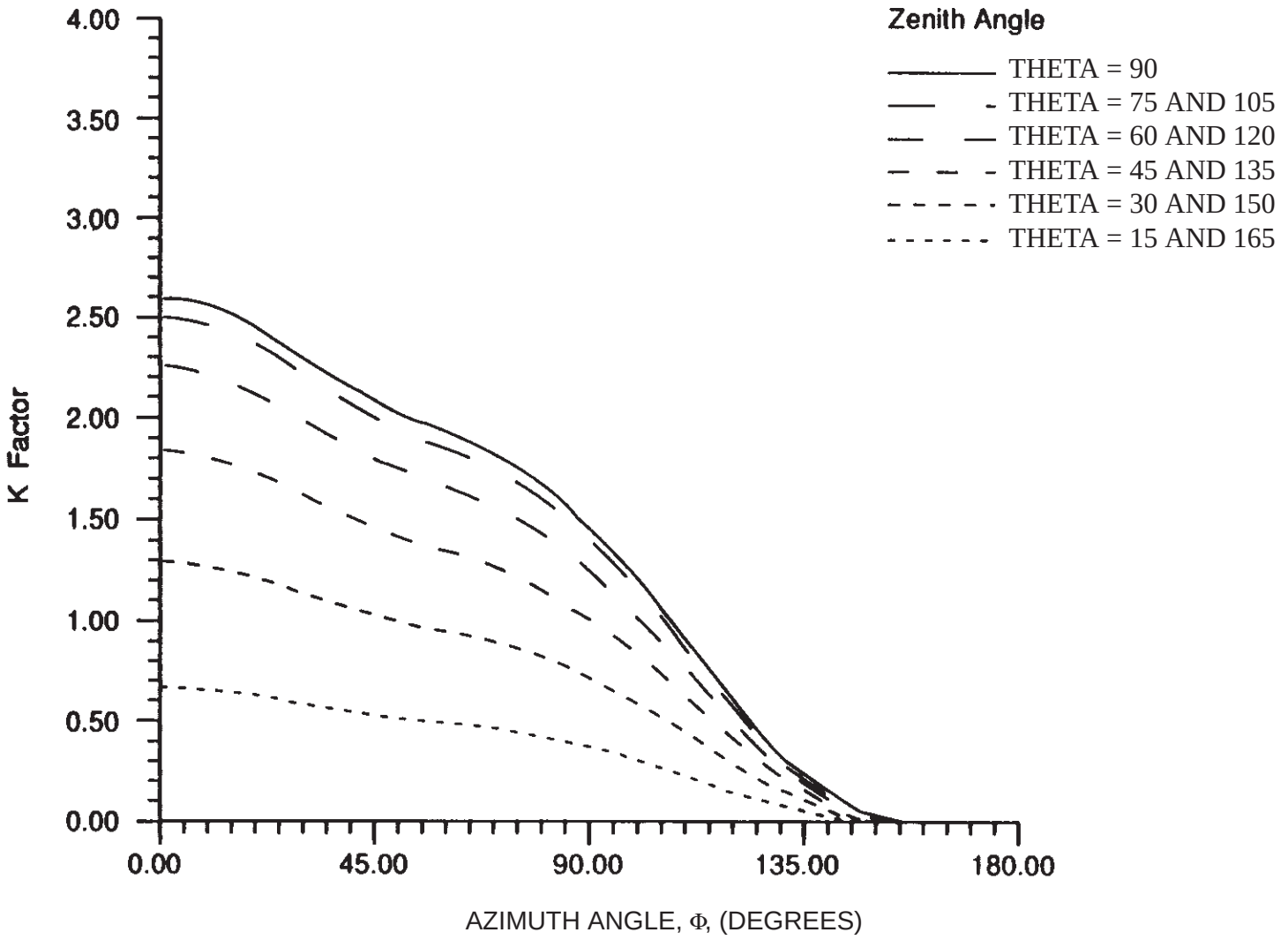

FIGURE 8.3–1 “K” FACTOR FOR SINGLE SIDED FLAT PLATES

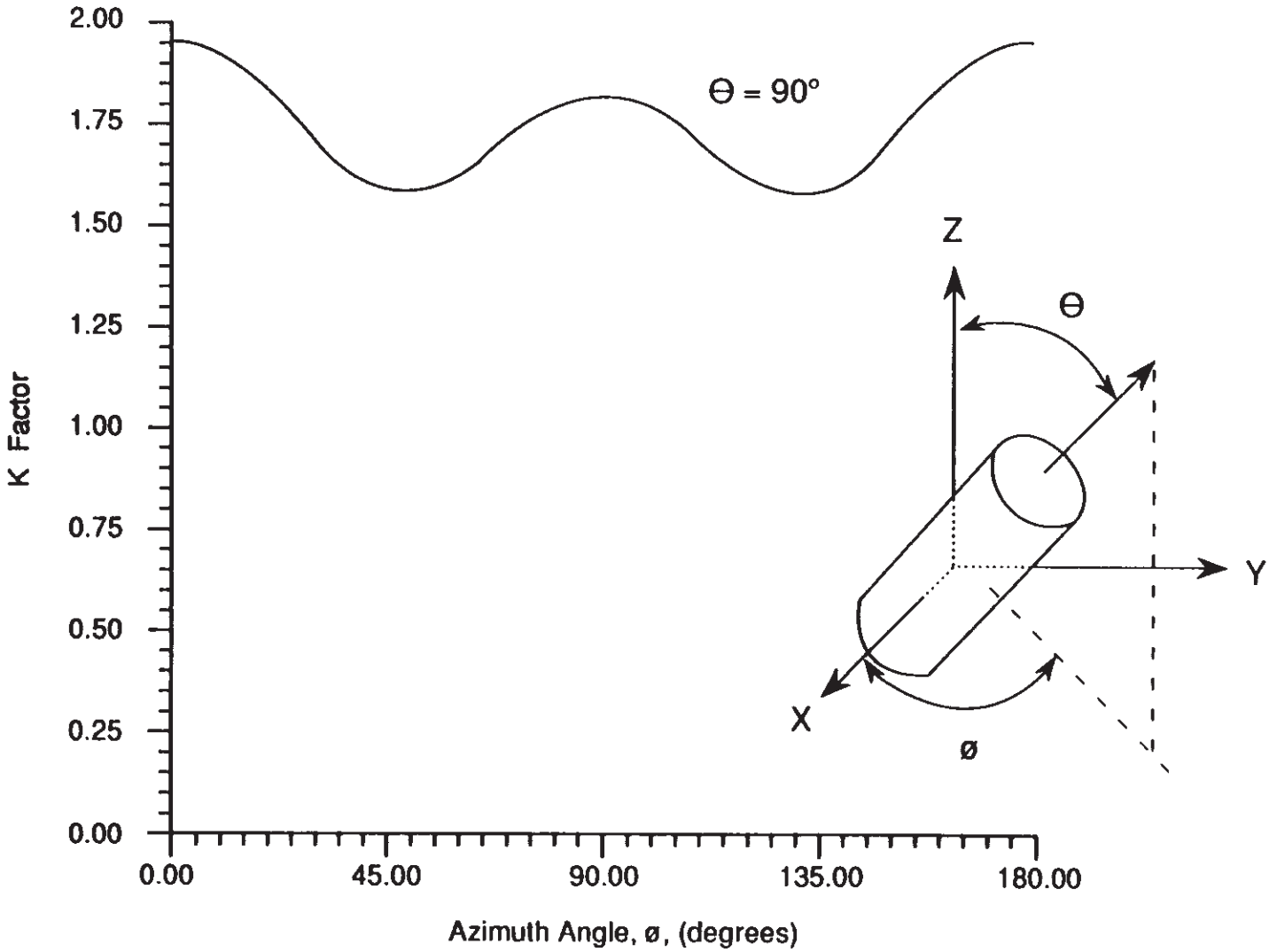

FIGURE 8.3–2 "K" FACTOR FOR A RIGHT CIRCULAR CYLINDER, LENGTH TO DIAMETER RATIO = 3.1, θ = 90°.

9.0 NATURAL MAGNETIC FIELD

As discussed in previous sections, the Earth has a magnetic field which greatly affects the environment in the Low Earth Orbit (LEO) region. The magnetic field traps charged particles (discussed in paragraphs 5.0 and 6.0) and deflects low–energy cosmic rays. The field is basically a dipole field, but the magnetic axis is not coincident with the rotation axis. The north pole of the magnetic field is rotated 11.5 degrees along the 69 west longitude line from the rotational north pole. The strength of the dipole results in a field strength at the Earth's surface of approximately 0.3 gauss at the equator and 0.6 gauss at the poles. The magnetic field direction at the equator is horizontal pointing north and at the magnetic north pole is pointing down into the Earth. Beyond an altitude of approximately 2000 kilometers, strong currents in the magnetosphere cause deviations from the near–Earth field.

The particle L–shell is most simply defined for a dipole field like the Earth's by the equation for a magnetic field line

$$r = L\, R_E \cos^2\lambda \qquad (9.0,1)$$

where λ is the magnetic latitude, r the radial distance to the L shell, and R_E the radius of the Earth. Thus, the L value of a field line is its distance in the magnetic equatorial plane from the center of the Earth expressed in Earth radii. The L–shell is a surface of revolution of this line about the dipole axis.

Unlike most Earth/Sun parameters which remain constant for hundreds of years, the magnetic field strength changes significantly on the scale of five to ten years. At present, the magnetic field strength is decreasing at approximately 0.1 percent per year. Thus, it is important to use a recent version of the model to correctly determine the magnetic field. Note, however, that as mentioned in paragraph 6.0 of this document, the current magnetic field (IGRF 1985) should not be used to calculate trapped radiation with the AP8 and AE8 radiation models because they do not correctly account for the effect of the atmosphere at SSPE altitudes.

In addition to the general decrease in the magnetic field strength, geomagnetic storms caused by solar activity can change the magnetic field by hundreds of gamma [1 gamma(Γ) is 10^{-5} gauss].

The magnetic field can be accurately represented using a spherical harmonic expansion. The expansion in terms of the Earth's rotational coordinate system (i.e., normal latitude, longitude) requires more terms than a simple dipole because the axes of the coordinate system are not coincident with the axes of the field. However, this coordinate system is

so familiar that it is the usual choice. The specification is given in terms of the magnetic potential, U and the field is derived from the potential by taking the negative gradient (which is the vector derivative):

$$\vec{B} = -\vec{\nabla} U \tag{9.0,2}$$

In particular:

$$B_{north} = (1/r)\ dU/d\theta \tag{9.0,3}$$

$$B_{east} = [-1/(r \sin\theta)]\ dU/d\phi \tag{9.0,4}$$

$$B_{down} = dU/dr \tag{9.0,5}$$

where

U = magnetic potential

r, θ, ϕ are the spherical coordinates

down means towards the center of the Earth.

Given that representation, the potential is expressed as Schmidt normalized Legendre polynomials with the following form:

$$U = R_E \sum_{n=1}^{\infty} \sum_{m=0}^{n} P_n^m (\cos\theta) (R_E/r)^{n+1} [g_n^m \cos(m\phi) + h_n^m \sin(m\phi)] \tag{9.0,6}$$

where

θ = colatitude (i.e., measured from the pole)

ϕ = east longitude

R_E = Earth radius = (6371.2 km)

r = radial distance

P_n^m = Schmidt–normalized associated Legendre polynomials

g_n^m and h_n^m = Schmidt–normalized coefficients.

The Schmidt–normalized Legendre polynomials are related to the normal associated Legendre polynomials as follows:

$$P_n^m = [\ \varepsilon_m\ (n-m)!/(n+m)!\ ]^{1/2} P_{nm} \tag{9.0,7}$$

where

P_{nm} = regular associated Legendre polynomial

$$\varepsilon_m = \begin{cases} 2 \text{ for m not } 0 \\ 1 \text{ if m } = 0 \end{cases} \tag{9.0,8}$$

Given that formalism, the coefficients g and h can be stated. Note that the h coefficient for m=0 is not stated because the sine function of 0 degrees is zero. The coefficients are given in units of gamma (Γ) which is 1.0E–5 gauss. Note also that the value of each coefficient depends on the radius of the Earth, so the stated radius (6371.2 kilometers) must be used with these coefficients. The coefficients, according to the current International Geomagnetic Reference Field (IGRF) 1991, are listed in Table 9.0–1, and Schmidt coefficients are listed in Table 9.0–2.

Since the polynomials P_n^m are of order unity, these terms will represent the field to approximately one percent in the worst case. The complete model has been calculated to degree and order 10 which is more accurate. Computer programs for determining the field values are available from the Space Station Program Office, Johnson Space Center, Houston, Texas.

TABLE 9.0–1 SPHERICAL HARMONIC COEFFICIENTS OF THE INTERNATIONAL GEOMAGNETIC REFERENCE FIELD (IGRF) 1991* (PAGE 1 OF 3)*

n	m	g_n^m	h_n	gt^mn	ht_n
1	0	–29775	0	18	0
1	1	–1851	5411	11	–16
2	0	–2136	0	–13	0
2	1	3058	–2278	2	–16
2	2	1693	–380	0	–14
3	0	1315	0	3	0
3	1	–2240	–287	–7	4
3	2	1246	293	0	2
3	3	807	–348	–6	–11
4	0	939	0	1	0
4	1	782	248	1	3
4	2	324	–240	–7	2
4	3	–423	87	1	3
4	4	142	–299	–6	–1
5	0	–211	0	1	0
5	1	353	47	0	0
5	2	244	153	–2	1
5	3	–111	–154	–3	0
5	4	–166	–69	0	2
5	5	–37	98	2	0
6	0	61	0	1	0
6	1	64	–16	0	0
6	2	60	83	2	–1
6	3	–178	68	1	0
6	4	2	–52	0	–1
6	5	17	–2	0	1

*Langel et. al. 1991, also D.R. Barraclough (1987)

TABLE 9.0–1 SPHERICAL HARMONIC COEFFICIENTS OF THE INTERNATIONAL GEOMAGNETIC REFERENCE FIELD (IGRF) 1991* (PAGE 2 OF 3)*

n	m	g_n^m	h_n	$gt^m n$	ht_n
6	6	–96	27	1	1
7	0	77	0	1	0
7	1	–64	–81	–1	1
7	2	4	–27	0	0
7	3	28	1	1	1
7	4	1	20	2	–1
7	5	6	16	0	0
7	6	10	–23	0	0
7	7	0	–5	0	0
8	0	22	0	0	0
8	1	5	10	–1	1
8	2	–1	–20	0	0
8	3	–11	7	0	0
8	4	–12	–22	–1	0
8	5	4	12	0	0
8	6	4	11	0	–1
8	7	3	–16	–1	0
8	8	–6	–11	–1	1

*Langel et. al. 1991, also D.R. Barraclough (1987)

TABLE 9.0–1 SPHERICAL HARMONIC COEFFICIENTS OF THE INTERNATIONAL GEOMAGNETIC REFERENCE FIELD (IGRF) 1991* (PAGE 3 OF 3)*

n	m	h_n	h_n
9	0	4	0
9	1	10	–21
9	2	1	15
9	3	–12	10
9	4	9	–6
9	5	–4	–6
9	6	–1	9
9	7	7	+9
9	8	2	–7
9	9	–6	2
10	0	–4	0
10	1	–4	1
10	2	2	0
10	3	–5	3
10	4	–2	6
10	5	4	–4
10	6	3	0
10	7	1	–1
10	8	2	4
10	9	3	0
10	10	0	–6

*Langel et. al. 1991, also D.R. Barraclough (1987)

TABLE 9.0–2 SCHMIDT COEFFICIENTS

n	m	h_n	h_n
Dipole Terms			
1	0	–29988	
1	1	–1957	5606
Quadrupole Terms			
2	0	–1997	
2	1	3028	–2129
2	2	1662	–199
Octupole Terms			
3	0	1279	
3	1	–2181	–335
3	2	1251	271
3	3	833	–252

10.0 THERMAL, PRESSURE, AND PHYSICAL CONSTANTS

The physical constants provided in this section are generally accepted values for use in environmental analysis. They are listed for convenience and to provide consistency among the user of this document, especially when the results are carried forward into other analyses of system design or performance. In a few instances, the models baselined elsewhere in this document were developed using alternate values for some of these constants. These cases have been noted in the model description. The alternate values should be used only with the specific model to assure accuracy of the model results. Elsewhere, the values provided here should be given preference.

10.1 SUN–EARTH CONSTANTS

Sun Earth physical constants are listed in Table 10.1–1.

10.2 PRESSURE PARAMETERS IN ORBIT

Estimates of the atmospheric pressure at orbital altitudes are provided in Table 10.2–1. For applications where precision values are requried the pressure shoudl be calculated for the specific circumstance using the MET model. (See paragraph 4.5.)

10.3 THERMAL ENVIRONMENT

10.3.1 GENERAL DISCUSSION

The Space Station will reach an energy balance, receiving radiant thermal energy form three sources and reflecting and radiating it out to the cold sink of space (3 Kevin). The three primary sources are the incoming solar radiation (described by Kelvin). The three primary sources are the incoming solar radiation (described by the solar constant), reflected solar energy (albedo) and outgoing longwave radiation emitted by the earth and atmosphere (OLR). If one considers the earth and its atmosphere as a whole and averages over long time periods, the incoming solar energy and outgoing longwave radiant energy are essentially in balance; the earth/atmosphere is very nearly in radiative equilibrium with the sun. However, it is not in balance everywhere on the globe and there are important variations with respect to local time, geography, and atmospheric conditions. A space vehicle’s motion with respect to the Earth results in its viewing only a ‘‘swath” across the full global thermal profile, so it sees these variations as functions of time constants of the hardware systems. Space Station, with an orbit inclination of 51.6 degrees, will see only the middle and low latitude portions of the globe. The data in this section has been tailored to provide a statistically correct description of this environment and its variations for this type of orbit.

10.3.1.1 SOLAR CONSTANT

The direct solar flux is the greatest source of heating for most spacecraft. The mean value of this solar flux at mean Earth–sun distance is termed the ‘‘solar constant”. Specifically, the solar constant is defined as the radiation that falls on a unit area of surface normal to the line from the sun, per unit time, outside the atmosphere, at one astronomical unit (the mean Earth – sun distance). In actuality, the incoming solar flux which impinges on an Earth orbiting spacecraft is not truly constant. There are tow factors influencing its variability. First, the amount of radiant energy that is emitted by the sun is known to vary throughout the 11 year solar cycle, and differs from cycle to cycle. The exact amount of this variation is still being studied, but it is estimated to be less than one percent. Second, the slightly elliptical orbit of maximum occurring at the winter solstice when the Earth – sun distance is a W/m^2 allows for the solar cycle variation and the measurement uncertainty. The variation with respect to Earth – sun distance must be added. It may be calculated by standard method dependent upon which season of the year is of interest to the user. Extreme values are listed in Table 10.3.1–1.

10.3.1.2 ALBEDO

The fraction of incident sunlight which is reflected off a planet is termed albedo. Albedo values typically are given as a fraction, but may also be given as a percent. This parameter gives a measure of the amount of solar energy which is reflected back to space. Therefore, albedo values are only applicable when a portion of the Earth–atmosphere system that is seen by the spacecraft is sunlit. Albedo values vary with solar zenith angle and care must be taken to correctly account for this effect, especially near the terminator. (See paragraph 10.3.2 below.) Albedo radiation has approximately the same spectral shape as the Sun’s spectrum which approximates a blackbody with a characteristic temperature of 5762K.

Albedo is highly variable across the globe and is dependent on the distribution of reflective properties of the surface and the amount and type of cloud cover. Albedo is generally highest over cloudy regions such as the Intertropical Convergence Zone, deserts, and ice and snow covered areas. If the sky is clear, the albedo over ocean areas in generally low. Albedo also increases as the solar zenith angle increases. Because of the snow and ice cover, decreasing solar elevation angle, and increasing cloud coverage, albedo tends to increase slightly with latitude if viewed on a large scale.

10.3.1.3 OUTGOING LONGWAVE RADIATION

A spacecraft’s thermal environment is not only made up of direct solar radiation and reflected solar radiation, but it also includes the outgoing longwave radiation (OLR) emitted by the Earth itself. This Earth emitted thermal radiation has a spectrum of a black body with a characteristic temperature of 288K.

ORL is not constant over the globe but the localized variations are much less severe than for albedo. Outgoing longwave radiation is principally influenced by the temperature of the Earth's surface will emit more radiation than a colder area. On a large scale, highest values of OLR will occur in tropical regions (as these are the regions of the globe receiving the maximum solar heating) and will decrease with latitude. Increasing cloud cover tends to lower OLR by absorbing up willing radiation from the Earth's surface. The solar elevation angle may also affect OLR because of its influence on the temperature of the surface and lower atmosphere. Thus, there are diurnal and seasonal variations of outgoing longwave emission, as well. This diurnal variation is small over the oceans, but it may be important over continental regions, especially desert areas where it can amount to about 20 percent.

10.3.1.4 THE EARTH RADIATION BUDGET EXPERIMENT

The data used to define the Space Station thermal environment were collected by the Earth Radiation Budget Experiment (ERBE). ERBE began in the 1980's and is still ongoing. ERBE is a mutti–satellite experiment which has as its primary objective global data collection of such earth radiation budget parameters as incident sunlight, reflected sunlight (albedo) and outgoing longwave radiation (OLR). This experiment was selected because of its thorough coverage and its up–to–date information. The experiment consisted of three satellites, the low inclination Earth Radiation Budget Satellite (ERBS) and two NOAA sun–synchronous satellites. The data used here are from the active cavity, flat plate radiometers in the fixed, non–scanning, wide field–of–view mode. This type of instrument was chosen to most closely approximate the albedo and OLR variations a spacecraft surface would encounter. The data are available in three separate sets, daily averaged values (S–4), hourly averaged values (S–10) and the direct sixteen second instrument measurements along the ERBS or NOAA satellite trajectory (S–7). The S–4 and S–10 data products were inappropriate for this application, the averaging times are much too long compared to the thermal time constant of most Space Station systems. Therefore, the design criteria presented below are based on twenty–eight files, representing one month of sixteen section data each, of S–7 data. The measurements were made from November of 1984 through July of 1987, with all seasons represented.

10.3.2 THERMAL DESIGN ENVIRONMENT

10.3.2.1 TEMPORAL VARIATIONS

For Space Station or any satellite system of similar complexity, different portions of the hardware will have different thermal response times ranging from a few minutes to hours. To enable the analyst to model the thermal response of a particular system as simply as

possible, a running mean analysis was developed for the albedo and OLR variations as a vehicle will view them moving along its orbit track. The statistics are derived for a 51.6 degree inclination orbit and are adjusted to the top of the atmosphere (30 km). Running averages were computed for averaging times ranging from a few seconds to an hour and a half. Since these parameters vary systematically with latitude, corrections were included to account for the differences in orbit inclinations between Space Station and the ERBE satellites. Cumulative percentile statistics of the running means describe the low and high extremes, 1, 3, 5, 95, 97, and 99 percentile, and the expectation value (50 percentile) for each parameter as a function of averaging time periods along an orbit track. These statistics are presented in Table 10.3.1.1–1 and are illustrated by Figures 10.3.2.1–1 and 10.3.2.1–2.

Because some diurnal variation of OLR was expected, separate statistics for day and night and day combined were derived. However, the resulting distributions were essentially identical. Clearly the seasonal variations and other factors dominate the statistics and it is not necessary to specify separate day and night or solar zenith angel dependent distributions for OLR. This result is not surprising since ocean and moist tropical areas dominate the area viewed by the Space Station orbit.

As an example of the correct interpretation of this data, consider an 1800 second (30 minute) averaging time and the 50 percentile frequency of occurrence. From Table 10.3.2.1–1 the albedo is 0.20, the OLR is 241 W/m^2. This means that half the time the 1800 second running mean albedo (corrected to zero SZA and the top of the atmosphere) was less than 0.20, and half the time it was greater, for the entire data set of 28 monthly files corrected to a 51.6 degree inclination orbit. Likewise, 241 W/m^2 was the median of the 1800's running mean OLRs. A 95th percentile value means the respective running average was less than or equal to this value 95 percent of the time. The ‘‘low observed” and ‘‘high observed” values represent the extremes observed in this data set. One would expect that more extreme conditions occasionally occur in nature, but for engineering purposes these can be considered as estimated worst–case conditions.

The OLR and albedo statistics presented in Table 10.3.1.1–1 were derived from paired data, i.e., each OLR value had an associated albedo value measured simultaneously. The dependence of OLR on solar zenith angle was investigated on a sub–set of the data, and it was found that the variation is not significant for a 51.6 degree orbit. The OLR distributions for all times of day and night combined differ from the daylight only statistics presented here by only 0.5 percent.

10.3.2.2 SOLAR ZENITH ANGLE CORRECTION FOR ALBEDO

For a first approximation albedo may be assumed to be independent of the solar zenith angle; that is, the scattering is ‘‘Lambertian” or equal in all directions. This approximation has been assumed for most engineering applications in the past. However,

the data quality and the capability of current engineering analysis methods warrants an improved approach. For the Space Station orbit which sees all solar zenith angles, the correction is most significant for subsystems with short thermal time constraints, less than 10 minutes. Maximum albedo energy occurs at small zenith angles (near but not at local noon) when the correction factor is small. Thus, the correction is not important in determining extreme values, but it becomes very important in analysis of the temporal variations of the thermal environment. Orbital average solar zenith angles for a 51.6 degree inclination orbit are illustrated in Figure 10.3.2.2–1.

Treatment of this topic in the scientific literature is generally ‘‘scene specific”, e.g., it depends on the geographic features in the field of view, data which is not generally available to the design engineer, and the algorithms tested did not fully remove the zenith angle dependence form this data set. Therefore, a zenith angle correction was derived specific for this data set in a manner which is specifically matched to the analysis tools most commonly used for engineering analysis, TRASYS (Thermal Radiation Analysis System) and TSS (Thermal Synthesizer System).

The correction term was derived from four months of data restricted to the –30 to + 30 latitude band. It was verified by testing another four months of data and testing to wider latitude bands. It removes the solar zenith angle dependence to within $\pm$ 0.04. The correction is:

Albedo (SZA) = Albedo (SZA = 0) + Correction

Correction = [C4 $(SZA)^4$ = C3 $(SZA)^3$ = C2 $(SZA)^2$ = C1 (SZA)]

where SZA is the Solar Zenith Angle in degrees and the albedo is expressed as a fraction.

C4 = 4.9115 E–9,
C3 = +6.0372 E–8,
C2 = –2.1793 E–5,
C1 = +1.3798 E–3

Figure 10.3.2.2–2 illustrates the correction. This term must be added to the albedo from Figure 10.3.2.1–1 or from the correlation or benchmark results below.

10.3.2.3 CORRELATION ANALYSIS AND BENCHMARKING

Figures 10.3.2.3–1a through –1d show plots of the running mean albedo against the running mean OLR from simultaneous measurements. The two parameters are not strongly correlated in the sense that, for almost any value of one parameter, a substantial range of values is encountered for the other. Thus, for design applications the albedo and emitted thermal radiation may be considered as independent parameters, both of which vary across a range of values. The range is quite large for systems with short thermal time constants, and thus short averaging times along the swath, but as longer averaging times are considered the range narrows toward the mean for the region covered by the spacecraft.

In selecting benchmarks for design purposes, it should be remembered that the joint probability of occurrence for independent parameters is given by the product of the individual probabilities. For example, OLR values in excess of the 95th percentile value may be expected to occur in combination with albedos in excess of the median 0.025 of the time, e.g, (0.05) (0.50) = 0.025. Thus, 97.5 percent of the data would lie outside this region in this example.

TABLE 10.0–1 SUN–EARTH PHYSICAL CONSTANTS

Distance to the sun (one Astronomical unit by definition)	1.4959787 E8 km
Eccentricity of Orbit (Note 1)	= 0.0167295
Orbital Period (Sidereal) (Note 2)	= 365.25636 days
Radius of the Earth (equatorial)	= 6378.140 km
Mass of the Earth	= 5.977E24 kg
Earth Rotation Rate	= 0.72921E–4 (radians)/second
Gravitational Constant for the Earth (μ_E)	= 3.986012E14 N m^2/kg
Inclination of the Equator (Note 3)	= 23.45 degrees
Period of Rotation (Sidereal)	= 23.934 hours (86162.4 seconds)
Solar Radiation Pressure at 1 Astronomical Unit	9.02 E–6 N/m^2 (100% reflecting)

Notes:

1. The eccentricity gives the noncircular nature of an orbit. The maximum distance from the Sun is (1 + ecc) times the average radius; the minimum distance is (1 – ecc) times the average radius.
2. The sidereal period is measured with respect to the “fixed“ stars rather than with respect to the Sun.
4. The inclination of the equator is with respect to the Earth’s orbital plane.

CAUTION: These are accepted values for general use. However, the various gravitational and other models may have been developed using other values. When this is the case, the values associated with the model should be used.

TABLE 10.0–2 EARTH THERMAL AND PRESSURE PARAMETERS (PAGE 1 0F 2)

Ambient Pressure in Pascal, Torr in parenthesis (Note 1):

Minimum	Nominal	Maximum	Altitude (km)
1.8E–6 (1.4E–8)	8.8E–6 (6.6E–8)	4.8E–5 (3.6e–7)	300
1.7E–7 (1.3E–9)	1.5E–6 (1.1E–8)	1.5E–5 (1.1E–7)	400
3.6E–8 (2.7E–10)	3.1E–7 (2.3E–9)	5.7E–6 (4.3E–8)	500
1.6E–8 (1.2E–10)	8.3E–8 (6.2E–10)	2.4E–6 (1.8E–8)	600
4.2E–9 (3.2E–11)	7.5E–9 (5.6E–11)	1.3E–7 (9.8E–10)	1000
1.0E–11 (7.5E–14)			Geosynchronous

Notes:

1. Orbit average values of low and high pressure were estimated with the MET Model for a 51.6° inclination orbit, assuming the following input conditions:

   Low Pressure Case: (less than 0.2 percentile frequency of occurrence)

   F10B = 70, F10 = 70, a_p = 0, Ascending node = 150° (orbit intersects solar bulge), Date = July 30, (primary minimum of semiannual variation).

   High Pressure Case: (exceeds 99.99 percentile frequency of occurrence)

   F10B = 243, F10 = 273, a_p = 234, Ascending node = 255° (orbit intersects solar bulge), Date = Oct. 28, (primary maximum of semiannual variation).

   Nominal pressure values were taken from U. S. Standard Atmosphere 1976 (Anon. 1976). Geosynchronous pressure values were taken from Smith and West, 1982. To convert from Pascal to Torr multiply by 7.5E–3.

TABLE 10.3.1.1–1 THERMAL PARAMETERS FOR 51.6 DEGREE LOW EARTH ORBIT

Solar constant at 1 Astronomical Unit (1 AU = mean Earth – sun distance)	1371 $\pm$ 5 W/m^2
Maximum solar energy flux (winter solstice) (at Perihelion = 5 W/m^2 included)	1423 W/m^2
Minimum solar energy flux (summer solstice0 (at Aphelion, –5 W/m^2 included)	1321 W/m2
Characteristic blackbody temperature of solar spectrum {Albedo radiation has approximately the same spectrum, but it is highly variable depending on cloud cover and surface reflectivity)}	5762 K
Space sink temperature	3K (absolute)

Albedo: (top of the atmosphere, 30 km, and corrected to zero solar zenith angle)

Ave. Time(s	Lowest Observed	1%	3%	5%	50%	95%	97%	99%	Highest Observed
16	0.07	0.08	0.09	0.10	0.19	0.33	0.35	0.40	0.53
64	0.07	0.08	0.09	0.10	0.19	0.33	0.35	0.39	0.53
128	0.07	0.08	0.09	0.10	0.19	0.32	0.34	0.38	0.53
256	0.07	0.09	0.10	0.11	0.19	0.31	0.33	0.37	0.52
512	0.08	0.10	0.11	0.12	0.20	0.29	0.31	0.34	0.47
896	0.09	0.11	0..13	0.13	0.20	0.27	0.28	0.31	0.42
1344	0.11	0.13	0.14	0.14	0.20	0.26	0.27	0.29	0.39
1800	0.12	0.14	0.14	0.15	0.20	0.26	0.27	0.29	0.38
2688	0.12	0.14	0.15	0.15	0.20	0.25	0.26	0.28	0.35
3600	0.13	0.15	0.15	0.16	0.20	0.25	0.26	0.28	0.33
5400	0.14	0.15	0.16	0.16	0.20	0.24	0.25	0.27	0.33

Outgoing Longwave Radiation: (top of the atmosphere, 30 km, units are W/m^2)

Ave. Time(s	Lowest Observed*	1%	3%	5%	50%	95%	97%	99%	Highest Ob-served
16	153	177	189	195	242	284	291	307	349
64	154	178	189	196	242	284	291	307	348
128	156	180	191	197	242	283	290	306	347
256	162	185	195	201	242	281	287	303	342
512	176	195	204	208	241	275	280	294	332
896	189	204	211	214	241	269	274	283	317
1344	197	209	215	218	241	266	270	278	303
1800	199	212	217	220	241	265	269	276	296
2688	204	215	219	221	241	263	267	273	291
3600	206	217	221	223	241	262	265	273	286
5400	208	219	223	225	241	260	263	270	281
* Set at 0.04 percentile, eliminating a very few, unrealistically low data points.									

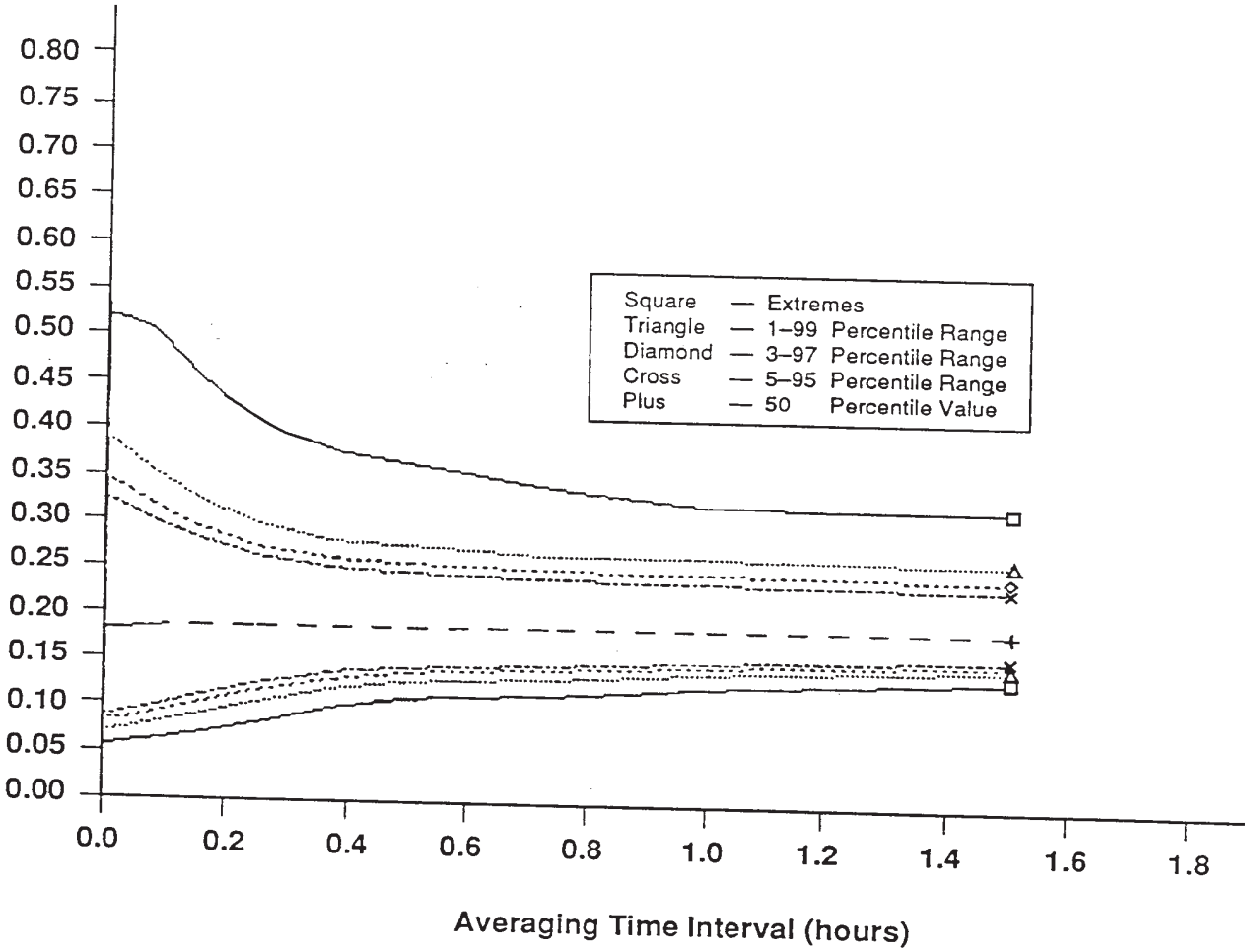

FIGURE 10.3.2.1–1 DISTRIBUTIONS OF RUNNING MEAN ALBEDOS FOR A 51.6° INCLINATION ORBIT

Data corrected to the top of the atmosphere (30 km) and zero solar zenith angle.

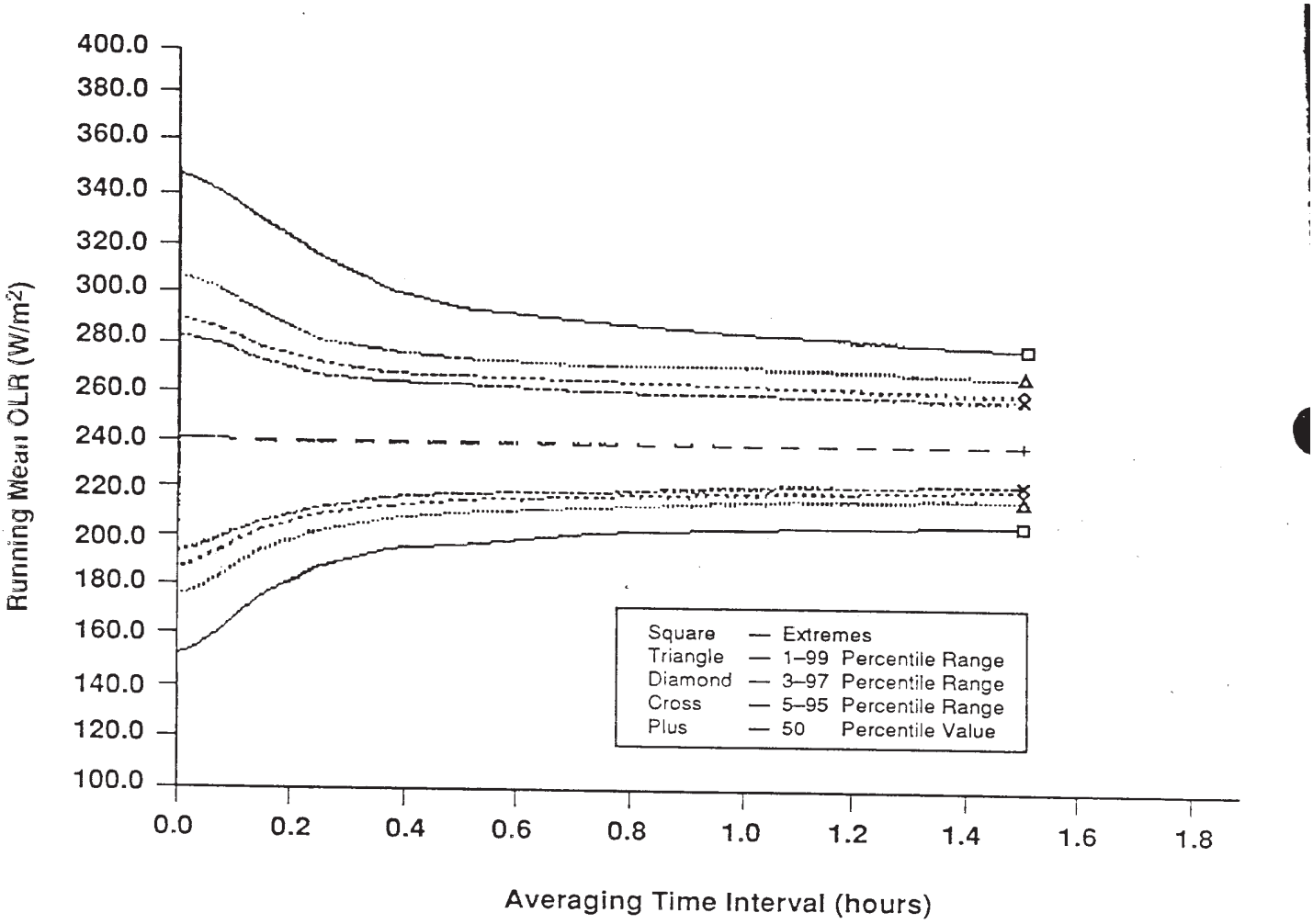

FIGURE 10.3.2.1–2 DISTRIBUTIONS OF RUNNING MEAN OUTGOING LONGWAVE RADIATION FOR A 51.6° INCLINATION ORBIT

Data referenced to the top of the atmosphere (30 km).

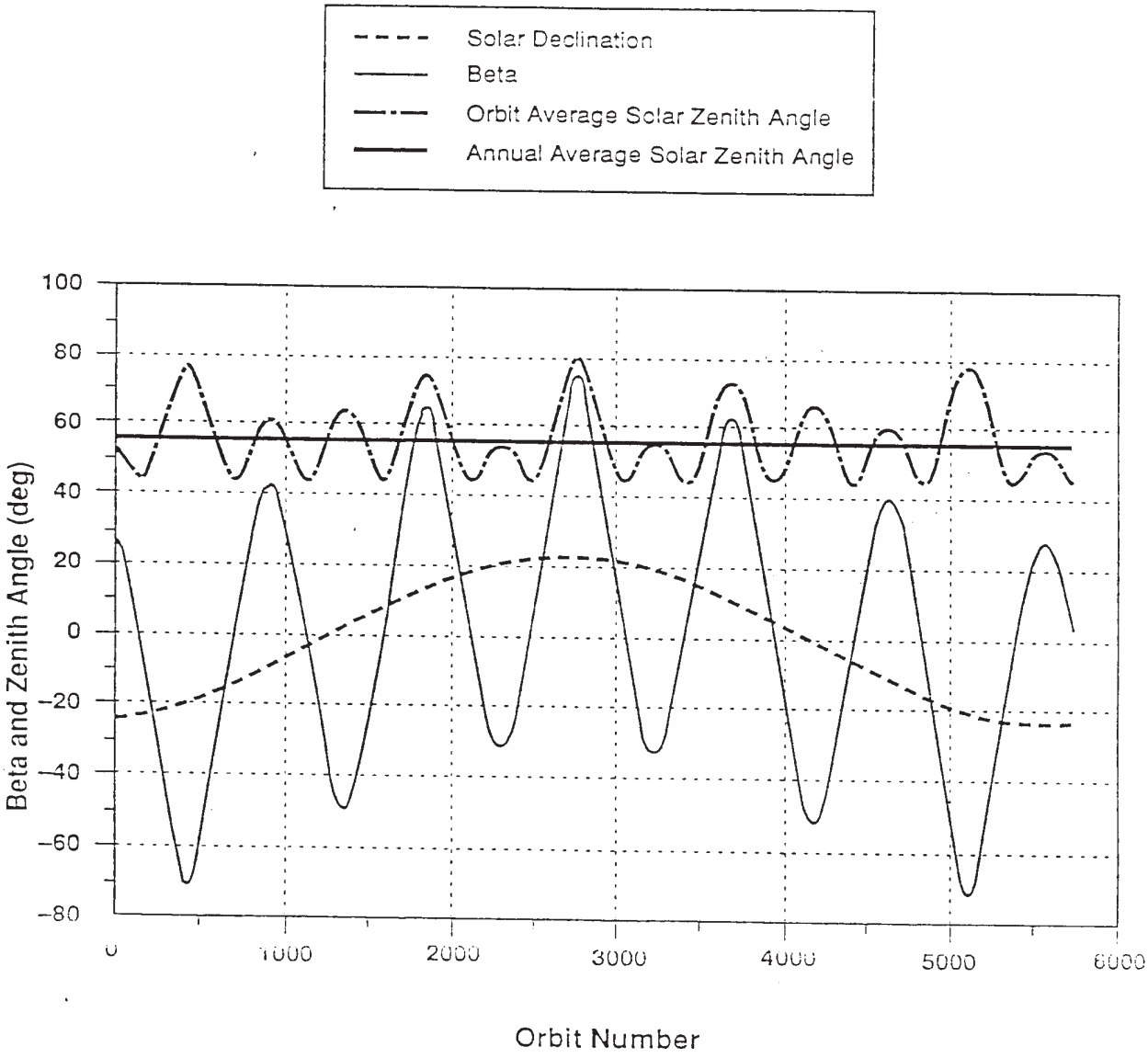

FIGURE 10.3.2.2–1 YEARLY VARIATION OF ORBIT AVERAGE SOLAR ZENITH ANGLE, BETA ANGLE, AND SOLAR DECLINATION ANGLE FOR A 51.6°INCLINATION ORBIT.

Annual average SZA is 56.29°. (Alt = 370 km, RAN = 0, ECC=0)

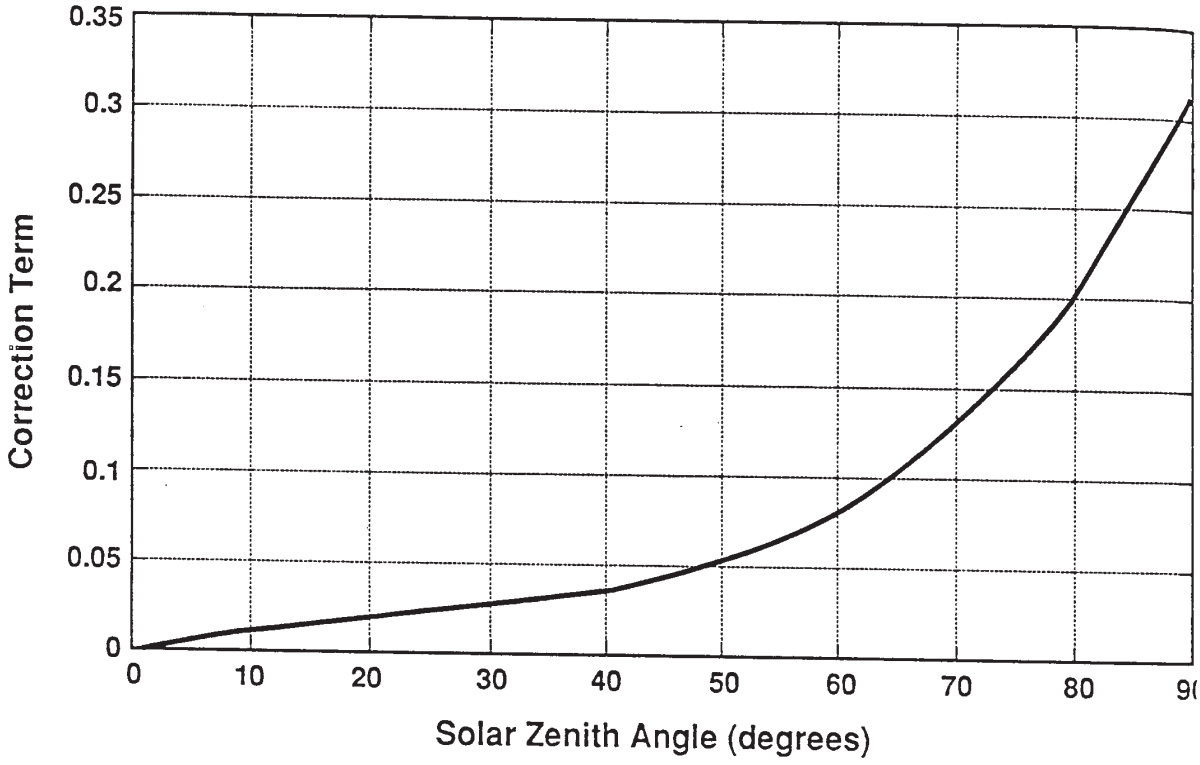

FIGURE 10.3.2.2–2 ALBEDO CORRECTION TERM

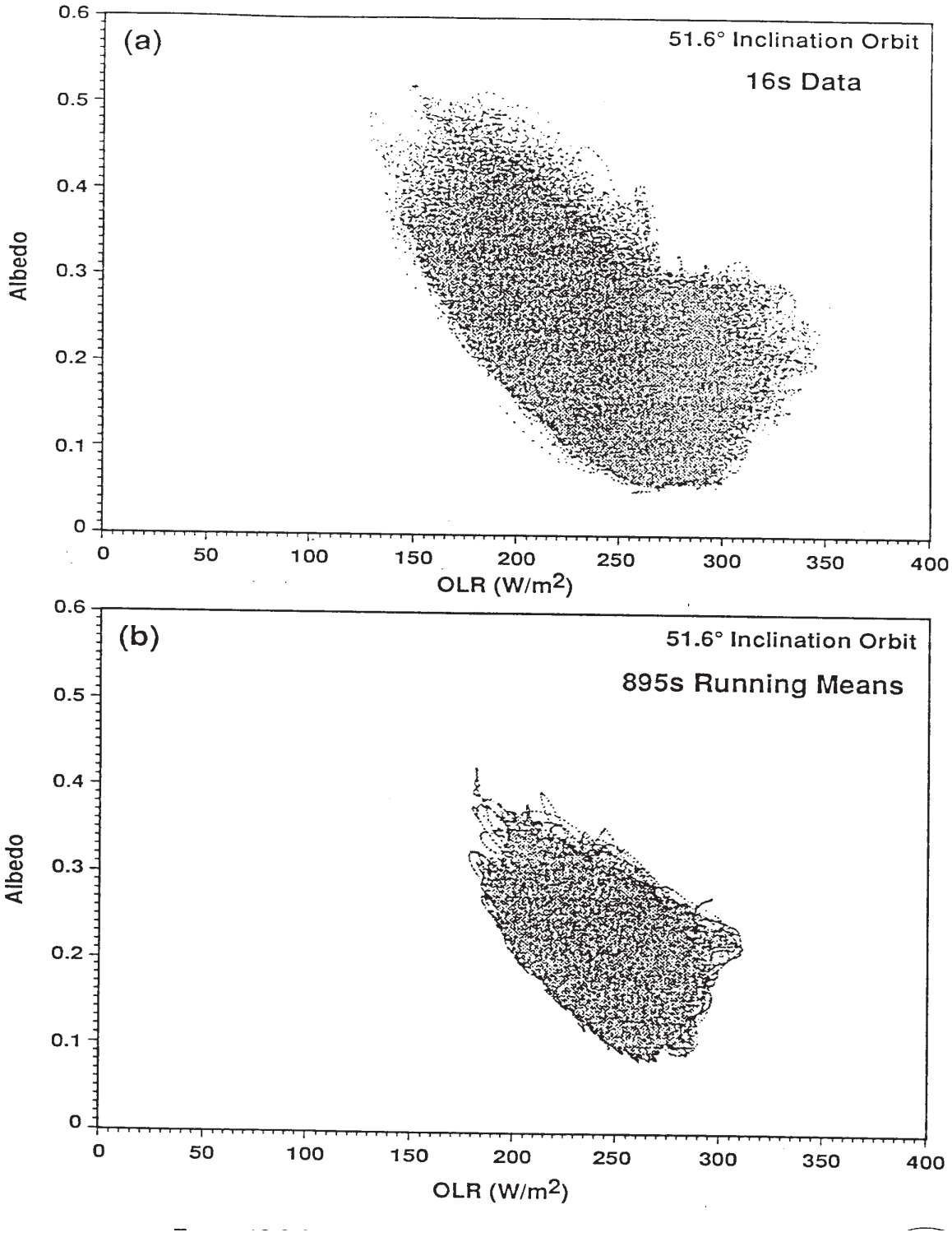

FIGURE 10.3.2.2–2 ALBEDO–OLR CORRELATED PAIRS

Albedo corrected to zero solar zenith angle.

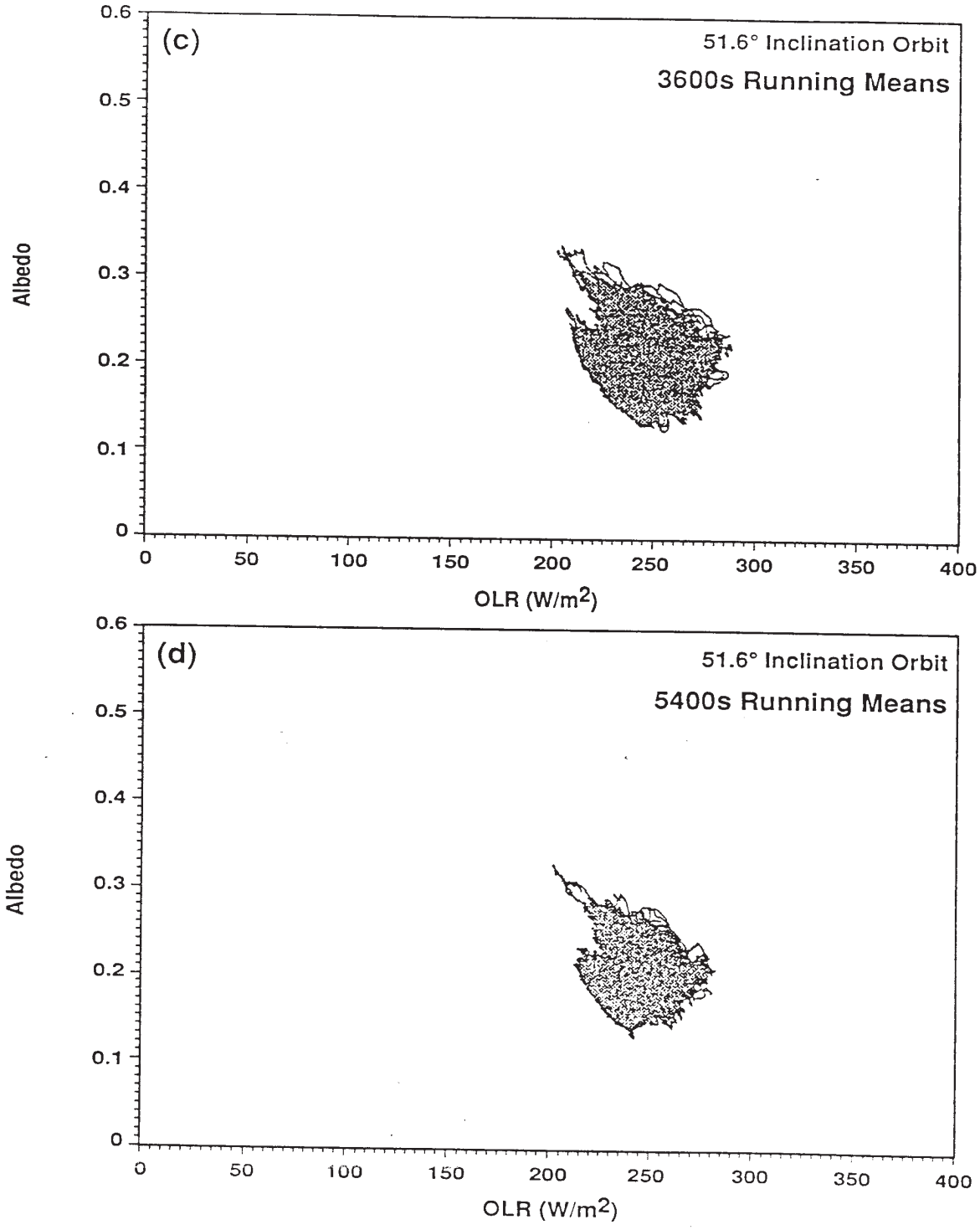

FIGURE 10.3.2.3–1 ALBEDO–OLR CORRELATED PAIRS

Albedo corrected to zero solar zenith angle.

11.0 GRAVITATIONAL FIELD

With the advent of Earth satellites, there has been a considerable advance in the accurate determination of the Earth's gravitational field. The current knowledge regarding the Earth's gravitational field has advanced far beyond the normal operational requirement. Adequate accuracy for determining most Space Station Program Element (SSPE) design values of gravitational interactions is obtained with the central inverse square field.

$$\vec{F} = -\frac{\mu_E\, m}{r^2}\,\hat{r} \qquad (11.0,1)$$

where:

$\vec{F}$ = vector force acting on a particle in Newtons;

m = mass of particle in kg;

μ_E = gravitational constant for the Earth

r = distance from the particle to the center of the Earth in meters;

$\hat{r}$ = unit vector from the center of the Earth to the particle, dimensionless.

The above central force model accurately represents the gravitational field to approximately 0.1 percent. If this accuracy is insufficient, a more detailed model of the gravitational field can be used that accounts for the non–uniform mass distribution within the Earth. This model gives the gravitational potential, V, to an accuracy of approximately a few parts in a million. The gravitational acceleration is the negative gradient (vector derivative) of the potential and introduces nonradial gravitational forces.

$$\vec{F} = m\vec{g} = m(-\vec{\nabla}\, V) \qquad (11.0,2)$$

The formula for V is shown below:

$$V(r,\phi,\lambda) = \frac{\mu_E}{r}\left\{1 + \sum_{n=1}^{\infty}\sum_{m=0}^{n}\left(\frac{R_E}{r}\right)^n P_{nm}(\sin\phi)[C_{nm}\cos(m\lambda) + S_{nm}\sin(m\lambda)]\right\} \qquad (11.0,3)$$

where

ϕ = latitude (geodetic)

λ = east longitude

μ_E = gravitational constant for the Earth

= 3.9860064E14 (N m^2/kg)* for the Marsh, et al., model discussed below.

R_E = 6378.137 km*

*Use these values only in this model. For other applications, use the values found in Table 10.0–1.

The coefficients C_{nm} and S_{nm} are the harmonic coefficients of the potential function and P_{nm} represents the associated Legendre functions of the first kind of degree n and order m. Because sin ϕ = Z/r = u, it is simply a direction cosine and the associated Legendre function may be expressed as:

$$P_{nm}(u) = \frac{(1-u^2)^{m/2}}{2^n\ n!} \frac{d^{n+m}(u^2-1)^n}{du^{n+m}} \qquad (11.0,4)$$

Un–normalized Legendre functions should be used with the 4x4 coefficients given in Table 11.0–1. They are adequate for calculation of orbit position to within a few hundred meters. Improved accuracy can be obtained by using additional terms. When computer capacity is an issue, it is best to use the model with the number of coefficients tailored to the application, rather than truncate a larger set. A recommended high accuracy set of coefficients (36x36) is presented in Marsh, et al., 1988. Additional information on normalization can be found in Anon., 1975.

TABLE 11.0–1 GRAVITATIONAL COEFFICIENTS (4 BY 4)

Zonal Harmonic Coefficients (Multiply by 10^{-6})

C10	0.0
C20	–1082.6258313
C30	2.5326124
C40	1.6161966

Tesseral Harmonic Coefficients (Multiply by 10^{-6})

n	m	C_{nm}	S_{nm}
1	1	0.0	0.0
2	1	0.0	0.0
2	2	+1.5743213	–0.90359264
3	1	+2.1924062	+0.2695930
3	2	+0.3086208	–0.2119137
3	3	+0.1005368	+0.1970571
4	1	–0.5060535	–0.4507374
4	2	+0.0775920	+0.1484817
4	3	+0.0592223	–0.0119894
4	4	–0.0040152	+0.0065174

(Derived from the normalized coefficients in Marsh et al., 1988, by the conversion defined in Zender, et al., 1975.)

APPENDIX A ABBREVIATIONS AND ACRONYMS

ac	Alternating Current
AL	Anomalously Large
A_p	Geomagnetic Activity Index (Daily)
a_p	Geomagnetic Activity Index (3–Hourly)
C	Celsius
CCD	Charge–Coupled Device
cm	Centimeter
CMG	Control Moment Gyro
dc	Direct Current
DMSP	Defense Meteorological Satellite Program
EMI	Electromagnetic Interference
EMR	Electromagnetic Radiation
EUV	Extreme Ultraviolet
$F_{10.7}$	10.7 Centimeter Solar Radio Noise Flux
eV	Electron Volt
EVA	Extravehicular Activity
FORTRAN	Formula Translation
GCR	Galactic Cosmic Ray
GEO	Geosynchronous Earth Orbit
GeV	Gigaelectron Volt
GHz	Gigahertz
μ_E	Gravitational Constant for the Earth
GN&C	Guidance, Navigation, and Control
GRAM	Global Reference Atmosphere Model
GSFC	Goddard Space Flight Center
GV	Gigavolt
Hg	Mercury
Hz	Hertz
IGRF	International Geomagnetic Reference Field
IOC	Initial Operational Capability
IR	Infrared
IRI	International Reference Ionosphere
JSC	Johnson Space Center

K	Kelvin
keV	Kiloelectron Volt
kg	Kilogram
kHz	Kilohertz
km	Kilometer
K_p	Logarithm of the Geomagnetic Activity Index A_p
LEO	Low Earth Orbit
LSI	Large Scale Integration
m	Meter
MET	Marshall Engineering Thermosphere
MeV	Megaelectron Volt
MHz	Megahertz
MSFC	Marshall Space Flight Center
MSIS	Mass Spectrometer Incoherent Scatter
mV	Millivolt
MW	Megawatt
NASA	National Aeronautics and Space Administration
nm	Nanometer
NSSDC	National Space Science Data Center
OR	Ordinary
PMC	Permanently Manned Capability
POP	Polar Orbiting Platform
R_E	Radius of the Earth
RF	Radio Frequency
s	Second
SEU	Single Event Upset
SSCB	Space Station Control Board
SSFPE	Space Station Freedom Program Element
μ	Atomic Mass Unit
UV	Ultraviolet
VLF	Very Low Frequency
VLSID	Very Large–Scale Integrated Device
W	Watt

APPENDIX B MARSHALL ENGINEERING THERMOSPHERE MODEL PROGRAM LISTING (PAGE 1 OF 30)

PROGRAM LISTING

```
C*************************************************************************
C*
C*                          The Marshall Space Flight Center
C*                  The Marshall Engineering Thermosphere (MET) Model
C*                  This program is a driving program for the following
C*                                  subroutines :
C*                                    ATMOSPHERES
C*                                      SOLSET
C*                                       TIME
C*                                        J70
C*
C*                  The atmospheric model is a modified Jacchia 1970 model
C*                          and is given in the subroutine J70.  All
C*                  of the other subroutines were designed to allow flexible
C*                  use of this model so that various input parameters could
C*                      be varied within a driving program with very little
C*                                    software development.
C*                  Thus, for example, driving routines can be written quite
C*                      easily to facilitate the plotting of output as line or
C*                  contour plots.  Control is achieved by setting the values
C*                  of four switches in the driving program, as described in
C*                                  subroutine ATMOSPHERES.
C*
C*************************************************************************
      REAL*4  INDATA (12) , OUTDATA (12) , AUXDATA (5)

      CHARACTER*1  SWITCH (4)

C*
C*   Set all switches to 'Y' so that only one particular
C*   calculation is performed
C*

      SWITCH (1) = 'Y'

      SWITCH (2) = 'Y'

      SWITCH (3) = 'Y'

      SWITCH (4) = 'Y'

      CALL ATMOSPHERES ( INDATA, OUTDATA, AUXDATA, SWITCH )

C*
C*  Now type output data
C*
```

APPENDIX B MARSHALL ENGINEERING THERMOSPHERE MODEL PROGRAM LISTING (PAGE 2 OF 30)

```
      Type *,' All output in MKS units'

            PROGRAM LISTING

      Type *,' '
      Type *,' Exospheric temperature      =  ',  OUTDATA    (1),'  K'
      Type *,' Temperature                 =  ',  OUTDATA    (2),'  K'
      Type *,' N2 number density           =  ',  OUTDATA    (3),'  /m3'
      Type *,' O2 number density           =  ',  OUTDATA    (4),'  /m3'
      Type *,' O number density            =  ',  OUTDATA    (5),'  /m3'
      Type *,' A number density            =  ',  OUTDATA    (6),'  /m3'
      Type *,' He number density           =  ',  OUTDATA    (7),' /m3'
      Type *,' H number density            =  ',  OUTDATA    (8),'  /m3'
      Type *,' Average molecular wt.       =  ',  OUTDATA    (9)
      Type *,' Total mass density          =  ',  OUTDATA    (10),'  kg/m3'
      Type *,' Log10 mass density          =  ',  OUTDATA    (11)
      Type *,' Total pressure              =  ',  OUTDATA    (12),'  Pa'
      Type *,' Local grav. acceln.         =  ',  AUXDATA    (1),'  m.sec–2'
      Type *,' Ratio specific heats        =  ',  AUXDATA    (2)
      Type *,' Pressure scale–height       =  ',  AUXDATA    (3),'  m'
      Type *,' Specific heat cons. p       =  ',  AUXDATA    (4),'m2.sec–2.K–1'
      Type *,' Specific heat cons. v       =  ',  AUXDATA    (5),'m2.sec–2.K–1'
      Type *,' '

      STOP

      END

      SUBROUTINE ATMOSPHERES ( INDATA, OUTDATA, AUXDATA, SWITCH )
C**********************************************************************
C*
C*            DESCRIPTION:–
C*
C*  Calculate atmospheric data in single precision using
C*  subroutine J70 and J70SUP.
C*
C*            SUBROUTINES:–
C*
C*       TIME, SOLSET, GMC, J70 and J70SUP
C*            INPUT:–
C*
C*  ————————— all single precision, either through ——————————
C*  ————————— subroutines or from main driver prog. ———————————
```

APPENDIX B MARSHALL ENGINEERING THERMOSPHERE MODEL PROGRAM LISTING (PAGE 3 OF 30)

```
C*
C*  INDATA (1) — altitude                          = Z
C*   ..  (2) — latitude                            = XLAT
C*   ..  (3) — longitude                           = XLNG
C*   ..  (4) — year (yy)                           = IYR
C*   ..  (5) — month (mm)                          = MN
C*   ..  (6) — day (dd)                            = IDA
C*   ..  (7) — hour (hh)                           = IHR
C*   ..  (8) — mins (mm)                          = MIN
C*   ..  (9) — geomagnetic index                   = IGEO_IND
C*   ..  (10)— solar radio noise flux              = F10
C*   ..  (11)— 162–day average F10                 = F10B
C*   ..  (12)— geomagnetic activity index          = GI=AP
C*
C*            OUTPUT:–
C*
C*        NOTE :  All output in MKS units
C*
C* ———————————————— all single precision ————————————————
C*
C*  OUTDATA (1) — exospheric temperature (K)
C*   ..  (2) — temperature at altitude Z
C*   ..  (3) — N2 number density                   (per meter–cubed)
C*   ..  (4) — O2 number density                   (    ..     )
C*   ..  (5) — O  number density                   (    ..     )
C*   ..  (6) — A  number density                   (    ..     )
C*   ..  (7) — He number density                   (    ..     )
C*   ..  (8) — H  number density                   (    ..     )
C*   ..  (9) — average molecular weight
C*   ..  (10)— total density
C*   ..  (11)— log10 ( total density )
C*   ..  (12)— total pressure ( Pa )
C*
C*  AUXDATA (1) — gravitational acceleration ( m/s–s )
C*   ..  (2) — ratio of specific heats
C*   ..  (3) — pressure scale–height ( m )
C*   ..  (4) — specific heat at constant pressure
C*   ..  (5) — specific heat at constant volume
C*
C*
```

APPENDIX B MARSHALL ENGINEERING THERMOSPHERE MODEL PROGRAM LISTING (PAGE 4 OF 30)

```
C*            COMMENTS:–
C*
C*  SWITCH(1) — if Y(es),      date and time are input from terminal
C*                             through subroutine TIME once only
C*  SWITCH(2) — if Y(es),      solar/magnetic activity are input from
C*                             terminal through subroutine SOLSET once only
C*  SWITCH(3) — if Y(es),      only ONE altitude value is input from
C*                             terminal through main calling program
C*  SWITCH(4) — if Y(es),      only ONE latitude AND longitude are input
C*                             from terminal through main calling program
C*
C*************************************************************
      EXTERNAL TIME

      DIMENSION AUXDATA (5)

      INTEGER HR

      REAL*4 LAT, LON, INDATA (12), OUTDATA (12)

      CHARACTER*1  SWITCH (4)

      PARAMETER PI = 3.14159265

C————————————————————————————————————————————
C*  This next section is only executed on the first call to ATMOSPHERES
C*
            DO WHILE ( CALL .EQ. 0.0 )

C*
C*  SECTION A:–
C*
      IF ( SWITCH(1) .EQ. 'Y' ) THEN
      CALL TIME ( IYR, MON, IDA, HR, MIN, SWITCH(1) )
      INDATA (4) = FLOATJ (IYR)
      INDATA (5) = FLOATJ (MON)
      INDATA (6) = FLOATJ (IDA)
      INDATA (7) = FLOATJ (HR)
      INDATA (8) = FLOATJ (MIN)
      END IF
C*
C*   SECTION B:–
C*
      IF ( SWITCH(2). EQ. 'Y' ) THEN
```

APPENDIX B MARSHALL ENGINEERING THERMOSPHERE MODEL PROGRAM LISTING (PAGE 5 OF 30)

```
            CALL SOLSET ( IGEO_IND, F10, F10B, GI, SWITCH(2) )
            INDATA (9) = FLOATJ (IGEO_IND)
            INDATA (10) = F10
            INDATA (11) = F10B
            INDATA (12) = GI
            END IF
C*
C*  SECTION C:–
C*
            IF ( SWITCH(3). EQ. 'Y' ) THEN

            TYPE *,' Input altitude, km'
            ACCEPT *, INDATA (1)
            Z = INDATA (1)
            END IF
C*
C*  SECTION D:–
C*
            IF ( SWITCH(4). EQ. 'Y' ) THEN
            TYPE *,' Input latitude and longitude, degrees'
            ACCEPT *, ( INDATA(I), I= 2,3 )
            LAT = INDATA (2)
            LON = INDATA (3)
            RLT = INDATA (2) * PI / 180. !  geographic latitude, radians
            END IF
            CALL1= 1.0
            END DO
C*
C*  End of first executable section
C*————————————————————————————————————————————————————————
C*  The following depend on the values of the switches
C*
C*  SECTION 1:–
C*
                  IF ( SWITCH(1). NE. 'Y' ) THEN
            IYR = JINT ( INDATA (4) )
            MON = JINT ( INDATA (5) )
            IDA = JINT ( INDATA (6) )
            HR  = JINT ( INDATA (7) )
            MIN = JINT ( INDATA (8) )
```

APPENDIX B MARSHALL ENGINEERING THERMOSPHERE MODEL PROGRAM LISTING (PAGE 6 OF 30)

```
      CALL TIME ( IYR, MON, IDA, HR, MIN, SWITCH(1) )

            END IF

C*
C*  SECTION 2:–
C*

            IF ( SWITCH(2). NE. 'Y' ) THEN

      IGEO_IND   = JINT ( INDATA (9) )
      F10        = INDATA (10)
      F10B       = INDATA (11)
      GI         = INDATA (12)
      CALL SOLSET ( IGEO_IND, F10, F10B, GI, SWITCH(2) )

            END IF

C*
C*  SECTION 3:–
C*

            IF ( SWITCH(3). NE. 'Y' ) THEN

      Z = INDATA (1)

            END IF

C*
C*  SECTION 4:–
C*

            IF ( SWITCH(4). NE. 'Y' ) THEN

      LAT = INDATA (2)
      LON = INDATA (3)
      RLT = INDATA (2) * PI / 180. !  geographic latitude, radians

            END IF

C*
C*  All setting–up complete.
C*

            CALL J70 ( INDATA, OUTDATA )

            CALL J70SUP ( Z, OUTDATA, AUXDATA )

      RETURN
      ENTRY ATMOS_ENT ( DUMMY )
      CALL1= DUMMY
      RETURN
```

APPENDIX B MARSHALL ENGINEERING THERMOSPHERE MODEL PROGRAM LISTING (PAGE 7 OF 30)

```
      END

      SUBROUTINE TIME ( IYR, MON, IDA, HR, MIN, SWITCH )
C*********************************************************************
C*
C*  This subroutine sets up time of year and day
C*
C*            INPUTS/OUTPUTS:
C*
C*  IYR  =  year ( 2 digits )
C*  MON  =  month
C*  IDA  =  day of month
C*  HR   =  hour of day
C*  MIN  =  minutes
C*
C*********************************************************************
      DIMENSION  IDAY ( 12 )

      INTEGER  HR

      CHARACTER*1  SWITCH

      DATA IDAY / 31, 28, 31, 30, 31, 30, 31, 31, 30, 31, 30, 31 /

      PARAMETER PI = 3.14159265
C*********************************************************************
C*  If  SWITCH = Y(es)  then input data and time from terminal
C*********************************************************************
      IF ( SWITCH.EQ.'Y'. OR. SWITCH.EQ.'y' )  THEN

      TYPE *, ' Input date and time of date? ( yy,mm,dd,hh,mm ) '

      ACCEPT *, IYR, MON, IDA, HR, MIN

      END IF

      IF ( JMOD (IYR,4) .EQ. 0) THEN

          IF ( JMOD (IYR,100) .NE. 0) IDAY ( 2 ) = 29

      ELSE

          IDAY ( 2 ) = 28

          END IF
```

APPENDIX B MARSHALL ENGINEERING THERMOSPHERE MODEL PROGRAM LISTING (PAGE 8 OF 30)

```
C*************************************************************************
      DAYTOT = 0.0

          DO 1 I = 1, 12

      DAYTOT = DAYTOT + FLOATJ ( IDAY ( I ) )
 1        CONTINUE
          IF ( MON. GT. 1 )  THEN

      KE = MON – 1

      ID = 0

          DO 2 I = 1, KE

      ID = ID + IDAY (I)
 2        CONTINUE
      ID = ID + IDA

          ELSE

      DD = IDA

          END IF

      RETURN

      END

            SUBROUTINE SOLSET ( IGEO_IND, F10, F10B, GI, SWITCH )
C*************************************************************************
C*
C*  This subroutine simply calls for a setup of the solar
C*  activity and auroral activity indices.
C*
C*                                        INPUTS/OUTPUTS:
C*
C*  IGEO_IND = geomagnetic index
C*  F10      = solar radio noise flux
C*  F10B     = 162–day average F10
C*  GI       = geomagnetic activity index
C*
C*************************************************************************
```

APPENDIX B MARSHALL ENGINEERING THERMOSPHERE MODEL PROGRAM LISTING (PAGE 9 OF 30)

```
                CHARACTER*1  SWITCH

                IGEO_IND = 2
C*
C*  If SWITCH = Y(es) then input geomagnetic indices from
C*  terminal ———————
C*********************************************************************
                IF ( SWITCH.EQ.'Y'. OR. SWITCH.EQ.'y' ) THEN
C*
C*  TYPE *, ' Input geomagnetic index ( 1–KP, 2–AP ) '
C*  ACCEPT *, IGEO_IND
C*
        TYPE *, ' Input solar radio noise flux ( F10 = 0–400 ) '
        ACCEPT *, F10
        TYPE *, ' Input 162–day average F10 ( F10B = 0–250 ) '
        ACCEPT *, F10B
C*
C*          IF ( IGEO_IND . EQ. 2 )                         THEN
C*
C*  TYPE *, ' Input geomagnetic activity index ( GI = 0–400 ) '
C*
C*                                                          ELSE
C*
C*  TYPE *, ' Input geomagnetic activity index ( GI = 0–9 ) '
C*
C*          END IF
C*
        TYPE *,' Input AP index ( AP = 0 – 400 ) '
        ACCEPT *, GI
            END IF
C*********************************************************************
            RETURN

            END


            SUBROUTINE J70SUP ( Z, OUTDATA, AUXDATA )
```

APPENDIX B MARSHALL ENGINEERING THERMOSPHERE MODEL PROGRAM LISTING (PAGE 10 OF 30)

```
C*********************************************************************
C*
C*                                   DESCRIPTION:–
C*
C*  J70SUP calculates auxilliary variables which are output in array
C*  AUXDATA, given data input from J70 which are contained in array
C*  OUTDATA.
C*
C*                                   INPUT DATA:–
C*
C*  Z       — altitude (km)
C*  TZZ     — temperature at altitude z          = OUTDATA (2)
C*          — N2 number density                  =  ..  (3)
C*          — O2  ..    ..                       =  ..  (4)
C*          — O   ..    ..                       =  ..  (5)
C*          — A   ..    ..                       =  ..  (6)
C*          — He  ..    ..                       =  ..  (7)
C*          — H   ..    ..                       =  ..  (8)
C*  EM      — average molecular weight           =  ..  (9)
C*  DENS    — total density                      =  ..  (10)
C*  P       — total pressure                     =  ..  (12)
C*
C*                                   OUTPUT DATA:–
C*
C*  G       — gravitational acceleration                    = AUXDATA (1)
C*  GAM     — ratio of specific heats                       = AUXDATA (2)
C*  H       — pressure scale–height                         = AUXDATA (3)
C*  CP      — specific heat at constant pressure = AUXDATA (4)
C*  CV      — specific heat at constant volume   = AUXDATA (5)
C*********************************************************************
      REAL*4  OUTDATA (12), AUXDATA (5), H

      G = 9.80665 / ( ( 1. + Z / 6.356766E3 )**2 )

      H = OUTDATA (12) / ( G * OUTDATA (10) )

      SUM1 = OUTDATA (3) + OUTDATA (4)

      SUM2 = 0.0

          DO 1  I = 5, 8

          PROGRAM LISTING

      SUM2 = SUM2 + OUTDATA (I)

    1     CONTINUE
```

APPENDIX B MARSHALL ENGINEERING THERMOSPHERE MODEL PROGRAM LISTING (PAGE 11 OF 30)

```
      GAM = ( 1.4 * SUM1 + 1.67 * SUM2 ) / ( SUM1 + SUM2 )
```

```
      CV = G * H / (   ( GAM – 1.0 ) * OUTDATA (2)   )

      CP = GAM * CV

      AUXDATA (1) = G

      AUXDATA (2) = GAM

      AUXDATA (3) = H

      AUXDATA (4) = CP

      AUXDATA (5) = CV


      RETURN

      END


      SUBROUTINE J70 ( INDATA, OUTDATA )
C**********************************************************************
C*
C*  INPUTS:  through the subroutine calling list
C*  OUTPUTS: through the subroutine calling list
C*
C*                                        INPUT DATA:
C*
C*          Z    —  altitude                 = INDATA (1)
C*          XLAT — latitude                  = INDATA (2)
C*          XLNG — longitude                 = INDATA (3)
C*          IYR — year (yy)                  = INDATA (4)
C*          MN — month (mm)                  = INDATA (5)
C*          IDA — day  (dd)                  = INDATA (6)
C*          IHR — hour (hh)                  = INDATA (7)
C*          MIN — mins (mm)                  = INDATA (8)
C*          I1 — geomagnetic index           = INDATA (9)
C*          F10  —  solar radio noise flux   = INDATA (10)
C*          F10B —  162–day average F10      = INDATA (11)
C*          GI —  geomagnetic activity index = INDATA (12)
C*
C*                                        OUTPUT DATA:
C*
```

APPENDIX B MARSHALL ENGINEERING THERMOSPHERE MODEL PROGRAM LISTING (PAGE 12 OF 30)

```
C*          T— exospheric temperature          = OUTDATA (1)
C*          TZZ— temperature at altitude Z     = OUTDATA (2)
C*          A(1)— N2 number density            = OUTDATA (3)
C*          A(2)— O2 number density            = OUTDATA (4)
C*          A(3)— O  number density            = OUTDATA (5)
C*          A(4)— A  number density            = OUTDATA (6)
C*          A(5)— He number density            = OUTDATA (7)
C*          A(6)— H  number density            = OUTDATA (8)
C*          EM— average molecular weight       = OUTDATA (9)
C*          DENS— total density                = OUTDATA (10)
C*          DL— log10 ( total density )        = OUTDATA (11)
C*          P— total pressure                  = OUTDATA (12)
C*
C*      NB.     Input through array 'INDATA'
C*              Output through array 'OUTDATA'
C*
C***********************************************************************
            DIMENSION  A ( 6 )

          REAL*4  INDATA ( 12 ), OUTDATA ( 12 )

          PARAMETER RGAS = 8.31432E3       !  J/kmol–K

          PARAMETER BFH = 440.0

C*  Calculations performed for only one latitude , one
C*  longitude and one altitude
C*
C*  Set parameters to INDATA values
C*
          Z          = INDATA (1)
          XLAT       = INDATA (2)
          XLNG       = INDATA (3)
          IYR        = JINT ( INDATA (4) )  + 1900
          MN         = JINT ( INDATA (5) )
          IDA        = JINT ( INDATA (6) )
          IHR        = JINT ( INDATA (7) )
          MIN        = JINT ( INDATA (8) )
          I1         = JINT ( INDATA (9) )
          F10        = INDATA (10)
          F10B       = INDATA (11)
          GI         = INDATA (12)

          CALL TME ( MN , IDA , IYR , IHR , MIN , XLAT , XLNG, SDA ,
```

APPENDIX B MARSHALL ENGINEERING THERMOSPHERE MODEL PROGRAM LISTING (PAGE 13 OF 30)

```
     1       SHA , DD , DY )
          CALL TINF ( F10 , F10B , GI , XLAT , SDA , SHA , DY , I1 , TE )

          CALL JAC ( Z , TE , TZ , A(1) , A(2) , A(3) , A(4) , A(5) ,
     1       A(6)  , EM , DENS , DL )
               DENLG = 0.

               DUMMY = DL

               DEN   = DL

          IF ( Z .LE. 170. )  THEN

               CALL SLV ( DUMMY , Z , XLAT , DD )

               DENLG = DUMMY

          END IF
C*
C*   'Fair' helium number density between base fairing height
C*   ( BFH ) and 500 km
C*
          IF ( Z. GE. 500. )  THEN

                    CALL SLVH ( DEN , A(5) , XLAT , SDA )

                    DL = DEN

          ELSE IF ( Z .GT. BFH )  THEN

                    DHEL1 = A ( 5 )

                    DHEL2 = A ( 5 )

                    DLG1 = DL

                    DLG2 = DL

               CALL SLVH ( DLG2 , DHEL2 , XLAT , SDA )

                    IH = Z

               CALL FAIR5 ( DHEL1 , DHEL2 , DLG1 , DLG2 , IH , FDHEL , FDLG )

                    DL = FDLG A ( 5 ) = FDHEL
```

APPENDIX B MARSHALL ENGINEERING THERMOSPHERE MODEL PROGRAM LISTING (PAGE 14 OF 30)

```
      END IF

            DL = DL + DENLG

            DENS = 10.**DL

            XLAT = XLAT * 57.29577951
C*
C*  Fill OUTDATA array
C*
      OUTDATA (1) = TE

      OUTDATA (2) = TZ

          DO 80 I = 1, 6

      OUTDATA (I+2) = 1.E6 * ( 10. ** A(I) )

   80     CONTINUE

      OUTDATA (9) = EM

      OUTDATA (10) = DENS * 1000.

      OUTDATA (11) = DL

      P = OUTDATA (10) * RGAS * TZ / EM

      OUTDATA (12) = P

      RETURN

      END

      SUBROUTINE FAIR5 ( DHEL1 , DHEL2 , DLG1 , DLG2 ,IH , FDHEL ,
     1    FDLG
C*********************************************************************** C*
C*  This subroutine fairs between the region above 500 km, which
C*  invokes the seasonal–latitudinal variation of the helium number
C*  density ( subroutine SLVH ), and the region below, which does not
C*  invoke any seasonal–latitudinal variation at all.
C*
C*  INPUTS:    DHEL1        = helium number density before invoking SLVH
C*             DHEL2        = helium number density after invoking SLVH
C*             DLG1         = total density before invoking SLVH
C*             DLG2         = total density after invoking SLVH
C*             IH           = height  ( km ) — INTEGER
```

APPENDIX B MARSHALL ENGINEERING THERMOSPHERE MODEL PROGRAM LISTING (PAGE 15 OF 30)

```
C*                IBFH          = base fairing height ( km ) — INTEGER
C*  OUTPUTS:  FDHEL         = faired helium number density
C*                FDLG          = faired total density
C*
C*********************************************************************

      DIMENSION CZ ( 6 )

      DATA CZ / 1.0, 0.9045085, 0.6545085, 0.3454915, 0.0954915, 0.0 /

      PARAMETER IBFH = 440

C*
C*  Height index
C*
      I = ( IH – IBFH ) /10 + 1

C*
C*  Non–SLVH fairing coefficient
C*
      CZI = CZ ( I )

C*
C*  SLVH fairing coefficient
C*
      SZI = 1.0 – CZI

C*
C*  Faired density
C*
      FDLG = ( DLG1 * CZI ) + ( DLG2 * SZI )

C*
C*  Faired helium number density
C*
      FDHEL = ( DHEL1 * CZI ) + ( DHEL2 * SZI )

      RETURN

      END

      SUBROUTINE TINF ( F10 , F10B , GI, XLAT, SDA , SHA , DY , I1 , TE )
```

APPENDIX B MARSHALL ENGINEERING THERMOSPHERE MODEL PROGRAM LISTING (PAGE 16 OF 30)

```
C**********************************************************************
C*
C*  Subroutine 'TINF' calculates the exospheric temperature
C*  according to L. Jacchia, Smithsonian Astrophysical
C*  Observatory 313, 1970.
C*
C*       F10 = solar radio noise flux ( x E–22 Watts / m2 )
C*       F10B= 162–day average F10
C*       GI  = geomagnetic activity index
C*       LAT = geographic latitude at perigee ( in rad )
C*       SDA = solar declination angle ( in rad )
C*       SHA = solar hour angle
C*       DY  = D / Y  ( day number / tropical year ) ; 1
C*       I1  = geomagnetic equation index  ( 1—GI=KP , 2—GI=AP )
C*       RE  = diurnal factor  KP, F10B, AVG
C*
C*       CONSTANTS          — C = solar activity variation
C*                          — BETA , etc = diurnal variation
C*                          — D = geomagnetic variation
C*                          — E = semiannual variation
C*
C**********************************************************************
          PARAMETER PI = 3.14159265, TPI = 6.28318531

          PARAMETER XM = 2.5, XNN = 3.0

C*
C*  Ci are solar activity variables
C*
          PARAMETER C1 = 383.0 , C2 = 3.32 , C3 = 1.80

C*
C*  Di are geomagnetic variation variables
C*
          PARAMETER D1 = 28.0 , D2 = 0.03 , D3 = 1.0 , D4 = 100.0

          PARAMETER D5 = –0.08

C*
C*  Ei are semiannual variation variables
C*
          PARAMETER E1 = 2.41 , E2 = 0.349 , E3 = 0.206 , E4 = 6.2831853

          PARAMETER E5 = 3.9531708, E6 = 12.5663706, E7 = 4.3214352

          PARAMETER E8 = 0.1145 , E9 = 0.5, E10 = 6.2831853
```

APPENDIX B MARSHALL ENGINEERING THERMOSPHERE MODEL PROGRAM LISTING (PAGE 17 OF 30)

```
      PARAMETER E11 = 5.9742620 , E12 = 2.16

      PARAMETER BETA = –0.6457718, GAMMA = 0.7504916, P = 0.1047198

      PARAMETER RE = 0.31

C*
C*  Solar Activity Variation
C*
      TC = C1 + C2 * F10B + C3 * ( F10 – F10B )

C*
C*  Diurnal variation
C*
      ETA       = 0.5 * ABS ( XLAT – SDA )

      THETA     = 0.5 * ABS ( XLAT + SDA )

      TAU       = SHA + BETA + P * SIN ( SHA + GAMMA )

      IF ( TAU. GT. PI ) TAU = TAU – TPI

      IF ( TAU. LT.–PI ) TAU = TAU + TPI

      A1 = ( SIN ( THETA ) )**XM

      A2 = ( COS ( ETA ) )**XM

      A3 = ( COS ( TAU / 2. ) )**XNN

      B1 = 1.0 + RE * A1

      B2 = ( A2 – A1 ) / B1

      TV = B1 * ( 1. + RE * B2 * A3 )

      TL = TC * TV

C*
C*  Geomagnetic variation
C*
      IF ( I1.EQ.1 ) THEN

          TG = D1 * GI + D2 * EXP(GI)

      ELSE

          TG = D3 * GI + D4 * ( 1 – EXP ( D5 * GI ) )

      END IF
```

APPENDIX B MARSHALL ENGINEERING THERMOSPHERE MODEL PROGRAM LISTING (PAGE 18 OF 30)

```
C*
C*  Semiannual variation
C*
          G3 = 0.5 * ( 1.0 + SIN ( E10 * DY + E11 ) )

          G3 = G3 ** E12

          TAU1 = DY + E8 * ( G3 – E9 )

          G1 = E2 + E3 * ( SIN ( E4 * TAU1 + E5 ) )

          G2 = SIN ( E6 * TAU1+ E7 )

          TS = E1 + F10B * G1 * G2
C*
C*  Exospheric temperature
C*
          TE = TL + TG + TS

          RETURN

          END

          SUBROUTINE TME ( MN , IDA , IYR , IHR , MIN , XLAT , XLNG ,
         1       SDA , SHA , DD , DY )
C*************************************************************************
C*
C*  Subroutine 'TME' performs the calculations of the solar declination
C*  angle and solar hour angle.
C*
C*  INPUTS:    MN          = month
C*             IDA         = day
C*             IYR         = year
C*             IHR         = hour
C*             MIN         = minute
C*             XMJD        = mean Julian date
C*             XLAT        = latitude ( input–geocentric latitude )
C*             XLNG        = longitude ( input–geocentric longitude, –180,+180 )
C*
C*  OUTPUTS:   SDA         = solar declination angle (rad)
C*             SHA         = solar hour angle (rad)
C*             DD          = day number from 1 JAN.
C*             DY          = DD / tropical year
C*
C*************************************************************************
```

APPENDIX B MARSHALL ENGINEERING THERMOSPHERE MODEL PROGRAM LISTING (PAGE 19 OF 30)

```
      DIMENSION IDAY(12)
      DATA IDAY / 31,28,31 ,30,31,30 ,31,31,30 ,31,30,31 /
      PARAMETER YEAR = 365.2422
      PARAMETER A1 = 99.6909833 , A2 = 36000.76892
      PARAMETER A3 = 0.00038708 , A4 = 0.250684477
      PARAMETER B1 = 0.0172028 , B2 = 0.0335 , B3 = 1.407 PARAMETER
      PI = 3.14159265 , TPI = 6.28318531
      PARAMETER PI2 = 1.57079633, PI32 = 4.71238898
      PARAMETER RAD_DEG = 0.017453293
      XLAT = XLAT / 57.29577951
       YR = IYR
      IF ( JMOD(IYR,4) .EQ. 0 ) THEN
          IF (JMOD(IYR,100) .NE. 0 ) IDAY(2) = 29  ! Century not a leap year
      ELSE
          IDAY(2) = 28
      END IF
          ID = 0 IF ( MN. GT. 1 ) THEN
          DO  20  I = 1 , MN–1
          ID = ID + IDAY(I)
   20     CONTINUE
      END IF
          ID = ID + IDA
          DD = ID
          DY = DD/YEAR
C*
C*  Compute mean Julian date
C*
      XMJD = 2415020. + 365. * ( YR – 1900. ) + DD
     1     + FLOATJ (  ( IYR – 1901 ) / 4 )
```

APPENDIX B MARSHALL ENGINEERING THERMOSPHERE MODEL PROGRAM LISTING (PAGE 20 OF 30)

```
C*
C*  Compute Greenwich mean time in minutes GMT
C*
          XHR = IHR
          XMIN = MIN
          GMT = 60 * XHR + XMIN
          FMJD = XMJD – 2435839. + GMT / 1440.
C*
C*  Compute Greenwich mean position – GP ( in rad )
C*
          XJ = ( XMJD – 2415020.5 ) / ( 36525.0 )
          GP = AMOD ( A1 + A2 * XJ + A3 * XJ * XJ + A4 * GMT , 360.)
C*
C*  Compute right ascension point – RAP ( in rad )
C*
C*  First convert geocentric longitude to deg longitude – west
C*  neg, + east
C*
          IF ( XLNG .GT. 180. ) XLNG = XLNG – 360.
          RAP = AMOD ( GP + XLNG, 360. )
C*
C*  Compute celestial longitude – XLS ( in rad ) – – zero
C*  to 2PI
C*
          Y1 = B1 * FMJD
          Y2 = 0.017202 * ( FMJD – 3. )
          XLS = AMOD ( Y1 + B2 * SIN(Y2) – B3 , TPI )
C*
C*  Compute solar declination angle – SDA ( in rad )
C*
          B4 = RAD_DEG * 23.4523 – 0.013 * XJ )
          SDA = ASIN ( SIN ( XLS ) * SIN ( B4 ) )
C*
C*  Compute right ascension of Sun – RAS ( in rad ) – – zero
C*  to 2PI
C*
          ARG = TAN (SDA)/TAN (B4)
          IF (ARG .GT. 1.0)  ARG = 1.0
          IF (ARG .LT. –1.0)  ARG = –1.0
          RAS = ASIN (ARG)
C*
C*  Put RAS in same quadrant as XLS
```

APPENDIX B MARSHALL ENGINEERING THERMOSPHERE MODEL PROGRAM LISTING (PAGE 21 OF 30)

```
      RAS = ABS ( RAS )

      TEMP = ABS ( XLS )

      IF ( TEMP.LE.PI .AND. TEMP.GT.PI2 )  THEN

          RAS = PI – RAS

      ELSE IF ( TEMP.LE.PI32 .AND. TEMP.GT.PI )  THEN

          RAS = PI + RAS

      ELSE IF ( TEMP.GT.PI32 )  THEN

          RAS = TPI – RAS

      END IF

          IF ( XLS. LT. 0. ) RAS = –RAS
C*
C*  Compute solar hour angle – SHA ( in deg ) – –
C*
      SHA = RAP * RAD_DEG – RAS

      IF ( SHA.GT.PI ) SHA = SHA – TPI

      IF ( SHA.LT.–PI ) SHA = SHA + TPI

      RETURN
      END


      SUBROUTINE JAC ( Z , T , TZ , AN , AO2 , AO , AA , AHE , AH ,
     1                 EM , DENS , DL )
C**********************************************************************
C*
C*  Subroutine 'JAC' calculates the temperature TZ , the total density
C*  DENS and its logarithm DL, the mean molecular weight EM, the
C*  individual species number densities for N, O2, O, A, HE and H
C*  ( each preceded with an 'A' ) at altitude Z given the exospheric
C*  temperature T.  This subroutine uses the subroutine 'GAUSS' and
C*  the function subprograms 'TEMP' and 'MOL_WT'.
C*
C**********************************************************************
      DIMENSION  ALPHA(6) , EI(6) , DI(6) , DIT(6)
      REAL*4  MOL_WT
```

APPENDIX B MARSHALL ENGINEERING THERMOSPHERE MODEL PROGRAM LISTING (PAGE 22 OF 30)

```
      PARAMETER AV = 6.02257E23
      PARAMETER QN = .78110
      PARAMETER QO2 = .20955
      PARAMETER QA = .009343
      PARAMETER QHE = 1.289E–05
      PARAMETER RGAS = 8.31432
      PARAMETER PI = 3.14159265
      PARAMETER T0 = 183.
      GRAVITY ( ALTITUDE ) = 9.80665 / ( ( 1. + ALTITUDE /
     1     6.356766E3 )**2 )
      DATA ALPHA / 0.0 , 0.0 , 0.0 , 0.0 , –.380 , 0.0 /
      DATA EI / 28.0134 , 31.9988 , 15.9994 , 39.948 , 4.0026 , 1.00797 /
      TX = 444.3807 + .02385 * T – 392.8292 * EXP ( –.0021357 * T )
      A2 = 2. * (T–TX) / PI
      TX_T0 = TX – T0
      T1 =  1.9 * TX_T0 /   35.
      T3 = –1.7 * TX_T0 / ( 35.**3 )
      T4 = –0.8 * TX_T0 / ( 35.**4 )
      TZ = TEMP ( Z , TX , T1 , T3 , T4 , A2 )
C*
C*  SECTION 1
C*
      A = 90.
      D = AMIN1 ( Z , 105. )
C*
C*  Integrate gM/T from 90 to minimum of Z or 105 km :–
C*
      CALL GAUSS ( A, D, 1, R, TX, T1, T3, T4, A2)
C*
C*  The number 2.1926E–8 = density x temperature/mean molecular
C*  weight at 90 km.
C*
      EM = MOL_WT ( D ) TD = TEMP ( D , TX , T1 , T3 , T4 , A2 )
      DENS = 2.1926E–8 * EM * EXP( –R / RGAS ) / TD
      FACTOR = AV * DENS
      PAR = FACTOR / EM
      FACTOR = FACTOR / 28.96
```

APPENDIX B MARSHALL ENGINEERING THERMOSPHERE MODEL PROGRAM LISTING (PAGE 23 OF 30)

```
C*
C*  For altitudes below and at 105 km calculate the individual
C*  species number densities from the mean molecular weight and
C*  total density.
C*
        IF ( Z. LE. 105 ) THEN
        DL = ALOG10 ( DENS )
        AN  = ALOG10 ( QN * FACTOR )
        AA  = ALOG10 ( QA * FACTOR )
        AHE = ALOG10 ( QHE * FACTOR )
        AO  = ALOG10 ( 2. * PAR * ( 1.–EM / 28.96 ) )
        AO2 = ALOG10 ( PAR * ( EM * ( 1.+QO2 ) / 28.96–1. ) )
        AH  = 0.
C*
C*  Return to calling program
C*
        RETURN

        END IF

C*
C*  SECTION 2 :  This section is only performed for altitudes
C*  above 105 km
C*
C*  Note that having reached this section means that D in
C*  section 1 is 105 km.
C*
C*  Calculate individual species number densities from the total
C*  density and mean molecular weight at 105 km altitude.
C*
            DI(1) = QN * FACTOR

            DI(2) = PAR * (EM * (1.+QO2) / 28.96–1.)

            DI(3) = 2. * PAR * (1.– EM / 28.96)

            DI(4) = QA * FACTOR

            DI(5) = QHE * FACTOR

C*
C*  Integrate  g/T  from  105 km  to  Z km :–
C*
```

APPENDIX B MARSHALL ENGINEERING THERMOSPHERE MODEL PROGRAM LISTING (PAGE 24 OF 30)

```
      CALL GAUSS ( D , Z , 2 , R , TX , T1 , T3 , T4 , A2 )

          DO  41  I = 1 , 5

      DIT(I) = DI(I) * ( TD / TZ ) **(1.+ALPHA(I)) * EXP(–EI(I) * R / RGAS)

          IF ( DIT(I). LE. 0. ) DIT(I) = 1.E–6

   41     CONTINUE
C*
C*  This section calculates atomic hydrogen densities above
C*  500 km altitude.  Below this altitude , H densities are
C*  set to 10**–6.
C*
C*                                          SECTION 3
C*
      IF ( Z .GT. 500. )  THEN

          A1 = 500.

          S = TEMP ( A1 , TX , T1 , T3 , T4 , A2 )

      DI(6) = 10.** ( 73.13 – 39.4 * ALOG10 (S) + 5.5 *
     1    ALOG10(S) *ALOG10(S))
      CALL GAUSS ( A1 , Z , 7 , R , TX , T1 , T3 , T4 , A2 )

          DIT(6) = DI(6) * (S/TZ) * EXP ( –EI(6) * R / RGAS )

      ELSE

          DIT (6) = 1.0

      END IF
C*
C*  For altitudes greater than 105 km , calculate total density
C*  and mean molecular weight from individual species number
C*  densities.
C*
          DENS=0

      DO  42  I = 1 , 6

          DENS = DENS + EI(I) * DIT(I) / AV

   42     CONTINUE
```

APPENDIX B MARSHALL ENGINEERING THERMOSPHERE MODEL PROGRAM LISTING (PAGE 25 OF 30)

```
      EM = DENS * AV / ( DIT(1)+DIT(2)+DIT(3)+DIT(4)+DIT(5)+DIT(6))

      DL = ALOG10 (DENS)

      AN        = ALOG10(DIT(1))
      AO2       = ALOG10(DIT(2))
      AO        = ALOG10(DIT(3))
      AA        = ALOG10(DIT(4))
      AHE       = ALOG10(DIT(5))
      AH        = ALOG10(DIT(6))

      RETURN

      END

    FUNCTION TEMP ( ALT , TX , T1 , T3 , T4 , A2 )
C*********************************************************************
C*
C*  Function subprogram 'TEMP' calculates the temperature at altitude
C*  ALT using equation (10) for altitudes between 90 and 125 km and
C*  equation (13) for altitudes greater than 125 km , from Smithsonian
C*  Astrophysical Observatory Report 313, 1970.
C*
C*********************************************************************
      PARAMETER BB = 4.5E–6

          U = ALT – 125.

      IF ( U .GT . 0. )  THEN

          TEMP = TX  +  A2 * ATAN ( T1 * U * ( 1. + BB * ( U ** 2.5 )
     1          ) / A2 )
      ELSE

          TEMP = TX  +  T1 * U  +  T3 * (U**3)  +  T4 * (U**4)

      END IF

      END

      REAL FUNCTION MOL_WT*4 ( A )
```

APPENDIX B MARSHALL ENGINEERING THERMOSPHERE MODEL PROGRAM LISTING (PAGE 26 OF 30)

```
C*********************************************************************
C*
C*  Subroutine 'MOL_WT' calculates the molecular weight for altitudes
C*  between 90 and 105 km according to equation (1) of Smithsonian
C*  Astrophysical Observatory Report 313, 1970.  Otherwise, MOL_WT is
C*  set to unity.
C*
C*********************************************************************
      DIMENSION  B (7)
      DATA B / 28.15204 , –0.085586 , 1.284E–4 , –1.0056E–5 ,
     1       –1.021E–5 , 1.5044E–6 , 9.9826E–8 /
      IF ( A. GT. 105. ) THEN
          MOL_WT = 1.
      ELSE
          U = A – 100.
          MOL_WT = B (1)
      DO  1  I = 2 , 7
      MOL_WT = MOL_WT  +  B (I) * U ** ( I–1 )
    1 CONTINUE
      END IF
      END
      SUBROUTINE GAUSS ( Z1 , Z2 , NMIN , R , TX , T1 , T3 , T4 , A2 )
C*********************************************************************
C*
C*  Subdivide total integration–altitude range into intervals suitable
C*  for applying Gaussian Quadrature , set the number of points for
C*  integration for each sub–interval , and then perform Gaussian
C*  Quadrature.
C*
C*********************************************************************
      REAL*4  ALTMIN (9) , C(8,6), X(8,6), MOL_WT
      INTEGER NG (8) , NGAUSS , NMIN , J
          GRAVITY ( ALTITUDE ) = 9.80665 / ( ( 1. + ALTITUDE / 6.356766E3
     1       )**2 )
```

APPENDIX B MARSHALL ENGINEERING THERMOSPHERE MODEL PROGRAM LISTING (PAGE 27 OF 30)

```
      DATA ALTMIN / 90., 105., 125., 160., 200., 300., 500., 1500., 2500. /

      DATA NG / 4 , 5 , 6 , 6 , 6 , 6 , 6 , 6 /
C*
C*  Coefficients for Gaussian Quadrature ...
C*
      DATA C /  .5555556 , .8888889 , .5555556 , .0000000 , ! n=3
     .          .0000000 , .0000000 , .0000000 , .0000000 , ! n=3
     .          .3478548 , .6521452 , .6521452 , .3478548 , ! n=4
     .          .0000000 , .0000000 , .0000000 , .0000000 , ! n=4
     .          .2369269 , .4786287 , .5688889 , .4786287 , ! n=5
     .          .2369269 , .0000000 , .0000000 , .0000000 , ! n=5
     .          .1713245 , .3607616 , .4679139 , .4679139 , ! n=6
     .          .3607616 , .1713245 , .0000000 , .0000000 , ! n=6
     .          .1294850 , .2797054 , .3818301 , .4179592 , ! n=7
     .          .3818301 , .2797054 , .1294850 , .0000000 , ! n=7
     .          .1012285 , .2223810 , .3137067 , .3626838 , ! n=8
     .          .3626838 , .3137067 , .2223810 , .1012285 / ! n=8
C*
C*  Abscissas for Gaussian Quadrature ...
C*
      DATA X /    –.7745967 ,       .0000000 ,       .7745967 ,       .0000000 ,   ! n=3
     .             .0000000,        .0000000  ,      .0000000  ,      .0000000  , ! n=3
     .            –.8611363       , –.3399810  ,    .3399810  ,      .8611363  , ! n=4
     .             .0000000  ,      .0000000  ,      .0000000  ,      .0000000  , ! n=4
     .            –.9061798       , –.5384693  ,    .0000000  ,      .5384693  , ! n=5
     .             .9061798  ,      .0000000  ,      .0000000  ,      .0000000  , ! n=5
     .            –.9324695       , –.6612094       , –.2386192  ,    .2386192  , ! n=6
     .             .6612094  ,      .9324695  ,      .0000000  ,      .0000000  , ! n=6
     .            –.9491079       , –.7415312       , –.4058452  ,    .0000000  , ! n=7
     .             .4058452  ,      .7415312  ,      .9491079  ,      .0000000  , ! n=7
     .            –.9602899       , –.7966665       , –.5255324       , –.1834346  , ! n=8
     .             .1834346  ,      .5255324  ,      .7966665  ,      .9602899  / ! n=8

        R = 0.0

      DO  2  K = NMIN , 8
     NGAUSS     = NG (K)
     A          = ALTMIN (K)
     D          = AMIN1 ( Z2 , ALTMIN (K+1) )
```

APPENDIX B MARSHALL ENGINEERING THERMOSPHERE MODEL PROGRAM LISTING (PAGE 28 OF 30)

```
      RR          = 0.0
      DEL         = 0.5 * ( D – A )
      J           = NGAUSS – 2
      DO  1  I = 1 , NGAUSS
          Z = DEL * ( X(I,J) + 1. ) + A
      RR = RR + C(I,J) * MOL_WT(Z) * GRAVITY(Z) / TEMP(Z,TX,T1,T3,
     1          T4,A2)
 1    CONTINUE
          RR = DEL * RR
          R = R + RR
          IF ( D .EQ. Z2 ) RETURN
 2    CONTINUE
      RETURN
      END
      SUBROUTINE SLV ( DEN , ALT , XLAT , DAY )
C*********************************************************************
C*
C*  Subroutine 'SLV' computes the seasonal–latitudinal variation of
C*  density in the lower thermosphere in accordance with L. Jacchia,
C*  Smithsonian Astrophysical Observatory 332, 1971. This affects the
C*  densities between 90 and 170 km.  This subroutine need not be
C*  called for densities above 170 km, because no effect is observed.
C*
C*  The variation should be computed after the calculation of density
C*  due to temperature variations and the density ( DEN ) must be in
C*  the form of a base 10 log.  No adjustments are made to the
C*  temperature or constituent number densities in the region affected by this variation.
C*
C*   DEN     = density (log10)
C*   ALT     = altitude (km)
C*   XLAT    = latitude (rad)
C*   DAY     = day number
C*
C*********************************************************************C*
C*  Initialize density (DEN) = 0.0
C*
      DEN = 0.0
```

APPENDIX B MARSHALL ENGINEERING THERMOSPHERE MODEL PROGRAM LISTING (PAGE 29 OF 30)

```
C*
C*  Check if altitude exceeds 170 km
C*
        IF ( ALT. GT. 170. ) RETURN
C*
C*  Compute density change in lower thermosphere
C*
        Z = ALT – 90.
        X = –0.0013 * Z * Z
        Y = 0.0172 * DAY + 1.72
        P = SIN (Y)
        SP = ( SIN (XLAT) ) **2
        S = 0.014 * Z * EXP (X)
        D = S * P * SP
C*
C*  Check to compute absolute value of 'XLAT'
C*
        IF ( XLAT. LT. 0. ) D = –D

        DEN = D

        RETURN

        END

        SUBROUTINE SLVH ( DEN , DENHE , XLAT , SDA )
C**********************************************************************
C*
C*  Subroutine 'SLVH' computes the seasonal–latitudinal variation of
C*  the helium number density according to L. Jacchia, Smithsonian
C*  Astrophysical Observatory 332, 1971.  This correction is not
C*  important below about 500 km.
C*
C*  DEN         = density (log10)
C*  DENHE       = helium number density (log10)
C*  XLAT        = latitude (rad)
C*  SDA         = solar declination angle (rad)
C*
C**********************************************************************
```

APPENDIX B MARSHALL ENGINEERING THERMOSPHERE MODEL PROGRAM LISTING (PAGE 30 OF 30)

```
      D0 = 10. ** DENHE

      A = ABS(0.65 * ( SDA / 0.40909079 ))

      B = 0.5 *XLAT
C*
C*  Check to compute absolute value of 'B'
C*
      IF ( SDA .LT. 0. ) B = –B
C*
C*  Compute X, Y, DHE and DENHE
C*
      X  = 0.7854 – B

      Y  = ( SIN (X) ) ** 3

      DHE= A * ( Y – 0.35356 )

      DENHE = DENHE + DHE
C*
C*  Compute helium number density change
C*
      D1 =        10. ** DENHE
      DEL=        D1 – D0
      RHO=        10. ** DEN
      DRHO        = ( 6.646E–24 ) * DEL
      RHO         = RHO + DRHO
      DEN         = ALOG10 (RHO)

      RETURN

      END
```